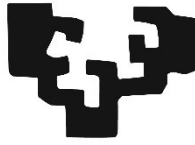


eman ta zabal zazu



Universidad
del País Vasco

Euskal Herriko
Unibertsitatea

MAGNETO DRIVEN SMART MATERIALS FOR SENSING AND ACTUATION

by

Udara Bimendra Gunatilake

Dissertation submitted to the

University of the Basque Country

for the degree of

Doctor of Philosophy

2022

Advisors

Assoc. Prof. Fernando Benito-Lopez

Prof. Lourdes Basabe-Desmots

Declaration

I hereby certify that this thesis has been composed solely by myself, and that it has not been submitted, in whole or in part, in any previous application for a degree, and I have fairly ensured the work is original to the best of my knowledge. Except where states otherwise by reference, citations or acknowledgment.

.....

Udara Bimendra Gunatilake

Date :

Table of Contents

| | |
|--|----|
| CHAPTER 1 | 1 |
| Introduction | |
| 1.1 General Introduction | 3 |
| 1.2 Flow of the thesis | 5 |
| 1.3 State of art and objectives of the thesis..... | 5 |
| 1.4 Introduction to the Chapters..... | 7 |
| 1.5 References..... | 10 |
| | |
| CHAPTER 2 | 15 |
| Literature Review | |
| 2.1 Magnetite (Fe ₃ O ₄) nanoparticles..... | 17 |
| 2.1.1 Synthesis of magnetite nanoparticles by the co-precipitation technique | 17 |
| 2.1.2 Superparamagnetic behaviour of the magnetite nanoparticles | 18 |
| 2.2 Fe (carbonyl iron) microparticles..... | 19 |
| 2.3 Magnetic alginate hydrogels | 19 |
| 2.4 Biosensor platforms for colorimetric detection of sweat biomarkers..... | 20 |
| 2.5 Magneto driven hydrogel colorimetric biosensor scaffolds..... | 23 |
| 2.6 Low surface energy magneto actionable particle systems..... | 24 |
| 2.6.1 Superhydrophobicity principle..... | 25 |
| 2.6.2 Synthesis of superhydrophobic magnetic particles..... | 25 |
| 2.7 Superhydrophobic magnetic particle systems and applications..... | 27 |
| 2.7.1 Magnetic liquid marbles | 28 |
| 2.7.2 Magnetic inverse liquid marbles | 36 |
| 2.7.3 Oil spills capturing oleophilic colloids | 37 |
| 2.8 References..... | 38 |

| | |
|---|----|
| CHAPTER 3 | 47 |
| <i>Ex situ</i> and <i>in situ</i> Magnetic Phase Synthesised Magneto-Driven Alginate Beads | |
| 3.1 Introduction..... | 50 |
| 3.2 Experimental | 52 |
| 3.2.1 Synthesis of the Fe ₃ O ₄ nanoparticles | 52 |
| 3.2.2 Synthesis of the alginate beads | 52 |
| 3.2.3 Characterisation of the nanoparticles and the magnetic beads | 53 |
| 3.3 Results and Discussion | 53 |
| 3.3.1 Stability of the beads in aqueous media..... | 54 |
| 3.3.2 Morphological characterisation of the beads | 58 |
| 3.3.3 Morphological characterisation of the magnetic nanoparticles synthesised in the bead-b type | 60 |
| 3.3.4 Chemical characterisation of the nanoparticles and the beads..... | 61 |
| 3.3.4.1 XRD | 61 |
| 3.3.4.2 Raman spectra..... | 62 |
| 3.3.4.3 FTIR spectra..... | 64 |
| 3.3.5 Magnetic characterisation | 66 |
| 3.4 Conclusions..... | 68 |
| 3.5 References..... | 69 |
| | |
| CHAPTER 4 | 77 |
| TiO₂ Nanotubes Alginate Hydrogel Scaffold for Rapid Sensing of Sweat Biomarkers - Lactate and Glucose | |
| 4.1 Introduction..... | 80 |
| 4.2 Experimental | 81 |
| 4.2.1 Synthesis and characterisation of the TiO ₂ nanotubes..... | 81 |
| 4.2.2 Preparation of the artificial sweat stock solution..... | 82 |
| 4.2.3 Fabrication of the alginate/TNT scaffolds and analysis | 82 |
| 4.2.4 Scaffold integration to filter paper | 84 |
| 4.3. Results and Discussion | 84 |

| | |
|--|-----|
| 4.3.1 Morphological and structural characterisation of the scaffold | 84 |
| 4.3.2 Artificial sweat biomarkers sensing reaction mechanism..... | 90 |
| 4.3.3 Biosensing performance of TNT/alginate scaffolds | 92 |
| 4.3.4 Colorimetric signal readout characterisation | 98 |
| 4.3.5 Study of the possible interferences caused by the catalytic properties of TNT | 99 |
| 4.3.6 Scaffold integration on paper-based sensing platform..... | 101 |
| 4.3.7 Stability of the TNT/alginate scaffold | 104 |
| 4.4 Conclusions..... | 105 |
| 4.5 References..... | 105 |
| | |
| CHAPTER 5 | 115 |
| Lab-in-a-Bead: Magnetic Janus Bead Probe for the Detection of Biomarkers in Whole Blood | |
| 5.1 Introduction..... | 118 |
| 5.2 Experimental..... | 120 |
| 5.2.1 Synthesis of TiO ₂ nanotubes | 120 |
| 5.2.2 Synthesis of C ₈ -Fe particles | 120 |
| 5.2.3 Fabrication of the Janus bead..... | 120 |
| 5.2.4 Colorimetric signal readout analysis..... | 121 |
| 5.2.5 Glucose determination by the Janus bead | 121 |
| 5.2.6 Characterisation | 122 |
| 5.3 Results and Discussion | 122 |
| 5.3.1 Synthesis and characterization of the Janus bead | 122 |
| 5.3.2 Remote stimuli Janus bead..... | 127 |
| 5.3.3 Non-interference of the red blood cells to the Janus bead | 129 |
| 5.3.4 Glucose sensing by the Janus bead. | 132 |
| 5.4 Conclusions..... | 134 |
| 5.5 References..... | 135 |

| | |
|---|-----|
| CHAPTER 6 | 139 |
| Magneto Twister: Magneto deformation of water-air interface by a superhydrophobic magnetic nanoparticles layer | |
| 6.1 Introduction..... | 144 |
| 6.2 Experimental..... | 145 |
| 6.2.1 Synthesis of superhydrophobic magnetic particles..... | 145 |
| 6.2.2 Magneto deformation of SMNPs confined water-solid-air interface | 145 |
| 6.2.3 Water droplet transport on aqueous media | 146 |
| 6.2.4 Magneto controllable plugs formation..... | 146 |
| 6.2.5 Removal of floating microplastics from the water interface | 147 |
| 6.2.6 Characterisation | 147 |
| 6.3 Results and Discussion | 147 |
| 6.3.1 Synthesis and characterisation of the superhydrophobic magnetic particles | 147 |
| 6.3.2 Magneto deformation of the water-air interface | 151 |
| 6.3.3 Water droplet transport on aqueous surface..... | 157 |
| 6.3.4 Magneto controllable plugs..... | 160 |
| 6.3.5 Removal of floating microplastics using the twister from the water interface | 162 |
| 6.4 Conclusions..... | 164 |
| 6.5 References..... | 165 |
| | |
| CHAPTER 7 | 169 |
| Underwater Magneto-Driven Air De-bubbler | |
| 7.1 Introduction..... | 174 |
| 7.2 Experimental..... | 177 |
| 7.2.1 Characterisation of the SMPs and the SMPs de-bubbler | 177 |
| 7.2.2 Fabrication of the microfluidic devices and removing of the air bubble in the channels..... | 177 |
| 7.3 Results and Discussion | 179 |
| 7.3.1 Characterisation of the magneto-driven underwater superaerophilic de-bubbler | 179 |

| | |
|--|-----|
| 7.3.2 Gas loading/attraction of SMPs under the magnetic field | 186 |
| 7.3.3 Underwater surfaces air de-bubbler: magneto targeted air collection, merging and manipulation..... | 190 |
| 7.3.4 Air de-bubbler application in microfluidics channels..... | 194 |
| 7.4 Conclusions..... | 197 |
| 7.5 References..... | 197 |
| | |
| CHAPTER 8 | 201 |
| Overall Conclusion | |
| | |
| Acknowledgements | 209 |
| | |
| Curriculum Vitae | 211 |
| | |
| Publications and Conferences | 213 |

List of Abbreviations

| | |
|-----------------|--|
| ∇B | Magnetic field gradient |
| 1-D | One-dimensional |
| 2-D | Two-dimensional |
| 3D | Three-dimensional |
| AMF | alternating magnetic field |
| B&W | black and white values |
| BCA, θ_b | Air-bubble contact angle |
| BM | Bubble-marble |
| B_r | Remanence field |
| BRE | Bubble removal efficiency |
| BSA | Bovine serum albumin |
| C_8 -Fe | Octyl carbon chain coated iron |
| CA | Contact angle |
| CS | Conical spike |
| D_c | Critical size D_c |
| DLS | Dynamic light scattering |
| DMSO | Dimethyl sulfoxide |
| DNA | Deoxyribonucleic acid |
| EDX | Energy Dispersive X-Ray |
| FD-POSS | Fluorinated decyl polyhedral oligomeric silsesquioxane |
| FLAMS | Ferrofluid-infused laser-ablated micro-structured surfaces |
| F_m | Magnetic force |
| FTIR | Fourier-transform infrared |
| GOX | Glucose oxidase |
| h | Height |
| H_c | Coercivity |
| HRP | Horseradish peroxidase |
| iNLMs | Hydrophobic Fe_3O_4 nanocubes coated liquid marbles |
| JCPDS | Joint Committee on Powder Diffraction Standards |
| LOC | Lab-on-a-Chip |
| LOD | Limit of detection |

| | |
|-----------------|---|
| LOQ | Limit of quantification |
| LOX | Lactate oxidase |
| MF | Magnetic field |
| MNPs | Magnetic nanoparticles |
| MOF | Metal–organic framework |
| Ms | Saturation magnetisation |
| n | Replications |
| NPs | Nanoparticles |
| P-aCrown | Particle-air Crown |
| PBS | Phosphate-buffered saline |
| PDI | Polydispersity index |
| PDMS | Poly(dimethylsiloxane) |
| PMMA | Polymethylmethacrylate |
| POSS | Polyhedral oligomeric silsesquioxane |
| PpIX | Protoporphyrin IX |
| PS | Polystyrene |
| PSA | Pressure sensitive adhesive |
| PTFE | Polytetrafluoroethylene |
| RBCs | Red blood cells |
| RGB | Red Green Blue |
| Rm | Remanence |
| SD | Standard deviation |
| SEM | Scanning electron microscopy |
| SMNPs | Superhydrophobic magnetic nanoparticles |
| SMPs | Superhydrophobic magnetic particles |
| SQUID | Superconducting quantum interference device |
| TEM | Transmission electron microscopy |
| TMB | 3,3',5,5' tetramethyl-benzidine |
| TNT | Titanium dioxide nanotubes |
| UCNPs | Up-conversion nanoparticles |
| UV-Vis | Ultraviolet–visible |
| WCA, θ_w | Water contact angle |
| WP | Work package |

| | |
|------------------|--|
| XRD | X-ray powder diffraction |
| $\Delta\chi$ | Magnetic susceptibilities |
| λ_{\max} | Strongest photon absorption wavelength |

Introduction

1.1 General introduction

The discovery of new materials and their continuous development are making a great impact on the evolution of human civilisation since the “Stone Age”. Nowadays, smart materials are reaching great attention, revolutionising the way humans develop new technologies. Remotely manipulable smart materials change their behaviour in a systematic and controllable manner as a response to a certain stimulus. The unlimited usability and their applicability span from small-scale domestics to high technological robotics and medicinal devices.

Nature is the origin of most of the phenomena that scientists try to understand and to mimic for the development of humankind and societal standards. Response to external stimuli is a widely available natural occurrence. Examples are the Venus flytrap plant, which closes their leaves under the mechanical stimulation of triggered hairs,¹ the Pine cones, which swell or shrink in response to humidity² or the *cis-trans* isomerism of retinal in vision, induced by light.³ Inspired by nature, scientists are developing smart materials that respond to stimuli such as light, temperature, pH, enzymes, electric field, magnetic field and forth on.⁴⁻¹¹

Among the above external stimuli, magnetic field responsive materials play an important role due to their remote controllability, easy adaptability in micro-technologies, non-invasiveness and biocompatibility. Wireless-based powering and actuation is the greatest advantage achieved by magneto responsive materials, where remote handling is possible by remotely connecting the magneto responsive materials (*e.g.* particles, beads, robots or composites) to a permanent magnet, electro magnet or to a programmed magnetic system. The integration of these materials into devices improves their operability increasing their value. As examples in microfluidics, magnetic nanoparticles were used to mix liquids due to the torque generation under a rotating magnetic field.¹² Recently, a magnetostaltic pumping method was introduced by surrounding liquid channels by an immiscible magnetic liquid, and stabilised by a quadrupolar magnetic field, to generate self-healing, non-clogging, anti-fouling and near-frictionless liquid-in-liquid fluidic channels.¹³

Most commonly, magneto responsive materials (micro/nanoparticles or particles integrated with a polymer or ceramic matrix) can be applied into microtechnology based applications by using different phenomena such as magnetic guidance, magnetic

deformation, thermal energy generation, and so on.¹⁴ The controlled displacement of the magneto responsive material to a targeted position is interpreted as magnetic guidance. This is used for biomedical, microfluidics and environmental applications such as the control of drug delivery,^{15,16} or the separation of analytes.¹⁷⁻¹⁹ Further, magnetic guidance is applied in liquid droplet transportation and manipulation in digital microfluidics.²⁰⁻²² In Lab-on-a-Chip (LOC) technology, which is a miniaturised microfluidics platform with multiple operational units such as liquid handling, chemical reaction and analysis,²³ the integration and manipulation of complex systems are challenging within the limited space provided by the LOC devices. In this regard, magnetic field-induced magneto guidance mode with engineered systems are emerging tools to handle the required chemical or biological samples. Another source of applications of magneto responsive materials is their deformation capacity under an applied magnetic field. Engineered soft magnetic materials (mostly magnetic particles integrated gels and elastomers) follow stretching, contracting and bending type of deformations under a programmed induction of magnetic field. This phenomenon is used by artificial cilia, for the creation of pumps in microfluidics devices²⁴⁻²⁷ and for the generation of smart surfaces for the manipulation of droplets and bubbles.²⁸ Magnetic particles or composite actuation enables the generation of thermal energy, which has been applied for bio medical applications such as magnetic hyperthermia. In addition, magnetic nanoparticles can be concentrated around a tumour and heated, by a remote applied magnetic field, achieving hyper-thermic temperatures (42 - 45 °C), removing the tumour.^{29,30} Moreover, heat induction through an applied magnetic field can be used to change the structure of materials for the controlled release of drugs in cancer therapy, called magneto-chemotherapy.³¹ Besides, magnetic particles integrated into thermo-responsive shape memory polymers have been found to trigger magnetic actuation and induce thermally driven shapeshifting.³²

In most of the cases discussed above, the magneto response phase is formed by magnetic micro/nanoparticles integrated, or not, into a non-magnetic polymer matrix, to achieve the required magneto responsive conditions for the desired applications.

Most of the elements in the periodic table are referred to as “non-magnetic or paramagnetic while Fe, Co, Ni in the d-block and the Gd from the f-block exhibit ferromagnetism at room temperatures, exhibiting good response to the magnetic field. In addition, emerging attention is taken to soft magnetic materials, which show low

coercivity and easy demagnetisation, for most of the previously presented applications. In particular, metallic Fe, Co, Ni micro/nanoparticles and their oxides are vastly investigated and applied in magnetic guidance, material deformation, and thermal generation because of their considerable high magnetisation, as mentioned above. Among them, magnetite (Fe_3O_4) and maghemite ($\gamma\text{-Fe}_2\text{O}_3$) nanoparticles, which comprise over 16 distinct species of iron oxides, play a vital role as magneto active materials for health and environmental applications due to their low toxicity, surface reactivity and high saturation magnetisation.

The main objective of this thesis is to introduce novel types of magneto-driven smart materials systems for biosensing and actuation purposes, their characterisation and applicability on microtechnology. The findings of this thesis add fundamental knowledge to the magnetism and smart material fields, while show direct applications of magnetic materials in the sensor and the microfluidics fields.

1.2 Flow of the thesis

This thesis focus on the investigation of remote stimuli, magneto-driven advanced materials for biosensing and actuation. In this regard, two research lines or working packages (WP) were investigated.

- WP-1: universal magneto-driven hydrogel scaffolds for efficient biosensing and actuation, divided in three experimental Chapters.
- WP-2: low surface energy magneto particle systems as actuators in LOC microtechnology, divided in two experimental Chapters.

1.3 State of art and the objectives of the thesis

The objective of this work is to investigate on magneto-based remote stimuli materials and on smart magnetic platforms based on those materials for applications in microfluidics (biosensing and actuation). Several scientific sub-objectives have been planned for the two WPs of this thesis.

WP-1 introduces a novel type of magneto-driven universal hydrogel-based sensor scaffold for rapid sensing of biomarkers in body fluids, sweat and blood.

Sub-objective 1: Stability of *ex-situ* and *in-situ* magnetic alginate matrixes. When integrating magnetic properties to a hydrogel (alginate) miniaturised scaffold for magnetic-driven applications, it is essential to understand the stability of the scaffold in an aqueous medium. In literature, both the *ex-situ* and *in-situ* magnetic phase fabrication and integration into alginate matrixes were reported, and presented in Chapter 2 and 3, but scarce knowledge is available on comparative understanding of the properties and the stability between those fabrication processes. In this regard, the properties and the stability of *ex-* and *in-situ* synthesised magnetic alginate hydrogels were investigated, and the results presented in Chapter 3.

Sub-objective 2: Sensing scaffolds based on alginate materials. In biosensing based microfluidics devices, sensing scaffolds are essential, acting as the brain of the device; in particular, for devices that require an enzyme-catalysed optical sensing signal. In this regard, different types of platforms were reported in the last decade, as discussed in Chapter 2. However, the improvement of the loading capacity of sensing assays into the scaffolds and fast colorimetric sensing is still challenging. Therefore, hydrogel based materials were investigated in Chapter 4 in order to achieve, better optical signals and response times by improving the loading capacity of the scaffolds.

Sub-objective 3: Sensing and actuation scaffolds based on magnetic alginate materials. The possibility to remotely handling, programming, and manipulating sensor scaffolds in microfluidics devices improves the functionality of the devices by adding-up extra value to the scaffold. However, the integration of the magnetic phase to the sensor scaffold, as mentioned in Chapter 3, is not possible due to the intrinsic dark colour of the magnetic phase, since it hinders the colorimetric response of the sensor. Therefore, in Chapter 5, the objective is to fabricate a colorimetric sensing system based on a polymeric scaffold with magnetic properties to be applied to the direct detection of biomarkers in blood samples.

WP-2 introduces superhydrophobic magnetic particles as novel magnetic manipulation systems in water medium.

Sub-objective 4: Low surface energy magnetic particles in micro-technologies. Magnetic particles with a reduced surface energy are able to repel water while showing magnetic properties. Recently, superhydrophobic magnetic particles systems (only

particles), which can be actuated by a magnetic field have been utilised significantly in microfluidics, biomedical and environmental applications, as presented in Chapter 2. With the objective of introducing new types of particles systems, capable of addressing the drawbacks faced by current systems such as the low stability of the magnetic liquid marble while magnetic transporting of liquid droplets and the study of novel microfluidics and environmental applications are presented in Chapter 6.

Sub-objective 5: Removal air bubbles in microfluidics channel by low surface energy magnetic particles. The deposition of air bubbles is one of the biggest problems in microfluidics channels and underwater systems. Moreover, air bubble evacuation in these types of systems is still a challenging task. Chemically modified magnetic particles have potential to address this problem, due to their remote controllability and superaerophilicity properties. In Chapter 7, the applicability of superhydrophobic magnetic particles (SMPs) was investigated with the purpose of introducing a cheap and simple protocol to remove air bubbles in microfluidic channels.

1.4 Introduction to the Chapters

Chapter 2:

The general principles and the properties of the main functional materials that will be utilised in the experimental Chapters 3-7 are presented in this Chapter. Moreover, an updated literature survey of the different sweat sensor material platforms and the progresses done on magnetic superhydrophobic particle systems are also included.

Chapter 3

Alginates are colloidal polysaccharides that readily cross-link with multivalent metal ions, which keeps the polymer as a three-dimensional hydrogel material. The material can show magnetic properties upon *ex-situ* or *in-situ* integration of magnetic phase (superparamagnetic Fe₃O₄ nanoparticles), Figure 1.1 (left). However, the *ex-situ* and *in-situ* magnetic hydrogels exhibit different behaviours in the aqueous medium. Therefore, a comparative comprehension of their properties is essential prior their implementation. In this Chapter, the hydrogels were synthesised following two fabrication processes and subsequently, fully characterised. It was found out that, they

exhibited particular stabilities to different pH and ionic strengths conditions in aqueous solutions. These are essential properties to be controlled when used for magneto-driven applications such as targeted drug delivery and water purification. This study will direct the path for the selection of the best magnetic bead synthesis protocol, according to the defined magneto-driven application.

Chapter 4

Versatile sensing matrices are essential for the development of enzyme immobilised optical biosensors. In this regard, this Chapter presents improved colorimetric sensing behaviour of a biosensor scaffold, by using a novel three-dimensional titanium dioxide nanotubes/alginate hydrogel. The scaffold was applied for the detection of sweat biomarkers, lactate and glucose, in artificial sweat. The superhydrophilicity and the capillarity of the synthesised titanium dioxide nanotubes, when incorporated into the alginate matrix, facilitate the rapid transfer of the artificial sweat components throughout the sensor scaffold, considerably decreasing detection times. Moreover, the scaffold was integrated on a cellulose paper to demonstrate the adaptability of the material to other type of matrixes, which could have important implications in the microfluidics field.

Chapter 5

In this Chapter, the magnetic properties investigated in Chapter 3 were integrated into the titanium dioxide nanotubes/alginate hydrogel scaffold from Chapter 4. A novel Janus bead was fabricated by coupling ferromagnetic Fe microparticles to the TiO₂ nanotubes/alginate biosensing hydrogel under an applied magnetic field, avoiding the inherent magnetic phase dark coloration in the colorimetric sensing side of the bead, Figure 1.1 (right). This Janus bead was applied for the colorimetric detection of blood biomarkers, showing an accurate optical signal response avoiding colour artefacts from the red blood cells. Therefore, the multiple functionalities of this magnetic TiO₂ nanotubes/alginate Janus bead facilitate to actuate (magnetically), sense (blood or body fluid biomarkers) and filter (red blood cells) with the same material, introducing a novel Lab-on-a Bead concept.

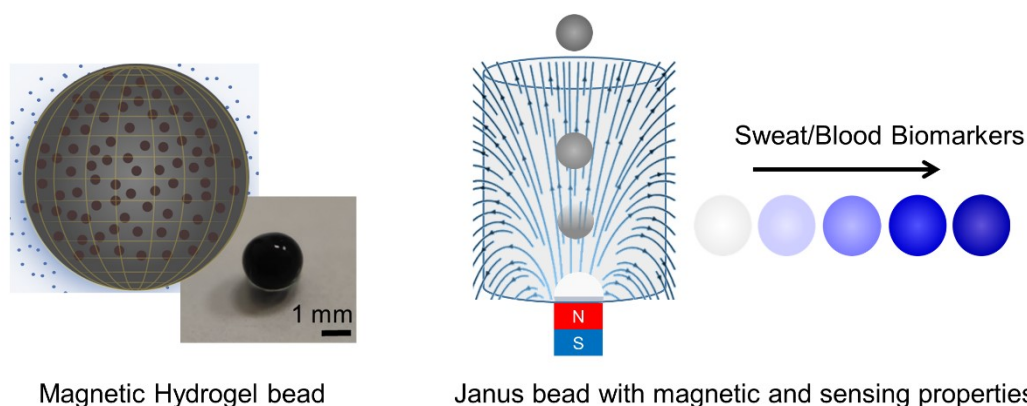


Figure 1.1. Schematic and a real image of the magneto driven alginate based hydrogels bead (left). Schematic illustration of the fabrication of the magneto driven alginate hydrogel platform, Janus bead, and colour variation for sweat and blood biomarker detection (right). (Based on Chapter 3-5).

Chapter 6

A novel remote stimulus, magneto responsive superhydrophobic nanoparticle ($C_8-Fe_3O_4$) system is introduced (exclusively by the particles), called magneto twister, Figure 1.2 (left). A floating layer of superhydrophobic magnetic particles bends downwards, forming a stable water-solid-air interface under an applied gradient magnetic field, presenting a twister like structure with a flipped conical shape under controlled water levels. When the tip of the twister structure touched the bottom of the water container, provides a stable magneto movable system in water. Three possible applications, as a proof of principle, of this structure were introduced: the cargo and transport of water droplets in aqueous media, the generation of magneto controllable plugs in open surface channels, and the removal of floating microplastics from the air-water interface.

Chapter 7

In this Chapter, superhydrophobic magnetic particles (SMPs, C_8-Fe) were applied to address one of the fundamental problems in microfluidics, the deposition of air bubbles in the surface of the aqueous channels, Figure 1.2 (right). These low surface energy C_8-Fe particles attract underwater air bubbles due to their underwater superaerophilicity while the high magnetisation of the SMPs facilitates the manipulation of the C_8-Fe - bubble system by using an external magnetic field, induced by a simple permanent magnet. The properties of the C_8-Fe -bubble system were characterised to understand

the behaviour of the proposed system in different bubble deposited surfaces. This highly efficient, cheap and simple targeted air bubble removal system brings a new solution to solve one of the biggest problems faced by microfluidics technology.

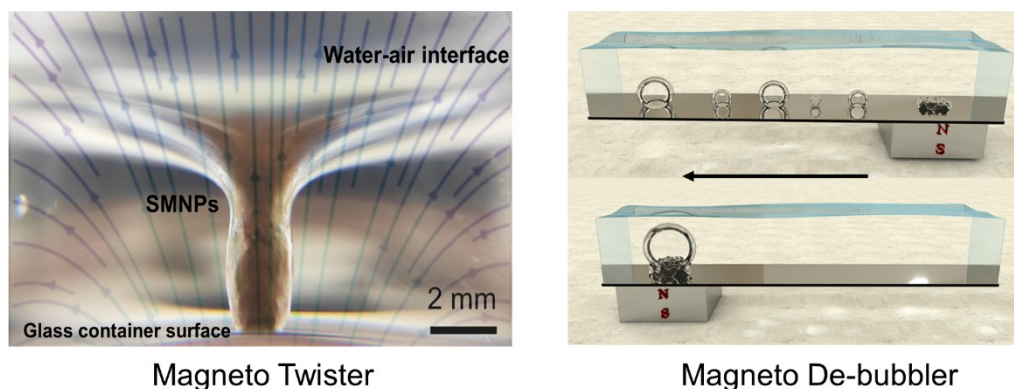


Figure 1.2. Magneto Twister: Magneto deformation of water-air interface by a superhydrophobic magnetic nanoparticle layer (left). Magneto de-bubbler: Trap, transport and evacuation of underwater free and surface deposited air bubbles by superhydrophobic magnetic particles (right). (SMNPs: superhydrophobic magnetic nanoparticles). (Based on Chapter 7-8).

Chapter 8

The overall conclusion of the work is presented in this Chapter. The generated key knowledge from the experimental, characterisation, and result of this work is briefly summarised. The importance and future challenges of these novel material platforms and systems are elaborated under the final concluding remarks.

1.5 References

- (1) Forterre, Y.; Skotheim, J. M.; Dumais, J.; Mahadevan, L. How the Venus Flytrap Snaps. *Nature* **2005**, *433* (7024), 421–425.
- (2) Reyssat, E.; Mahadevan, L. Hygromorphs: From Pine Cones to Biomimetic Bilayers. *J. R. Soc. Interface* **2009**, *6* (39), 951–957.
- (3) Saari, J. C. Vitamin A and Vision. *Subcell. Biochem.* **2016**, *81*, 231–259.
- (4) Manouras, T.; Vamvakaki, M. Field Responsive Materials: Photo-, Electro-, Magnetic- and Ultrasound-Sensitive Polymers. *Polym. Chem.* **2016**, *8* (1), 74–96.

- (5) Zhang, W.; Shi, L.; Wu, K.; An, Y. Thermoresponsive Micellization of Poly(Ethylene Glycol)-b-Poly(N-Isopropylacrylamide) in Water. *Macromolecules* **2005**, *38* (13), 5743–5747.
- (6) Lee, Y.; Fukushima, S.; Bae, Y.; Hiki, S.; Ishii, T.; Kataoka, K. A Protein Nanocarrier from Charge-Conversion Polymer in Response to Endosomal PH. *J. Am. Chem. Soc.* **2007**, *129* (17), 5362–5363.
- (7) Calderón, M.; Graeser, R.; Kratz, F.; Haag, R. Development of Enzymatically Cleavable Prodrugs Derived from Dendritic Polyglycerol. *Bioorg. Med. Chem. Lett.* **2009**, *19* (14), 3725–3728.
- (8) Mendes, P. M. Stimuli-Responsive Surfaces for Bio-Applications. *Chem. Soc. Rev.* **2008**, *37* (11), 2512–2529.
- (9) Toonder, J. den; Bos, F.; Broer, D.; Filippini, L.; Gillies, M.; Goede, J. de; Mol, T.; Reijme, M.; Talen, W.; Wilderbeek, H.; Khatavkar, V.; Anderson, P. Artificial Cilia for Active Micro-Fluidic Mixing. *Lab Chip* **2008**, *8* (4), 533–541.
- (10) Khaderi, S. N.; Toonder, J. M. J. den; Onck, P. R. Magnetically Actuated Artificial Cilia: The Effect of Fluid Inertia. *Langmuir* **2012**, *28* (20), 7921–7937.
- (11) Fleige, E.; Quadir, M. A.; Haag, R. Stimuli-Responsive Polymeric Nanocarriers for the Controlled Transport of Active Compounds: Concepts and Applications. *Adv. Drug Deliv. Rev.* **2012**, *64* (9), 866–884.
- (12) Hajiani, P.; Larachi, F. Magnetic-Field Assisted Mixing of Liquids Using Magnetic Nanoparticles. *Chem. Eng. Process. Process Intensif.* **2014**, *84*, 31–37.
- (13) Dunne, P.; Adachi, T.; Dev, A. A.; Sorrenti, A.; Giacchetti, L.; Bonnin, A.; Bourdon, C.; Mangin, P. H.; Coey, J. M. D.; Doudin, B.; Hermans, T. M. Liquid Flow and Control without Solid Walls. *Nature* **2020**, *581* (7806), 58–62.
- (14) Thévenot, J.; Oliveira, H.; Sandre, O.; Lecommandoux, S. Magnetic Responsive Polymer Composite Materials. *Chem. Soc. Rev.* **2013**, *42* (17), 7099–7116.
- (15) Arias, J. L.; Reddy, L. H.; Othman, M.; Gillet, B.; Desmaële, D.; Zouhiri, F.; Dosio, F.; Gref, R.; Couvreur, P. Squalene Based Nanocomposites: A New Platform for the Design of Multifunctional Pharmaceutical Theragnostics. *ACS Nano* **2011**, *5* (2), 1513–1521.

- (16) Dames, P.; Gleich, B.; Flemmer, A.; Hajek, K.; Seidl, N.; Wiekhorst, F.; Eberbeck, D.; Bittmann, I.; Bergemann, C.; Weyh, T.; Trahms, L.; Rosenecker, J.; Rudolph, C. Targeted Delivery of Magnetic Aerosol Droplets to the Lung. *Nat. Nanotechnol.* **2007**, *2* (8), 495–499.
- (17) Xu, F.; Geiger, J. H.; Baker, G. L.; Bruening, M. L. Polymer Brush-Modified Magnetic Nanoparticles for His-Tagged Protein Purification. *Langmuir* **2011**, *27* (6), 3106–3112.
- (18) Lai, J. J.; Nelson, K. E.; Nash, M. A.; Hoffman, A. S.; Yager, P.; Stayton, P. S. Dynamic Bioprocessing and Microfluidic Transport Control with Smart Magnetic Nanoparticles in Laminar-Flow Devices. *Lab Chip* **2009**, *9* (14), 1997–2002.
- (19) Rocher, V.; Siaugue, J. M.; Cabuil, V.; Bee, A. Removal of Organic Dyes by Magnetic Alginate Beads. *Water Res.* **2008**, *42* (4–5), 1290–1298.
- (20) Zhao, Y.; Xu, Z.; Parhizkar, M.; Fang, J.; Wang, X.; Lin, T. Magnetic Liquid Marbles, Their Manipulation and Application in Optical Probing. *Microfluid. Nanofluidics* **2012**, *13* (4), 555–564.
- (21) Wang, W.; Timonen, J. V. I.; Carlson, A.; Drotlef, D.-M.; Zhang, C. T.; Kolle, S.; Grinthal, A.; Wong, T.-S.; Hatton, B.; Kang, S. H.; Kennedy, S.; Chi, J.; Blough, R. T.; Sitti, M.; Mahadevan, L.; Aizenberg, J. Multifunctional Ferrofluid-Infused Surfaces with Reconfigurable Multiscale Topography. *Nature* **2018**, *559* (7712), 77–82.
- (22) Nasirimarekani, V.; Benito-Lopez, F.; Basabe-Desmonts, L. Tunable Superparamagnetic Ring (TSPRing) for Droplet Manipulation. *Adv. Funct. Mater.* **2021**, *31* (32), 2100178.
- (23) Yilmaz, B.; Yilmaz, F. Lab-on-a-Chip Technology and Its Applications. *Omi. Technol. Bio-engineering Towar. Improv. Qual. Life* **2018**, *1*, 145–153.
- (24) Zrínyi, M.; Barsi, L.; Büki, A. Deformation of Ferrogels Induced by Nonuniform Magnetic Fields. *J. Chem. Phys.* **1998**, *104* (21), 8750.
- (25) Hilber, W. Stimulus-Active Polymer Actuators for next-Generation Microfluidic Devices. *Appl. Phys. A* **2016**, *122* (8), 1–39.

- (26) Zhang, S.; Wang, Y.; Lavrijsen, R.; Onck, P. R.; den Toonder, J. M. J. Versatile Microfluidic Flow Generated by Moulded Magnetic Artificial Cilia. *Sensors Actuators B Chem.* **2018**, *263*, 614–624.
- (27) Li, J.; Zhang, M.; Wang, L.; Li, W.; Sheng, P.; Wen, W. Design and Fabrication of Microfluidic Mixer from Carbonyl Iron–PDMS Composite Membrane. *Microfluid. Nanofluidics* **2010**, *10* (4), 919–925.
- (28) Guo, P.; Wang, Z.; Heng, L.; Zhang, Y.; Wang, X.; Jiang, L. Magnetocontrollable Droplet and Bubble Manipulation on a Stable Amphibious Slippery Gel Surface. *Adv. Funct. Mater.* **2019**, *29* (11), 1808717.
- (29) Fortin, J.-P.; Gazeau, F.; Wilhelm, C. Intracellular Heating of Living Cells through Néel Relaxation of Magnetic Nanoparticles. *Eur. Biophys. J.* **2007**, *37* (2), 223–228.
- (30) Medeiros, S. F.; Santos, A. M.; Fessi, H.; Elaissari, A. Stimuli-Responsive Magnetic Particles for Biomedical Applications. *Int. J. Pharm.* **2011**, *403* (1–2), 139–161.
- (31) Sanson, C.; Diou, O.; Thévenot, J.; Ibarboure, E.; Soum, A.; Brûlet, A.; Miraux, S.; Thiaudière, E.; Tan, S.; Brisson, A.; Dupuis, V.; Sandre, O.; Lecommandoux, S. Doxorubicin Loaded Magnetic Polymersomes: Theranostic Nanocarriers for MR Imaging and Magneto-Chemotherapy. *ACS Nano* **2011**, *5* (2), 1122–1140.
- (32) Mohr, R.; Kratz, K.; Weigel, T.; Lucka-Gabor, M.; Moneke, M.; Lendlein, A. Initiation of Shape-Memory Effect by Inductive Heating of Magnetic Nanoparticles in Thermoplastic Polymers. *Proc. Natl. Acad. Sci.* **2006**, *103* (10), 3540–3545.

Literature Review

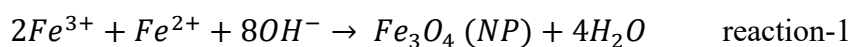
2.1 Magnetite (Fe₃O₄) nanoparticles

Magnetite crystals, Fe₃O₄ or formally FeO·Fe₂O₃, exhibit a black or dark brown colour with a density of 5.18 g cm⁻³ and a molar ratio of ferrous (Fe²⁺) to ferric (Fe³⁺) ions 1:2.¹ In magnetite, Fe³⁺ ions have five lone pair electrons at 3d orbitals ([Ar]3d⁵) and Fe²⁺ ions have four lone pair electrons at 3d orbitals ([Ar]3d⁶), showing magnetic properties. Moreover, it possesses an inverse spinel structure, occupying Fe³⁺ in tetrahedral sites and both Fe³⁺ and Fe²⁺ in octahedral sites. Furthermore, the Fe³⁺ in tetrahedral sites and Fe³⁺/Fe²⁺ in octahedral sites exhibit a ferromagnetic and antiferromagnetic alignment of the magnetic moments, respectively, by obtaining an overall ferrimagnetic behaviour for the magnetite crystals.

2.1.1 Synthesis of magnetite nanoparticles by the co-precipitation technique

Among the diverse methods of magnetite nanoparticles synthesis, such as hydrothermal and high temperature reactions, sol-gel reactions, polyol processes, electrochemical protocols, aerosol/vapour method, microemulsions and sonochemical reactions, the co-precipitation technique attract great attention since its efficiency, cost-effectiveness and simplicity are well demonstrated.²

During the co-precipitation chemical process, aqueous salts of Fe³⁺:Fe²⁺ with 2:1 ratio react with a highly basic solution under a non-oxygen environment at room or raised (40-90 °C) temperatures according to the stoichiometric ratios mentioned in reaction-1.³ Complete precipitation of black or dark brown coloured Fe₃O₄ nanoparticles are expected at pHs between 10 to 14.



The nucleation, growth and phase transition of the magnetite nanoparticles at the reaction pathways in the co-precipitation of magnetite depend on the pH of the system, as depicted in the Figure 2.1. Akaganeite phase is nucleated and transformed through goethite to the magnetite while the slow addition of the base (low pH system) and ferrous hydroxide phase is nucleated and transformed through lepidocrocite to magnetite during the fast addition of the base (high pH system) to the Fe³⁺/Fe²⁺ salt solution, respectively.⁴

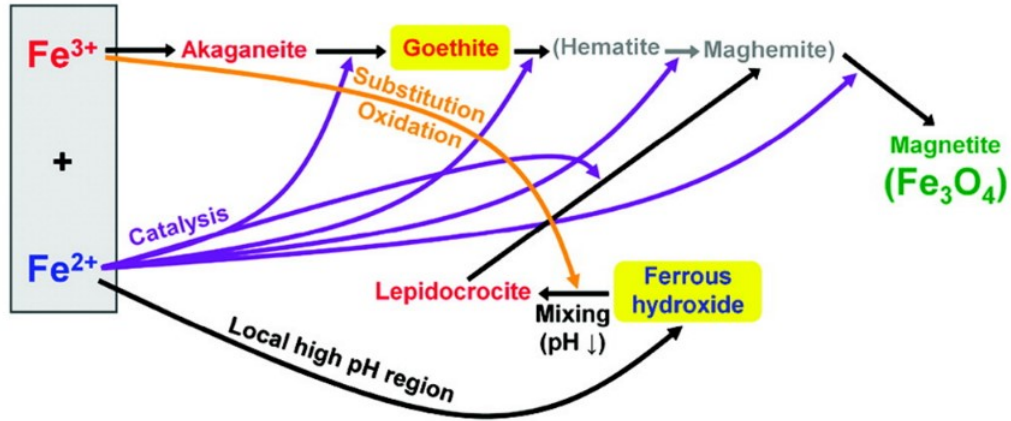


Figure 2.1. Formation pathways of magnetite nanoparticles by the co-precipitation method. (Adapted and reproduced from the ref.⁴ with the permission from ©2012 American Chemical Society.)

However, bare magnetite nanoparticles are not highly stable, since they are sensitive to the oxidation to maghemite ($\gamma\text{Fe}_2\text{O}_3$). The oxidation of the ferrous ion causes the formation of a cation vacancy in the octahedral site. As well, the desorption of the Fe^{2+} ion as a hexa-aqua complex is also possible under acidic and anaerobic conditions.² However, the lack of proper crystallinity and the broad particle size distribution are the main drawbacks of this co-precipitation method.

2.1.2 Superparamagnetic behaviour of the magnetite nanoparticles

In ferromagnetic or ferrimagnetic nanoparticles if the diameter of the particles reduces to a certain size, called the critical size (D_c), then the particles become a single domain. The estimated D_c for Fe_3O_4 is $\sim 64 \text{ nm}$.⁵ In these particles, the Neel's relaxation time, the time between random two flips of magnetisation, is lower than the time to take the measure of the magnetisation in the nanoparticles without the magnetic field. Thus, their magnetisation appeared to be zero. Therefore, this state is set to be superparamagnetic in which no hysteresis loop can be observed as depicted in Figure 2.2. These superparamagnetic particles show zero or no remanence and coercivity. In the superparamagnetic state, the magnetic particles can be magnetised with an external magnetic field and going back to the non-magnetic state, when removing the magnetic field, without keeping residual magnetisation as paramagnets, but with a much larger magnetic susceptibility.⁵ Therefore, this property is utilised in biomedical, ferrofluids

and actuators applications due to their low remanence and the high magnetisation. Saturation magnetisation of co-precipitately synthesised Fe_3O_4 nanoparticles are usually from 50 to 80 $\text{Am}^2 \text{kg}^{-1}$.

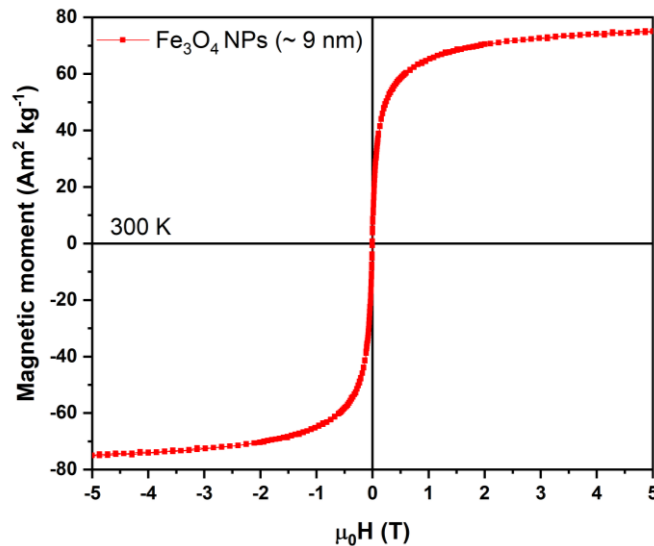


Figure 2.2. Superconducting quantum interference device (SQUID) magnetisation loop of co-precipitately synthesised ~ 9 nm magnetite nanoparticles. (Own laboratory synthesised nanoparticles).

2.2 Fe (carbonyl iron) microparticles

Fe microparticles are ferromagnetic soft magnetic material synthesised by treating Fe with the carbon monoxide under heat and pressure, followed by the decomposition of the resulting pentacarbonyl iron $\text{Fe}(\text{CO})_5$ under controlled conditions.⁶ Usually, these particles show grey colour with a spherical shape and 1-10 μm average size. They show high saturation magnetisation $\sim 240 \text{Am}^2 \text{kg}^{-1}$, 4 times higher than Fe_3O_4 nanoparticles, due to their ferromagnetic behaviour. They are widely used magnetorheological suspensions, in which the rheological properties can be reversibly changed by a magnetic field. They assemble to a chain-like structure along the direction of the field, under an external magnetic field, behaving as viscoplastic solids.⁷

2.3 Magnetic alginate hydrogels

Hydrogels are water-swollen polymeric hydrophilic materials with a three-dimensional network structure, which form by chemical or physical crosslinking. They are made of

natural or synthetic polymers, homo or copolymeric fractions and blends. The water absorption capability of the hydrogels mainly arises from the hydrophilic functional groups attached to the polymeric backbone, while their resistance to the degradation or dissolution comes from the strength of the crosslinks between network chains.⁸

In particular, alginates are colloidal polysaccharides isolated from brown algae, which are abundant in coastal waters. They are linear copolymers containing *D*-mannuronic acid and *L*-guluronic acid residues covalently linked together in different configurations.⁹ Alginates cross-link with multivalent metal ions (*e.g.* Ca²⁺, Ba²⁺)¹⁰ following the “egg-box” model, which keeps the polymer as a three dimensional gelling material.¹¹

Magnetic alginate nanocomposites are attracting attention because of their excellent biocompatibility and the possibility of remote manipulation.^{12,13} These magneto-driven alginate nanocomposites have been used in biomedical applications like targeted drug delivery, magnetic triggering drug release, enzyme immobilisation and magnetic hyperthermia.^{14–18} Moreover, they have been employed for environmental applications like the magnetic removal of heavy metals, organic contaminants and dyes from water.^{19–21} Interestingly, magnetic alginate nanocomposites microstructures have been fabricated and applied as magnetic actuators and micro-helical capsule robots.²² There are several methods to fabricate magnetic alginate materials by physical cross-linking such as, *ex-situ* blending of Fe₃O₄ nanoparticles with the alginate matrix or *in-situ* synthesis of Fe₃O₄ nanoparticles in the alginate matrix.^{23,24} In the second method, a cross-linking process with ferrous and ferric cations forms the alginate hydrogel. Then, the alginate is subjected to a highly alkaline solution where the Fe₃O₄ NPs are synthesised inside.²⁴ A comparative fundamental understanding of the properties and the behaviour of the *ex-situ* and *in-situ* magnetic phase derived hydrogels, particularly their stabilities in aqueous medium is essential, and generates the background knowledge while implementing in applications as mentioned in the sub-objective 1.

2.4 Biosensor platforms for colorimetric detection of sweat biomarkers

Miniaturised biosensors have been widely investigated due to their low production cost, portability and ease of operation.^{25–29} In general, a power-free, simple signal-reading phenomenon is essential for real time body fluid (particularly sweat) analysis in a

wearable device format. In this regard, colorimetric sensing provides simple signal readout capabilities and it provides rapid analysis, by measuring the colour variation of the analyte by absorbance measurements or analysing colour parameters such as RGB or HUE by image analysis. Thereby, colorimetric detection of biomarkers becomes a simple, cheap and easily implementation in wearable devices.

Nevertheless, the performance of the sensing platform also plays a vital role in these types of wearable devices, where investigations and developments of different sensor scaffolds will bringing these devices from the lab to society.²⁸ In particular, paper is one of the most commonly used matrixes for colorimetric analysis in wearable microfluidics due to its low cost, biodegradability, biocompatibility, flexibility and reduced weight. A paper-based skin patch pH test paper device, based on an anion exchanger is introduced for the colorimetric detection of anions, Figure 2.3a.³⁰ In another example, a wearable advanced microfluidic device for the capture, storage, and analysis of the sweat components by integrating a paper matrix to immobilise the colorimetric assays is presented in Figure 2.3b.³¹ Recently, as shown in the Figure 2.3c, Promphet *et al.*³² fabricated a chitosan modified cotton textile platform to detect pH and lactate from sweat in a wearable format.³² An interesting example was presented by He *et al.*³³, as a skin mounted superhydrophobic-superhydrophilic, silica coated polyethylene terephthalate band with microarrays, to be used as a sensor platform for sweat sensing, Figure 2.3d.

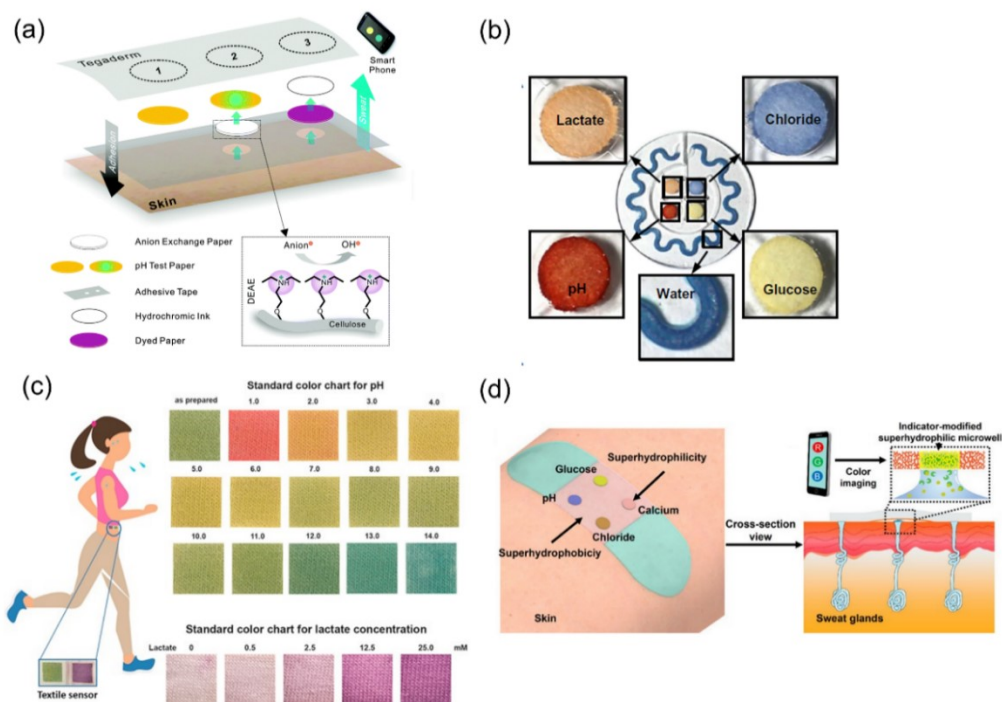


Figure 2.3. (a) Flexible paper-based skin patch consisting of both anion exchange and pH test papers to enable the quantitative, colorimetric and on-skin detection of sweat anions. (b) Colorimetric detection paper based reservoirs that enable determination of lactate, glucose, pH and chloride levels. (c) Textile-based sensor for the detection of sweat pH and lactate. (d) Superwetable and flexible band as a platform for sweat sampling and monitoring. (Adapted and reproduced from the refs.^{30, 31, 32, 33} with the permission from © The Royal Society of Chemistry 2015, ©2017 American Association for the Advancement of Science, ©2018 Elsevier B.V, ©2019 American Chemical Society.)

In the context of hydrogels, few hydrogel types were reported as sweat biomarkers sensing scaffolds. Among those, Tatiya *et al.*³⁴ reported a bacterial cellulose/ carboxymethyl cellulose hydrogel as a potential platform for non-invasive sensors for sweat pH and glucose, obtaining a signal readout after 10 min while Rusell *et al.*³⁵ reported a poly(ethylene glycol) based hydrogel with a 10-12 min response time for glucose respectively. However, long-time efficient and effective immobilisation of enzymatic biological and/or colorimetric assays, with high loading capacity and rapid sensing capabilities, are still challenging in sweat sensors, as depicted in the sub-objective 2.

2.5 Magneto driven hydrogel colorimetric biosensor scaffolds

In most of the hydrogel based miniaturised sensing systems, programmable manipulation of sensing scaffold brings an enormous value to the system. In particular, the non-invasive handling of miniaturised scaffolds for LOC technology allows automating the operational process of analytes capture, transport and sensing. Moreover, the molecules of the assay, entrapped in the hydrogel sensing scaffold, usually diffuse to the surrounding analyte solution over time. This causes ionic densities imbalances between the hydrogel and the outer solution, leading to the reduction of the amount of reactants needed for detection inside of the hydrogel scaffold, over time.³⁶ In this regard, as problem solving technique, the fast removal of the scaffold from the solution, using a smart remote controlled manipulation system, could reduce or eliminate assay leaking from the hydrogel scaffold. However, the manipulation of miniaturised biosensor scaffolds involves immense difficulties such as damaging the scaffold due to mechanical handling, contamination and requirement of human power and tools leading to inefficiency of the biosensor. As a solution, remote manipulation of the scaffold by using magnetic fields is a promising technique in miniaturised systems in order to control the scaffold in a non-invasive way. In this regard, magnetic properties can be added to the hydrogel scaffold by integrating soft magnetic particles such as magnetite nanoparticles or Fe particles, as discussed in the sections 2.1 and 2.2 with the protocols mentioned in the sub-objective 1. However, the appearance of the intrinsic dark coloration of the above-mentioned magnetic particles deviates the accuracy of the colorimetric signal readout by interfering or hindering the expecting read out.³⁷ Highly magnetic materials absorb a broad range of visible light based on the excitation of electrons close to the Fermi level, resulting in their dark appearance. This drawback is overcome by changing the outer surface colour (white or lighter) of the magnetic particles by advanced particle coating systems since it is expected that typical white colouration reflects light instead of absorb it. Recently, Seuffert *et al.*³⁸ reported an advanced particle system that combined the properties of white colour, white light emission and strong magnetism, Figure 2.4. A coating layer of titania particles was generated around iron metal (α -iron) microparticles or iron oxide (magnetite, Fe_3O_4) microparticles followed by white light emitting metal–organic framework (MOF) EuTb@IFP-1 (Imidazolate Framework Potsdam 1) modification. However, the heavy coating resulted on the reduction of the magnetisation of the particles, which led to the need of increasing the amount of the particles in the hydrogel system to get the required

magnetic moment to manipulate the hydrogel sensor. Therefore, there is still an unfilled gap to fabricate smart inexpensive and efficient magneto driven colorimetric biosensors that is led to the sub-objective 3, which is mentioned in section 1.3.

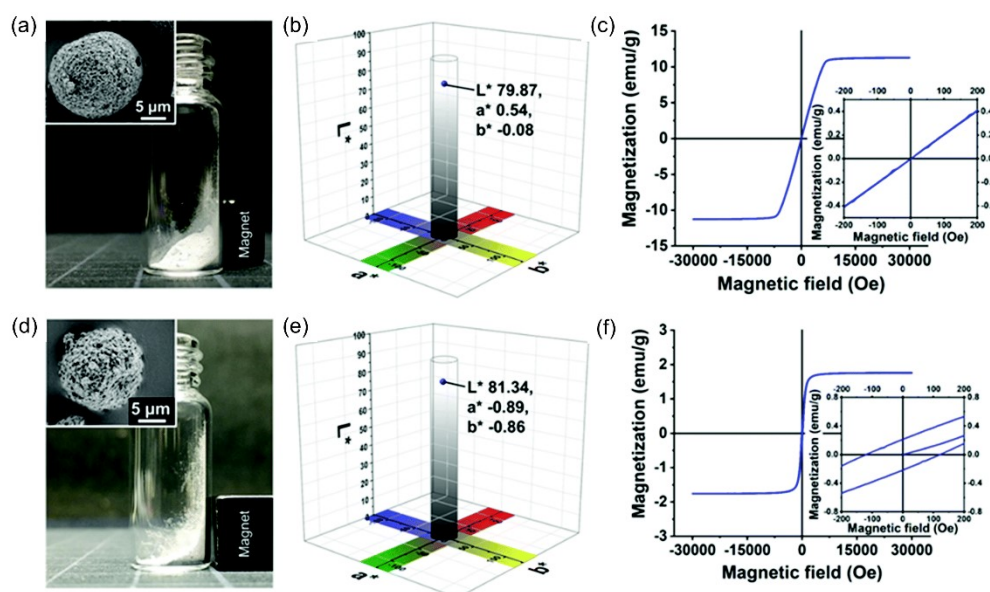


Figure 2.4. Photographs and scanning electron micrographs as insets (a and d), as well as CIE (Commission Internationale de l'Éclairage) $L^*a^*b^*$ colour values (b and e) and magnetisation measurements (c and f) of either white magnets containing iron, (a–c) or iron oxide (d–f). (Adapted and reproduced from the ref. ³⁸ with the permission from © The Royal Society of Chemistry 2020)

2.6 Low surface energy magneto actionable particle systems

The magnetic nanoparticles mentioned in the section 2.1 and the particles discussed in sub-objective 1 possess high surface energy, showing a superhydrophilic nature. As well, the surface bound hydroxyls in iron oxide nanoparticles readily attract with the water due to polar-polar interactions between surface hydroxyls and water. However, these magnetic nanoparticles can be chemically modified to settle on the water surface (water-air interface) in their low surface energy, superhydrophobic state, showing interesting phenomena, under an applied magnetic field. Therefore, in this section, different models of superhydrophobic magnetic particles systems and their water interfaces are discussed with the latest findings and the applications as a literature survey to sub-objective 4 and 5.

2.6.1 Superhydrophobicity principle

For a solid substrate, when the contact angle of water on its surface is larger than 150 °, it is called superhydrophobic. In this case, when an aqueous droplet contacts with a solid surface, the liquid can remain as a droplet by repelling the surface according to the nature of the intermolecular bonding, functional groups and physical properties of both, the solid and the liquid phases. In addition, the contact angle hysteresis is a very important phenomenon when considering liquid repellent surfaces because it exhibits the dynamic wettability of the surface. Surface energies correspond with the formation of adhesive bonds between the solid surface and the liquid. This is demonstrated by the contact angle θ (equation 2.1), which is related with the surface energies according to Young's equation 2.2.^{39,40}

$$\cos \theta = \frac{\gamma_{sv} - \gamma_{sl}}{\gamma_{lv}} \quad \text{equation 2.1}$$

$$\gamma_{sl} + \gamma_{lv} \cos \theta = \gamma_{sv} \quad \text{equation 2.2}$$

If solid-vapour interfacial energy γ_{sv} , *i.e.* the surface energy of the solid surface is higher than the solid-liquid interfacial energy and ($\gamma_{sv} > \gamma_{sl}$), $\cos \theta > 0$ then, the contact angle is below 90 °. According to this behaviour, the surface is wet by the liquid. If the solid-vapour interfacial energy γ_{sv} is lower than the solid-liquid interfacial energy and ($\gamma_{sv} < \gamma_{sl}$), $\cos \theta < 0$ then, the contact angle exceed the 90 ° and the surface is not wet by the liquid.

2.6.2 Synthesis of superhydrophobic magnetic particles

In literature, the surface of the metal oxides is usually found to bound with hydroxyls (-OH), which attract to the water molecules due to polar-polar and hydrogen bond attractions, keeping the material as hydrophilic. Therefore, in order to synthesise hydrophobic particles, the surface of the magnetic materials (*i.e.* Fe₃O₄) is covered with low surface energy materials such as, long chain hydrocarbons or fluorocarbon molecules.^{41,42} The non-polarity of these molecules repels the polar water molecules, and the higher surface roughness of the particle layer increases the hydrophobicity, achieving superhydrophobicity. Qing *et al.*⁴³ synthesised thermally stable, porous and superhydrophobic core-shell Fe₂O₃@C nanoparticles with 30-200 nm size, showing a 162.9 ° water contact angle. According to the synthesis protocol depicted in Figure 2.5a, Fe₂O₃@C nanoparticles were synthesised by the thermal decomposition of a ferric benzoate precursor at 600 °C for 6 h, followed by a treatment with 2 wt% vinyl

triethoxysilane and subsequent particles drying at 140 °C for 8 h. Moreover, Fang *et al.*⁴⁴ functionalised Fe₃O₄ magnetic nanoparticles, which were synthesised by the coprecipitation method presented in section 2.1.1, with a thin layer of fluoroalkyl silica, by using tridecafluorooctyl triethoxysilane, Figure 2.5b. In another example, Wang *et al.*⁴⁵ reported on superhydrophobic Fe₃O₄@PDA@Ag nanoparticles, which fabrication protocol included several steps of solvothermal reduction of Fe₃O₄ nanoparticles synthesis, coating of polydopamine-PDA spherical shell by a self-polymerisation process of dopamine, and coating of Ag nanoparticles on Fe₃O₄@PDA via self-assembly (Figure 2.5c), and a surface modification of 1H,1H,2H,2H-perfluorodecanethiol by a simple immersion step.

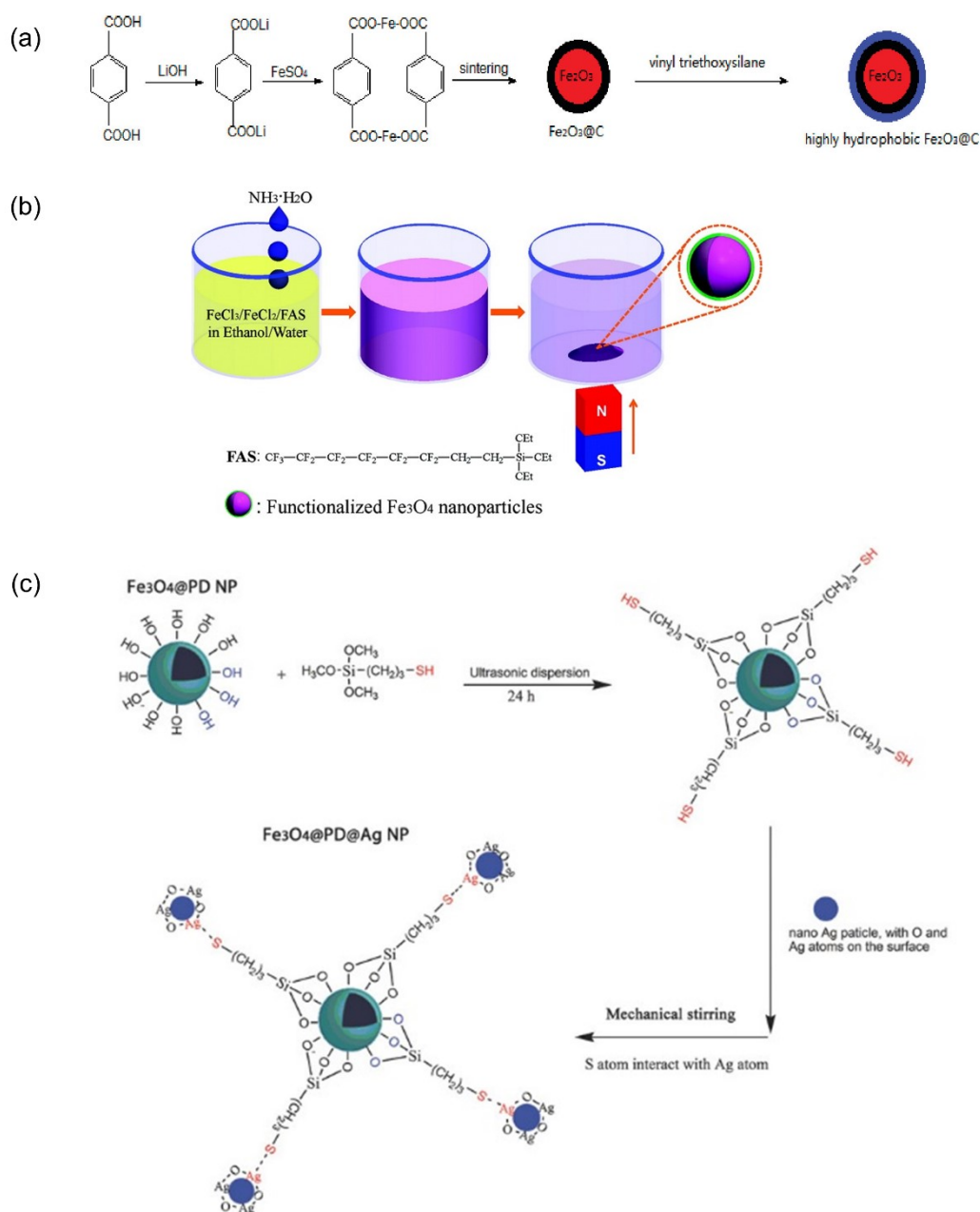


Figure 2.5. (a) Scheme of the preparation of highly hydrophobic $\text{Fe}_2\text{O}_3@\text{C}$ nanoparticles. (b) One-pot synthesis route of fluoroalkyl silica coated Fe_3O_4 hydrophobic magnetic nanoparticles. (c) Schematic illustration of the fabrication of $\text{Fe}_3\text{O}_4@\text{PDA}@\text{Ag}$ nanoparticles. (Adapted and reproduced from the refs. ^{43,44,45} with the permission from © Copyright © 2010 American Chemical Society and © 2015 WILEY-VCH Verlag GmbH & Co. KGaA, Weinheim)

2.7 Superhydrophobic magnetic particle systems and applications

Superhydrophobic nanoparticles can be used as the magnetic phase for numerous types of materials such as oil-based ferrofluids, magnetic aerogels, films, and foams.^{46–48}

Recently, emerging attraction has taken towards exclusive superhydrophobic magnetic particles systems (without any polymer or ceramic matrix), such as magnetic liquid marbles, reverse magnetic liquid marbles and oleophilic collides due to their hydrophobicity, oleophilicity, lateral capillarity, remote controllability and superparamagnetic behaviour. Therefore, in the next section the fundamentals of these models and the reported applications will be discussed.

2.7.1 Magnetic liquid marbles

Liquid marbles are stabilised discrete liquid droplets, encapsulated by hydrophobic micro or nanoparticles as shown in Figure 2.6a and b. Aussillous *et al.*⁴⁹ primarily reported this semi solid like material concept by encapsulating water by 20 μm size hydrophobic particles (silane-treated lycopodium grains). However, in Nature, this type of mechanism is commonly used. For instance, gall-dwelling aphids are protected from drowning in the sticky honeydew by covering the honeydew with a powdery wax, which is secreted by the aphid, Figure 2.6c.⁵⁰

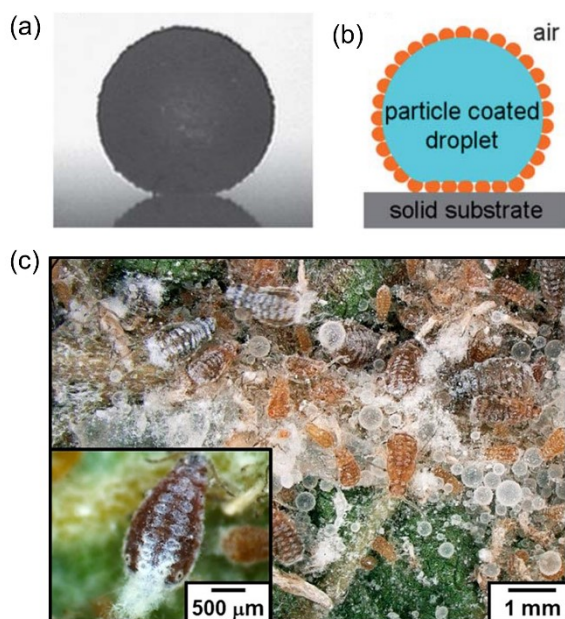


Figure 2.6. (a) A quasi-spherical liquid marble (volume 1 mL and radius 0.7 mm). (b) Illustration of the particles encapsulated liquid and the gravitationally determined flat –spot. (c) Inside of the gall, the inset shows an aphid carrying waxes on its body. (Adapted and reproduced from the ref ^{50,51} with the permission from © The Royal Society of Chemistry 2011 and Copyright © 2019 American Chemical Society)

In particular, hydrophobic particles (in the form of a monolayer or a multilayer) adhere to the liquid (aqueous based) droplet surface while the liquid droplet simply rolls across the particles bed, by replacing the liquid–air interface with a liquid–solid interface creating a soft sphere. The capillary forces and the electrostatic forces govern the adherence of the monolayer or multilayer of hydrophobic particles. This particles adhering system reduces the effective surface free energy by achieving an energetically favourable state.⁵¹ Moreover, small volume liquid marbles assemble in a spherical shape (Figure 2.6a) while large volume ones become gravitationally flattened puddles like shapes. In liquid marbles, the contact with a sitting solid substrate converts from a liquid-on-solid substrate contact to a solid-on-solid substrate contact reducing the contact angle hysteresis. Nevertheless, faster moving of the liquid marble tends to reshape it like a doughnut and peanut shapes due to larger centrifugal forces.⁴⁹ The magnetic material has to be integrated into the liquid marble to bring off the magnetic properties by the magnetic actuation. The integration of magnetic particles or colloids inside of the liquid marble or with the hydrophobic particle layer (without a bond) leads to an easy detachment of the magnetic phase from the marble regime, due to the individual magnetic attraction force. Therefore, Zhao *et al.*⁵² introduced the magnetic liquid marble concept by coating highly hydrophobic superparamagnetic Fe₃O₄ nanoparticles on a water droplet. The dual functionality, hydrophobicity and magnetic responsibility of the nanoparticles, led to the generation of a liquid marble by encapsulating and actuating the liquid droplet, respectively. Figure 2.7a shows the attraction of a liquid marble towards a permanent magnet without losing its shape and functionality. Moreover, the shell of the liquid marble can be opened and closed in a reversible manner by modulating the effecting magnetic force, Figure 2.7b. Based on this behaviour, the functionality and the applicability of the liquid marbles can be upgraded. For instance, two magnetic liquid marbles can be merged by shell opening as shown in Figure 2.7c. Xue *et al.*⁵³ fabricated the liquid marble with a fluorinated decyl polyhedral oligomeric silsesquioxane (FD-POSS) composite with a significantly low surface energy in combination with hydrophobic magnetic nanoparticles, forming stable aqueous solutions and organic liquids based liquid marbles as shown in Figure 2.7d. In addition, water droplets in a hexadecane liquid marble were generated, Figure 2.7e, to demonstrate its applicability as a miniaturised reactor. The ability to manipulate (translocation of the liquid marble) is shown in the Figure 2.7f by following the motion

of a FD-POSS/Fe₃O₄ hexadecane marble under a magnetic field on both glass and on a water surface.⁵³

The ability to perform a chemical reaction in the magnetic liquids marbles is demonstrated in Figure 2.7g and h. Coalescence of different liquid marbles containing the reagents, hydrogen peroxide and bis(2,4,6-trichlorophenyl)oxalate and dye, facilitated a chemiluminescence reaction, when forming the larger liquid marble, after magnetic actuation (Figure 2.7g top). Moreover, under gentle movement actuated by a magnet bar, two core droplets, which were stabilised in a same liquid marble, were merged triggering the chemiluminescence reaction (Figure 2.7g bottom). The integration of analysis tools to the liquid marble such as a chromatographic strip is possible due to the magnetically actuated shell opening property, as shown in Figure 2.7h.⁵³

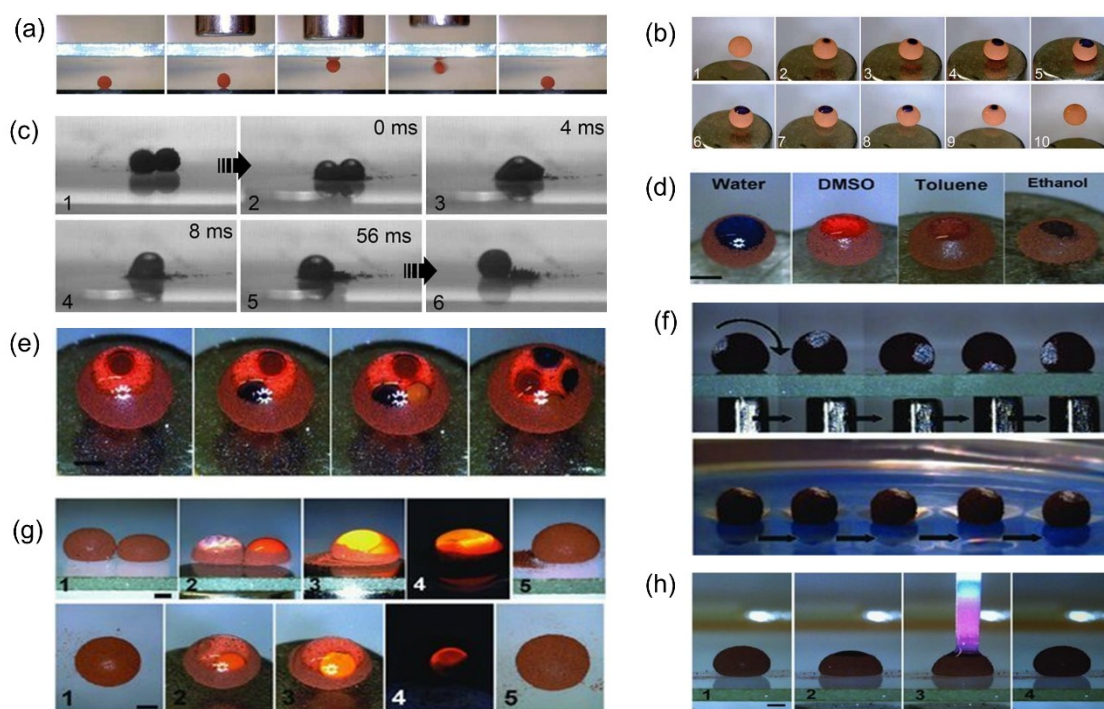


Figure 2.7. (a) Transfer of a liquid marble between two parallel glass plates, 4.5 mm apart, by placing and displacing a magnet bar above the top glass plate. (b) Video frames depicting the opening and closing of a liquid marble containing a blue-coloured water droplet, under magnetic force. (c) Frames captured from a high-speed video, showing different stages of the coalescence of two liquid marbles, under magnetic force. (d) Magnetic shell opened liquid marbles of different solvents (droplet size 7 μ L). (e) Magnetic shell opened hexadecane marbles before and after the addition of different numbers of coloured water droplets (overall droplet size 10 μ L). (f) Magnet-driven motion of a FD-POSS-stained FD-POSS/Fe₃O₄ hexadecane

marble on a glass slide (top) and on a water surface (bottom) (droplet size 7 μL). (g) Chemiluminescence reaction that occurs as a result of coalescing two magnetic liquid marbles that contain different reagents (top). The same chemiluminescence reaction within a single liquid marble (bottom) (droplet size 10 μL). (h) Chromatographic analysis of the liquid in the opened liquid marble (droplet size 10 μL). Scale bar: 1 mm. (a-c and d-h adapted and reproduced from the refs. ⁵² and ⁵³ with the permission from © 2010 WILEY-VCH Verlag GmbH & Co. KGaA, Weinheim, respectively).

An interesting example is the work published by Zhao *et al.*⁵⁴ They reported the optical analysis of the liquid present inside of a liquid marble with a reflection mode probe. The magnetic liquid marble was moved towards the probe position under the magnetic field and the upper shell of the marble was opened by increasing the magnetic field as shown in the Figure 2.8a. Then the droplet sample was analysed and remotely marble closed and moved again to another destination. As shown in the Figure 2.8b and c, the same optical absorption peaks were observed for both the magnetic liquid marble droplet and the bulk phase liquid.

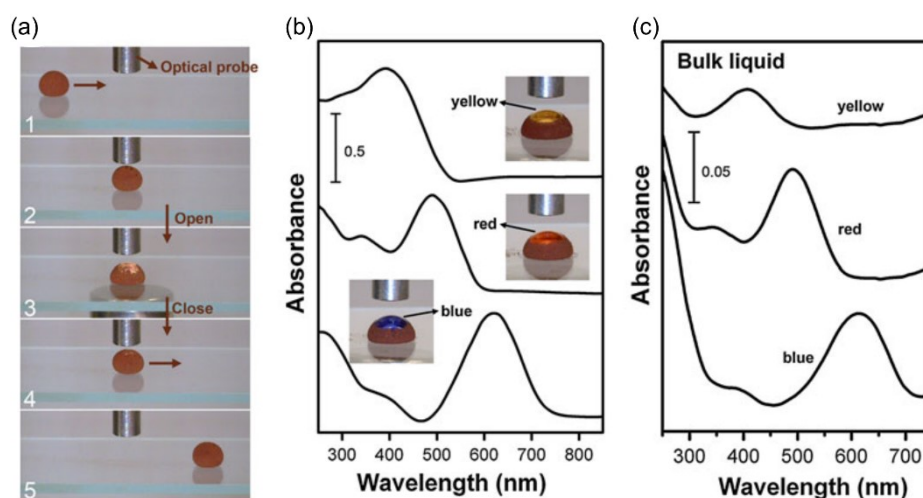


Figure 2.8. (a) Optical probe detection, a sequence of images showing a magnetic liquid marble (20 μL) being moved toward an optical probe (1-2), opened for optical detection (3), closed and moved away, after the detection (4-5). (b) Optical absorption curves of acid yellow 14, acid red 183, and acid blue 25 aqueous solutions in a magnetic liquid marble and (c) in bulk liquid. (Adapted and reproduced from the ref. ⁵⁴ with the permission from © 2012 Springer Nature Switzerland AG. Part of Springer Nature.)

Moreover, the same group immersed electrode tips into the droplet of an open liquid marble to perform electrochemical measurements too. Square-wave voltammograms were recorded for dopamine sample liquid marble droplets, as shown in the Figure 2.9a-c, while manipulating the liquid marble by a magnetic field.⁵⁵ Further, a transmission mode optical absorption analysis protocol was tested with 8 mM aqueous solution of acid blue 25 in a magnetic marble. In this example, the shell of the magnetic marble should be fully opened to avoid the possible scattering coming from the magnetic particles of the shell, Figure 2.9d. The characteristic absorption of acid blue-25 at 615 nm was successfully detected for a magnetic liquid marble containing 8 mM aqueous solution of acid blue 25, providing a high-precision quantitative type of measurement. By integrating all the above analysing techniques of reflection and transmission mode optical detection and electrochemical detection with the magneto based remote handling capability, the “Lab-in-a-droplet” concept was introduced, as illustrated in Figure 2.9e.⁵⁵

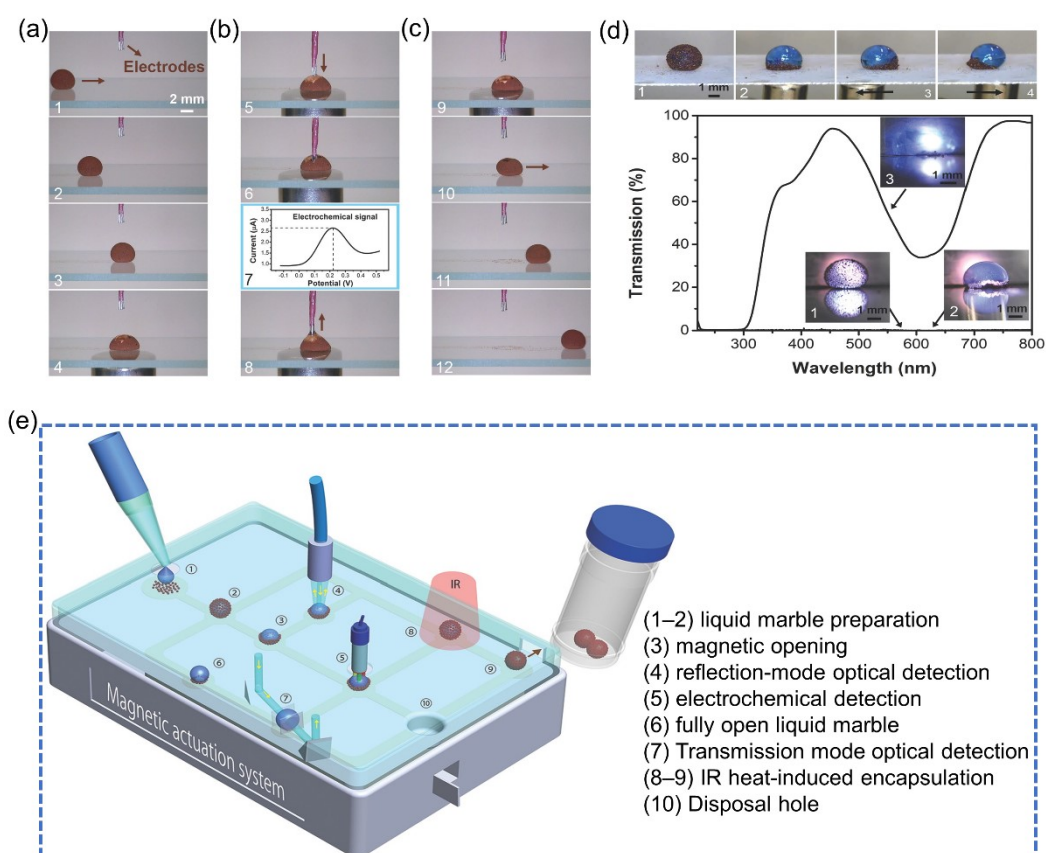


Figure 2.9. Electrochemical detection. (a) Transport and opening of the magnetic liquid marble on a glass substrate with a magnet (b) Moving three-electrode probe into the droplet and

recording the signal, and (c) moving probe out of the droplet, closing and moving away of the liquid marble after detection. Optical absorbance detection. (d) Fully opening of a magnetic liquid marble and its moving around with a magnet and Transmission spectra of a liquid marble (1) the droplet of an open liquid marble (2) and the squashed droplet of an open liquid marble between two parallel hydrophobic glass slides (3) (Droplet: 8 mM aqueous solution of acid blue 25. Insets show the photo of light beam irradiation on each object.) (e) Illustration of detection of a sample on magnetic liquid marbles (Lab-in-a-droplet concept). (Adapted and reproduced from the refs.⁵⁵ with the permission from © 2014 WILEY-VCH Verlag GmbH & Co. KGaA, Weinheim)

Most of the traditional magnetic liquid marbles based on iron oxide nanoparticles are opaque and are not suitable for photo-related applications. In order to address this limitation, Wang *et al.*⁵⁶ reported a photo and magneto active liquid marble in which a droplet, coated with magnetic lanthanide-doped up-conversion ($\text{Yb}^{3+}/\text{Er}^{3+}/\text{Gd}^{3+}$ -doped NaYF_4) nanoparticles (UCNPs), can convert near-infrared light into visible light. The magnetic properties allow opening the marble tip with directed magneto movements. The marbles were applied as miniaturised reactors for photodynamic therapy of cancer cells. Cells were incubated inside the UCNP liquid marbles, along with protoporphyrin IX (PpIX) as a reactive oxygen species generator (ROS), providing the required irradiation (Figure 2.10a-e). The large contact area between the UCNP-POSS (polyhedral oligomeric silsesquioxane) powder coating and the cell culture media, together with the spherical 3D geometry exhibited low cell viability compared to the same treatment performed using conventional two-dimensional culture dishes (sample VI vs IV in Figures 2.10d,e), showing excellent improved photodynamic therapy. Moreover, Sharma *et al.*⁵⁷ fabricated a magnetic digital microfluidic device system (Figure 2.10f-h) to isolate biological entities (microbeads, bovine serum albumin (BSA) and *Escherichia coli*), which are carried by a magnetic liquid marble, to a micro well plate. The magnetic liquid marble was shuttled back and forth between two plates (top – micro-wells and bottom micro-pillars, Figure 2.10g) under the magnetic field. The efficiency of the capture to the micro-wells was analysed by fluorescence microscopy.

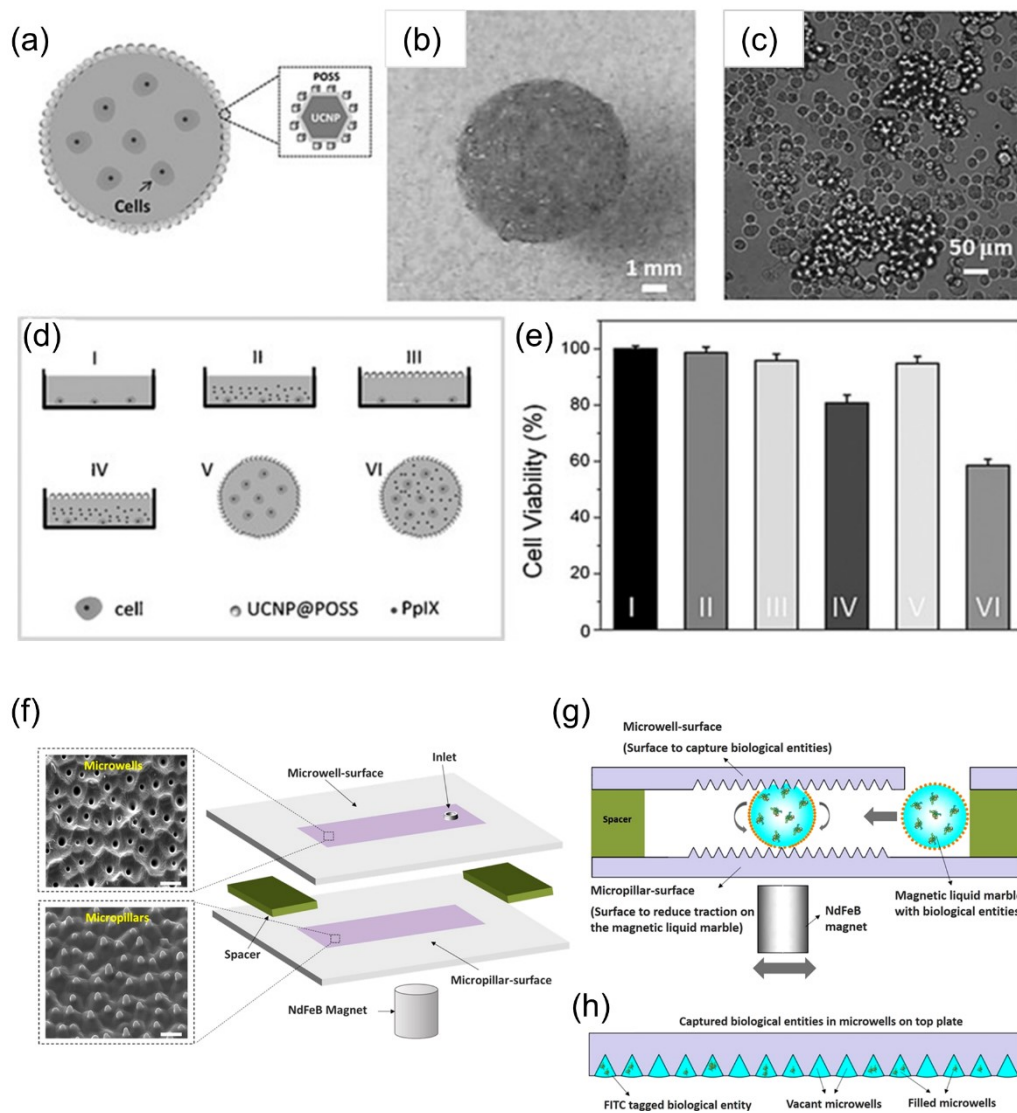


Figure 2.10. (a) Schematic representation of a cell-encapsulating liquid marble. (b) Photographs of a liquid marble based on UCNPs-POSS powder and cell culture media (drop size 200 μL) (c) optical microscopy image of MAD-MD-231 cells. (d) Schematic representations of cells in culture dishes without PpIX (I), with PpIX (II), without PpIX but with UCNPs-POSS powder (III), with both PpIX and UCNPs-POSS powder (IV), and of cells in a liquid marble without PpIX (V) and with PpIX (VI). (e) Cell viability of the cells in (d) after irradiation with a 980 nm laser (1 Wcm^{-2}) for 4 min. (f) Microdevice for isolating biological entities in microwells. (g) Magnetic liquid marble (open shell) through a upper plate containing an array of microwells and a bottom plate containing an array of micropillars. (h) A schematic representation of captured biological entities in the microwells. (Adapted and reproduced from the refs.^{56,57} with the permission from © 2016 Wiley-VCH Verlag GmbH & Co. KGaA, Weinheim and Copyright © 2018.

Recently, Li *et al.*⁵⁸ introduced a magnetothermal-miniaturised reactor by the formation of hydrophobic Fe₃O₄ nanocubes coated liquid marbles (iNLMs). The reactor can be heated with an alternating magnetic field (AMF) as shown in Figure 2.11 a, b. Authors showed that the 18.4 nm Fe₃O₄ nanocubes provided the maximum heating capacity under AMF due to the localised magnetic heating at the well-defined edges and tips of the nanocubes. Moreover, the temperature increment (recorded max. temperature 86 °C) of the Fe₃O₄ nanocubes magnetic liquid marble when compared to other liquid marbles (titanium oxide, graphene, polytetrafluoroethylene (PTFE), silica nanoparticles) and a bare droplet was found to be 18 folds higher, Figure 2.11c-f. This effect was applied to generate a magnetothermal miniature reactor. Further, they showed improved DNA amplification in liquid marbles, achieving a 25 % superior amplification rate, compared with that in a common thermal cycler, by proving the usability of the magnetic liquid marbles for molecular biological reactions.

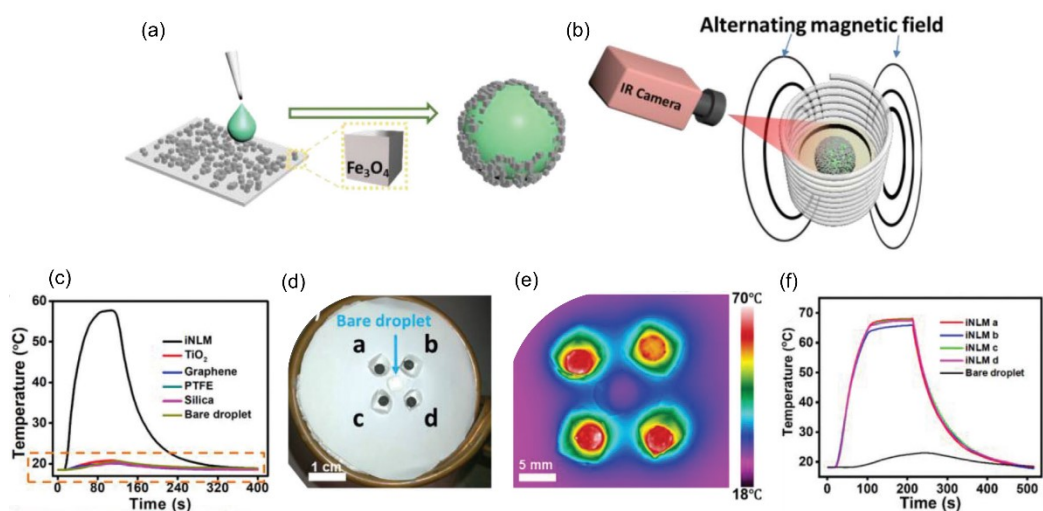


Figure 2.11. (a) Preparation of iNLMs. (b) Schematic representation of the AMF setup and temperature detection. (c) Temperature vs time profiles of liquid marbles coated by different materials. (d) Setup of multi centric heating in the AMF. (e) Thermograms indicating the temperature of the iNLMs and water droplets in a plateau state. (f) Bulk temperature vs time profiles of iNLMs and water droplets during a heating and cooling process. (Adapted and reproduced from the ref.⁵⁸ with the permission from © 2021 WILEY-VCH Verlag GmbH & Co. KGaA, Weinheim.)

Hydrophobic magnetic particles encapsulated in a magnetic liquid marble-based digital microfluidic platform is a promising platform for miniaturised chemical and biological applications. However, the friction between the liquid marble and the sitting surface,

during magnetic transporting, destabilises the marble by losing magnetic particles from the droplet. In this regard, Khaw *et al.*⁵⁹ reported a magnetically actuated floating liquid marble on a water surface to transport the droplet with a minimum friction force, when compared to solid surfaces. However, careful handling is required to manipulate magnetic liquid marbles. For instance, the magnetic shell easily opens by tiny external forces resulting on the mix of the droplet contents with the bulk liquid, smashing the droplet manipulation system. These systems demonstrated that stable droplet handling with magnetic particles is still challenging and it will be addressed in sub-objective 4.

2.7.2 Magnetic inverse liquid marbles

Another model of magnetic hydrophobic particles was reported by Meir *et al.*⁶⁰ called “bubble marble effect” that is the inverse liquid marble model. The insertion and confinement of floating hydrophobic metallic powder underwater by a gradient magnetic field were able to encapsulate an air bubble by a hydrophobic metallic shell, Figure 2.12a and b. In air superhydrophobicity and the underwater superhydrophilicity of the low surface energy particles stabilise the air bubble underwater by holding under the magnetic attraction forces. Further, by using this model, the same group demonstrated the underwater ignition of a thermite-bubble marble by localised microwaves, Figure 2.12c and d, which opened up a platform for potential underwater industrial applications. Apart from that, this model has an immense potential for underwater air bubble manipulation and the capability of solid or liquid transportation inside of the bubble marble.

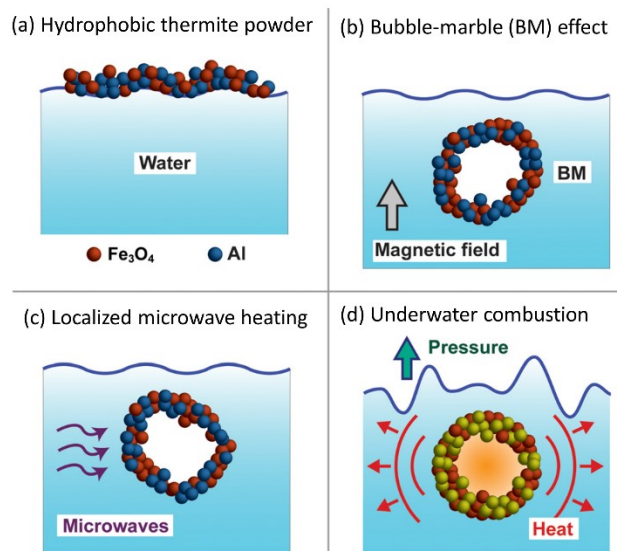


Figure 2.12. Schematic illustration of the underwater thermite ignition enabled by the bubble-marble (BM). (a) Thermite powder initially resides on the water-air interface. (b) Applied magnetic field attracts the thermite into the water, and forms the BM. (c) The BM is irradiated underwater by localised microwaves and (d) self-propagating combustion of the thermite batch. (Adapted and reproduced from the ref.⁶¹ with the permission from © VC 2015 AIP Publishing LLC.)

2.7.3 Oil spills capturing oleophilic colloids

Hydrocarbon functionalised superhydrophobic nanoparticles show superoleophilic properties that can absorb oil spills onto the particle surface by none polar-none polar attractions between the oil and the hydrophobic particle surface. Apart of that, the magnetic properties of the particles help to manipulate the absorbed oil layers under the magnetic field. As shown in Figure 2.13a, Zhu *et al.*⁴³ showed the water treatment possibility of the superhydrophobic Fe₂O₃ nanoparticles by rapidly and selectively removing oils from water surface under magnetic field. Then, the recovered oils were able to be removed from the surfaces of the nanoparticles by a simple ultrasonic treatment, recycling the particles. Moreover, when the magnetic particles/oil collide was drawn under water, and a colloid sphere was formed when removing the magnetic field, referred as an oil marble (Figure 2.13a and b)⁶² can be easily controlled with the magnetic field. This simple and rapid oil spills cleaning protocol, with bare superhydrophobic magnetic particles, can be used to replace the highly advanced and expensive oil-water separating membranes systems used in environmental applications.

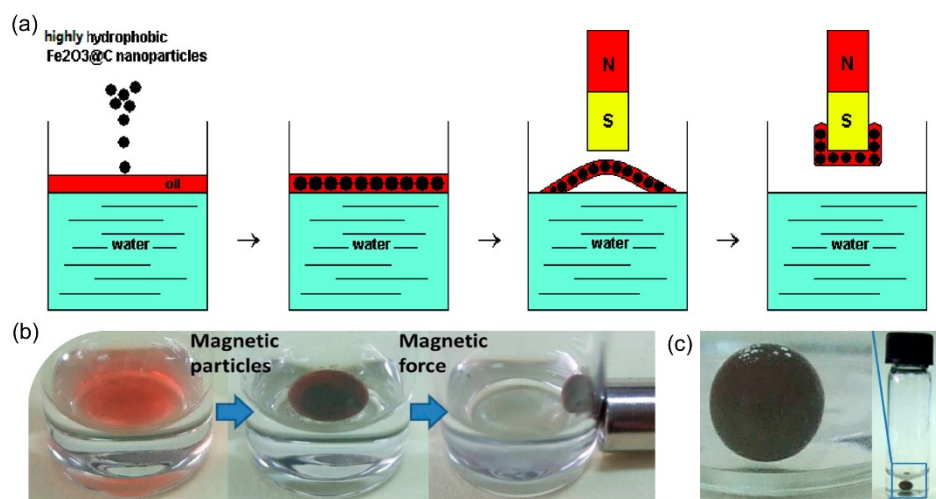


Figure 2.13. (a) Schematic illustration of the removal of oil from the water surface, through hydrophobic Fe₂O₃@C nanoparticles under an external magnetic field. Images of (b) water/oil separation and (c) an “oil marble” under water. (Adapted and reproduced from the refs.^{43,62} with the permission from Copyright © 2010/2012 American Chemical Society.)

This Chapter summarises the essential information about to properties of magnetic particles (Fe₃O₄) and alginate-based magnetic hydrogels. It provides the background to understand the fundamental properties and important behaviours needed to address sub-objective 1. In addition, the short overview of currently developed colorimetric sensor platforms and the ability of remote manipulation of those platforms facilitates comparing the efficiency of the proposed platforms in sub-objectives 2 and 3. Finally, the different superhydrophobic magnetic particle systems covered in section 2.7, highlight the fascinating phenomena, their applicability and the challenges faced in microfluidics with background information to approach the systems proposed in sub-objectives 4 and 5.

2.8 References

- (1) Blaney, L. *Magnetite (Fe₃O₄): Properties, Synthesis, and Applications*, Volume 15.; 2007.
- (2) Laurent, S.; Forge, D.; Port, M.; Roch, A.; Robic, C.; Elst, L. Vander; Muller, R. N. Magnetic Iron Oxide Nanoparticles: Synthesis, Stabilization, Vectorization, Physicochemical Characterizations, and Biological Applications. *Chem. Rev.*

2008, *108* (6), 2064–2110.

- (3) Kandasamy, G.; Maity, D. Recent Advances in Superparamagnetic Iron Oxide Nanoparticles (SPIONs) for in Vitro and in Vivo Cancer Nanotheranostics. *Int. J. Pharm.* **2015**, *496* (2), 191–218.
- (4) Ahn, T.; Kim, J. H.; Yang, H.-M.; Lee, J. W.; Kim, J.-D. Formation Pathways of Magnetite Nanoparticles by Coprecipitation Method. *J. Phys. Chem. C* **2012**, *116* (10), 6069–6076.
- (5) Bedanta, S.; Kleemann, W. Supermagnetism. *J. Phys. D. Appl. Phys.* **2008**, *42* (1), 013001.
- (6) Arias, J. L.; Gallardo, V.; Linares-Molinero, F.; Delgado, A. V. Preparation and Characterization of Carbonyl Iron/Poly(Butylcyanoacrylate) Core/Shell Nanoparticles. *J. Colloid Interface Sci.* **2006**, *299* (2), 599–607.
- (7) Plachy, T.; Kutalkova, E.; Sedlacik, M.; Vesel, A.; Masar, M.; Kuritka, I. Impact of Corrosion Process of Carbonyl Iron Particles on Magnetorheological Behavior of Their Suspensions. *J. Ind. Eng. Chem.* **2018**, *66*, 362–369.
- (8) Ahmed, E. M. Hydrogel: Preparation, Characterization, and Applications: A Review. *J. Adv. Res.* **2015**, *6* (2), 105–121.
- (9) Rehm, B. H. A. Alginate Production: Precursor Biosynthesis, Polymerization and Secretion. In *Alginates: Biology and applications*; 2009; pp 55–71.
- (10) Papageorgiou, S. K.; Kouvelos, E. P.; Favvas, E. P.; Sapalidis, A. A.; Romanos, G. E.; Katsaros, F. K. Metal–Carboxylate Interactions in Metal–Alginate Complexes Studied with FTIR Spectroscopy. *Carbohydr. Res.* **2010**, *345* (4), 469–473.
- (11) Braccini, I.; Serge, P. Molecular Basis of Ca²⁺-Induced Gelation in Alginates and Pectins: The Egg-Box Model Revisited. *Biomacromolecules* **2001**, *2* (4), 1089–1096.
- (12) Tamhankar, P. M.; Kulkarni, A. M.; Watawe, S. C.; Tamhankar, P. M.; Kulkarni, A. M.; Watawe, S. C. Functionalization of Cobalt Ferrite Nanoparticles with Alginate Coating for Biocompatible Applications. *Mater. Sci. Appl.* **2011**, *2* (9), 1317–1321.

- (13) Finotelli, P. V.; Da Silva, D.; Sola-Penna, M.; Rossi, A. M.; Farina, M.; Andrade, L. R.; Takeuchi, A. Y.; Rocha-Leão, M. H. Microcapsules of Alginate/Chitosan Containing Magnetic Nanoparticles for Controlled Release of Insulin. *Colloids Surf. B* **2010**, *81* (1), 206–211.
- (14) Kondaveeti, S.; Semeano, A. T. S.; Cornejo, D. R.; Ulrich, H.; Petri, D. F. S. Magnetic Hydrogels for Levodopa Release and Cell Stimulation Triggered by External Magnetic Field. *Colloids Surf. B* **2018**, *167*, 415–424.
- (15) Mitsumata, T.; Kakiuchi, Y.; Takimoto, J. I. Fast Drug Release Using Rotational Motion of Magnetic Gel Beads. *Res. Lett. Phys. Chem.* **2008**, *2008*, 1–5.
- (16) Yang, C.-H.; Yen, C.-C.; Jheng, J.-J.; Wang, C.-Y.; Chen, S.-S.; Huang, P.-Y.; Huang, K.-S.; Shaw, J.-F. Immobilization of Brassica Oleracea Chlorophyllase 1 (BoCLH1) and Candida Rugosa Lipase (CRL) in Magnetic Alginate Beads: An Enzymatic Evaluation in the Corresponding Proteins. *Molecules* **2014**, *19* (8), 11800–11815.
- (17) Brulé, S.; Levy, M.; Wilhelm, C.; Letourneur, D.; Gazeau, F.; Ménager, C.; Visage, C. Le. Doxorubicin Release Triggered by Alginate Embedded Magnetic Nanoheaters: A Combined Therapy. *Adv. Mater.* **2011**, *23* (6), 787–790.
- (18) Amiri, M.; Salavati-Niasari, M.; Pardakhty, A.; Ahmadi, M.; Akbari, A. Caffeine: A Novel Green Precursor for Synthesis of Magnetic CoFe₂O₄ Nanoparticles and PH-Sensitive Magnetic Alginate Beads for Drug Delivery. *Mater. Sci. Eng. C* **2017**, *76*, 1085–1093.
- (19) Rocher, V.; Siaugue, J. M.; Cabuil, V.; Bee, A. Removal of Organic Dyes by Magnetic Alginate Beads. *Water Res.* **2008**, *42* (4–5), 1290–1298.
- (20) Zhimin, L.; Shangru, Z.; Jialiang, L.; Yuan, F.; Qingda, A.; Zuoyi, X. Sodium Alginate-Based Magnetic Carbonaceous Biosorbents for Highly Efficient Cr(vi) Removal from Water. *RSC Adv.* **2015**, *5* (95), 77932–77941.
- (21) Bée, A.; Talbot, D.; Abramson, S.; Dupuis, V. Magnetic Alginate Beads for Pb(II) Ions Removal from Wastewater. *J. Colloid Interface Sci.* **2011**, *362* (2), 486–492.
- (22) Yanting, L.; Yuanyuan, Y.; Xiong, Y.; Liu, Y.; Yajing, S.; Wanfeng, S. Multi-

- Functionalized Micro-Helical Capsule Robots with Superior Loading and Releasing Capabilities. *J. Mater. Chem. B* **2021**, *9* (5), 1441–1451.
- (23) Hammouda, S. Ben; Adhoum, N.; Monser, L. Synthesis of Magnetic Alginate Beads Based on Fe₃O₄ Nanoparticles for the Removal of 3-Methylindole from Aqueous Solution Using Fenton Process. *J. Hazard. Mater.* **2015**, *294*, 128–136.
- (24) Soumia, A.; Adel, M.; Amina, S.; Bouhadjar, B.; Amal, D.; Farouk, Z.; Abdelkader, B.; Mohamed, S. Fe₃O₄-Alginate Nanocomposite Hydrogel Beads Material: One-Pot Preparation, Release Kinetics and Antibacterial Activity. *Int. J. Biol. Macromol.* **2020**, *145*, 466–475.
- (25) Jia, W.; Bandodkar, A. J.; Valdés-Ramírez, G.; Windmiller, J. R.; Yang, Z.; Ramírez, J.; Chan, G.; Wang, J. Electrochemical Tattoo Biosensors for Real-Time Noninvasive Lactate Monitoring in Human Perspiration. *Anal. Chem.* **2013**, *85* (14), 6553–6560.
- (26) Gao, W.; Emaminejad, S.; Nyein, H. Y. Y.; Challa, S.; Chen, K.; Peck, A.; Fahad, H. M.; Ota, H.; Shiraki, H.; Kiriya, D.; Lien, D. H.; Brooks, G. A.; Davis, R. W.; Javey, A. Fully Integrated Wearable Sensor Arrays for Multiplexed in Situ Perspiration Analysis. *Nature* **2016**, *529* (7587), 509–514.
- (27) He, X.; Xu, T.; Gu, Z.; Gao, W.; Xu, L.-P.; Pan, T.; Zhang, X. Flexible and Superwetable Bands as a Platform toward Sweat Sampling and Sensing. *Anal. Chem.* **2019**, *91* (7), 4296–4300.
- (28) Parlak, O.; Curto, V. F.; Ojeda, E.; Basabe-Desmonts, L.; Benito-Lopez, F.; Salleo, A. Wearable Biosensors and Sample Handling Strategies. In *Wearable Bioelectronics*; 2020; pp 65–88.
- (29) Adkins, J. A.; Boehle, K.; Friend, C.; Chamberlain, B.; Bisha, B.; Henry, C. S. Colorimetric and Electrochemical Bacteria Detection Using Printed Paper- and Transparency-Based Analytic Devices. *Anal. Chem.* **2017**, *89* (6), 3613–3621.
- (30) Mu, X.; Xin, X.; Fan, C.; Li, X.; Tian, X.; Xu, K. F.; Zheng, Z. A Paper-Based Skin Patch for the Diagnostic Screening of Cystic Fibrosis. *Chem. Commun.* **2015**, *51* (29), 6365–6368.
- (31) Koh, A.; Kang, D.; Xue, Y.; Lee, S.; Pielak, R. M.; Kim, J.; Hwang, T.; Min, S.;

- Banks, A.; Bastien, P.; Manco, M. C.; Wang, L.; Ammann, K. R.; Jang, K. I.; Won, P.; Han, S.; Ghaffari, R.; Paik, U.; Slepian, M. J.; Balooch, G.; Huang, Y.; Rogers, J. A. A Soft, Wearable Microfluidic Device for the Capture, Storage, and Colorimetric Sensing of Sweat. *Sci. Transl. Med.* **2016**, *8* (366), 366ra165-366ra165.
- (32) Promphet, N.; Rattanawaleedirojn, P.; Siralermukul, K.; Soatthiyanon, N.; Potiyaraj, P.; Thanawattano, C.; Hinestroza, J. P.; Rodthongkum, N. Non-Invasive Textile Based Colorimetric Sensor for the Simultaneous Detection of Sweat PH and Lactate. *Talanta* **2019**, *192*, 424–430.
- (33) He, X.; Xu, T.; Gu, Z.; Gao, W.; Xu, L. P.; Pan, T.; Zhang, X. Flexible and Superwetable Bands as a Platform toward Sweat Sampling and Sensing. *Anal. Chem.* **2019**, *91* (7), 4296–4300.
- (34) Siripongpreda, T.; Somchob, B.; Rodthongkum, N.; Hoven, V. P. Bacterial Cellulose-Based Re-Swellable Hydrogel: Facile Preparation and Its Potential Application as Colorimetric Sensor of Sweat pH and Glucose. *Carbohydr. Polym.* **2021**, *256*, 117506.
- (35) Russell, R. J.; Pishko, M. V.; Gefrides, C. C.; McShane, M. J.; Cote, G. L. A Fluorescence-Based Glucose Biosensor Using Concanavalin A and Dextran Encapsulated in a Poly(Ethylene Glycol) Hydrogel. *Anal. Chem.* **1999**, *71* (15), 3126–3132.
- (36) Garcia-Rey, S.; Ojeda, E.; Gunatilake, U. B.; Basabe-Desmonts, L.; Benito-Lopez, F. Alginate Bead Biosystem for the Determination of Lactate in Sweat Using Image Analysis. *Biosensors* **2021**, *11* (10), 379.
- (37) Bimendra Gunatilake, U.; Venkatesan, M.; Basabe-Desmonts, L.; Benito-Lopez, F. Ex Situ and in Situ Magnetic Phase Synthesised Magneto-Driven Alginate Beads. *J. Colloid Interface Sci.* **2022**, *610*, 741–750.
- (38) Seuffert, M. T.; Wintzheimer, S.; Oppmann, M.; Granath, T.; Prieschl, J.; Alrefai, A.; Holdt, H.-J.; Müller-Buschbaum, K.; Mandel, K. An All White Magnet by Combination of Electronic Properties of a White Light Emitting MOF with Strong Magnetic Particle Systems. *J. Mater. Chem. C* **2020**, *8* (45), 16010–16017.

- (39) Thomas Young, B.; For Sec, M. D. III. An Essay on the Cohesion of Fluids. *Philos. Trans. R. Soc. London* **1805**, *95*, 65–87.
- (40) Darmanin, T.; Guittard, F. Superhydrophobic and Superoleophobic Properties in Nature. *Mater. Today* **2015**, *18* (5), 273–285.
- (41) Hooda, A.; Goyat, M. S.; Pandey, J. K.; Kumar, A.; Gupta, R. A Review on Fundamentals, Constraints and Fabrication Techniques of Superhydrophobic Coatings. *Prog. Org. Coatings* **2020**, *142*, 105557.
- (42) Bao, X. M.; Cui, J. F.; Sun, H. X.; Liang, W. D.; Zhu, Z. Q.; An, J.; Yang, B. P.; La, P. Q.; Li, A. Facile Preparation of Superhydrophobic Surfaces Based on Metal Oxide Nanoparticles. *Appl. Surf. Sci.* **2014**, *303*, 473–480.
- (43) Zhu, Q.; Tao, F.; Pan, Q. Fast and Selective Removal of Oils from Water Surface via Highly Hydrophobic Core–Shell Fe₂O₃@C Nanoparticles under Magnetic Field. *ACS Appl. Mater. Interfaces* **2010**, *2* (11), 3141–3146.
- (44) Fang, J.; Wang, H.; Xue, Y.; Wang, X.; Lin, T. Magnet-Induced Temporary Superhydrophobic Coatings from One-Pot Synthesized Hydrophobic Magnetic Nanoparticles. *ACS Appl. Mater. Interfaces* **2010**, *2* (5), 1449–1455.
- (45) Wang, B.; Liu, Y.; Zhang, Y.; Guo, Z.; Zhang, H.; Xin, J. H.; Zhang, L. Bioinspired Superhydrophobic Fe₃O₄@Polydopamine@Ag Hybrid Nanoparticles for Liquid Marble and Oil Spill. *Adv. Mater. Interfaces* **2015**, *2* (13), 1500234.
- (46) Imran, M.; Shaik, A. H.; Ansari, A. R.; Aziz, A.; Hussain, S.; Aboutiaa, A. F. F.; Khan, A.; Chandan, M. R. Synthesis of Highly Stable γ -Fe₂O₃ Ferrofluid Dispersed in Liquid Paraffin, Motor Oil and Sunflower Oil for Heat Transfer Applications. *RSC Adv.* **2018**, *8* (25), 13970–13975.
- (47) Nagappan, S.; Ha, C.-S. Emerging Trends in Superhydrophobic Surface Based Magnetic Materials: Fabrications and Their Potential Applications. *J. Mater. Chem. A* **2015**, *3* (7), 3224–3251.
- (48) Zhang, L.; Li, L.; Dang, Z. M. Bio-Inspired Durable, Superhydrophobic Magnetic Particles for Oil/Water Separation. *J. Colloid Interface Sci.* **2016**, *463*, 266–271.

- (49) Aussillous, P.; Quéré, D. Liquid Marbles. *Nature* **2001**, *411* (6840), 924–927.
- (50) Kasahara, M.; Akimoto, S.; Hariyama, T.; Takaku, Y.; Yusa, S.; Okada, S.; Nakajima, K.; Hirai, T.; Mayama, H.; Okada, S.; Deguchi, S.; Nakamura, Y.; Fujii, S. Liquid Marbles in Nature: Craft of Aphids for Survival. *Langmuir* **2019**, *35* (18), 6169–6178.
- (51) McHale, G.; Newton, M. I. Liquid Marbles: Principles and Applications. *Soft Matter* **2011**, *7* (12), 5473–5481.
- (52) Zhao, Y.; Fang, J.; Wang, H.; Wang, X.; Lin, T. Magnetic Liquid Marbles: Manipulation of Liquid Droplets Using Highly Hydrophobic Fe₃O₄ Nanoparticles. *Adv. Mater.* **2010**, *22* (6), 707–710.
- (53) Xue, Y.; Wang, H.; Zhao, Y.; Dai, L.; Feng, L.; Wang, X.; Lin, T. Magnetic Liquid Marbles: A “Precise” Miniature Reactor. *Adv. Mater.* **2010**, *22* (43), 4814–4818.
- (54) Zhao, Y.; Xu, Z.; Parhizkar, M.; Fang, J.; Wang, X.; Lin, T. Magnetic Liquid Marbles, Their Manipulation and Application in Optical Probing. *Microfluid. Nanofluidics* **2012**, *13* (4), 555–564.
- (55) Zhao, Y.; Xu, Z.; Niu, H.; Wang, X.; Lin, T. Magnetic Liquid Marbles: Toward “Lab in a Droplet.” *Adv. Funct. Mater.* **2015**, *25* (3), 437–444.
- (56) Wang, D.; Zhu, L.; Chen, J.-F.; Dai, L. Liquid Marbles Based on Magnetic Upconversion Nanoparticles as Magnetically and Optically Responsive Miniature Reactors for Photocatalysis and Photodynamic Therapy. *Angew. Chemie Int. Ed.* **2016**, *55* (36), 10795–10799.
- (57) Sharma, H.; John, K.; Gaddam, A.; Navalkar, A.; Maji, S. K.; Agrawal, A. A Magnet-Actuated Biomimetic Device for Isolating Biological Entities in Microwells. *Sci. Rep.* **2018**, *8* (1), 1–14.
- (58) Li, H.; Liu, P.; Gunawan, R.; Simeneh, Z. M.; Liang, C.; Yao, X.; Yang, M. Magnetothermal Miniature Reactors Based on Fe₃O₄ Nanocube-Coated Liquid Marbles. *Adv. Healthc. Mater.* **2021**, *10* (6), 2001658.
- (59) Khaw, M. K.; Ooi, C. H.; Mohd-Yasin, F.; Vadivelu, R.; John, J. S.; Nguyen, N. T. Digital Microfluidics with a Magnetically Actuated Floating Liquid Marble.

Lab Chip **2016**, *16* (12), 2211–2218.

- (60) Meir, Y.; Jerby, E. Insertion and Confinement of Hydrophobic Metallic Powder in Water: The Bubble-Marble Effect. *Phys. Rev. E* **2014**, *90* (3), 030301.
- (61) Meir, Y.; Jerby, E. Underwater Microwave Ignition of Hydrophobic Thermite Powder Enabled by the Bubble-Marble Effect. *Appl. Phys. Lett.* **2015**, *107* (5), 054101.
- (62) Zhang, L.; Wu, J.; Wang, Y.; Long, Y.; Zhao, N.; Xu, J. Combination of Bioinspiration: A General Route to Superhydrophobic Particles. *J. Am. Chem. Soc.* **2012**, *134* (24), 9879–9881.

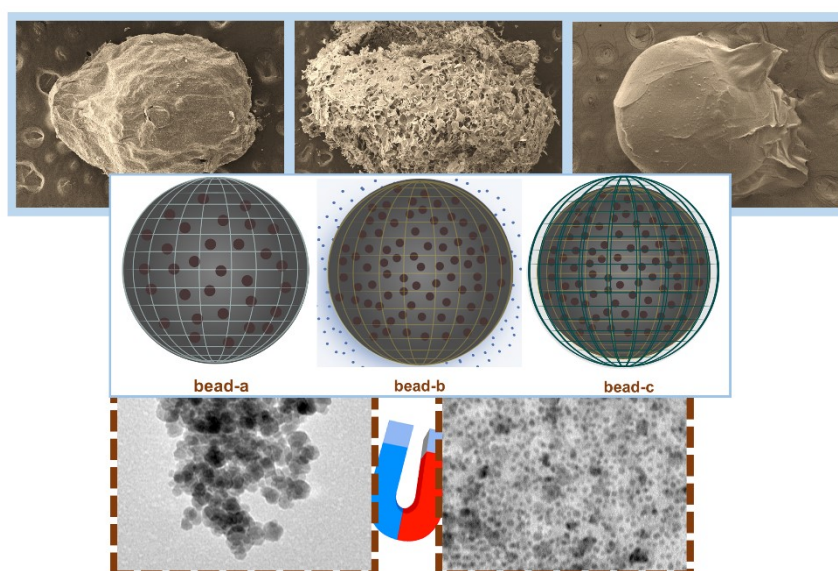
Ex situ and *in situ* Magnetic Phase Synthesised Magneto-Driven Alginate Beads

This Chapter is partially reproduced from:¹

Gunatilake, U.B.; Venkatesan, M.; Basabe-Desmonts, L.; Benito-Lopez, F. *Ex Situ* and *In Situ* Magnetic Phase Synthesised Magneto-Driven Alginate Beads. *Journal of Colloid and Interface Science*, 2022, 610, 741–750.

<https://doi.org/10.1016/j.jcis.2021.11.119>

Abstract. Biocompatible magnetic hydrogels provide a great source of synthetic materials, which facilitate remote stimuli, enabling safer biological and environmental applications. Prominently, *ex situ* and *in situ* magnetic phase integration are used to fabricate the magneto-driven hydrogels, exhibit different behaviours in the aqueous medium, in which comparable comprehension of the properties is essential while implementing the nanocomposite in the applications. In this investigation, three different types of magnetic alginate beads were synthesised. First, by direct, *ex situ*, calcium chloride gelation of a mixture of Fe_3O_4 nanoparticles with an alginate solution. Second, by *in situ* synthesis of Fe_3O_4 nanoparticles inside of the alginate beads and third, by adding an extra protection alginate layer on the *in situ* synthesised Fe_3O_4 nanoparticles alginate beads. The three types of magnetic beads were chemically and magnetically characterised. It was found that, they exhibited particular stability to different pH and ionic strength conditions in aqueous solution. These are essential properties to be controlled when used for magneto-driven applications such as targeted drug delivery and water purification. Therefore, this fundamental study will direct the path to the selection of the best magnetic bead synthesis protocol according to the defined magneto-driven application.



3.1 Introduction

Alginates are colloidal polysaccharides isolated from brown algae, which is abundant in coastal waters.² They are linear copolymers containing *D*-mannuronic acid and *-L*-guluronic acid residues covalently linked together in different configurations³. Alginates cross-link with multivalent metal ions (*e.g.* Ca^{2+} , Ba^{2+})⁴ following the “egg-box” model, which keeps the polymer as a three dimensional gelling material⁵. They are very versatile materials which are currently used for applications like delivery of low molecular weight drugs^{3,6-8} and proteins,⁹⁻¹¹ wound dressing,¹²⁻¹⁵ tissue engineering,^{16,17} food industry,^{18,19} removal of water pollutants/heavy metals,^{20,21} among others.^{14,22}

Magnetic alginate nanocomposites are attracting attention because of their excellent biocompatibility and the possibility of remote stimuli manipulation.^{23,24} When considering their magnetic properties, the inorganic magnetic phase is usually a metal oxide of Fe, Co, Ni, which is introduced into the polymer matrix²⁵. These magneto-driven alginate nanocomposites have been applied for biomedical applications like targeted drug delivery, magnetic triggering drug release, enzyme immobilisation and magnetic hyperthermia.²⁶⁻³⁰ Moreover, they have been employed for environmental applications like the magnetic removal of heavy metals, organic contaminants and dyes from water.³¹⁻³³ Interestingly, magnetic alginate nanocomposites microstructures have been fabricated and applied as magnetic actuators as micro-helical capsule robots.³⁴

Iron oxide Fe_3O_4 (magnetite) is the main material used in all these applications, due to its low toxicity, high magnetisation and availability at low cost. In particular, Fe_3O_4 nanoparticles (NPs) are commercially accessible or easy to synthesise, by the co-precipitation method of ferrous and ferric salts under alkaline solution in a controlled N_2 environment, presenting superparamagnetic properties with a saturation magnetisation of $\sim 80 \text{ Am}^2 \text{ kg}^{-1}$.³⁵ There are several methods to fabricate magnetic alginate materials by physical cross-linking such as, *ex-situ* blending of Fe_3O_4 NPs with the alginate matrix or *in situ* synthesis of Fe_3O_4 NPs in the alginate matrix. The most used method in literature is the blending of alginate and magnetic nanoparticles (MNPs), followed by a traditional di-cationic cross-linking protocol.³⁶ In the second method, *in situ* synthesis of Fe_3O_4 NPs inside of the alginate hydrogel matrix, the alginate hydrogel material is formed by a cross-linking process with ferrous and ferric

cations. Then, the material is subjected to a highly alkaline solution and, by diffusion, the Fe₃O₄ NPs are synthesised inside of the material.³⁷

In biomedical applications using magnetic beads, drug releasing phenomena is achieved over pH ~ 7, since beads swell due to the electrostatic repulsion of the carboxylate groups at this Ph.^{38,39} Moreover, it has been reported that beads might bust, due to the exchange of the cross-linking cations at that conditions too.⁴⁰ On the other hand, a stable and non-degradable hydrogel matrix is in high demand for environmental applications, especially for organic contaminants and heavy metal removal in water resources. In this regard, fundamental understanding of the properties of the nanocomposite obtained when alginate beads are fabricated by both, the *ex situ* and *in situ* processes, is of high relevance, especially their stability in aqueous medium. In this regards, it is necessary to carry out fundamental studies of the properties and the behaviour of these type of magnetic alginate beads, and to characterise their stability in aqueous medium. Furthermore, it is of special interest to provide to the research community and the biotechnological industry with less complicated synthesis protocols, which overcome the inherent low stability behaviour of magnetic alginate materials.

In this work, magnetic alginate beads (alginate as the polymer matrix and iron oxide as the inorganic matrix) were synthesised using two different methods. First, the direct mix of Fe₃O₄ NP with the alginate solution, *ex situ*, and subsequent gelation with a cationic solution, bead-a, and second, by the *in situ* synthesis of Fe₃O₄ NPs inside of the alginate bead, bead-b. Moreover, in order to improve the stability of the bead-b type, an extra alginate layer was generated on the bead-b by dip coating synthesis, producing bead-c. The stability of the beads was investigated at different pH values and ionic densities in aqueous solution. Moreover, the synthesised magnetic nanoparticles and the beads were characterised by TEM (transmission electron microscopy), SEM (scanning electron microscopy), XRD (X-ray powder diffraction), FTIR (Fourier-transform infrared), DLS (dynamic light scattering), Raman and SQUID (superconducting quantum interference device) in order to understand the behaviour of these magnetic alginate nanocomposites in aqueous solutions.

3.2 Experimental

3.2.1 Synthesis of the Fe₃O₄ nanoparticles

First, a 0.5 M ferric solution was prepared by dissolving 2.71 g of FeCl₃·6H₂O (> 99 %, Sigma-Aldrich, Spain) in 20 mL of distilled water and a 0.5 M ferrous solution was prepared by dissolving 1.39 g of FeSO₄·7H₂O (> 99 %, Sigma-Aldrich, Spain) in 10 mL distilled water. Then, 30 mL Fe³⁺/Fe²⁺ (Fe³⁺:Fe²⁺, 2:1) solution (deoxygenated) was added drop by drop in a 40 mL 1 M NaOH (> 98 %, Sigma-Aldrich, Spain) solution kept at 40 °C under vigorous stirring and N₂ atmosphere. A black precipitate was immediately formed. Then, the precipitate was heated at 90 °C for 30 min. After that, the precipitate was separated from the solution with a magnet and washed 3 times with distilled water. Finally, the Fe₃O₄ nanoparticles were dried by rotary evaporation at 40 °C, under vacuum to obtain a black nanoparticle powder.⁴¹

3.2.2 Synthesis of the alginate beads

Sodium alginate powder (Sigma-Aldrich, Spain), extracted from brown algae with mannuronate (M)/guluronate (G) ratio of ~1.56 and molecular weight of 12,000 – 40,000 g mol⁻¹, was used in all synthesised beads.

Bead-a type: 75 mg of Fe₃O₄ NPs were mixed with 5 mL of 1 % (w/v) of sodium alginate solution (1:100, sodium alginate: distilled water). Then, a 15 µL drop of Fe₃O₄ /alginate solution was dipped into a 0.1 M calcium chloride (> 93 %, Sigma-Aldrich, Spain) solution. The magnetic alginate beads were instantly formed inside of the calcium chloride solution. After 10 min, the beads were removed from the solution and washed with distilled water.

Bead-b type: 15 µL drop of sodium alginate solutions was dropped to a 30 mL Fe³⁺/Fe²⁺ (Fe³⁺:Fe²⁺, 2:1) solution (deoxygenated). Yellow coloured beads were formed instantly. The beads were allowed to settle in the solution for 15 min. Then, the beads were washed with distilled water and transferred to a 1 M NaOH solution (deoxygenated) for 10 min to synthesise, *in situ*, the Fe₃O₄ nanoparticles inside of the alginate beads. The yellow colour of the beads instantly turned to black. Finally, the beads were washed with distilled water.

Bead-c type: Beads-b type were dipped into a 0.5 % (w/w) alginate solution and subsequently, transferred to a 0.1 M CaCl₂ solution to coat them (10 min) with another alginate layer. Then, the beads were washed with distilled water.

The stability of the beads in aqueous solutions at different pH's was evaluated. In order to do that, pH 2 ± 0.2 solution was prepared by diluting HCl ($> 37\%$, Sigma-Aldrich, Spain) and pH 12 ± 0.2 solution was prepared using NaOH (Sigma-Aldrich, Spain). Finally, distilled water was used as the neutral pH solution (pH 7 ± 0.5). The images of the beads were captured by a Sony Cyber-shot DSC-RX100 camera, over time.

3.2.3 Characterisation of the nanoparticles and the magnetic beads

TEM images of the Fe₃O₄ nanoparticles (in water suspension) were collected from JEOL JEM 1400 Plus (JEOL, Japan). SEM images of the freeze-dried beads were recorded by Hitachi S-4800 (Hitachi Japan) and QUANTA 200FEG, FESEM for the hydrated beads. FTIR spectra of the dehydrated nanoparticles and beads were carried out, in transmittance mode, using a Jasco 4200 spectrometer. The Raman spectra were recorded by a Renishaw InVia Raman spectrometer, joined to a Leica DMLM microscope. The spectra were acquired with the Leica 50x N Plan (0.75 aperture) objective and 785 nm laser (diode laser, Toptica). XRD patterns were collected by using a Philips X'pert PRO automatic diffractometer operating at 40 kV and 40 mA, in theta-theta configuration, secondary monochromator with Cu-K α radiation ($\lambda = 1.5418 \text{ \AA}$) and a PIXcel solid-state detector (active length in 2θ 3.347°). Data were collected from 6 to $80^\circ 2\theta$, step size 0.026° and time per step of 450 s at RT (scan speed $0.015^\circ \text{ s}^{-1}$). Magnetisation measurements for the iron oxide nanoparticles and the dehydrated beads were carried out in a 5 T Quantum Design MPMS XL-5 (SQUID) magnetometer at room temperature. DLS data were obtained by Malvern Zetasizer Nano-ZS ZEN 3600. Data, statistical and image analysis were carried out in Microsoft Excel, Origin Pro 2018 and Image-J software.

3.3 Results and Discussion

A schematic illustration of the three types of magnetic alginate beads is presented in Figure 3.1. In general, for the three methods, iron oxide alginate nanocomposite liquid suspension or sodium alginate droplets of $15 \mu\text{L}$ were pipetted into a gelling bath solution containing a Ca²⁺ solution for the bead-a types or into a Fe²⁺/Fe³⁺ solution for the bead-b types, generating beads of $2.2 \pm 0.3 \text{ mm}$ diameter. The droplets rapidly cross-linked and formed an external outer layer of alginate as a capsule. Then, cations

penetrated through the capsule to fully cross-link the alginate polymer to form the bead.⁴²

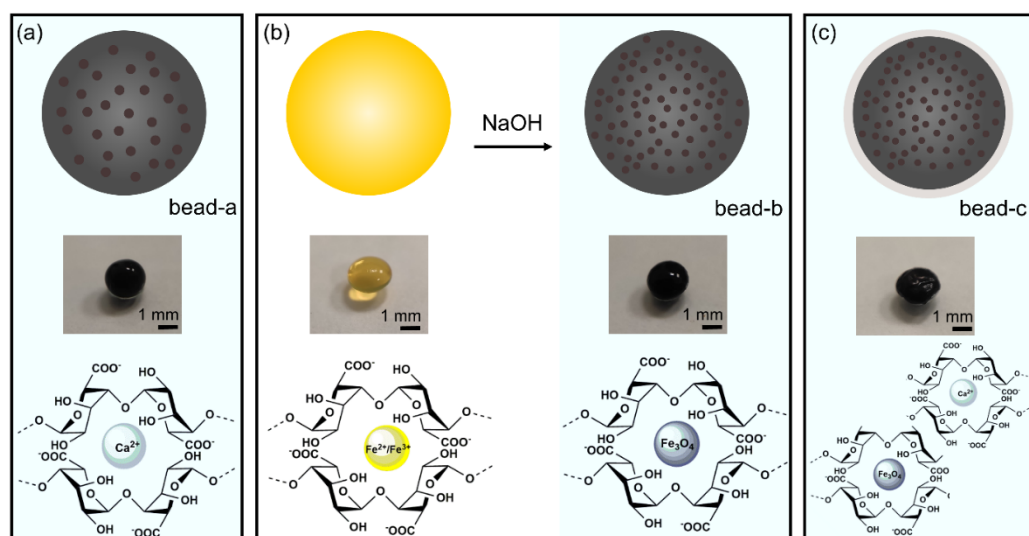


Figure 3.1. Illustration and images of the three types of Fe_3O_4 /alginate beads. (a) Bead-a, obtained by direct addition of Fe_3O_4 NPs to the alginate solution, *ex situ*, and subsequent cross-link of the bead in a solution containing Ca^{2+} ions. (b) Bead-b, obtained from an alginate bead cross-linked by $\text{Fe}^{3+}/\text{Fe}^{2+}$ (yellow bead image) followed by *in situ* synthesis of the Fe_3O_4 nanoparticles inside of the bead (black bead image). (c) Bead-c, obtained from bead-b, followed by the formation of an extra alginate layer cross-linked by a solution of Ca^{2+} ions. The images of the real beads and the chemical illustration for the hydrogels are shown under each bead category.

3.3.1 Stability of the beads in aqueous media

Magnetic beads are frequently used for water-based magneto-driven applications.³¹ Therefore, it is of great importance to study the stability of the alginate beads in aqueous media, at different pH, over time. In order to do that, the alginate beads were investigated at $\text{pH } 2.0 \pm 0.2$, 7.0 ± 0.5 and 12.0 ± 0.2 water solutions up to 21 h. Figure 3.2a (left), shows a schematic representation of the behaviour of bead-a at different pH. Bead-a type presented good stability, for all the pH investigated, demonstrating a stable equilibrium, between the water absorption of the bead, over time, and its surrounding medium, as expected for this type of material. Alginate beads generally undertake differentiated swelling/shrinking behaviours in the acidic and in the basic pH solutions. Alginate polymer contains carboxylate groups ($-\text{COO}^-$) which are converted to carboxylic acid ($-\text{COOH}$) in the acidic medium attracting other hydroxyls ($-\text{OH}$) and $-\text{COOH}$ groups by intermolecular hydrogen attraction. This effect causes a contraction

of the alginate beads over time. On the other hand, at pH values over 7, and especially at basic pH values, the carboxylate groups remain as negative COO^- anions generating electrostatic repulsions forces between the negatively charged groups, expanding the bead resultant to absorb more water molecules and causing the swelling over time until reaching equilibrium.⁴³ A significant size variation was observed at both pH conditions. The diameter of the beads got reduced by a $16 \pm 11 \%$ in the acidic pH medium and increased by a $15 \pm 8 \%$ in the basic pH medium, see Figure 3.3a and b.

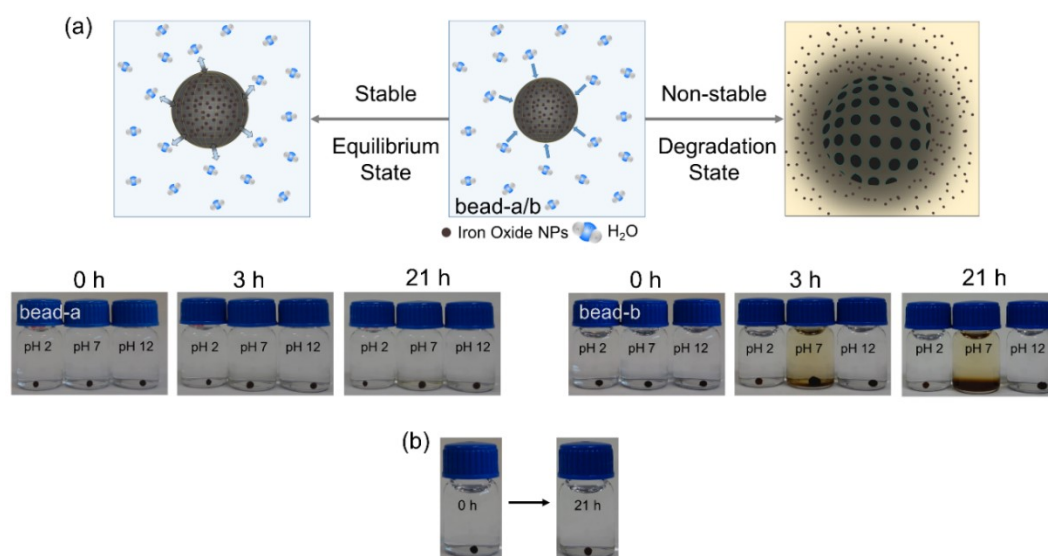


Figure 3.2. (a) Schematic illustration of the bead-a and bead-b behaviour at neutral pH solutions and pictures of the beads under pH ~ 2 , ~ 7 and ~ 12 , from 0 to 21 h. (b) Stability of the bead-b in a NaCl solution (1M) at pH ~ 7 , up to 21 h.

On the other hand, the bead-b type presented a different behaviour compared to bead-a. The beads were found to be stable at high and low pH ranges, obtaining a similar swelling/shrinking behaviour than the bead-a type. However, at neutral pH, the bead-b presented an unstable behaviour, deteriorating rapidly over time, see Figure 3.2a schematic diagram (right). This observation is very important to investigate, since neutral pH needs to be used for most of the possible biological applications of these types of beads. The pictures Figure 3.2a (right), clearly show that at pH ~ 7 , alginate bead-b rapidly degraded, showing the leaking of the magnetic nanoparticles to the medium. After the first hour, bead-b type was found to swell up to 60 % of its initial size, contributing to the fast degradation of the bead structure and thus, the releasing of the Fe_3O_4 nanoparticles, as a homogeneous suspension, see Figure 3.3c and d.

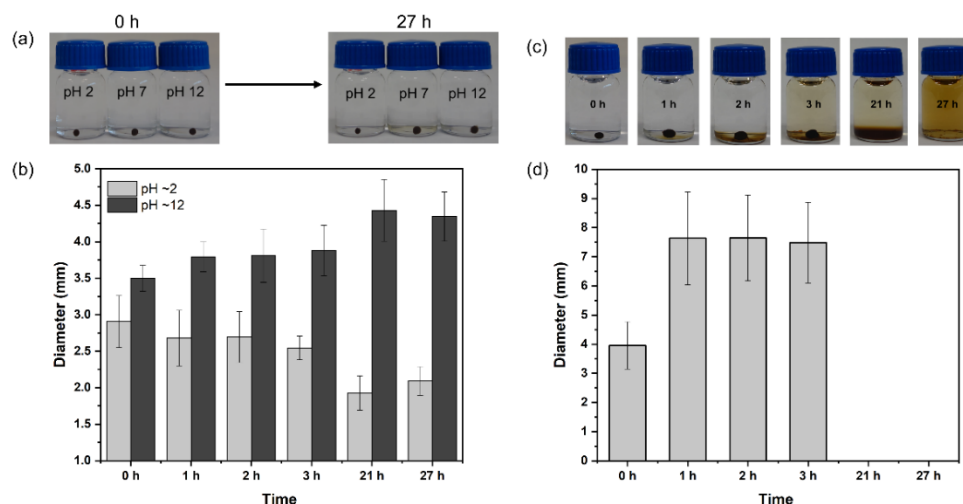
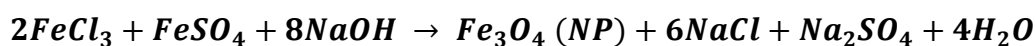


Figure 3.3. (a) Images of the bead-a at 0 and 27 h, at different pH solutions. (b) Diameter of the bead-a at pH ~ 2 and at pH ~ 12 solutions, over time. (c) Images of a magnetic alginate bead-b at pH ~ 7, over time. (d) Diameter of the bead at pH ~ 7 for 27 h. Sizes were analysed from the images captured by the camera, (n = 3, diameter).

This behaviour can be explained considering the instability of the ionic density inside and outside of the beads. In bead-b, the alginate was cross-linked with $\text{Fe}^{3+}/\text{Fe}^{2+}$ using a ferrous sulphate and ferric chloride solution and then, the Fe_3O_4 nanoparticles were *in situ* synthesised, using a sodium hydroxide solution, inside the beads, as shown by the chemical reaction-3.1.



reaction-3.1

Sodium sulphate and sodium chloride salts remained inside of the alginate beads increasing their internal ionic density. Therefore, when the bead-b is immersed in a neutral pH solution, the bead-b reduced its ionic density by absorbing water molecules, which promoted the rapid swelling of the bead. Besides, the strength of the cross-linked bonds is weaker in the bead-b than in the bead-a, since the nucleation of the Fe_3O_4 nanoparticles decreased the number of available pre-cross-linked bonds. Although, it is expected that the Fe_3O_4 nanoparticles were predominantly formed using the unbounded $\text{Fe}^{3+}/\text{Fe}^{2+}$ ions present inside of the matrix of the bead, $\text{Fe}^{3+}/\text{Fe}^{2+}$ ion coming from the cross-linked alginate could get used as well, weakening the stability of the beads at pH ~ 7. These two effects promoted the fast degradation of the structure of the bead when

the osmotic pressure overcome the bond (cross-linking) strength, releasing the magnetic nanoparticles.

On the other hand, at acidic and basic conditions (pH \sim 2 and \sim 12), the ionic density of the solutions was high, compared to the pH \sim 7 solution thus, water molecules did not rapidly penetrate inside of the bead, reminding in an equilibrium state for longer times. In order to confirm this behaviour, the magnetic bead-b types were immersed in a solution of 1 M NaCl at neutral pH and monitored over time. Figure 3.2b clearly shows that the beads are stable up to 21 h at this high ionic density, confirming that the instability of the ionic density of the inside and the outside of bead is the responsible of the degradation of the bead-b.

Bead-b types have an important advantage compared to bead-a types for the fabrication of magnetic alginate beads. Their simpler synthesis methodology permits the cross-linking of the bead without the inorganic nanoparticles, obtaining higher loadings of the magnetic inorganic material (Fe_3O_4 nanoparticles). Nevertheless, as described above, it has a mayor disadvantage, the low stability and fast degradation of the beads when immersed in a low ionic density medium, becoming an important drawback for most applications. Therefore, in order to overcome this limitation, a third synthesis methodology for the fabrication of magnetic alginate beads was carried out. Bead-c type was synthesised by adding an extra alginate layer cross-linked by calcium divalent ions over the bead-b. Figure 3.4a shows the stability of the bead-c at different pH values up to 21 h. Bead-c types are stable in all the pH solutions investigated, preventing the degradation of the beads under low ionic density aqueous media. The extra layer of alginate acts as a protecting shield for the bead-b types. Moreover, during the formation of the extra layer, the diffusion of Ca^{2+} ions reinforced the strength of the entire bead by forming extra cross-linked sides in the bead-b, preventing the breaking of the bead and releasing of the magnetic nanoparticles. As depicted in Figure 3.4b, swelling and shrinking behaviour at high and low pH levels, can be clearly seen in bead-c, following the same mechanism mentioned for bead-a. It is remarkable to mention that, larger viability on the diameter of the beads were obtained during the fabrication of the bead-c type, due to the two steps needed for their fabrication.

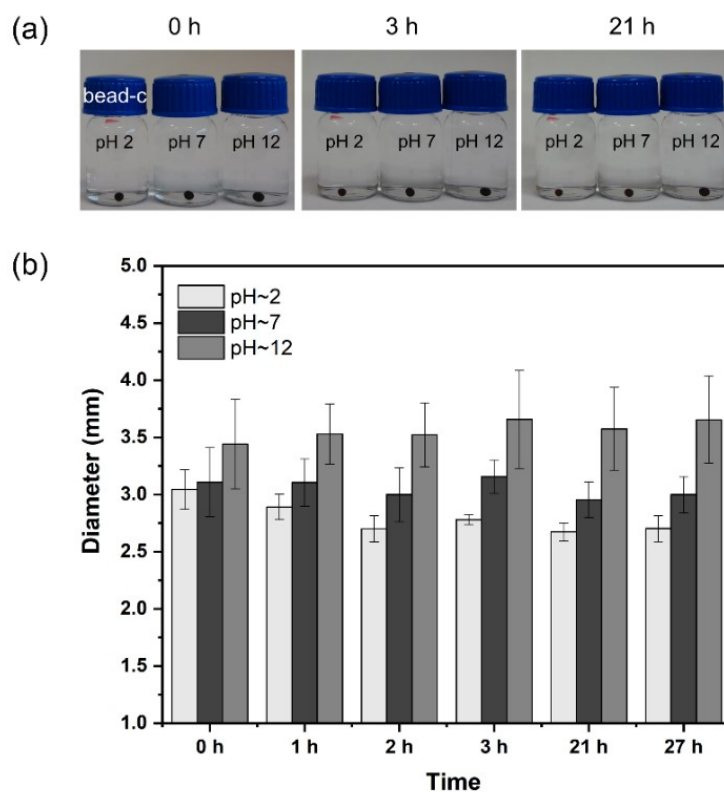


Figure 3.4. (a) Pictures of the bead-c in aqueous solutions at pH ~ 2, ~ 7 and ~ 12 for up to 21 h. b) Diameter of the bead-c at the three pH solutions, over time. Sizes were analysed from the images captured by the camera, (n = 3, diameter).

3.3.2 Morphological characterisation of the beads

The morphology of the surface and the cross-section of the three bead types were investigated by SEM (from freeze-dried beads) and FESEM (from hydrated beads). Figure 5a shows the SEM images of the bead-a, bead-b and bead-c surfaces, respectively. Bead-a and bead-c types presented a homogeneously polymerised surface structure without corrosion, which prevented degradation in aqueous environments. On the other hand, a highly porous and corroded surface was observed for the bead-b type. This structure was explained considering that the whole bead, including the surface, contributed to synthesise the Fe_3O_4 nanoparticles inside of the alginate matrix and on the surface of the bead, generating the corroded surface. Further, the morphology of the beads surface was observed by FESEM in their hydrated state. Bead-a presented less porous globular structure, while the bead-b type evidenced an much higher porosity, which facilitated the fast absorption of water and thus, its degradation, see Figure 3.6. The cross-sectional SEM images of the three beads showed that the porosity is obtained inside of the bead as well, see Figure 3.5b. The nucleation of the magnetic phase in the

polymer matrix of the bead-b, modified the cross-linking between $-\text{COOH}$ and $\text{Fe}^{3+}/\text{Fe}^{2+}$. Therefore, the internal porosity of the bead-b also increased in the same way as its surface porosity. In addition, for bead-c type, the diffusion of extra alginate together with extra cross-linkers generates a shield layer of calcium alginate, strengthening the bead, as shown in Figure 3.5b.

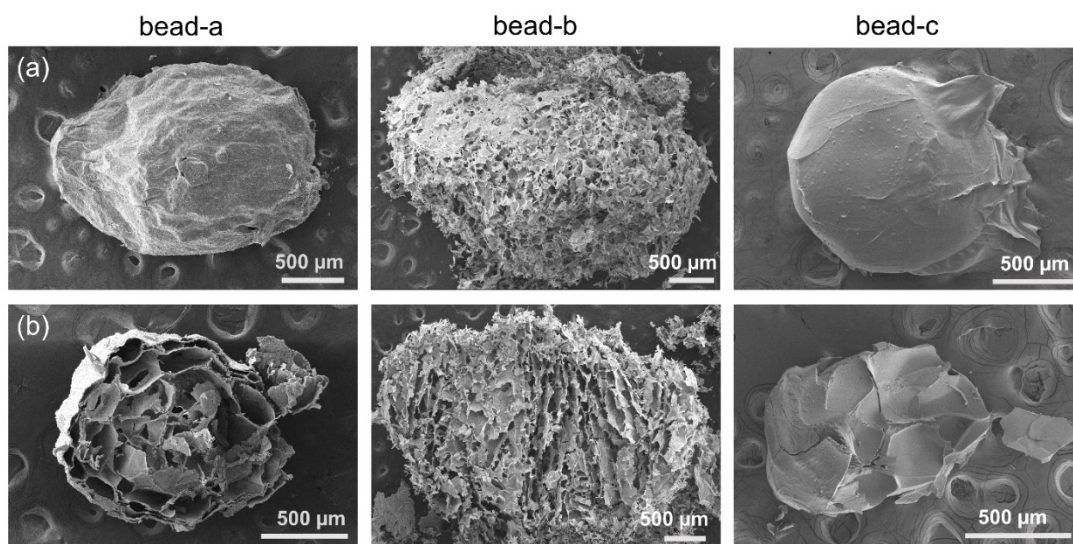


Figure 3.5. SEM images of freeze-dried beads. Surface images (a) and cross-section images (b) of the three bead types.

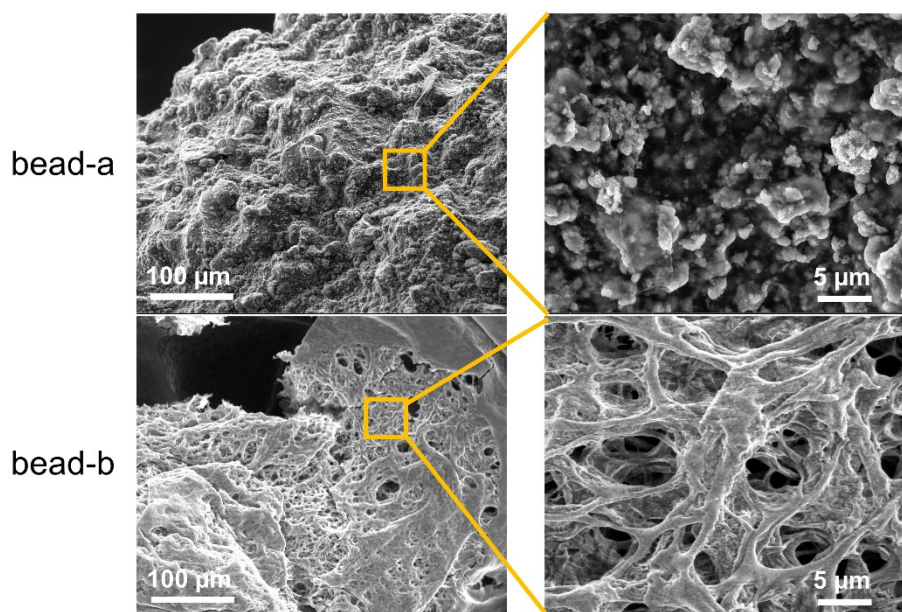


Figure 3.6. SEM images of surface of the hydrated beads and a zoom image of an area of the surface.

3.3.3 Morphological characterisation of the magnetic nanoparticles synthesised in the bead-b type

The Fe_3O_4 nanoparticles synthesised inside of the bead-b were fully characterised. They presented a stable suspension in contrast to the conventionally synthesised Fe_3O_4 nanoparticles (nanoparticles used for the magnetic alginate beads-a type). Figure 3.7 shows both types of nanoparticles in suspension and after 14 days, and their TEM images. The nanoparticles used for the synthesis of the beads-a aggregated over time due to the dipole-dipole interactions occurring among magnetic nanoparticles⁴⁴. On the other hand, the nanoparticles synthesised inside the bead-b type did not suffer aggregation, presenting a stable nanoparticle suspension in water. Further, high zeta potential of -57.6 mV, in *in situ* synthesised Fe_3O_4 NPs confirmed the stability of the suspension in Figure 3.7b, when compared to low zeta potential, -5.79 mV, of Fe_3O_4 NPs used in bead-a. As well, the lower polydispersity index (PDI) value of *in situ* synthesised Fe_3O_4 NPs (0.230) compared to *ex situ* Fe_3O_4 NPs (0.542), convey the increment of monodispersivity in *in situ* Fe_3O_4 NPs; see supplementary information Table-3.1 for dynamic light scattering data. Moreover, the TEM images confirmed that, the dimensions of the particles synthesised in the bead-b are significantly smaller than the nanoparticles employed for the synthesis of bead-a, being in average ~ 3 and ~ 8 nm, respectively. The smaller dimensions of the *in situ* synthesised NPs can be explained considering that the nucleation and the growth of the nanoparticles in bead-b occurred under a pressurised and contracted environment in the polymer matrix, inhibiting their growth.

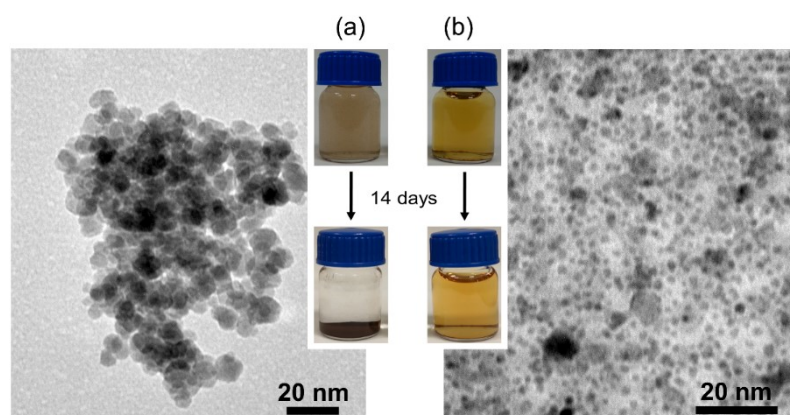


Figure 3.7. TEM images of the nanoparticles used in (a) bead-a and (b) *in situ* synthesised in bead-b. Pictures of the dispersed nanoparticles in a bottle when dispersed in water and after 14 days.

Table 3.1. DLS data for *ex situ* and *in situ* Fe₃O₄ nanoparticles (NPs).

| Sample | Zeta Potential (mV) | PDI (Polydisperse index) |
|---|---------------------|--------------------------|
| 1. <i>Ex situ</i> Fe ₃ O ₄ (aqueous media) | -5.79 | 0.542 |
| 2. <i>Ex situ</i> Fe ₃ O ₄ (0.003 % alginate media) | -17.00 | 0.504 |
| 3. <i>Ex situ</i> Fe ₃ O ₄ (0.015 % alginate media) | -20.60 | 0.500 |
| 4. <i>In situ</i> Fe ₃ O ₄ (aqueous media) | -57.60 | 0.230 |

3.3.4 Chemical characterisation of the nanoparticles and the beads

3.3.4.1 XRD

The XRD patterns of the *ex situ* co-precipitated, from bead-a type, and *in situ* synthesised, from bead-b type, nanoparticles were examined in order to check their phase and the iron oxide state. The XRD pattern of the nanoparticles used in bead-a corresponded to magnetite-Fe₃O₄ (JCPDS 75-0449) with main 2 θ values at 30.40 °, 35.81 °, 43.38 °, 53.75 °, 57.33 °, 62.93 ° and 18.40 °. On the other hand, the XRD pattern of the nanoparticles synthesised in bead-b matched two XRD data patterns, the magnetite-Fe₃O₄ (JCPDS 88-0315) with 2 θ values of 30.40 °, 35.78 °, 43.45 °, 53.88 °, 57.46 ° and 63.064 ° and the sodium chloride (halite crystalline match JCPDS 001-0994) with the 2 θ values of 31.87 ° and 45.62 °, see Figure 3.8a^{45,46}. XRD results demonstrated that the magnetite phase of the iron oxide is obtained in both nanoparticles types. In general, in co-precipitated magnetite nanoparticles, the maghemite phase might be presented, which comes from the oxidation of magnetite, this was not clearly appreciated by the XRD analysis, as the X-ray diffraction angles of both maghemite and magnetite are located in the same positions. According to the XRD results, the *in situ* synthesised nanoparticles in bead-b were contaminated with a significant amount of sodium chloride, which is a by-product coming during the synthetic process. Nevertheless, this interference could be removed by performing a hard particle washing step before analysis.

The XRD pattern for the air-dried bead-a and bead-b types matched with the magnetite-Fe₃O₄ (JCPDS 88-0315, JCPDS 75-1609), see Figure 3.8b. Besides, bead-a type shows

an extra phase at 2θ values of 31.80° and 45.55° (JCPDS 001-0994) since NaCl formed during the cross-linking process of Na-alginate with CaCl_2 in bead-a. In the case of the bead-b type, Na_2SO_4 , NaCl and NaOH are bi-products coming from the *in situ* synthesis of the Fe_3O_4 nanoparticles and by the extra diffusion of ions coming from the basic solution. 2θ values at 28.09° , 29.50° , 32.55° , 33.91° and 38.01° can be assigned to Na_2SO_4 (JCPDS 75-0914) while the peaks at 46.30° and 55.8° (JCPDS 75-0306) and the peaks at 36.99° , 40.22° and 52.68° (JCPDS 01-1173)^{45,46} can be assigned to NaCl and NaOH, respectively. These results confirmed that inside the bead-b type there is a significant ionic contamination, contributing to the lower stability of bead-b at neutral pHs, as explained above.

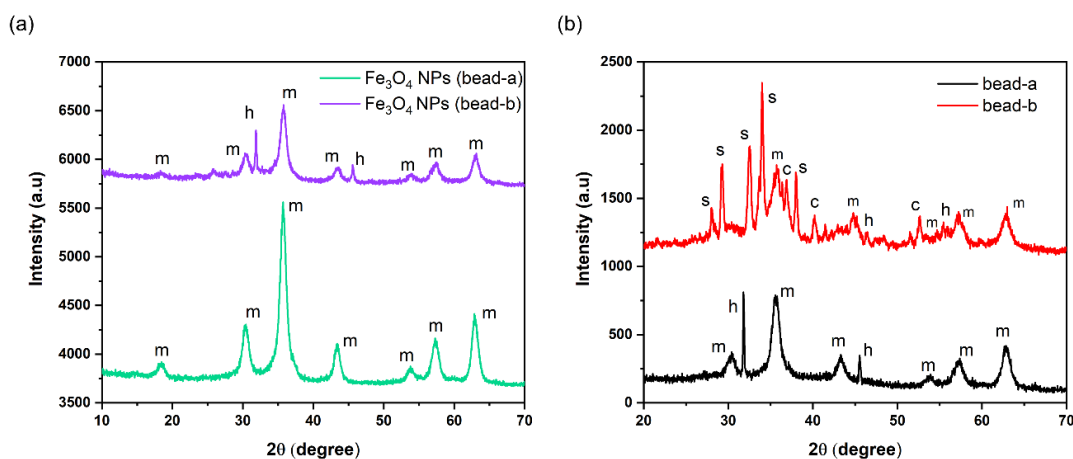


Figure 3.8. (a) XRD spectra of the nanoparticles used in bead-a (top) and the *in situ* synthesised in bead-b (bottom). (b) XRD patterns of the bead-a and the bead-b. m - magnetite- Fe_3O_4 , h - NaCl, s - Na_2SO_4 , c - NaOH.

3.3.4.2 Raman spectra

Raman spectroscopy is able to provide distinguishable identification between magnetite and maghemite phases in synthesised iron oxide nanoparticles, which is usually difficult during XRD analysis. Fe_3O_4 has an inverse spinel type structure, showing five Raman active bands due to the symmetry combination of $A_{1g} + E_g + 3T_{2g}$.⁴⁷ In literature, a sharp band at $\sim 668\text{ cm}^{-1}$ and two weak bands at ~ 306 and $\sim 538\text{ cm}^{-1}$ were observed for A_{1g} and T_{2g} Raman modes, respectively, for magnetite. On the other hand, for maghemite, a wide band with split peaks at ~ 660 and ~ 710 , and $\sim 500\text{ cm}^{-1}$ were attributed for A_{1g} and E_g modes, respectively. Furthermore, two high intense red shifted, 306 cm^{-1} , and a blue shifted, 538 cm^{-1} (by magnetite T_{2g}), bands were reported, for

magnetite to maghemite oxidation.⁴⁸ The Raman spectrum of the Fe₃O₄ nanoparticles used for the synthesis of the bead-a, and the spectrum of the alginate magnetic bead-a were carried out at different laser irradiation powers, Figure 3.9a and b respectively. The sharp band at 670 cm⁻¹ can be attributed to the magnetite A_{1g} mode, while the bands at 490 and 330 cm⁻¹ under higher laser power intensity (1.5 mW) were attributed to the oxidation of magnetite (T_{2g}) to maghemite, in Figure 3.9a. In literature, the oxidation of magnetite to maghemite has been reported by Ying-Sing Li *et al.*⁴⁹ under high laser power irradiations for Fe₃O₄ nanoparticles as the ones used in the synthesis of the bead-a type, confirming this band assignation. The Raman spectra of the bead-a, shown in Figure 3.9b, at 1.5 mW presented very weak bands at 540 and 307 cm⁻¹, indicating that the oxidation of magnetite to maghemite under high laser power intensities is avoided by the presence of the alginate matrix. The alginate polymer acts as a protective layer for the nanoparticles within the bead-a.

The Raman spectrum of the *in situ* synthesised Fe₃O₄ nanoparticles in bead-b type can be compared to the one of the bare Fe₃O₄ nanoparticles used during the synthesis of the bead-a at 1.5 mW laser power intensity. The absence of the maghemite peaks in *in situ* synthesised Fe₃O₄, according to the Figure 3.9c, indicates that the *in situ* synthesised Fe₃O₄ were coated with an alginate layer, which avoid the oxidation of *in situ* synthesised Fe₃O₄. Both bead-a and bead-b Raman spectra depicted in Figure 3.9d, exhibited only the magnetite bands at 670 (sharp), 540 (very weak) and 307 (weak) cm⁻¹, avoiding the oxidation due to the alginate matrix shielding. Moreover, an extra band at 1070 cm⁻¹ was observed in the Raman spectra of the bead-b, which was attributed to the sodium sulphate⁵⁰, confirming again the high ionic density inside of the bead-b type. The dried beads and *in situ* synthesised Fe₃O₄ nanoparticles did not present any band attributed to maghemite since the nanoparticles were protected with an alginate layer during synthesis process. However, the bare Fe₃O₄ nanoparticles in bead-a have a tendency to oxidise in high (1.5 mW) laser irradiation during the Raman spectra recording.

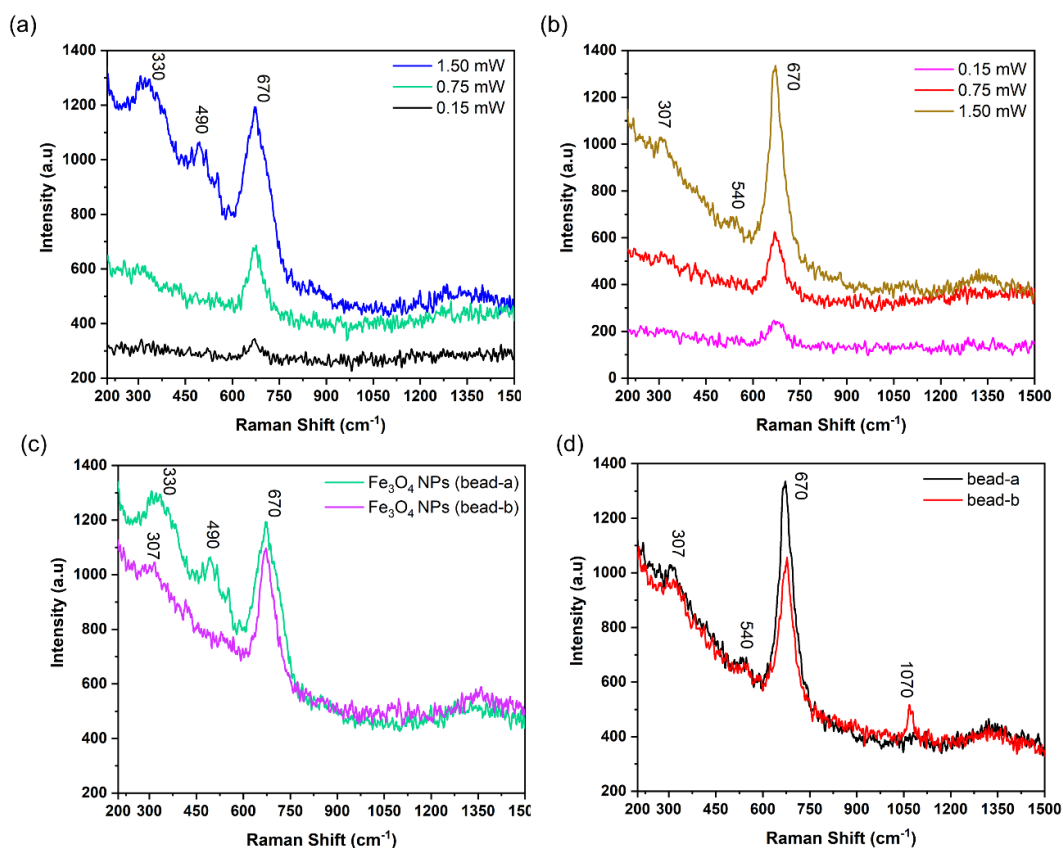


Figure 3.9. Raman spectra of (a) Fe_3O_4 nanoparticles (NPs) used during the synthesis of the bead-a and (b) bead-a at different laser power intensities. (b) Fe_3O_4 nanoparticles (NPs) used during the synthesis of the bead-a and *in situ* synthesised Fe_3O_4 nanoparticles in bead-b at 1.5 mW laser power intensity. (c) Raman spectra of bead-a and bead-b at 1.5 mW laser power intensity.

3.3.4.3 FTIR spectra

Figure 3.10a, shows the FTIR spectra of the two types of magnetic nanoparticles. Similar peaks were obtained for both type of nanoparticles. The bands at 570 and 590 cm^{-1} were attributed to the FeO stretching vibrational bands in tetrahedral and octahedral sites of the Fe_3O_4 , while the broad bands at ~ 3400 and ~ 1630 cm^{-1} came from the OH stretching and bending vibrations modes of surface absorbed hydroxyl/water bonds, respectively. Extra bands were observed in the spectrum of the *in situ* synthesised nanoparticles inside the bead-b type. The bands at 1410, 1117 and 1030 cm^{-1} were attributed to the carboxylate COO symmetric stretching vibrations and COC stretching vibrations^{47,51}. Moreover, the peak at 1627 cm^{-1} was assigned to the COO asymmetric vibrational band, overlapping with the OH bending vibrations. The presence of these extra peaks demonstrated that the nanoparticles synthesised in the

bead-b were coated with an organic alginate layer during nanoparticle nucleation. As explained before, this layer prevented the aggregation of the nanoparticles in the water solution and promoted the formation of smaller, lower nucleation, and more homogeneous distributed nanoparticle suspensions, as presented in Figure 3.7b.

Moreover, the FTIR spectra of the two type of beads (bead-a and bead-b) were also performed and compared, Figure 3.10b. Considering the peak ascription in the nanoparticle spectra, the bands at 3420/3450, 570/615, 1610/1640, 1405/1445, 1025/1120 cm^{-1} were attributed to the OH stretching, Fe-O stretching, COO asymmetric, COO symmetric and COC stretching vibrational bands, respectively⁴⁷.

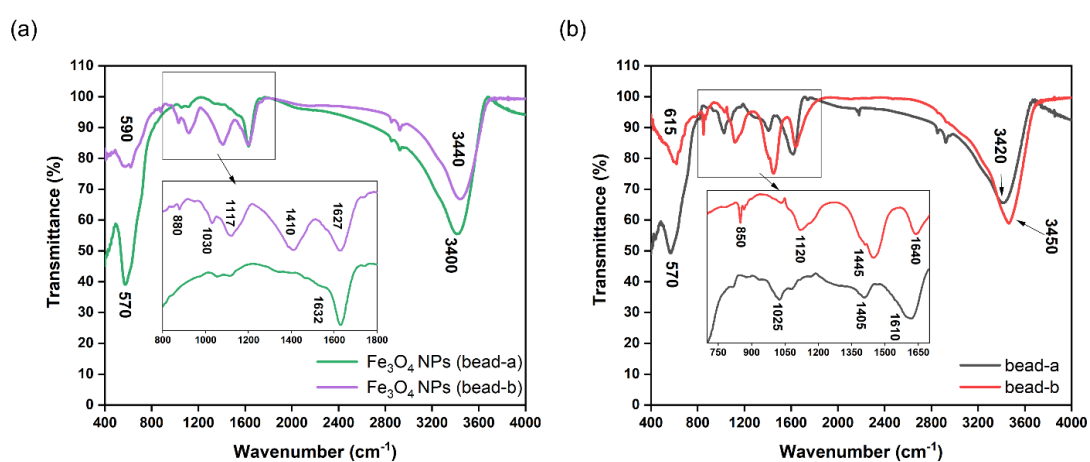


Figure 3.10. (a) FTIR spectra of the nanoparticles used for the synthesis of bead-a (Fe_3O_4 nanoparticles (bead-a)) and the *in situ* synthesised nanoparticles inside the bead-b type (Fe_3O_4 nanoparticles (bead-b)); inset shows the magnified peaks at 800 - 1800 cm^{-1} range. (b) FTIR spectra of bead-a, and bead-b; inset shows the magnified peaks at 750 - 1650 cm^{-1} range.

The difference between band position values ($\Delta\nu$) of asymmetric and symmetric COO stretching vibrational modes provides information about the coordination or the interaction between the inorganic metal phases and the carboxylate groups in alginate polymer matrixes when compared to the $\Delta\nu$ of sodium alginate, as demonstrated by Papageorgiou *et al.*⁴ According to the Figure 3.10b, the calculated values of $\Delta\nu$ for bead-a and bead-b are 205 and 195 cm^{-1} , respectively; while the $\Delta\nu$ for an Na-alginate was calculated to be 192 cm^{-1} , see Figure 3.11. Calculated $\Delta\nu$ values for calcium alginate and $\text{Fe}^{3+}/\text{Fe}^{2+}$ alginate are 170 and 179, respectively, Figure 3.11. In theory,^{4,52} when $\Delta\nu(\text{COO})_{\text{composite}} \ll \Delta\nu(\text{COO})_{\text{alginate}}$ the coordination could be considered to be bidentate chelating, $\Delta\nu(\text{COO})_{\text{composite}} \sim \Delta\nu(\text{COO}^-)_{\text{alginate}}$ bidentate bridging coordination

and unidentate coordination if $\Delta\nu(\text{COO})_{\text{composite}} \gg \Delta\nu(\text{COO})_{\text{alginate}}$. Therefore, considering the $\Delta\nu$ values obtained from the different spectra, the addition of Fe_3O_4 nanoparticles to the calcium alginate matrix converted the interaction of bidentate chelating coordination mode to a more unidentate coordination type, which is a stronger egg box model⁴. In the case of the bead-b, bidentate chelating coordination of $\text{Fe}^{3+}/\text{Fe}^{2+}$ and alginate was converted to bidentate bridging coordination (*in situ* Fe_3O_4 –alginate), after magnetite phase synthesis. In base of the obtained results, it could be speculated that the coordination of the cross-linked metal and the carboxylate group changed after the magnetic phase was introduced into the hydrogel bead-b.

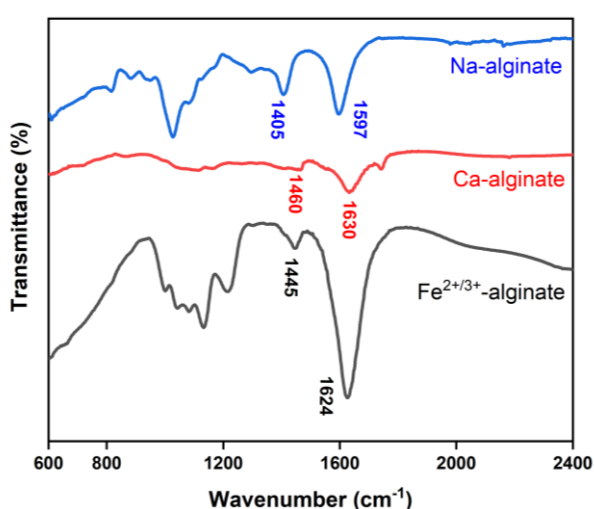


Figure 3.11. FTIR spectra of sodium alginate powder, Ca-alginate and $\text{Fe}^{2+/3+}$ -alginate dehydrated hydrogel bead.

3.3.5 Magnetic characterisation

The magnetic properties of the synthesised beads (dry state) were characterised by superconducting quantum interference device (SQUID) magnetometer, at room temperature. The magnetisation curves for the synthesised Fe_3O_4 nanoparticles used in bead-a and for the magnetic bead-a, bead-b and bead-c types are presented in the Figure 3.12a and b, respectively. The obtained values for the saturation magnetisation (M_s), coercivity (H_c) and remanence (R_m) are depicted in the Table-3.2.

Table-3.2. Magnetic properties of the Fe₃O₄ nanoparticles used for the synthesis of bead-a, bead-a, bead-b and bead-c.

| Sample | Ms (Am ² kg ⁻¹) | Hc (*10 ⁻³ T) | Rm (Am ² kg ⁻¹) |
|--|---|-----------------------------|---|
| Fe ₃ O ₄ nanoparticle (bead-a) | 73.0 | 1.00 | 0.895 |
| bead-a | 28.2 | 0.96 | 0.329 |
| bead-b | 41.1 | 1.09 | 0.870 |
| bead-c | 33.5 | 1.11 | 0.536 |

The Ms value of the bead-a, which contains a 60 % and Fe₃O₄ nanoparticles loading in the alginate, was significantly lower than the expected value, 43.8 Am² kg⁻¹, corresponding to Fe₃O₄ nanoparticles (Ms 73.0 Am² kg⁻¹) weight ratio during synthesis. The obtained value, 28.2 Am² kg⁻¹, can be explained considering the participation of the cross-linkers, Ca²⁺ ions (non-magnetic), in the formation of hydrogel, which caused the reduction of the Ms. Moreover, in this type of hydrogels, a low percentage of magnetic phase loading resulted on the reduction of the magnetisation of the bead in a greater extent, compared to a high percentage of loading, since the participation of none magnetic cross-linkers increases with the alginate percentage. Bead-a exhibited a low or no hysteresis with a very low coercivity and residual magnetisation, close to a superparamagnetic like material, as shown in the inset of Figure 3.12a.

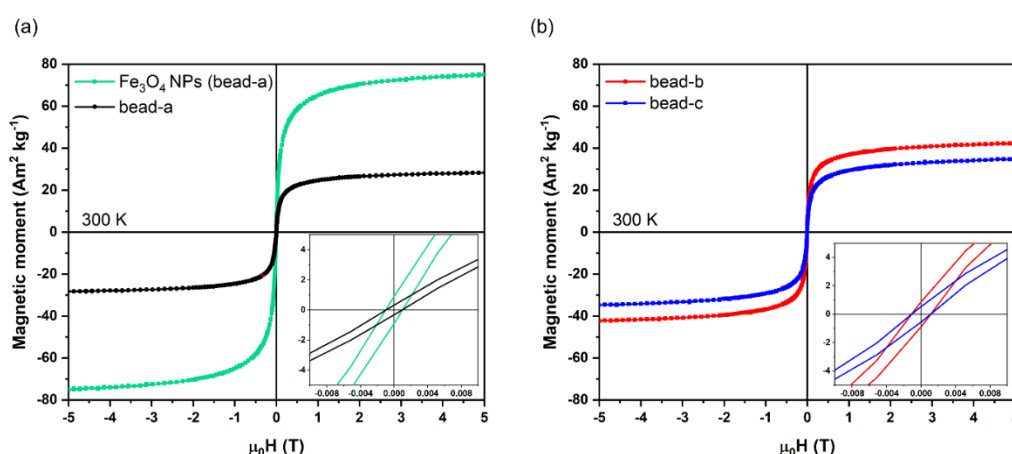


Figure 3.12. M-H curves generated by the superconducting quantum interference device (SQUID) magnetometer, at room temperature for the synthesised iron oxide nanoparticles used in the synthesis of bead-a, bead-b and bead-c, and for the Fe₃O₄ nanoparticles used in bead-a.

The bead-b, which contains the *in situ* synthesised Fe₃O₄ nanoparticles presented a Ms of 41.1 Am² kg⁻¹. The magnetic properties of the *in situ* synthesised iron oxide nanoparticles in the bead-b type can be easily manipulated by varying the Fe²⁺/Fe³⁺ concentrations, the cross-linking concentrations and the diffusing time during the fabrication process. In addition, the smaller size of the magnetic nanoparticles synthesised in the bead-b, resulting in a reduced value of the saturation magnetisation. The extra alginate/Ca²⁺ (non-magnetic) layer to cover the bead-b and generate the bead-c type led to a further reduction of the Ms value, down to 33.5 Am² kg⁻¹. Bead-b and bead-c exhibited, as in the case of bead-a, a low or no hysteresis with a very low coercivity and residual magnetisation, reaching to superparamagnetism, see the inset in Figure 3.12b. Therefore, considering the flexibility of the fabrication of these types of beads, they could be used for magneto-driven applications.

3.4 Conclusions

Three different synthesis methods for the fabrication of magnetic alginate beads were carried out and compared. Moreover, the beads were morphologically, chemically and magnetically characterised. Bead-a used the direct blending of Fe₃O₄ nanoparticles (*ex situ*) within an alginate solution, followed by gelation with calcium chloride solution. The bead-b presented the cross-link of the alginate with a Fe³⁺/Fe²⁺ solution followed by the *in situ* synthesis of Fe₃O₄ nanoparticles inside of the alginate beads, which is a cheap and efficient protocol to synthesise nanocomposites. Finally, the method-c added an extra alginate layer, cross-linked with calcium ions to the bead-b in order to improve resistance at neutral pH. The stability of the three types of beads was investigated under aqueous solutions at different pH values, over time. It was found that the bead-b type, suffered a fast degradation process at neutral pH, due to the high ionic density inside of the beads.

The *in situ* synthesised nanoparticles, generated in bead-b type, exhibit a low particles size of ~ 3 nm when compared to the Fe₃O₄ nanoparticles used for the synthesis of bead-a (~ 8 nm). This was due to the confinement of Fe³⁺ /Fe²⁺ in the alginate hydrogel matrix during the nucleation and growth of the Fe₃O₄ nanoparticles in the bead-b. Moreover, aqueous medium stable suspension of *in situ* synthesised nanoparticles were obtained,

with high zeta potential (-57.6 mV), due to the coating of an alginate layer around these particles. In addition, these particles, in bead-b, showed a magnetite crystal phase with a low tendency to oxidise due to the alginate coating. Their magnetisation values, in combination with their low magnetic hysteresis, possibility of using these alginate beads for magneto-driven applications.

This investigation provides with a fundamental framework to understand the properties of blended, *ex situ*, and *in situ* synthesised magnetic metal-oxide based alginate hydrogels. This study will direct the path to select the magnetic bead mode (bead-a, bead-b, bead-c) for different kind of magneto-driven hydrogel applications.

3.5 References

- (1) Gunatilake, U. B.; Venkatesan, M.; Basabe-Desmonts, L.; Benito-Lopez, F. Ex Situ and in Situ Magnetic Phase Synthesised Magneto-Driven Alginate Beads. *J. Colloid Interface Sci.* **2022**, *610*, 741–750.
- (2) Draget, K. I. Alginates. *Handb. Hydrocoll. Second Ed.* **2009**, 807–828.
- (3) Rehm, B. H. A. Alginate Production: Precursor Biosynthesis, Polymerization and Secretion. In *Alginates: Biology and applications*; 2009; pp 55–71.
- (4) Papageorgiou, S. K.; Kouvelos, E. P.; Favvas, E. P.; Sapalidis, A. A.; Romanos, G. E.; Katsaros, F. K. Metal–Carboxylate Interactions in Metal–Alginate Complexes Studied with FTIR Spectroscopy. *Carbohydr. Res.* **2010**, *345* (4), 469–473.
- (5) Braccini, I.; Serge, P. Molecular Basis of Ca²⁺-Induced Gelation in Alginates and Pectins: The Egg-Box Model Revisited. *Biomacromolecules* **2001**, *2* (4), 1089–1096.
- (6) Boonthekul, T.; Kong, H. J.; Mooney, D. J. Controlling Alginate Gel Degradation Utilizing Partial Oxidation and Bimodal Molecular Weight Distribution. *Biomaterials* **2005**, *26* (15), 2455–2465.
- (7) Sarmiento, B.; Ribeiro, A.; Veiga, F.; Sampaio, P.; Neufeld, R.; Ferreira, D. Alginate/Chitosan Nanoparticles Are Effective for Oral Insulin Delivery. *Pharm. Res.* **2007**, *24* (12), 2198–2206.

- (8) García-Astrain, C.; Avérous, L. Synthesis and Evaluation of Functional Alginate Hydrogels Based on Click Chemistry for Drug Delivery Applications. *Carbohydr. Polym.* **2018**, *190*, 271–280.
- (9) Wells, L. A.; Sheardown, H. Extended Release of High PI Proteins from Alginate Microspheres via a Novel Encapsulation Technique. *Eur. J. Pharm. Biopharm.* **2007**, *65* (3), 329–335.
- (10) Park, J.; Lee, S. J.; Lee, H.; Park, S. A.; Lee, J. Y. Three Dimensional Cell Printing with Sulfated Alginate for Improved Bone Morphogenetic Protein-2 Delivery and Osteogenesis in Bone Tissue Engineering. *Carbohydr. Polym.* **2018**, *196*, 217–224.
- (11) E, W.; D, K. Alginate Matrices for Protein Delivery - a Short Review. *Physiol. Res.* **2018**, *67* (Suppl 2), s319–s334.
- (12) Ma, R.; Wang, Y.; Qi, H.; Shi, C.; Wei, G.; Xiao, L.; Huang, Z.; Liu, S.; Yu, H.; Teng, C.; Liu, H.; Murugadoss, V.; Zhang, J.; Wang, Y.; Guo, Z. Nanocomposite Sponges of Sodium Alginate/Graphene Oxide/Polyvinyl Alcohol as Potential Wound Dressing: In Vitro and in Vivo Evaluation. *Compos. Part B Eng.* **2019**, *167*, 396–405.
- (13) Aderibigbe, B. A.; Buyana, B. Alginate in Wound Dressings. *Pharmaceutics* **2018**, *10* (2), 42.
- (14) Batista, P. S. P.; Morais, A. M. M. B. de; Pintado, M. M. E.; Morais, R. M. S. C. de. Alginate: Pharmaceutical and Medical Applications. **2019**, 649–691.
- (15) Mir, M.; Ali, M. N.; Barakullah, A.; Gulzar, A.; Arshad, M.; Fatima, S.; Asad, M. Synthetic Polymeric Biomaterials for Wound Healing: A Review. *Prog. Biomater.* **2018**, *71* **2018**, *7* (1), 1–21.
- (16) Kuo, C. K.; Ma, P. X. Ionically Crosslinked Alginate Hydrogels as Scaffolds for Tissue Engineering: Part 1. Structure, Gelation Rate and Mechanical Properties. *Biomaterials* **2001**, *22* (6), 511–521.
- (17) Contessi Negrini, N.; Bonnetier, M.; Giatsidis, G.; Orgill, D. P.; Farè, S.; Marelli, B. Tissue-Mimicking Gelatin Scaffolds by Alginate Sacrificial Templates for Adipose Tissue Engineering. *Acta Biomater.* **2019**, *87*, 61–75.

- (18) Álvarez, K.; Alvarez, V. A.; Gutiérrez, T. J. Biopolymer Composite Materials with Antimicrobial Effects Applied to the Food Industry. **2018**, 57–96.
- (19) Qin, Y.; Jiang, J.; Zhao, L.; Zhang, J.; Wang, F. Applications of Alginate as a Functional Food Ingredient. *Biopolym. Food Des.* **2018**, 409–429.
- (20) Thakur, S.; Sharma, B.; Verma, A.; Chaudhary, J.; Tamulevicius, S.; Thakur, V. K. Recent Progress in Sodium Alginate Based Sustainable Hydrogels for Environmental Applications. *J. Clean. Prod.* **2018**, 198, 143–159.
- (21) Yuan, Z.; Yan, K.; Xuechun, W.; Baoyou, S. Novel One Step Preparation of a 3D Alginate Based MOF Hydrogel for Water Treatment. *New J. Chem.* **2019**, 43 (19), 7202–7208.
- (22) Peng, N.; Ding, X.; Wang, Z.; Cheng, Y.; Gong, Z.; Xu, X.; Gao, X.; Cai, Q.; Huang, S.; Liu, Y. Novel Dual Responsive Alginate-Based Magnetic Nanogels for Onco-Theranostics. *Carbohydr. Polym.* **2019**, 204, 32–41.
- (23) Tamhankar, P. M.; Kulkarni, A. M.; Watawe, S. C.; Tamhankar, P. M.; Kulkarni, A. M.; Watawe, S. C. Functionalization of Cobalt Ferrite Nanoparticles with Alginate Coating for Biocompatible Applications. *Mater. Sci. Appl.* **2011**, 2 (9), 1317–1321.
- (24) Finotelli, P. V.; Da Silva, D.; Sola-Penna, M.; Rossi, A. M.; Farina, M.; Andrade, L. R.; Takeuchi, A. Y.; Rocha-Leão, M. H. Microcapsules of Alginate/Chitosan Containing Magnetic Nanoparticles for Controlled Release of Insulin. *Colloids Surf. B* **2010**, 81 (1), 206–211.
- (25) Schmidt, A. M. Thermoresponsive Magnetic Colloids. *Colloid Polym. Sci.* **2007** 2859 **2007**, 285 (9), 953–966.
- (26) Kondaveeti, S.; Semeano, A. T. S.; Cornejo, D. R.; Ulrich, H.; Petri, D. F. S. Magnetic Hydrogels for Levodopa Release and Cell Stimulation Triggered by External Magnetic Field. *Colloids Surf. B* **2018**, 167, 415–424.
- (27) Mitsumata, T.; Kakiuchi, Y.; Takimoto, J. I. Fast Drug Release Using Rotational Motion of Magnetic Gel Beads. *Res. Lett. Phys. Chem.* **2008**, 2008, 1–5.
- (28) Yang, C.-H.; Yen, C.-C.; Jheng, J.-J.; Wang, C.-Y.; Chen, S.-S.; Huang, P.-Y.; Huang, K.-S.; Shaw, J.-F. Immobilization of Brassica Oleracea Chlorophyllase

- 1 (BoCLH1) and Candida Rugosa Lipase (CRL) in Magnetic Alginate Beads: An Enzymatic Evaluation in the Corresponding Proteins. *Molecules* **2014**, *19* (8), 11800–11815.
- (29) Brulé, S.; Levy, M.; Wilhelm, C.; Letourneur, D.; Gazeau, F.; Ménager, C.; Visage, C. Le. Doxorubicin Release Triggered by Alginate Embedded Magnetic Nanoheaters: A Combined Therapy. *Adv. Mater.* **2011**, *23* (6), 787–790.
- (30) Amiri, M.; Salavati-Niasari, M.; Pardakhty, A.; Ahmadi, M.; Akbari, A. Caffeine: A Novel Green Precursor for Synthesis of Magnetic CoFe₂O₄ Nanoparticles and pH-Sensitive Magnetic Alginate Beads for Drug Delivery. *Mater. Sci. Eng. C* **2017**, *76*, 1085–1093.
- (31) Rocher, V.; Siaugue, J. M.; Cabuil, V.; Bee, A. Removal of Organic Dyes by Magnetic Alginate Beads. *Water Res.* **2008**, *42* (4–5), 1290–1298.
- (32) Zhimin, L.; Shangru, Z.; Jialiang, L.; Yuan, F.; Qingda, A.; Zuoyi, X. Sodium Alginate-Based Magnetic Carbonaceous Biosorbents for Highly Efficient Cr(vi) Removal from Water. *RSC Adv.* **2015**, *5* (95), 77932–77941.
- (33) Bée, A.; Talbot, D.; Abramson, S.; Dupuis, V. Magnetic Alginate Beads for Pb(II) Ions Removal from Wastewater. *J. Colloid Interface Sci.* **2011**, *362* (2), 486–492.
- (34) Yanting, L.; Yuanyuan, Y.; Xiong, Y.; Liu, Y.; Yajing, S.; Wanfeng, S. Multi-Functionalized Micro-Helical Capsule Robots with Superior Loading and Releasing Capabilities. *J. Mater. Chem. B* **2021**, *9* (5), 1441–1451.
- (35) Philippova, O.; Barabanova, A.; Molchanov, V.; Khokhlov, A. Magnetic Polymer Beads: Recent Trends and Developments in Synthetic Design and Applications. *Eur. Polym. J.* **2011**, *47* (4), 542–559.
- (36) Hammouda, S. Ben; Adhoum, N.; Monser, L. Synthesis of Magnetic Alginate Beads Based on Fe₃O₄ Nanoparticles for the Removal of 3-Methylindole from Aqueous Solution Using Fenton Process. *J. Hazard. Mater.* **2015**, *294*, 128–136.
- (37) Soumia, A.; Adel, M.; Amina, S.; Bouhadjar, B.; Amal, D.; Farouk, Z.; Abdelkader, B.; Mohamed, S. Fe₃O₄-Alginate Nanocomposite Hydrogel Beads Material: One-Pot Preparation, Release Kinetics and Antibacterial Activity. *Int.*

J. Biol. Macromol. **2020**, *145*, 466–475.

- (38) Rashidzadeh, B.; Shokri, E.; Mahdavinia, G. R.; Moradi, R.; Mohamadi-Aghdam, S.; Abdi, S. Preparation and Characterization of Antibacterial Magnetic-/pH-Sensitive Alginate/Ag/Fe₃O₄ Hydrogel Beads for Controlled Drug Release. *Int. J. Biol. Macromol.* **2020**, *154*, 134–141.
- (39) Wang, W.; P, L.; JP, Z.; AQ, W.; Q, W. A Novel pH-Sensitive Magnetic Alginate-Chitosan Beads for Albendazole Delivery. *Drug Dev. Ind. Pharm.* **2010**, *36* (7), 867–877.
- (40) Supramaniam, J.; Adnan, R.; Mohd Kaus, N. H.; Bushra, R. Magnetic Nanocellulose Alginate Hydrogel Beads as Potential Drug Delivery System. *Int. J. Biol. Macromol.* **2018**, *118*, 640–648.
- (41) Laurent, S.; Forge, D.; Port, M.; Roch, A.; Robic, C.; Elst, L. Vander; Muller, R. N. Magnetic Iron Oxide Nanoparticles: Synthesis, Stabilization, Vectorization, Physicochemical Characterizations, and Biological Applications. *Chem. Rev.* **2008**, *108* (6), 2064–2110.
- (42) Leong, J. Y.; Lam, W. H.; Ho, K. W.; Voo, W. P.; Lee, M. F. X.; Lim, H. P.; Lim, S. L.; Tey, B. T.; Poncelet, D.; Chan, E. S. Advances in Fabricating Spherical Alginate Hydrogels with Controlled Particle Designs by Iontropic Gelation as Encapsulation Systems. *Particuology* **2016**, *24*, 44–60.
- (43) Bajpai, S. K.; Sharma, S. Investigation of Swelling/Degradation Behaviour of Alginate Beads Crosslinked with Ca²⁺ and Ba²⁺ Ions. *React. Funct. Polym.* **2004**, *59* (2), 129–140.
- (44) Gutiérrez, L.; Cueva, L. de la; Moros, M.; Mazarío, E.; Bernardo, S. de; Fuente, J. M. de la; Morales, M. P.; Salas, G. Aggregation Effects on the Magnetic Properties of Iron Oxide Colloids. *Nanotechnology* **2019**, *30* (11), 112001.
- (45) Gates-Rector, S.; Blanton, T. The Powder Diffraction File: A Quality Materials Characterization Database. *Powder Diffr.* **2019**, *34* (4), 352–360.
- (46) Gražulis, S.; Chateigner, D.; Downs, R. T.; Yokochi, A. F.; Quirós, M.; Lutterotti, L.; Manakova, E.; Butkus, J.; Moeck, P.; Le Bail. Crystallography Open Database - an Open-Access Collection of Crystal Structures. *J. Appl.*

Crystallogr. **2009**, *42* (Pt 4), 726–729.

- (47) Srivastava, M.; Singh, J.; Yashpal, M.; Gupta, D. K.; Mishra, R. K.; Tripathi, S.; Ojha, A. K. Synthesis of Superparamagnetic Bare Fe₃O₄ Nanostructures and Core/Shell (Fe₃O₄/Alginate) Nanocomposites. *Carbohydr. Polym.* **2012**, *89* (3), 821–829.
- (48) Schwaminger, S.; Bauer, D.; Fraga-García, P.; Wagner, F. E.; Berensmeier, S. Oxidation of Magnetite Nanoparticles: Impact on Surface and Crystal Properties. *CrystEngComm* **2017**, *19* (2), 246–255.
- (49) Li, Y. S.; Church, J. S.; Woodhead, A. L. Infrared and Raman Spectroscopic Studies on Iron Oxide Magnetic Nano-Particles and Their Surface Modifications. *J. Magn. Magn. Mater.* **2012**, *324* (8), 1543–1550.
- (50) Mabrouk, K.; Kauffmann, T.; Aroui, H.; Fontana, M. Raman Study of Cation Effect on Sulfate Vibration Modes in Solid State and in Aqueous Solutions. *J. Raman Spectrosc.* **2013**, *44* (11), 1603–1608.
- (51) Mohammadi, A.; Daemi, H.; Barikani, M. Fast Removal of Malachite Green Dye Using Novel Superparamagnetic Sodium Alginate-Coated Fe₃O₄ Nanoparticles. *Int. J. Biol. Macromol.* **2014**, *69*, 447–455.
- (52) Nakamoto, K. Infrared and Raman Spectra of Inorganic and Coordination Compounds. *Handb. Vib. Spectrosc.* **2006**.

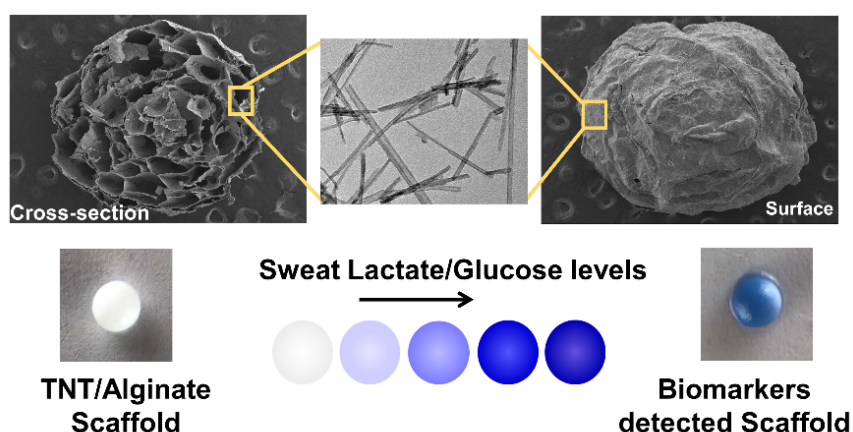
TiO₂ Nanotubes Alginate Hydrogel Scaffold for Rapid Sensing of Sweat Biomarkers - Lactate and Glucose

This Chapter is partially reproduced from:¹

Gunatilake, U. B.; Garcia-Rey, S.; Ojeda, E.; Basabe-Desmonts, L.; Benito-Lopez, F. TiO₂ Nanotubes Alginate Hydrogel Scaffold for Rapid Sensing of Sweat Biomarkers: Lactate and Glucose. *ACS Applied Materials & Interfaces*, 2021, 13 (31), 37734–37745.

<https://doi.org/10.1021/acsami.1c11446>

Abstract. Versatile sensing matrixes are essential for the development of enzyme immobilised optical biosensors. A novel three-dimensional titanium dioxide nanotubes/alginate hydrogel scaffold is proposed for the detection of sweat biomarkers, lactate and glucose, in artificial sweat. Hydrothermally synthesised titanium dioxide nanotubes were introduced to the alginate polymeric matrix, followed by nanocomposite crosslink with di-cationic calcium ions, to fabricate the scaffold platform. Rapid colorimetric detection (blue colour optical signal) was carried out for both, lactate and glucose, biomarkers in artificial sweat at 4 and 6 min, respectively. The superhydrophilicity and the capillarity of the synthesised titanium dioxide nanotubes, when incorporated into the alginate matrix, facilitate the rapid transfer of the artificial sweat components throughout the sensor scaffold, decreasing detection times. Moreover, the scaffold was integrated on a cellulose paper to demonstrate the adaptability of the material to other matrixes, obtaining fast and homogeneous colorimetric detection of lactate and glucose in the paper substrate, when image analysis was performed. The properties of this new composite provide new avenues in the development of paper-based sensor devices. The biocompatibility, the efficient immobilisation of biological enzymes/colorimetric assays and the quick optical signal readout behaviour of the titanium dioxide nanotubes/alginate hydrogel scaffolds provide a prospective opportunity for integration into wearable devices.



4.1 Introduction

Real time sweat analysis opens a non-invasive route to gather valuable information on the variability of biomolecules and ions concentrations over time; where sodium, chloride, potassium, calcium, ammonia, glucose and lactate are important parameters used to monitor sport performance and health.²⁻⁴ For instance, lactate is an important biomarker, acting as a vital metabolite in the anaerobic metabolic pathway.⁵ Blood lactate is usually monitored during physical performance, since its production is activated by the anaerobic metabolism to provide the required energy to the body by glucose breakdown.⁵⁻⁷ Interestingly, it has been demonstrated that sweat lactate increases with blood lactate levels after intense workouts or physical activities.^{8,9} In the same way, glucose is a vital metabolite found in sweat, that can be correlated to blood glucose too.¹⁰ If uncontrolled, is well known to affect diabetics due to high glucose levels, reaching to severe medical complications.

Biosensors have attracted scientists' attention due to their potential to change classical medical diagnosis and enable novel health monitoring concepts.^{11,12} Miniaturised biosensors have been recently developed, in where electrochemical transducers are widely used due to their low production cost, portability and ease of operation.^{6,13-18} However, a power free, simple signal reading phenomena is essential for real time sweat analysis wearable devices. Optical detection, and in particular colorimetric sensing, provides simpler signal readout capabilities. It offers rapid quantification of certain analytes, measuring their colour variation by absorbance measurements or analysing colour parameters such as RGB or HUE, by image analysis.^{16,19-21} Thereby, colorimetric detection of biomarkers in sweat becomes simple, cheap and easily implementable in wearable devices.^{19,22}

In this regard, researchers have investigated different sensing platforms which are deeply discussed in Chapter-2 section 2.4, for colorimetric sweat biomarkers detection. However, long-time efficient and effective immobilisation of enzymatic biological and/or colorimetric assays, with high loading capacity and rapid sensing capabilities, are still challenging in sweat sensors.

Wearable devices are directly in contact with the human skin therefore, the biocompatibility of the sensor is essential when designing sensor scaffolds.²³ In this regard, alginate is a biocompatible polysaccharide material, which crosslinks with di-

cationic metal ions to form hydrogels widely used for the food and the pharmaceutical industries.^{24–26} Because of the hydrophilicity and porosity of the alginate hydrogel, external aqueous fluids are easily absorbed by the alginate hydrogel scaffold. Moreover, the water enriched alginate hydrogel polymer matrix facilitates storing relevant colorimetric assays and catalytic enzymes inside without damaging them.²⁷ These properties make alginate, an excellent candidate for the fabrication of biosensors.

On the other hand, titanium dioxide (TiO₂) is a thermally stable, highly insoluble, non-hazardous, biocompatible, hydrophilic and photocatalytic inorganic substance, which is used to manufacture nanostructures.^{28–31} In particular, these titanium dioxide nanostructures have been recently used for biosensing applications.^{32–34} TiO₂ with 1-D structures such as nanotubes, nanowires or fibrous are candidates to enhance the superhydrophilicity and capillary activity of sensor platforms.^{29,35} Therefore, the combination of both alginate hydrogels and the TiO₂ nanostructures could lead to an upstanding nanocomposite material to be employed as a biosensing platform.

Herein, we present a three-dimensional TiO₂ nanotubes/alginate hydrogel scaffold as a colorimetric biosensor for the detection of lactate and glucose in artificial sweat. The fabrication of the matrix requires two steps, the titanium dioxide nanotubes (TNT) synthesis and the cationic crosslinking of alginate to generate a nanocomposite hydrogel. The analytical performance of the sensing scaffold was carried out using spherical shape sensors. They were used for the detection of glucose and lactate concentrations in artificial sweat by image analysis. Finally, we integrated the scaffold to a paper substrate by *in situ* hydrogel polymerisation, to enhance sensing and signal read out performance of the paper matrix.

4.2 Experimental

4.2.1 Synthesis and characterisation of the TiO₂ nanotubes

First, TiO₂ nanoparticles were synthesised by a precipitation method similar to the one described in reference.³⁶ Briefly, a titanium precursor solution was prepared by adding 5 mL of titanium isopropoxide (97 %, Sigma-Aldrich, Spain) to 15 mL of isopropanol (EssentQ, Sharlab, Spain). The solution was transferred to a 250 mL distilled water (pH ~ 2 by 1 M nitric acid (65 %, Sigma-Aldrich, Spain) solution, under vigorous stirring. Hydrolysis of titanium isopropoxide occurred rapidly, showing a turbid solution. Then,

the solution was heated at 60 °C under stirring for 12 h. Then, the precipitate was washed with water and ethanol for three times and the particles were separated by rotary evaporation at 60 °C, under vacuum.

TiO₂ nanotubes were synthesised by a hydrothermal method using the synthesised TiO₂ nanoparticles.^{37,38} 1.0 g of TiO₂ nanoparticles were stirred in 20 mL of 10 M NaOH (98 %, Sigma-Aldrich, Spain) for 2 h. Then, the basic titania dispersion was transferred to a Teflon lined hydrothermal autoclave vessel and was heated at 150 °C for 48 h inside of the furnace. The precipitate was removed after the vessel was cooled to room temperature and was washed with water and 0.1 M HCl (37 %, Sigma-Aldrich, Spain) until the pH of the synthesised TiO₂ nanotubes reached pH 7-8. Finally, the TiO₂ nanotubes were separated by rotary evaporation at 60 °C under vacuum.

Transmission electron microscopy (TEM) images of the TiO₂ nanotubes (in water suspension) were collected from JEOL JEM 1400 Plus (JEOL, Japan) at an accelerating voltage of 120 kV. Scanning electron microscopy (SEM) images of the freeze-dried TNT/alginate scaffolds were recorded by Hitachi S-4800 (Hitachi Japan) at an accelerating voltage of 10 kV. UV-Visible spectrums were recorded by Infinite M200 (TECAN Trading AG, Switzerland) microplate reader.

4.2.2 Preparation of the artificial sweat stock solution

A stock solution of artificial sweat was made by using 300 mM NaCl (99 %, Sigma-Aldrich, Spain), 40 mM urea (Fisher BioReagent, Spain), 100 mM sodium *L*-lactate (> 99 %, Sigma-Aldrich, Spain) and 100 mM *D*-(+)-Glucose (> 99.5 %, Sigma-Aldrich, Spain) in 100 mL of distilled water. The pH of the solution was adjusted ~ 5.0 (4.8-5.5) by 0.2 M HCl (37 %, Sigma-Aldrich, Spain). The desired lactate and glucose concentrations were prepared by diluting the solution with distilled water.

In order to perform the assay, 15 µL of sample was calculated to be enough to surround the full scaffold, without covering it. This volume allowed us to obtain a homogeneous optical signal. However, this volume can be reduced or increased by just engineering the hydrogel shape and dimension and/or the optical detection system.

4.2.3 Fabrication of the alginate/TNT scaffolds and analysis

First, 5 mg of TiO₂ nanotubes were mixed with 1 mL of 1 % (w/v) of alginate (Sigma-Aldrich, Spain) (1.00 g alginate/100 mL distilled water) for 15 min under sonication, followed by 48 h magnetic stirring (TNT/alginate polymer suspension), the pH of the

solution was measured to be ~ 7.5 . For the lactate scaffold a $5 \mu\text{L}$ of 0.4 mg mL^{-1} lactate oxidase (LOX) (AG scientific, Spain) solution, a $5 \mu\text{L}$ of 0.05 mg mL^{-1} horseradish peroxidase (HRP) (Sigma-Aldrich, Spain) solution and a $5 \mu\text{L}$ 3,3',5,5' tetramethylbenzidine (TMB) (Sigma-Aldrich, Spain) in dimethyl sulfoxide (DMSO) ($> 99.7 \%$, Sigma-Aldrich, Spain) (TMB:DMSO, 24:2.25) solution were mixed with $30 \mu\text{L}$ of the TNT/alginate polymer suspension. The suspension was vortexed for 10 s, the pH of the solution was measured to be ~ 8.2 . Then, $20 \mu\text{L}$ of the assay mixed polymer mixture was dripped to a 0.4 M CaCl_2 (93 %, Sigma-Aldrich, Spain, pH 7.5) solution to form the TNT/alginate hydrogel scaffold in a spherical shape. The hydrogel scaffold was kept in the bath for 1 min. Then, the scaffold was washed with distilled water for 30 s. The obtained scaffolds were air dried for 2 min. to evaporate extra surface water. The same protocol was followed to fabricate the glucose sensing scaffolds. In this case, $5 \mu\text{L}$ of 0.4 mg mL^{-1} glucose oxidase (GOX) (AG scientific, Spain) solution was used instead of the LOX solution.

In order to confirm the internal pH of the scaffolds, 15 scaffolds were crushed, stored and settled in 1 mL distilled water for 24 h and then, the pH of the solution was measured, obtaining a value of 6.54. This value suggest that the enzymes, within the scaffold, are stable and active, since their active pH range is 5.5-9.0, in average, see Table 4.1.

Then the scaffolds were tested for lactate and glucose sensing with the desired artificial sweat solutions. $15 \mu\text{L}$ of artificial sweat was pipetted on to the TNT/alginate scaffolds, which was placed on a glass slide and the images and videos of the scaffold colour change were captured by a Sony Cyber-shot DSC-RX100 camera over time under controlled light conditions. The images were extracted from the videos at the desired times and analysed by Image-J software.³⁹ The intensity of the images were analysed by mean grey value (black and white, B&W value) 0-255 scale (black = 0, white = 255). Data, statistical and image analysis were carried out in Excel, Origin Pro 2018 and Image-J.

Table-4.1. Active pH ranges of the enzymes

| Enzyme | Active pH range | Optimum pH |
|--------------------------------------|-----------------|------------|
| Lactate Oxidase ⁴⁰ | 5.5- 9.5 | 6.5–7.5 |
| Glucose Oxidase ⁴¹ | 4.0-7.0 | 5.5 |
| Horseradish peroxidase ⁴² | 5.0 - 9.0 | 6.0-6.5 |

4.2.4 Scaffold integration to filter paper

Circles of 0.7 cm diameter were printed on cellulose filter paper, Whatman filter paper #1 (Sigma Aldrich, Spain) by a Xerox ColorQube 8570 wax printer and the wax barriers were generated with a FLC oven, set at 125 °C for 5 min. Next, a 30 µL TNT/alginate nanocomposite with the enzymatic and colorimetric assay (same ratios as experimental 2.3) was drop casted on to the sensing region of the paper and allowed to absorb in paper for 10 min. Then, the sensing region was dipped in a 0.4 M CaCl₂ solution for 3 min to generate the scaffold on the filter paper. Finally, the scaffold area was washed with water to remove the excess CaCl₂. The modified filter paper circles were tested for lactate and glucose sensing with the desired artificial sweat solutions, as explained in section 2.3.

The glucose sensing scaffolds (both spherical hydrogel and the paper modified scaffolds) were stored in a sealed and moistened conditions at mild temperature (5-25 °C) up to 10 days. The sensing readouts of the scaffolds were recorded by using a 1 mM glucose artificial sweat solution to determine the stability of the sensor.

4.3. Results and Discussion

4.3.1 Morphological and structural characterisation of the scaffold

The TiO₂ nanoparticles (pre-synthesised by precipitation) reacted with concentrated NaOH_(aq) to form the sheet-like titanate, *i.e.* layered sodium titanate, which is formed through either dissolution or delamination of titania (reaction-1 and -2). Subsequently, these nanosheets were transformed into nanotube like structures by exfoliation from the layered sodium titanate (reaction-3). These single or multi layered nanosheets scrolled and folded to make tubes due to the unbalanced surface energy of the upper and lower sides of the sheets, under hydrothermal conditions.⁴³ Extreme pressure and temperature

conditions inside of the hydrothermal vessel led to the formation of different 1D structures like nanofibers, nanorods and nanowires. Finally, the sodium titanate nanotubes were washed with an HCl diluted acid solution (0.1 M) to obtain the titanium dioxide nanotubes (reaction-4).



First, the TNT dimensions and shape were investigated by TEM image analysis, Figure 4.1 and 4.2a. The images demonstrated that the titanium nanostructures were synthesised in a combination of mainly nanotubes with traces of nanorods and nanofibers (1D structural shapes). Figure 4.1a, b clearly shows a darker intensity in the edges of the nanostructures, due to the high electron density of the bending edges of the nanotubes. However, traces of nanorods and nanofibers, Figure 4.1c, d, were also observed. The average diameter and the length of the TNT were ~ 10 nm and ~ 110 nm, respectively. Nevertheless, the synthesis protocol used by us generated a wide range of dimensions including microtubes (Figure 4.1c, d).

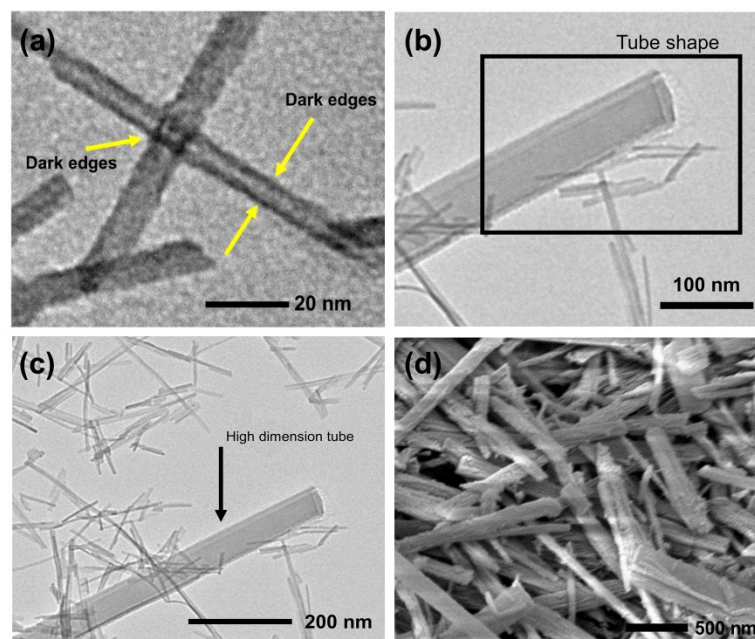


Figure 4.1. TEM images of the TiO₂ nanotubes (a) dark edges are due to the high electron density in the side edges, thanks to TiO₂ nanosheet bending, (b) cylindrical tube shape, (c) Mixture of TiO₂ nanotubes and a high dimensional (micro) tube. (d) Mixture of TiO₂ nanotubes, SEM image.

A hanging drop of blended TNT, alginate and the colorimetric enzymatic assay was generated by a pipette and let to drop into a calcium chloride solution bath, generating a spherical shape hydrogel scaffolds, crosslinking first, the surface of the scaffold. The reaction occurred since the di-cationic calcium ions and the alginate carboxylate groups cross-linked, following an egg-box model.⁴⁴ Then, the diffusion of calcium ions into the hydrogel allowed the full crosslinking of the scaffold. An optical image of the TNT/alginate scaffold is shown in Figure 4.2b, exhibiting a 3D spherical shape, which contained the TNT, the bioenzymatic assay, the colorimetric assay and the CaCl₂ crosslinked alginate. The diameter of the scaffolds was 3.0 ± 0.2 mm and it depended on the volume of the polymer nanocomposite solution used to form the 3D TNT/alginate scaffold. The morphology of the scaffold was studied by SEM. Images of the freeze-dried scaffolds both, the cross-section and the outer surface, are shown in the Figure 4.2c, d respectively. According to Figure 4.2c, a micro-porous honeycomb like internal cross-sectional structure was seen in the scaffold, where the petal like plates held an average thickness of ~ 700 nm.

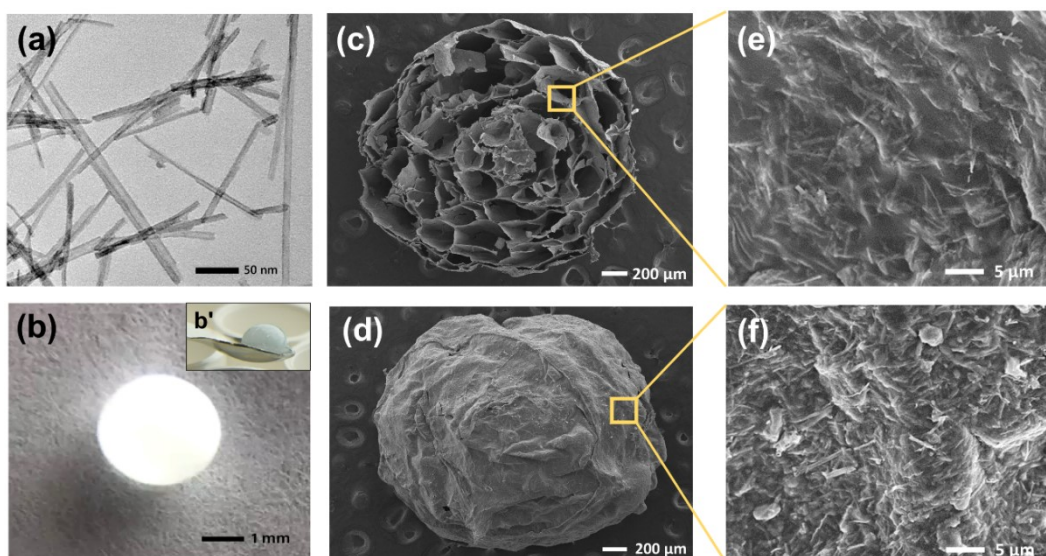


Figure 4.2. (a) TEM image of synthesised TiO₂ nanotubes. (b) Optical image of a TNT/alginate scaffold (spherical bead shape), b' shows the scaffold in a different angle- sitting on a spatula, slightly blue due to the TMB. SEM images of the freeze-dried TNT/alginate scaffold (c) cross-sectional image and (d) outer surface. (e) High magnification image of the cross-section of a petal and (f) high magnification image of the outer surface.

The micro-porous inter cross-sections were due to vacancies of water accommodating sites (evacuation of water after freeze drying) and de-swelling of the hydrogel polymer. Interestingly, when comparing the bare alginate scaffold (without the TNT), Figure 4.3a, b, with the TNT/alginate scaffolds (Figure 4.3c, d), higher internal porosity and better-defined internal honey comb patterns were observed for the TNT/alginate scaffolds. This could be explained by the inorganic phase of TNT that, during the crosslinking process, reduced the crosslinking capability of the mixture increasing the porosity.⁴⁵ TiO₂ nanotubes contain hydroxyl bonds since is in a moisture condition (Ti-OH).⁴⁶ Therefore, the TNT promotes hydrogen interactions with oxygen moieties present in the alginate polymer backbone, including the crosslinking carboxylate sites thus, the crosslinking density between -COOH and Ca²⁺ ions is reduced and the porosity increased. Moreover, the increased hydrophilicity of the mixture due to the TNT,³⁵ allowed more water to get allocated within the matrix during crosslinking, generating bigger cavities. The enlarged SEM images of the TNT/alginate scaffold surface and the surface of a petal, Figure 4.2e, f show sub-micron length TNT, demonstrating the immobilisation of the TNT both, at the surface and inside the scaffolds. Moreover, the high rugosity observed in both surfaces was an added advantage of the scaffold when

used as a biosensor, since increased the hydrophilicity of the materials and thus, the capacity to absorb liquids inside the scaffold, reducing detection times. Additionally, the internal and external high surface areas of the generated scaffolds helped to immobilise the enzymes and increase the number of reactive sites, improving enzymatic catalysis and thus, both biosensing reactions.

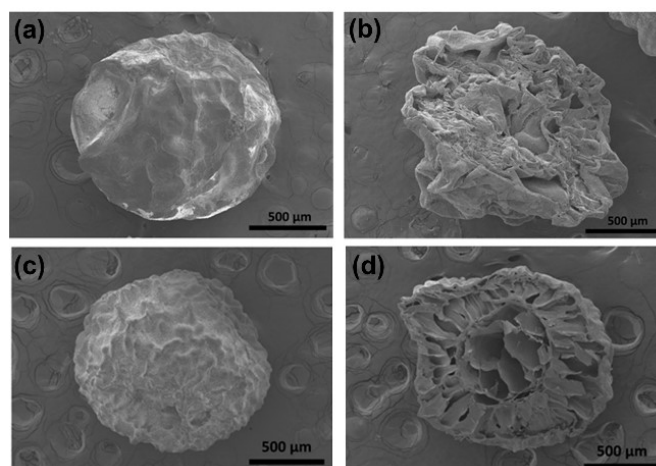


Figure 4.3. SEM image of freeze-dried (a) surface of an alginate scaffold, (b) cross-section of an alginate scaffold (c) surface of a TNT/alginate scaffold, (d) cross-section of a TNT/alginate scaffold.

The alginate:CaCl₂ ratio 1 %:0.4 M was set to be the optimum amount of material needed to keep the hydrogel in a 3D stable spherical shape. Higher percentages of alginate (over 1%) made the solution too viscous to be easily handled during the formation of the scaffold. On the other hand, lower percentage of alginate and crosslinker resulted on hydrogels with poor spherical shapes due to the low kinetic of the crosslinking while exposing the extruded droplet to the CaCl₂ bath. Mostly because of the reduced amount of carboxylates and Ca²⁺ ions.

The composition of the TNT/alginate in the TNT/alginate polymer suspension was responsible of the mechanical, biosensing and optical read out properties of the scaffold. The optimisation of the composition is discussed in Figure 4.4. According to the Figure 4.4a and b, the blue colour development is lower over 20 mg TNT than for 5 mg TNT due to the overload of TNT in the scaffold. Bigger error values were obtained at higher TNT concentrations, Figure 4.4c, therefore, 5 mg of TNT was chosen as the optimal composition for the colorimetric assay. 5 mg of TNT in 1 mL of 1 % alginate

presents a 2:1 alginate: TNT ratio thus, one scaffold of 20 μL of alginate contains 0.125 mg of TNT. The optimum TNT concentration was obtained by varying the amount of TNT (5 - 25 mg) in the scaffold. The lactate detection assay was performed and, the colour intensity and homogeneity of the colorimetric signal evaluated. In view of these results, 0.5 % (w/V) of TNT in alginate matrix (5 mg of TNT in 1 mL of alginate matrix) will be used from now on as the optimised TNT composition for the scaffold, alginate:TNT (2:1). In the hydrogel solution, the concentration of the TNT/alginate with respect to the CaCl_2 solution was set to 1 % (1.00 g of alginate in 100 mL of water) and 0.4 M, respectively.

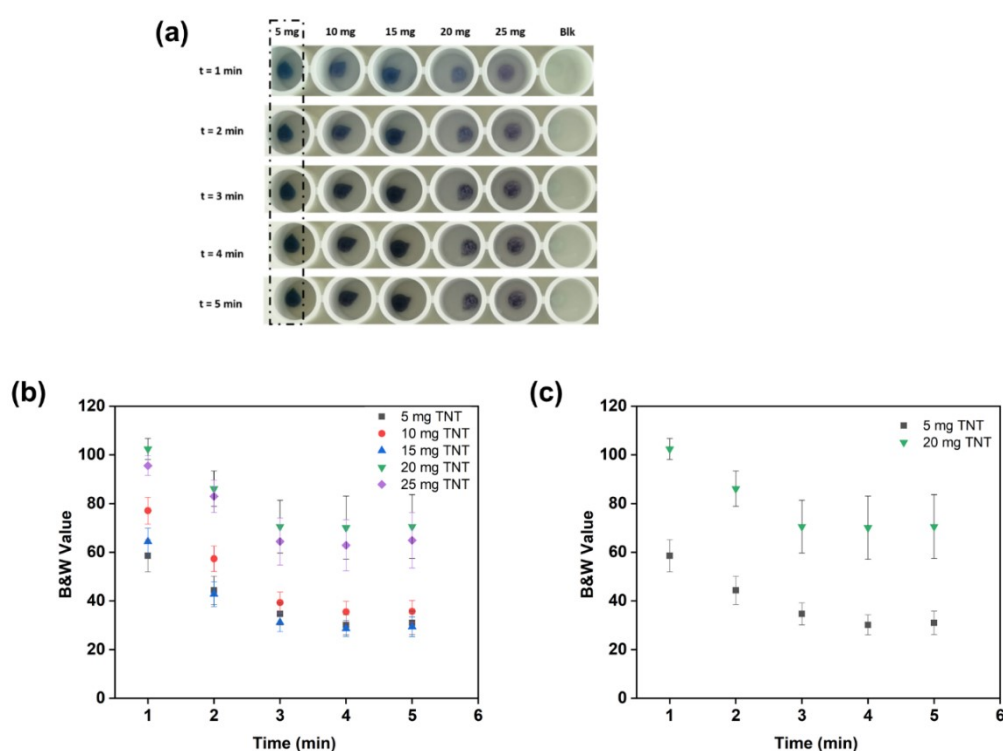


Figure 4.4. (a) Optical signal readout up to 5 min, for lactate detection (colour development) in TNT/alginate scaffolds at different TNT compositions (5-25 mg of TNT in 1 mL of 1 % alginate solution). (b) 5 -25 mg TNT in 1 mL of 1 % alginate (c) comparison of 5 and 20 mg TNT in 1 mL of 1 % alginate scaffolds. A 25 mM of lactate solution was added to the scaffolds and the B&W values of the scaffold images taken at different times were analysed by Image-J software. Error bars correspond to mean values \pm SD (B&W value deviation withing the scaffold).

4.3.2 Artificial sweat biomarkers sensing reaction mechanism

LOX and HRP were immobilised in the TNT/alginate scaffold as the catalytic biological enzymes, while the TMB was immobilised as the colorimetric assay (chromophore) for the determination of lactate in artificial sweat samples. The reaction mechanism is shown in Figure 4.5.

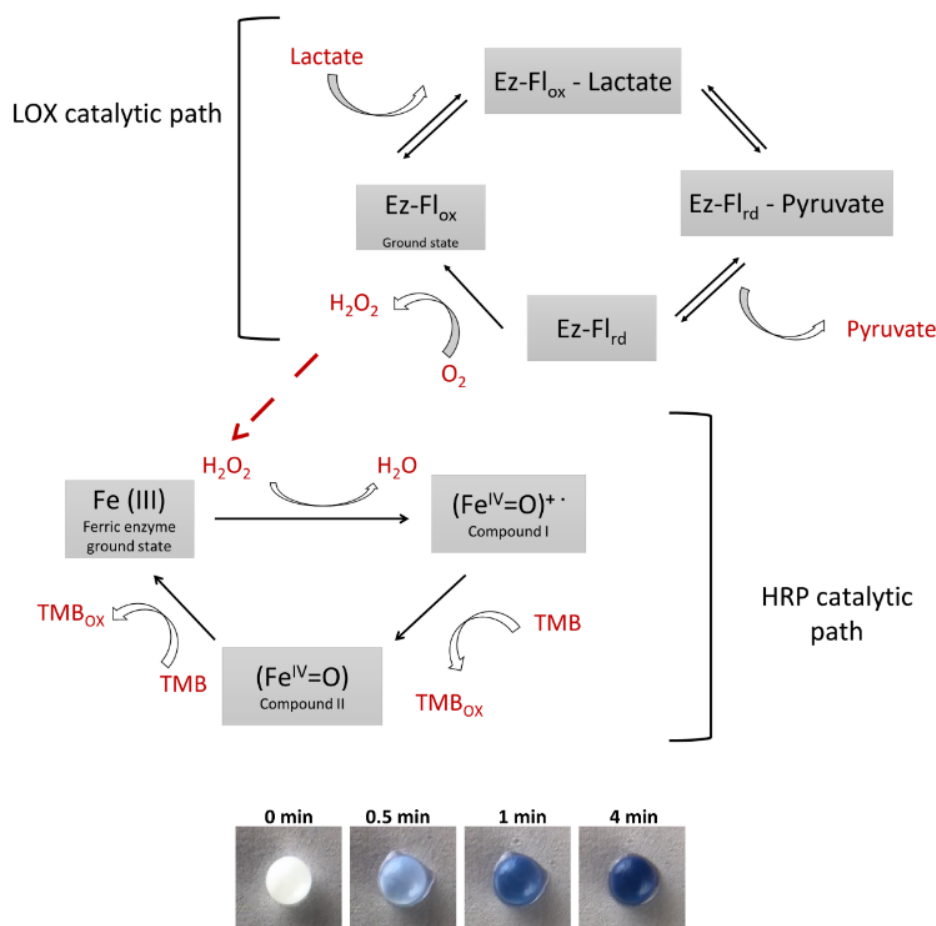


Figure 4.5. Mechanism of lactate detection under LOX and HRP catalytic pathways, ($Ez-FI$ – flavoenzyme). TNT/alginate scaffolds pictures, at different times, are shown to illustrate the blue colour formation (optical signal readout).

In short, the lactate is oxidised to the pyruvate under the LOX catalysis path and the oxygen (O_2) is reduced to hydrogen peroxide (H_2O_2).^{47,48} Next, the H_2O_2 is reduced to H_2O and the TMB is oxidised to the TMB_{ox} form turning the TNT/alginate scaffold to blue colour, under the HRP catalysis path.⁴⁹

In the first pathway, after lactate entered into the TNT/alginate scaffold, a complex is formed between lactate and the LOX enzyme ($Ez-FI_{ox}$).⁴⁸ The rate of the complex

formation was increased by the superhydrophilicity of the TiO₂ nanotubes, which rapidly incorporated the lactate sample into the scaffold by capillary effect. In addition to that, as explained above, due to the high surface area of the TiO₂ nanotubes, catalytic enzymes had more freedom to spread throughout the scaffold increasing reaction sites and getting bonded to the TNTs.⁵⁰ Then, the enzyme-lactate complex (Ez-Fl_{ox} - lactate) was converted to enzyme-pyruvate structure (Ez-Fl_{re} - Pyruvate) by oxidising lactate and reducing the LOX enzyme (Ez-Fl_{re}). Next, the pyruvate left the reduced state of the enzyme complex. After that, Ez-Fl_{re} was oxidised to its primary state (Ez-Fl_{ox}) by releasing electrons that were consumed to reduce molecular O₂ to H₂O₂. In the second cycle, the HRP mediated redox catalytic reaction was initiated by utilising the H₂O₂, which was formed in the first LOX catalytic pathway. In the HRP catalytic path, the H₂O₂ bound to the heme group (Fe³⁺ state) of HRP by making heme- H₂O₂ hydroperoxo ferric complex.⁵¹ Then the cleavage of the peroxide bond, heme-H₂O₂ was forwarded to form H₂O by reducing H₂O₂. Meanwhile, the oxidised form of the heme, compound I, which is a oxoferryl group with a cation radical (Fe^{IV}=O)⁺ was generated. Then, the oxidised heme went back, via compound II (Fe^{IV}=O), to its native form (Fe³⁺ state) by two steps, accepting electrons from the oxidation of TMB, which turned to the blue colour (TMB_{ox}).⁵² The blue coloration was recorded as the optical signal readout, which was directly proportional to the lactate concentration. The blue product was due to the charge transfer complex of the di-imine oxidised state and parental diamine of TMB. However, a yellow coloration was expected for the complete oxidation state of di-imine too, but in our case since the concentration of TMB was very high, the complete oxidation was not promoted. The same kind of mechanism can be observed for the glucose detection, as illustrated in Figure 4.6.

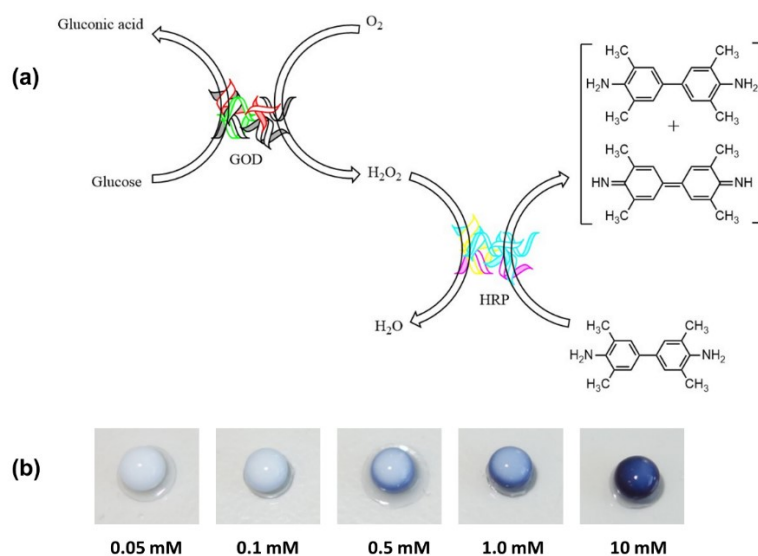


Figure 4.6. (a) Schematic diagram of the mechanism for glucose detection. First, glucose is oxidised to gluconic acid under GOX (catalyst) and the oxygen is reduced to hydrogen peroxide. Next, the generated hydrogen peroxide is reduced to water while TMB is oxidised, giving a blue colour in the presence of the HRP catalysis. (b) Optical images of the scaffold, 4 min after the addition of 0.05 mM to 10 mM lactate in artificial sweat.

4.3.3 Biosensing performance of TNT/alginate scaffolds

The optical signal readout (blue coloration of the scaffold) was recorded by capturing photos and videos of the TNT/alginate scaffold while subjected to the lactate/glucose biosensing in artificial sweat solutions. The optical readings (colour) of the scaffold were analysed by Image-J software. The colour scale was defined by the black and white values (B&W value) of the captured images, since there was not a colour change but an increase of the blue colour intensity in the colorimetric signal. The B&W values of the scaffold were getting lower when the intensity of the blue colour was increased. Therefore, the signal intensity (blue colour) was proportional to the lactate/glucose concentration but the B&W value of the analysed images was inversely proportional to the lactate concentration.

For real time biomarkers analysis using wearable devices, the sensing time is an important parameter to obtain a useful biosensor. Fast detection times ensure, real time data acquisition and accurate analysis since evaporation, contamination and degradation of the sample is minimised. Therefore, the sensing time (signal recording time) of the biomarkers using the TNT/alginate scaffolds was investigated. The assay

was performed with the TNT/alginate scaffolds in 0.1 to 5 mM lactate concentration solution of artificial sweat. The colour variation was determined following the protocol presented in the experimental section 4.2.3, Figure 4.7a for lactate and Figure 4.7b for glucose.

According to the plot, after 4 min for lactate and 6 min for glucose, the blue colour intensity value can be differentiated in all the studied concentrations. Moreover, the blue colour started to saturate at those times, increasing the error of the signal reading (image of the scaffold). Hence, the sensing time was determined to be 4 min for lactate and 6 min for glucose at the studied colorimetric assay conditions. Moreover, the artificial sweat biomarkers detection time for the bare alginate scaffolds (without TNT) was tested in the same way, as depicted in Figure 4.8. The obtained detection time was 12 min, obtaining a much lower response (3x for lactate and 2x for glucose) compared to the TNT/alginate scaffold.

The detection time was fast for the scaffold configuration. In literature, Siripongpreda *et al.*⁵³ reported a bacterial cellulose-based hydrogel scaffold with a signal readout at 10 min, while Rusell *et al.*⁵⁴ reported a poly(ethylene glycol) based hydrogel with a 10-12 min response time for glucose, which are longer response times compared to our scaffold. TiO₂ nanotubes promoted the absorption and transport of the sweat biomarkers inside the scaffold reaching fast the enzymatic centres, speeding up the signal observation time, thanks to their superhydrophilicity and capillarity properties. Moreover, the high surface area of the scaffold both, at the surface and inside the matrix promoted signal observation times.

The lactate and glucose calibration curves are shown in the Figure 4.7c and Figure 4.7d, respectively. The signal read outs were recorded for each concentrations at 4 min for lactate and 6 min for glucose from the pictures or video taken at those times, see images below the calibration curves. Both biosensor responses showed good linearity, between 0.1 and 1.0 mM for lactate and between 0.1 and 0.8 mM for glucose. The dependency between the sensor response and lactate or glucose concentration can be approximated by a linear function with a correlation factor R² of 0.981 for lactate and of 0.989 for glucose. The statistical limit of detection (LOD) was calculated to be 0.069 mM with a limit of quantification (LOQ) = 0.23 mM for lactate. In the case of glucose the obtained values were, LOD = 0.044 mM and LOQ = 0.15 mM; (LOD = 3S/K, LOQ = 10S/K,

where S is the standard deviation of the blank sample and the K is the slope of the calibration curve). Our sensor scaffold could be directly integrated into real-time glucose sensing devices since it has a quantitative detectable range of glucose, compatible with human sweat glucose ranges. However, for lactate concentrations, a dilution factor of the sweat sample would be necessary in order to decrease lactate concentrations, which normally are high, *e.g.* 60 mM and thus far from our calibration range. It needs to be considered that, these values are highly sensible to the image recording protocol, in which different camera lenses, camera image processing software, light conditions and object distance or focal distance could alter the obtained results.

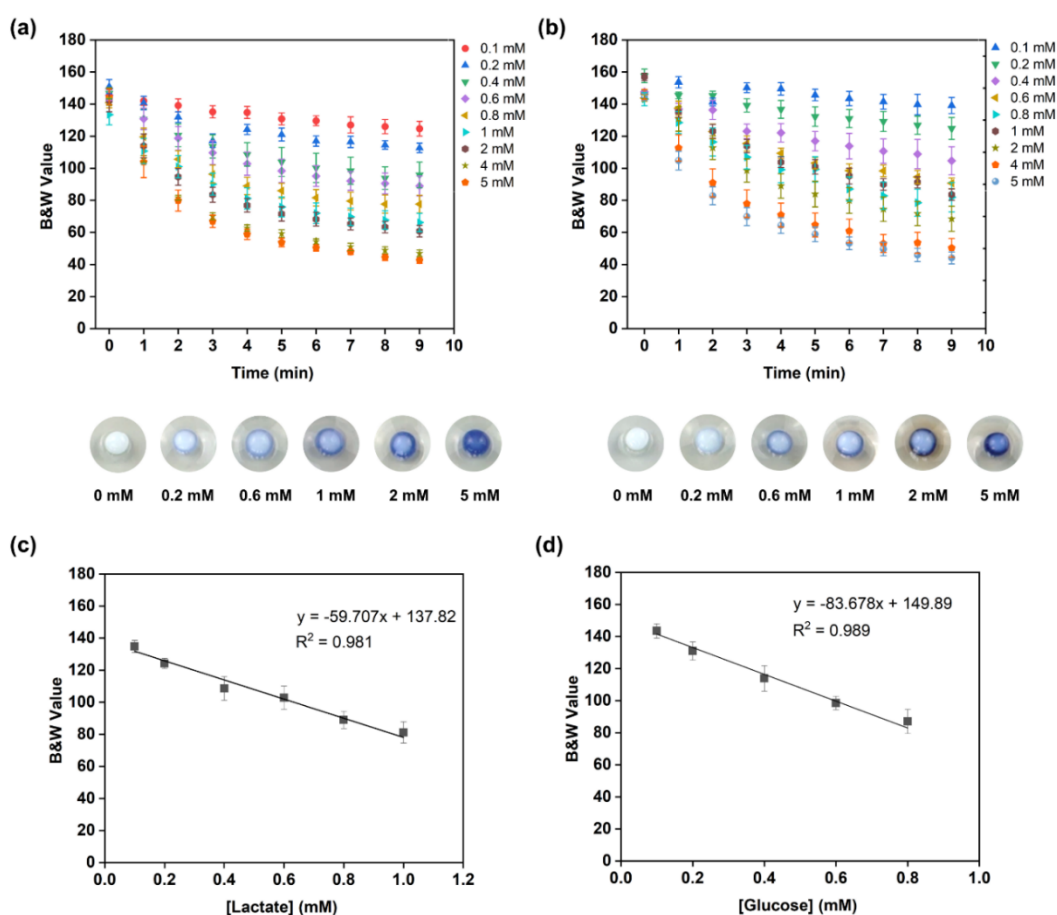


Figure 4.7. (a) Lactate and (b) glucose detection (blue colour development) over time, by the TNT/alginate scaffold, lactate and glucose ranges 0-5 mM in artificial sweat. B&W value was analysed by Image-J software, max black - 0 and max white - 255). Calibration plot for (c) lactate and (d) glucose detection in artificial sweat by the TNT/alginate scaffold. Images of the scaffolds at different lactate and glucose concentrations, taken at 4 min time, are shown above the calibration curves. Error bars correspond to mean values \pm SD ($n = 3$).

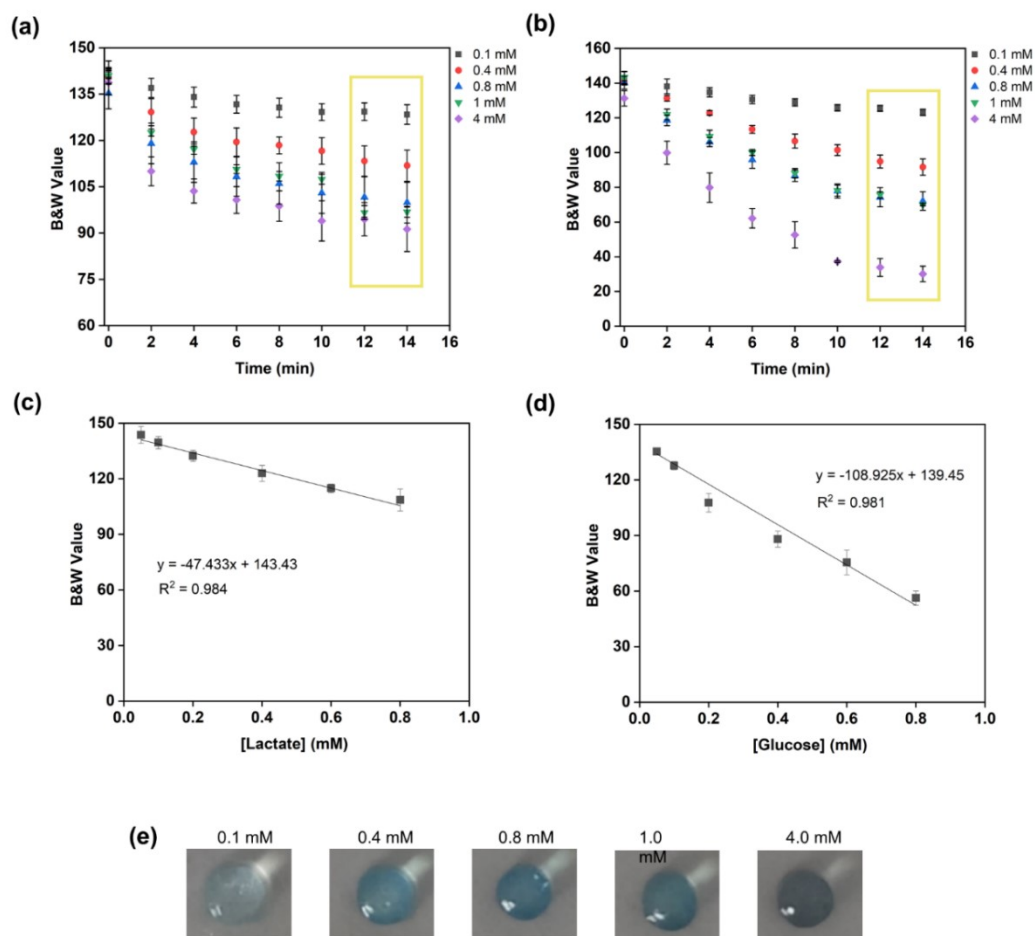


Figure 4.8. Colorimetric signal formation (colour development) of alginate scaffold for 0.1 to 4 mM of (a) lactate in artificial sweat, (b) glucose in artificial sweat over time, up to 14 min. A saturation of the signal was observed after 12 min, see the yellow square. (c) Calibration curves for lactate and (d) for glucose in artificial sweat by the alginate scaffolds. A linear regression was obtained in the range 0 to 0.8 mM for both biomolecules. (e) Optical images of the alginate scaffold captured at 12 min in 0.1 to 4 mM lactate artificial sweat solutions. Error bars correspond to mean values \pm SD ($n = 3$).

The linear behaviour of the calibration curve deviated above 1 mM concentrations (Figure 4.9a, for lactate detection). Therefore, the quantitative detection in both biomarkers was restricted to 1 mM when measured at 4 and 6 min, respectively. The signal readout for concentrations from 0 to 100 mM lactate are also shown in the Figure 4.9a, where their values were the same (10 mM to 100 mM), within the error (B&W value = 70 ± 5), quantitatively undistinguishable using this image analysis methodology. This behaviour can be attributed to the fast colour formation at those

concentrations. The time to reach plateau was found to be very fast for high concentrations of lactate or glucose, less than one minute, but the values were indistinguishable, regardless the biomarker concentration. Figure 4.9b shows the colour development for a TNT/alginate scaffold in 10 mM lactate concentration and the pictures of the scaffold at different times during the assay performance. The signal analysing protocol relies on the blue colour intensity analysis by image-J program. The saturation of the blue colour in the scaffold was responsible from the limitation of the quantitative analysis to just low concentrations of biomarkers (0.1-1 mM). However, the quantitative ranges would be shifted by manipulating the colorimetric assay and the enzymatic ratio in the scaffold. On the other hand, as shown in Figure 4.9b and c, the signal read out recording time could be reduced to detect the colour variation at high biomarker concentrations.

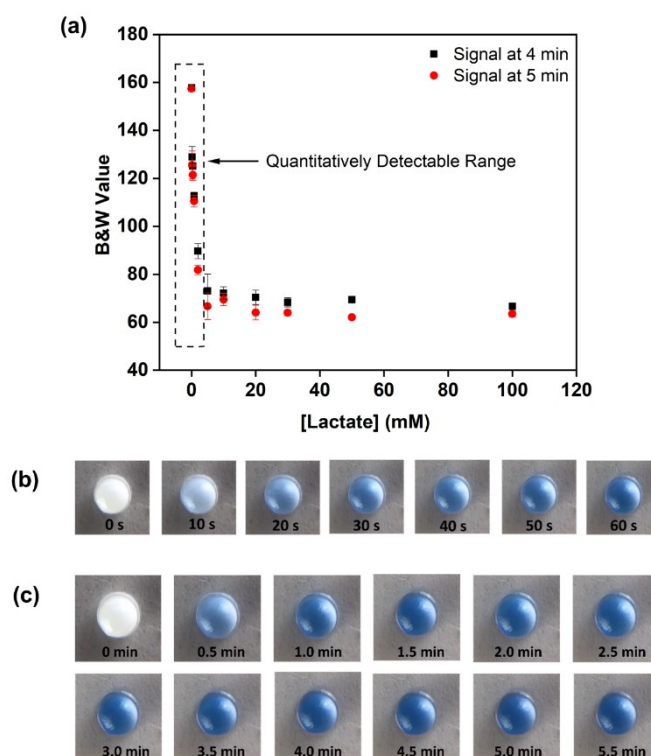


Figure 4.9. (a) Performance of the TNT/alginate scaffolds for a 0 to 100 mM range of lactate in artificial sweat; the signal was recorded at 4 and 5 min. A linear tendency was observed for 0 to 1 mM lactate concentration range (dashed square). Error bars correspond to mean values \pm SD (n = 3). (b) Images of the TNT/alginate scaffolds for the 10 mM lactate detection within 0 - 60 s and (c) 0-5.5 min.

The scaffolds were also tested with real sweat samples, as a proof of concept. The glucose and the lactate concentrations were calculated using the calibration curves, obtaining values of 35 ± 4 and 0.07 ± 0.01 mM concentration of lactate and glucose, respectively. In this case, sweat samples were acquired with a pipette from a human (33 years, male, no previous recorded diabetic like complications) while cycling (avg. heart rate 120 bpm, atmospheric temperature 12 °C, aerobic phase exercise), from the forehead area of the body; the biomarkers detection was performed at the same time. 15 μ L of sweat was directly pipetted to the glucose sensor scaffold while 100 times diluted, with distilled water; sweat was used for the lactate biosensor.

The tested scaffolds are shown in Figure 4.10. The glucose and the lactate concentrations were calculated using the calibration curves (adjusting the optical errors in blanks). 35 ± 4 and 0.07 ± 0.01 mM concentration of lactate and glucose, respectively, were obtained by the TNT/alginate scaffold for the real sweat samples. These values were compared to the values obtained with commercially available glucometer (Freestyle freedom lite, USA) and lactometer (Lactate Plus, Nova biomedical, USA), obtaining a 24.8 mM concentration for lactate. The glucose concentration was not possible to be measure using the commercial available glucometer, since it worked at higher concentration values > 1.2 mM. This is necessary due to the high concentration of lactate in sweat due to the accumulation of analytes since enough sample volume for the analysis need to be obtained. It needs to be considered here that, those values are not providing any valuable information about the real analyte concentrations in the sweat sample. Nevertheless, this experiment shows the possibility to use this material as a sensing probe for the detection of lactate and glucose concentrations from real sweat samples, as previously demonstrated using artificial sweat.

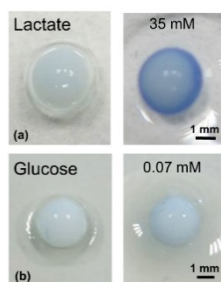


Figure 4.10. (a) Lactate and (b) glucose tested scaffolds using real sweat, before and after the detection. The response time was set to 4 and 6 min for lactate and glucose, respectively.

4.3.4 Colorimetric signal readout characterisation

The colour of the optical signal readout was examined by UV-Visible spectroscopy before the hydrogel scaffold was formed, pre-hydrogel solutions, and once the scaffold was fabricated. A 1 mM lactate concentration solution of artificial sweat was added to the samples and UV-Vis spectra were recorded. The colour formation of the TMB was analysed in aqueous solution (Figure 4.11a) showing the conventional absorbance peaks of the TMB_{ox}, charge transfer complex λ_{max} at 652 nm and 370 nm. The absorbance of the λ_{max} increased while increasing the lactate concentration from 0.2 to 10 mM in both alginate and TNT/alginate solutions, Figure 4.11b and Figure 4.11c graphs, respectively. However, as shown in Figure 4.11d, a significant blue shift of the λ_{max} was observed from solution, 652 nm, to alginate, 622 nm, and in the TNT/alginate solutions, 564 nm. A similar behaviour was observed for the two scaffolds, 620 nm for the alginate scaffold and 568 nm for the TNT/alginate scaffold, Figure 4.11e. The variation of solvent media/matrix might affect the TMB_{ox} to generate a blue shift in the spectra. Moreover, for the experiments containing TNT, the amine group of the TMB could be physically absorbed to the -OH groups at the TiO₂ nanotube surface, forming NH-O-Ti hydrogen interactions, which could alter the characteristics of the conjugation system of the TMB_{ox}, by contributing to the blue shift of TMB_{ox}.

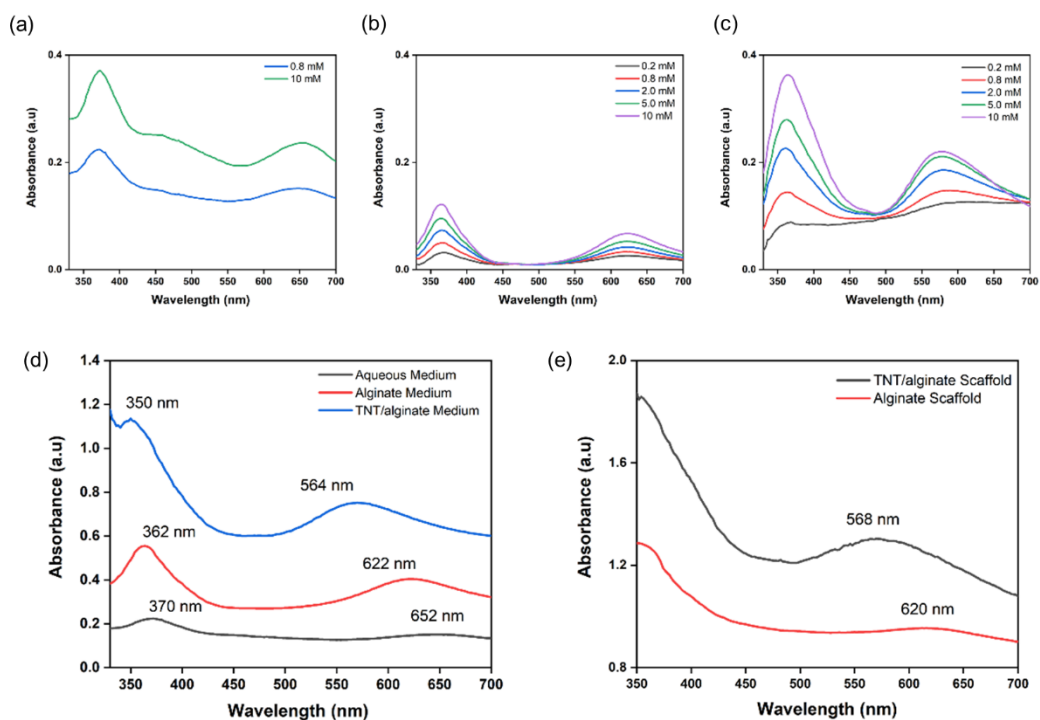


Figure 4.11. UV-Visible spectra of the TMB colour formation at different lactate concentrations in artificial sweat: (a) in aqueous solution, without the scaffold, (b) in alginate pre-gel solution, (c) in TNT/alginate pre-gel solution. (d) UV-Visible spectra of the TMB_{ox} colour formation in aqueous medium, alginate medium and TNT/alginate medium due to 1 mM lactate detection in artificial sweat. (e) UV-Visible spectra of TMB colour formation in the alginate scaffold and in the TNT/alginate scaffold, 1 mM lactate concentration in artificial sweat. The UV visible spectra were recorded from thin layers of hydrogels, placed at the bottom of a transparent 92 well-plate.

4.3.5 Study of the possible interferences caused by the catalytic properties of TNT

TiO₂ is a photoactive material, which can generate reactive oxygen species under UV irradiation. The generation of electron-hole pairs would, in theory, interfere on the oxidation/reduction mechanism of the assay inside the TNT/alginate scaffolds, acting as a photocatalyst.^{55,56} Therefore, this possible effect was investigated for the TNT/alginate scaffolds using the lactate assay. At normal diffuse light conditions, the TNT/alginate scaffolds kept white colouration up to 30 min, Figure 4.12a. This confirmed that H₂O₂ was not formed without addition of lactate and that the presence of TNT in the scaffold did not promote the self-oxidation of TMB, most probably due to the lack of sufficient energy, in the diffuse light, to generate a photocatalytic effect by the TNT.

Nevertheless, this effect could be triggered during lactate detection, as the generated blue colour of the scaffold could absorb enough light to activate the photocatalytic effect of TNTs. Figure 4.12b shows the colorimetric signal analysis of the TNT/alginate scaffold in normal diffuse light conditions and in the dark after the addition of 0.4, 1.0 and 5.0 mM lactate concentrations. The B&W values of TNT/alginate scaffold obtained after 4 min did not show any significant difference, within the error, revealing no considerable photocatalytic effect in our experimental conditions.

Recently, TiO₂ based nanostructures and nanocomposites have been reported to be able to mimic peroxidase activity.^{57,58} Therefore, we investigated this effect by measuring the TMB oxidation activity, without the HRP, in the TNT/alginate scaffolds, at our experimental conditions. Figure 4.12c presents the images of TNT/alginate scaffolds (lactate assay) for two lactate concentrations, 0.8 and 10 mM, after 0, 4 and 10 min addition of the artificial sweat solutions. The scaffolds without HRP presented no colour formation upon addition of the lactate solutions thus, the possible catalytic activity of TNT in the scaffolds can be considered negligible, under the given experimental conditions.

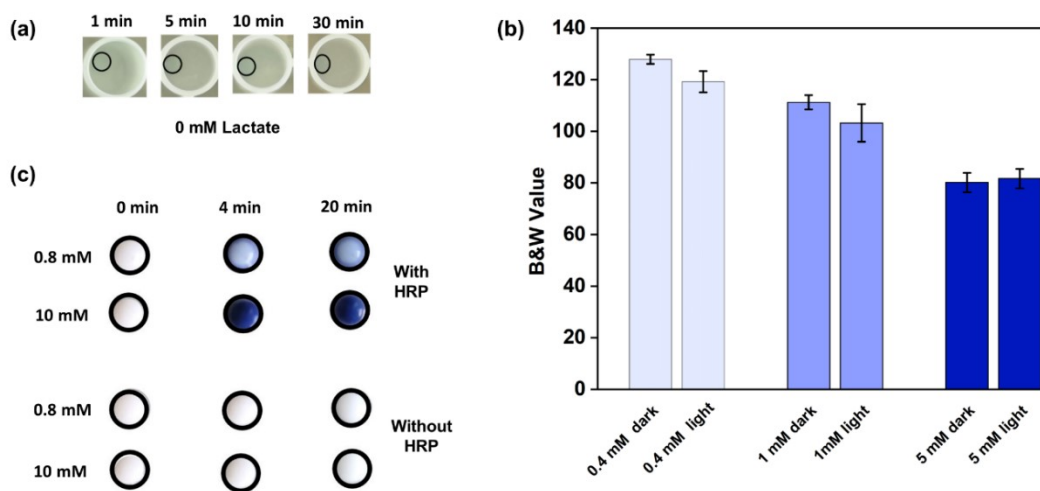


Figure 4.12. (a) TNT/alginate scaffolds without lactate in artificial sweat, images captured at 1, 5, 10, 30 min. (b) B&W values of the TNT/alginate scaffold activity at 0.4, 1.0 and 5.0 mM lactate concentration under diffuse and dark light conditions. (c) Lactate detection (0.8 and 10 mM) in TNT/alginate scaffolds with and without HRP, images taken at 0, 4 and 20 min. Error bars correspond to mean values \pm SD ($n = 3$).

4.3.6 Scaffold integration on paper-based sensing platform

Recently, paper-based microfluidics technology is vastly investigated as an easy to implement and cheap technology to address body fluid analysis at the point of need (wearable devices).⁵⁹⁻⁶¹ Therefore, the possibility to integrate the TNT/alginate hydrogel scaffolds in a paper format as well as the performance of the integrated scaffold were investigated. The TNT/alginate hydrogel was immobilised in paper as described in the experimental section 2.4. The scaffold was physically bonded to the paper substrate, generating a stable bond between the paper fibres and the hydrogel matrix, under moisture and hydrated conditions as shown in Figure 4.13a. In this case, hydroxyl groups in cellulose can bond with the -OH/-COOH in alginate, mostly by polar-polar and H-bonding interactions. However, that bond was found to get weaker while drying the hydrogel scaffold. The different contraction coefficients of the cellulose and the TNT/alginate scaffold, while dehydrating, weaken the bond as a consequent of the mechanical tension, delaminating the hydrogel. See SEM picture in Figure 4.13b. The performance of the scaffold-paper substrate was investigated for the lactate and the glucose assays using artificial sweat, Figure 4.13c. Images were captured at different times, 4 min for lactate and 6 min for glucose, using three concentrations (0.4, 0.8 and 2.0 mM). Moreover, the calibration curves for both lactate and glucose are shown in Figure 4.13g and h. The quantitative linear detection range did not significantly deviated from the one values obtained for the TNT/alginate scaffolds, in both lactate and glucose. However, the detection range in glucose was extended to 1 mM from 0.8 mM.

A homogeneous optical signal read out was obtained in the scaffold-paper substrate when compared with performing the same assay in the bare paper. In conventional paper substrates, high percentage of sensing assay loading is limited due to the inherent wettability properties of the paper fibres.⁶² By adding the TNT/alginate scaffold to the paper substrate, the swelling capability of the scaffold, liquid intake, and the porous character of the alginate, permitted a fast absorption of the liquid sample and a homogeneous distribution towards the whole surface of the sensor. Moreover, the high surface area of the TNT, as explained before, generated extra reaction sites for the assay inside the scaffold-paper substrate. An image of a conventional paper substrate, which was used to detect 0.4 mM of lactate, is shown in Figure 4.13d and compared to the same experiment but using the scaffold-paper substrate, Figure 4.13e. In many

microfluidic paper-based analytical devices, coffee ring effects and low homogeneity of the colour generated on the sensing areas are common drawbacks that decrease the sensitivity and the precision of the analytical measurement.⁶³⁻⁶⁵ However, in the scaffold-paper substrate, these effects were minimised. A comparison between the colour spreading of the B&W values over the whole paper surface obtained from Figure 4.13d and Figure 4.13e showed a narrower spread of colour in the scaffold-paper (21 B&W values, 61-82 range) than in the bare paper (45 B&W values, 137-182 range), approximately 2 times higher for the paper, demonstrating the lower homogeneity of the sensing area of the bare paper, Figure 13f. Moreover, the intensity of the colour was greatly improved when using the scaffold-paper, in Figure 4.13f mean B&W value of the scaffold-paper was lower (69) compared to the bare paper (161), while the evaporation time of the sensing area was substantially increased, allowing the acquisition of the results for longer periods of time without increasing the error of the measurement.

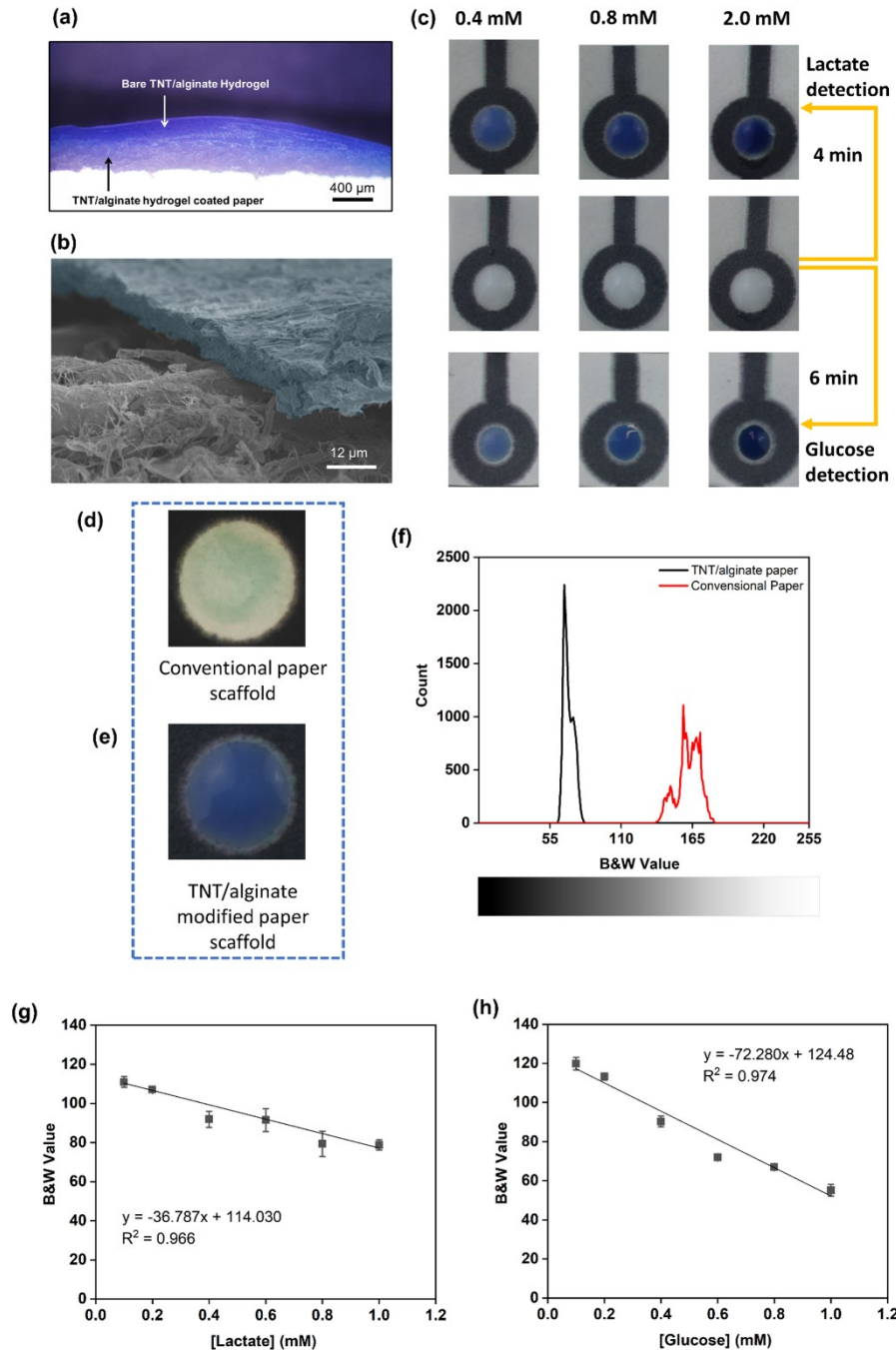


Figure 4.13. (a) Optical images of the TNT/alginate scaffold-paper surfaces before and after lactate and glucose addition. White colour sensing area represent the modified paper sensing region at 0 min (middle). The scaffolds-paper surfaces were checked for 0.4, 0.8 and 2.0 mM of lactate and glucose concentrations in artificial sweat. The images were captured at 4 min (lactate) and 6 min (glucose), respectively. (b) Image of a bare paper surface after addition of 0.4 mM lactate in artificial sweat solution captured at 4 min. (c) Image of a TNT/alginate- paper surface after addition of 0.4 mM lactate in artificial sweat solution captured at 4 min. (d) B&W value spreading count from images b and c, analysed by the Image-J software. (e) Microscope

image of the cross-section of TNT/alginate modified paper in its hydrated stage (f) SEM image of dehydrated hydrogel (blue) on the paper surface (grey). Calibration curves for (g) lactate (signal recoded after 4 min.) and (h) glucose (signal recoded after 6 min) in artificial sweat by the TNT/alginate-Paper platform. A linear regression was obtained in the range 0.1 to 1 mM for both biomolecules. The statistical limit of detection (LOD) was calculated to be 0.195 mM with a limit of quantification (LOQ) = 0.65 mM for lactate. In the case of glucose the obtained values were, LOD = 0.074 mM and LOQ = 0.25 mM; (LOD = 3S/K, LOQ = 10S/K, where S is the standard deviation of the blank sample and the K is the slope of the calibration curve). Error bars correspond to mean values \pm SD (n = 3).

4.3.7 Stability of the TNT/alginate scaffold

The dehydration of the hydrogel, reduced the sensing performance since the enzymes lost their activity. To avoid this, the scaffolds were stored in a moistened, sealed and low temperature (5-25 °C) conditions in order to keep the enzymes and the assays in an active domain. The sensing performance was stable without presenting any significant change even after 10 days of storage, Figure 4.14a and b.

In base of these preliminary observations, it is stated that the TNT/alginate scaffold is a promising composite material, integrable into microfluidic paper-based analytical devices, able to improve the optical sensing performance of the device. Moreover, it shows a bright future to be used in wearable microfluidic devices for sweat monitoring due to its ease integration and biocompatibility.^{19,66}

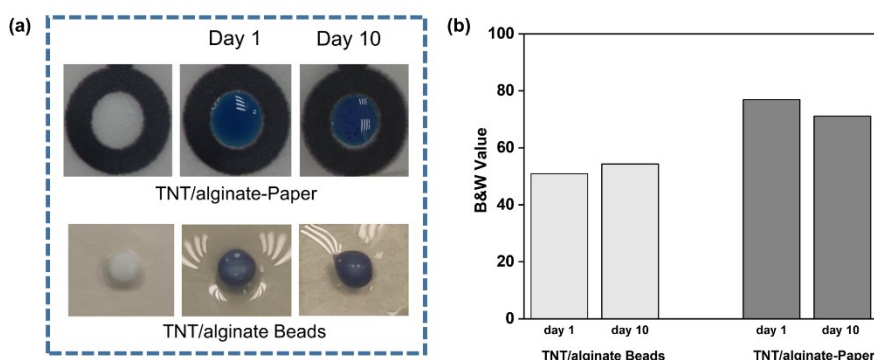


Figure 4.14. (a) Pictures of the performance of both, TNT/alginate hydrogel in paper and scaffold format, after 1 and 10 days storage at hydrated conditions. 1 mM of glucose was added to the samples. (b) Colour Intensity analysis of the pictures.

4.4 Conclusion

In conclusion, we have introduced a novel platform based on a TNT/alginate hydrogel scaffold for lactate and glucose monitoring in artificial sweat. The scaffold was fabricated by immobilising enzymatic catalytic assays of LOX/GOX and HRP with TMB chromophore in a TNT/alginate nanocomposite. A rapid colorimetric detection (blue colour optical signal read out) was observed for artificial sweat biomarkers in TNT/alginate hydrogel platform. Thus, obtaining signal read out recording times (sensing time) of 4 min for lactate and 6 min for glucose, whereas, the detection time for the alginate scaffold (without TNT) is 12 min. The superhydrophilicity and the capillarity of the TNT was found to increase the detection rate of the biomarkers within the scaffold for both biomarkers. Linear calibration curves for the quantitative detection of lactate and glucose in the 0.1-1 mM concentration range for lactate and 0.1-0.8 mM concentration range for glucose were obtained with acceptable correlation factors. Furthermore, the TNT/alginate scaffold was successfully integrated into a paper substrate to demonstrate the versatility of the TNT/alginate scaffold to enhance the sensing properties of the paper. High biological assay loadings and quick signal responses were obtained, opening new avenues to improve microfluidic paper-based analytical devices by the incorporation of alginate-based materials. Moreover, this biocompatible colorimetric biosensor scaffold is a promising platform to implement real time detection of sweat biomarkers in wearable devices.

4.5 References

- (1) Gunatilake, U. B.; Garcia-Rey, S.; Ojeda, E.; Basabe-Desmonts, L.; Benito-Lopez, F. TiO₂ Nanotubes Alginate Hydrogel Scaffold for Rapid Sensing of Sweat Biomarkers: Lactate and Glucose. *ACS Appl. Mater. Interfaces* **2021**, *13* (31), 37734–37745.
- (2) Heikenfeld, J. Bioanalytical Devices: Technological Leap for Sweat Sensing. *Nature* **2016**, *529* (7587), 475–476.
- (3) Heikenfeld, J. Non-Invasive Analyte Access and Sensing through Eccrine Sweat: Challenges and Outlook circa 2016. *Electroanalysis* **2016**, *28* (6), 1242–1249.

- (4) Espel, J. C.; Palac, H. L.; Bharat, A.; Cullina, J.; Prickett, M.; Sala, M.; McColley, S. A.; Jain, M. The Relationship between Sweat Chloride Levels and Mortality in Cystic Fibrosis Varies by Individual Genotype. *J. Cyst. Fibros.* **2018**, *17* (1), 34–42.
- (5) Derbyshire, P. J.; Barr, H.; Davis, F.; Higson, S. P. J. Lactate in Human Sweat: A Critical Review of Research to the Present Day. *J. Physiol. Sci.* **2012**, *62* (6), 429–440.
- (6) Jia, W.; Bandodkar, A. J.; Valdés-Ramírez, G.; Windmiller, J. R.; Yang, Z.; Ramírez, J.; Chan, G.; Wang, J. Electrochemical Tattoo Biosensors for Real-Time Noninvasive Lactate Monitoring in Human Perspiration. *Anal. Chem.* **2013**, *85* (14), 6553–6560.
- (7) Rathee, K.; Dhull, V.; Dhull, R.; Singh, S. Biosensors Based on Electrochemical Lactate Detection: A Comprehensive Review. *Biochem. Biophys. Reports* **2016**, *5*, 35–54.
- (8) Karpova, E. V.; Laptev, A. I.; Andreev, E. A.; Karyakina, E. E.; Karyakin, A. A. Relationship Between Sweat and Blood Lactate Levels During Exhaustive Physical Exercise. *ChemElectroChem* **2020**, *7* (1), 191–194.
- (9) Sakharov, D. A.; Shkurnikov, M. U.; Vagin, M. Y.; Yashina, E. I.; Karyakin, A. A.; Tonevitsky, A. G. Relationship between Lactate Concentrations in Active Muscle Sweat and Whole Blood. *Bull. Exp. Biol. Med.* **2010**, *150* (1), 83–85.
- (10) Karpova, E. V.; Shcherbacheva, E. V.; Galushin, A. A.; Vokhmyanina, D. V.; Karyakina, E. E.; Karyakin, A. A. Noninvasive Diabetes Monitoring through Continuous Analysis of Sweat Using Flow-through Glucose Biosensor. *Anal. Chem.* **2019**, *91* (6), 3778–3783.
- (11) Hammond, K. B.; Turcios, N. L.; Gibson, L. E. Clinical Evaluation of the Macroduct Sweat Collection System and Conductivity Analyzer in the Diagnosis of Cystic Fibrosis. *J. Pediatr.* **1994**, *124* (2), 255–260.
- (12) Mu, X.; Xin, X.; Fan, C.; Li, X.; Tian, X.; Xu, K. F.; Zheng, Z. A Paper-Based Skin Patch for the Diagnostic Screening of Cystic Fibrosis. *Chem. Commun.* **2015**, *51* (29), 6365–6368.

- (13) Gao, W.; Emaminejad, S.; Nyein, H. Y. Y.; Challa, S.; Chen, K.; Peck, A.; Fahad, H. M.; Ota, H.; Shiraki, H.; Kiriya, D.; Lien, D. H.; Brooks, G. A.; Davis, R. W.; Javey, A. Fully Integrated Wearable Sensor Arrays for Multiplexed in Situ Perspiration Analysis. *Nature* **2016**, *529* (7587), 509–514.
- (14) He, W.; Wang, C.; Wang, H.; Jian, M.; Lu, W.; Liang, X.; Zhang, X.; Yang, F.; Zhang, Y. Integrated Textile Sensor Patch for Real-Time and Multiplex Sweat Analysis. *Sci. Adv.* **2019**, *5* (11), eaax0649.
- (15) Choi, J.; Ghaffari, R.; Baker, L. B.; Rogers, J. A. Skin-Interfaced Systems for Sweat Collection and Analytics. *Sci. Adv.* **2018**, *4* (2), eaar3921.
- (16) Bandodkar, A. J.; Gutruf, P.; Choi, J.; Lee, K. H.; Sekine, Y.; Reeder, J. T.; Jeang, W. J.; Aranyosi, A. J.; Lee, S. P.; Model, J. B.; Ghaffari, R.; Su, C. J.; Leshock, J. P.; Ray, T.; Verrillo, A.; Thomas, K.; Krishnamurthi, V.; Han, S.; Kim, J.; Krishnan, S.; Hang, T.; Rogers, J. A. Battery-Free, Skin-Interfaced Microfluidic/Electronic Systems for Simultaneous Electrochemical, Colorimetric, and Volumetric Analysis of Sweat. *Sci. Adv.* **2019**, *5* (1), eaav3294.
- (17) Parlak, O.; Curto, V. F.; Ojeda, E.; Basabe-Desmonts, L.; Benito-Lopez, F.; Salleo, A. Wearable Biosensors and Sample Handling Strategies. In *Wearable Bioelectronics*; 2020; pp 65–88.
- (18) Adkins, J. A.; Boehle, K.; Friend, C.; Chamberlain, B.; Bisha, B.; Henry, C. S. Colorimetric and Electrochemical Bacteria Detection Using Printed Paper- and Transparency-Based Analytic Devices. *Anal. Chem.* **2017**, *89* (6), 3613–3621.
- (19) Koh, A.; Kang, D.; Xue, Y.; Lee, S.; Pielak, R. M.; Kim, J.; Hwang, T.; Min, S.; Banks, A.; Bastien, P.; Manco, M. C.; Wang, L.; Ammann, K. R.; Jang, K. I.; Won, P.; Han, S.; Ghaffari, R.; Paik, U.; Slepian, M. J.; Balooch, G.; Huang, Y.; Rogers, J. A. A Soft, Wearable Microfluidic Device for the Capture, Storage, and Colorimetric Sensing of Sweat. *Sci. Transl. Med.* **2016**, *8* (366), 366ra165-366ra165.
- (20) Promphet, N.; Rattanawaleedirojn, P.; Siralermukul, K.; Soatthiyanon, N.; Potiyaraj, P.; Thanawattano, C.; Hinestroza, J. P.; Rodthongkum, N. Non-Invasive Textile Based Colorimetric Sensor for the Simultaneous Detection of

Sweat PH and Lactate. *Talanta* **2019**, *192*, 424–430.

- (21) Choi, J.; Bandodkar, A. J.; Reeder, J. T.; Ray, T. R.; Turnquist, A.; Kim, S. B.; Nyberg, N.; Hourlier-Fargette, A.; Model, J. B.; Aranyosi, A. J.; Xu, S.; Ghaffari, R.; Rogers, J. A. Soft, Skin-Integrated Multifunctional Microfluidic Systems for Accurate Colorimetric Analysis of Sweat Biomarkers and Temperature. *ACS Sensors* **2019**, *4* (2), 379–388.
- (22) Xiao, J.; Liu, Y.; Su, L.; Zhao, D.; Zhao, L.; Zhang, X. Microfluidic Chip-Based Wearable Colorimetric Sensor for Simple and Facile Detection of Sweat Glucose. *Anal. Chem.* **2019**, *91* (23), 14803–14807.
- (23) Wang, L.; Lou, Z.; Jiang, K.; Shen, G. Bio-Multifunctional Smart Wearable Sensors for Medical Devices. *Adv. Intell. Syst.* **2019**, *1* (5), 1900040.
- (24) Draget, K. I. Alginates. In *Handbook of Hydrocolloids: Second Edition*; 2009; pp 807–828.
- (25) Rehm, B. H. A. Alginate Production: Precursor Biosynthesis, Polymerization and Secretion. In *Alginates: Biology and applications*; 2009; pp 55–71.
- (26) Papageorgiou, S. K.; Kouvelos, E. P.; Favvas, E. P.; Sapolidis, A. A.; Romanos, G. E.; Katsaros, F. K. Metal-Carboxylate Interactions in Metal-Alginate Complexes Studied with FTIR Spectroscopy. *Carbohydr. Res.* **2010**, *345* (4), 469–473.
- (27) Bilal, M.; Iqbal, H. M. N. Naturally-Derived Biopolymers: Potential Platforms for Enzyme Immobilization. *Int. J. Biol. Macromol.* **2019**, *130*, 462–482.
- (28) Enyashin, A. N.; Seifert, G. Structure, Stability and Electronic Properties of TiO₂ Nanostructures. *Phys. Status Solidi Basic Res.* **2005**, *242* (7), 1361–1370.
- (29) Gunatilake, U. B.; Bandara, J. Efficient Removal of Oil from Oil Contaminated Water by Superhydrophilic and Underwater Superoleophobic Nano/Micro Structured TiO₂ nanofibers Coated Mesh. *Chemosphere* **2017**, *171*, 134–141.
- (30) Tian, J.; Zhao, Z.; Kumar, A.; Boughton, R. I.; Liu, H. Recent Progress in Design, Synthesis, and Applications of One-Dimensional TiO₂ Nanostructured Surface Heterostructures: A Review. *Chem. Soc. Rev.* **2014**, *43* (20), 6920–6937.

- (31) Roy, P.; Berger, S.; Schmuki, P. TiO₂ Nanotubes: Synthesis and Applications. *Angew. Chemie - Int. Ed.* **2011**, *50* (13), 2904–2939.
- (32) Grochowska, K.; Szkoda, M.; Karczewski, J.; Śliwiński, G.; Siuzdak, K. Ordered Titanium Templates Functionalized by Gold Films for Biosensing Applications – Towards Non-Enzymatic Glucose Detection. *Talanta* **2017**, *166*, 207–214.
- (33) Koike, K.; Sasaki, T.; Hiraki, K.; Ike, K.; Hirofuji, Y.; Yano, M. Characteristics of an Extended Gate Field-Effect Transistor for Glucose Sensing Using an Enzyme-Containing Silk Fibroin Membrane as the Bio-Chemical Component. *Biosensors* **2020**, *10* (6), 57.
- (34) Solovei, D.; Žák, J.; Majzlíková, P.; Sedláček, J.; Hubálek, J. Chemical Sensor Platform for Non-Invasive Monitoring of Activity and Dehydration. *Sensors (Switzerland)* **2015**, *15* (1), 1479–1495.
- (35) Miyauchi, M.; Tokudome, H. Super-Hydrophilic and Transparent Thin Films of TiO₂ Nanotube Arrays by a Hydrothermal Reaction. *J. Mater. Chem.* **2007**, *17* (20), 2095–2100.
- (36) Mahshid, S.; Askari, M.; Ghamsari, M. S. Synthesis of TiO₂ Nanoparticles by Hydrolysis and Peptization of Titanium Isopropoxide Solution. *J. Mater. Process. Technol.* **2007**, *189* (1–3), 296–300.
- (37) Liu, N.; Chen, X.; Zhang, J.; Schwank, J. W. A Review on TiO₂-Based Nanotubes Synthesized via Hydrothermal Method: Formation Mechanism, Structure Modification, and Photocatalytic Applications. *Catal. Today* **2014**, *225*, 34–51.
- (38) Akilavasan, J.; Wijeratne, K.; Moutinho, H.; Al-Jassim, M.; Alamoud, A. R. M.; Rajapakse, R. M. G.; Bandara, J. Hydrothermally Synthesized Titania Nanotubes as a Promising Electron Transport Medium in Dye Sensitized Solar Cells Exhibiting a Record Efficiency of 7.6% for 1-D Based Devices. *J. Mater. Chem. A* **2013**, *1* (17), 5377–5385.
- (39) Schneider, C. A.; Rasband, W. S.; Eliceiri, K. W. NIH Image to ImageJ: 25 Years of Image Analysis. *Nat. Methods* **2012**, *9* (7), 671–675.
- (40) Stoisser, T.; Brunsteiner, M.; Wilson, D. K.; Nidetzky, B. Conformational

- Flexibility Related to Enzyme Activity: Evidence for a Dynamic Active-Site Gatekeeper Function of Tyr215 in *Aerococcus Viridans* Lactate Oxidase. *Sci. Rep.* **2016**, *6* (1), 1–13.
- (41) Pazur, J. H.; Kleppe, K. The Oxidation of Glucose and Related Compounds by Glucose Oxidase from *Aspergillus Niger*. *Biochemistry* **1964**, *3* (4), 578–583.
- (42) Schomburg, D.; Salzmann, M.; Stephan, D. Enzyme Handbook 7. In *Springer*; Springer, Ed.; 1993; p EC 1.11.1.7:1–6.
- (43) Bavykin, D. V; Walsh, F. C. *Titanate and Titania Nanotubes*; Nanoscience & Nanotechnology Series; 2009.
- (44) Sikorski, P.; Mo, F.; Skjåk-Bræk, G.; Stokke, B. T. Evidence for Egg-Box-Compatible Interactions in Calcium - Alginate Gels from Fiber x-Ray Diffraction. *Biomacromolecules* **2007**, *8* (7), 2098–2103.
- (45) Jang, J.; Seol, Y. J.; Kim, H. J.; Kundu, J.; Kim, S. W.; Cho, D. W. Effects of Alginate Hydrogel Cross-Linking Density on Mechanical and Biological Behaviors for Tissue Engineering. *J. Mech. Behav. Biomed. Mater.* **2014**, *37*, 69–77.
- (46) Lee, K. E.; Gomez, M. A.; Elouatik, S.; Demopoulos, G. P. Further Understanding of the Adsorption Mechanism of N719 Sensitizer on Anatase TiO₂ Films for DSSC Applications Using Vibrational Spectroscopy and Confocal Raman Imaging. *Langmuir* **2010**, *26* (12), 9575–9583.
- (47) Stoisser, T.; Brunsteiner, M.; Wilson, D. K.; Nidetzky, B. Conformational Flexibility Related to Enzyme Activity: Evidence for a Dynamic Active-Site Gatekeeper Function of Tyr215 in *Aerococcus Viridans* Lactate Oxidase. *Sci. Rep.* **2016**, *6* (1), 1–13.
- (48) Kean, K. M.; Karplus, P. A. Structure and Role for Active Site Lid of Lactate Monooxygenase from *Mycobacterium Smegmatis*. *Protein Sci.* **2019**, *28* (1), 135–149.
- (49) Berglund, G. I.; Carlsson, G. H.; Smith, A. T.; Szöke, H.; Henriksen, A.; Hajdu, J. The Catalytic Pathway of Horseradish Peroxidase at High Resolution. *Nature* **2002**, *417* (6887), 463–468.

- (50) Kim, B. C.; Jeong, E.; Kim, E.; Hong, S. W. Bio-Organic–Inorganic Hybrid Photocatalyst, TiO₂ and Glucose Oxidase Composite for Enhancing Antibacterial Performance in Aqueous Environments. *Appl. Catal. B Environ.* **2019**, *242*, 194–201.
- (51) Denisov, I. G.; Makris, T. M.; Sligar, S. G. Formation and Decay of Hydroperoxo-Ferric Heme Complex in Horseradish Peroxidase Studied by Cryoradiolysis. *J. Biol. Chem.* **2002**, *277* (45), 42706–42710.
- (52) David, J.; Elingg, T.; Ronald, M. The Horseradish Peroxidase-Catalyzed Oxidation of 3,5,3',5'-Tetramethylbenzidine. Free Radical and Charge-Transfer Complex Intermediates. *J. Biol. Chem.* **1982**, *257* (7), 3669–3675.
- (53) Siripongpreda, T.; Somchob, B.; Rodthongkum, N.; Hoven, V. P. Bacterial Cellulose-Based Re-Swellable Hydrogel: Facile Preparation and Its Potential Application as Colorimetric Sensor of Sweat PH and Glucose. *Carbohydr. Polym.* **2021**, *256*, 117506.
- (54) Russell, R. J.; Pishko, M. V.; Gefrides, C. C.; McShane, M. J.; Cote, G. L. A Fluorescence-Based Glucose Biosensor Using Concanavalin A and Dextran Encapsulated in a Poly(Ethylene Glycol) Hydrogel. *Anal. Chem.* **1999**, *71* (15), 3126–3132.
- (55) Schneider, J.; Matsuoka, M.; Takeuchi, M.; Zhang, J.; Horiuchi, Y.; Anpo, M.; Bahnemann, D. W. Understanding TiO₂ photocatalysis: Mechanisms and Materials. *Chem. Rev.* **2014**, *114* (19), 9919–9986.
- (56) Hashimoto, K.; Irie, H.; Fujishima, A. TiO₂ Photocatalysis: A Historical Overview and Future Prospects. *Japanese J. Appl. Physics, Part 1 Regul. Pap. Short Notes Rev. Pap.* **2005**, *44* (12), 8269–8285.
- (57) Zhao, H.; Dong, Y.; Jiang, P.; Wang, G.; Zhang, J. Highly Dispersed CeO₂ on TiO₂ Nanotube: A Synergistic Nanocomposite with Superior Peroxidase-like Activity. *ACS Appl. Mater. Interfaces* **2015**, *7* (12), 6451–6461.
- (58) Zhang, L.; Han, L.; Hu, P.; Wang, L.; Dong, S. TiO₂ Nanotube Arrays: Intrinsic Peroxidase Mimetics. *Chem. Commun.* **2013**, *49* (89), 10480–10482.
- (59) Park, C.; Kim, H. R.; Kim, S. K.; Jeong, I. K.; Pyun, J. C.; Park, S. Three-

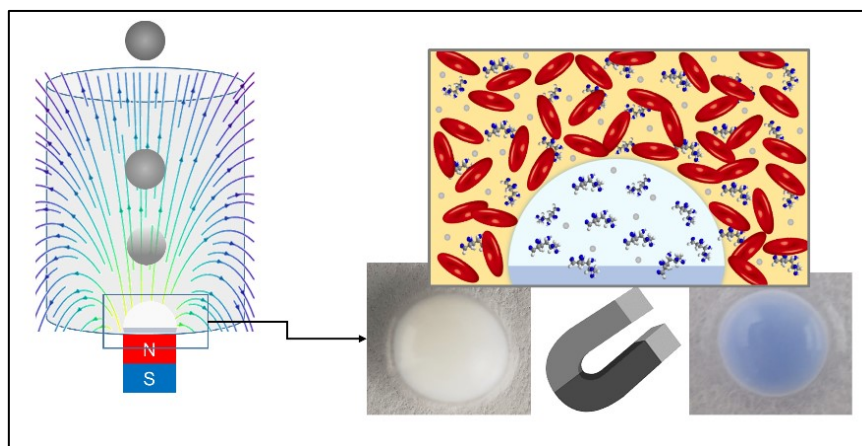
- Dimensional Paper-Based Microfluidic Analytical Devices Integrated with a Plasma Separation Membrane for the Detection of Biomarkers in Whole Blood. *ACS Appl. Mater. Interfaces* **2019**, *11* (40), 36428–36434.
- (60) Li, F.; Wang, X.; Liu, J.; Hu, Y.; He, J. Double-Layered Microfluidic Paper-Based Device with Multiple Colorimetric Indicators for Multiplexed Detection of Biomolecules. *Sens. Actuators B Chem.* **2019**, *288*, 266–273.
- (61) Calabria, D.; Caliceti, C.; Zangheri, M.; Mirasoli, M.; Simoni, P.; Roda, A. Smartphone-Based Enzymatic Biosensor for Oral Fluid L-Lactate Detection in One Minute Using Confined Multilayer Paper Reflectometry. *Biosens. Bioelectron.* **2017**, *94*, 124–130.
- (62) Akyazi, T.; Tudor, A.; Diamond, D.; Basabe-Desmonts, L.; Florea, L.; Benito-Lopez, F. Driving Flows in Microfluidic Paper-Based Analytical Devices with a Cholinium Based Poly(Ionic Liquid) Hydrogel. *Sensors Actuators, B Chem.* **2018**, *261*, 372–378.
- (63) Määttänen, A.; Fors, D.; Wang, S.; Valtakari, D.; Ihalainen, P.; Peltonen, J. Paper-Based Planar Reaction Arrays for Printed Diagnostics. *Sensors Actuators, B Chem.* **2011**, *160* (1), 1404–1412.
- (64) Yunker, P. J.; Still, T.; Lohr, M. A.; Yodh, A. G. Suppression of the Coffee-Ring Effect by Shape-Dependent Capillary Interactions. *Nature* **2011**, *476* (7360), 308–311.
- (65) Azuaje-Hualde, E.; Arroyo-Jimenez, S.; Garai-Ibabe, G.; de Pancorbo, M. M.; Benito-Lopez, F.; Basabe-Desmonts, L. Naked Eye Y Amelogenin Gene Fragment Detection Using DNAzymes on a Paper-Based Device. *Anal. Chim. Acta* **2020**, *1123*, 1–8.
- (66) Kim, S.; Lee, B.; Reeder, J. T.; Seo, S. H.; Lee, S. U.; Hourlier-Fargette, A.; Shin, J.; Sekine, Y.; Jeong, H.; Oh, Y. S.; Aranyosi, A. J.; Lee, S. P.; Model, J. B.; Lee, G.; Seo, M. H.; Kwak, S. S.; Jo, S.; Park, G.; Han, S.; Park, I.; Jung, H. Il; Ghaffari, R.; Koo, J.; Braun, P. V.; Rogers, J. A. Soft, Skin-Interfaced Microfluidic Systems with Integrated Immunoassays, Fluorometric Sensors, and Impedance Measurement Capabilities. *Proc. Natl. Acad. Sci. U. S. A.* **2020**, *117* (45), 27906–27915.

Lab-in-a-Bead: Magnetic Janus Bead Probe for the Detection of Biomarkers in Whole Blood

This Chapter is partially reproduced from:

Gunatilake, U. B.; Abalos, A.C.; Garcia-Rey, S; Ruiz, J.M; Basabe-Desmonts, L.; Benito-Lopez, F. Lab-in-a-Bead: Magnetic Janus Bead Probe for the Detection of Biomarkers in Whole Blood , *Small*, (18-03-2022) Under review- ID sml.202201710.

Abstract. Remotely handled miniaturised colorimetric sensor platforms with multiple functionalities are able to mimic conventional laboratory operations with reduced assets. The integration of a magnetic phase in a miniaturised hydrogel sensor system allows the manipulation of the sensor, under a magnetic field, in a programmable manner. However, dark color interferences of conventional magnetic phases (Fe_3O_4 , Fe_2O_3 , Fe micro/nanoparticles) affect the signal readout, hindering the colorimetric response. Therefore, a novel Janus bead configuration is introduced and tested by the localised incorporation of ferromagnetic iron microparticles to a TiO_2 nanotubes/alginate hydrogel bead biosystem, under an applied magnetic field. The so-called hydrogel Janus bead showed both, magnetic translocation and biosensing properties in the same bead. These beads are used for the direct colorimetric analysis of biomarkers from whole blood. The surface of the Janus bead prevents the biofouling of red blood cells, keeping the sensor surface clean for accurate optical colorimetric analysis. Moreover, the external magnetic manipulation of the bead permits a precise control of the time and position of the bead in the sample. Therefore, the multiple functionalities presented by a single magnetic TiO_2 nanotubes/alginate Janus bead such as actuation, low biofouling and sensing, position this technology as a truly Lab-in-a-Bead System.



5.1 Introduction

Colorimetric signal reading is becoming a very promising detection technology for portable and Point of Care (POC) devices due to its power-free, simple operability, portability and low-cost.¹⁻³ In particular, solid or semi-solid materials with immobilised colorimetric assays integrated in miniaturised colorimetric sensors continue appearing in literature, where hydrogels are rising as promising materials.^{4,5} They provide with a water rich solid matrix able to load and immobilise the required colorimetric assay to perform the desired detection.⁴ For instance, glucose oxidase (GOX) and horseradish peroxidase (HRP) were used as enzymatic catalysts and 3,3',5,5' tetramethyl-benzidine (TMB) as chromophore for the detection of glucose as like discussed in Chapter 4 for sweat glucose.⁶ Therefore, a safe and stable immobilisation of the enzymes and chromophore in the solid platform plays an important role for accurate sensing. However, fast drying is a drawback in hydrogel based sensors, which is usually addressed by a sealed storing environment. Moreover, the molecules of the assay, entrapped in the hydrogel sensing scaffold, usually diffuse to the surrounding analyte solution over time. This causes ionic densities imbalances between the hydrogel and the outer solution, leading to the reduction of the amount of reactants need for detection inside of the hydrogel scaffold, over time.⁷ In this regard, as a problem solving technique, the fast removal of the scaffold from the solution, using a smart remote controlled manipulation system, could reduce or eliminate assay leaking from the hydrogel scaffold.

Biocompatible and remotely manipulable organic-inorganic hybrid materials offer tremendous applicability when integrated into biosystems.^{8,9} In particular, magneto-driven actuators provide a good alternative when compared to other type of remote stimuli, such as temperature, electric or light.¹⁰ Zhao *et al.* presented lab-in-a-droplet system based on superhydrophobic magnetic particles able to encapsulate reagents and samples. The interior of the droplet was addressable by applying the magneto induced shell opening and closing property of the magnetic liquid marbles.¹¹ Nevertheless, the integration of the magnetic phase in hydrogel-based miniaturised sensor scaffolds is required to ensure their manipulation. In this regard, *in situ* or *ex situ* nano/micro structured magnetic inorganic phases can be incorporated into the hydrogel matrix as deeply studied in Chapter 3, not only to promote remote controllable responses but also to increase the mechanical properties of the hydrogel.^{12,13} The incorporation of

magnetic properties to the sensor scaffold facilitates the remote manipulation of the scaffold, even at a programmable manner, and it could bring new applicability in the microfluidic sector. Moreover, this remote manipulation can be used to minimise leaching of the assay by promoting the fast separation of the scaffold from the analyte solution, using an external magnetic field. However, the intrinsic dark colour of most commonly used magnetic particles (*e.g.* Fe₃O₄ –black, γ -Fe₂O₃ –brown, Fe –grey) interferes with the colorimetric system, by distracting the optical signal reading. Therefore, the fabrication of magneto driven hydrogel colorimetric systems is challenging when using conventional magnetic materials.

In addition to that, the colorimetric analysis of biomarkers in whole blood, which is the gold standard biofluid used for health care, persists as a complicated and costly operation due to the interference of the red colour from the haemoglobin to the optical read-out system.¹⁴ In this regard, before analysis, whole blood needs to be separated into plasma or serum prior biomarker detection. At laboratory premises, systems that use mechanical forces, such as centrifuges, are commonly used to separate red blood cells from plasma. Moreover, when using miniaturised systems or point of care devices, although sedimentation and external field based systems like acoustic, electrical, magnetic are also used,¹⁵ nonetheless filter membranes^{16,17} are more widely employed. However, the challenge faced by this type of analysis is to avoid the red blood cells (RBC) separation additional step, which leads to complicate and costly instrumentation or to the fabrication of sophisticate detection systems for whole blood detection. Park *et al.*¹⁸ reported a 3D printed plasma separating membrane where RBCs were filtered out and plasma was moved to the detection zone to analyse glucose from whole blood. Recently, Jing *et al.*¹⁹ developed a nanometer scale porous structured poly(ethylene) glycol-diacrylate hydrogel disc with an immobilised glucose sensing assay for the direct colorimetric measurement of glucose in whole blood. In this system, the glucose diffused through the hydrogel matrix while preventing RBCs interfering with the sensing signal in a single step blood analysis protocol.

Herein, a novel magneto driven hydrogel Janus bead with multiple functionalities is presented as a Lab-in-a-Bead system. Magnetic properties were integrated to the TiO₂ nanotubes/alginate hydrogel optical biosensor bead by introducing superhydrophobic Fe particles to the polymer matrix in which the polymer nanocomposite was cross-linked under a specific magnetic field induced protocol. The synthesised Janus bead

showed efficient optical biosensing (glucose tested as a model) and, at the same time, magneto actuation properties. Moreover, the Janus bead acted as a membrane to repel the red blood cells from the whole blood, minimising red colour artefacts during colorimetric sensing. This Lab-in-a-bead system opens new avenues for the magneto programmable, colorimetric detection of blood biomarkers in a simple and cheap manner, acting as a probe when immersed in whole blood.

5.2 Experimental

5.2.1 Synthesis of TiO₂ nanotubes

First, TiO₂ nanoparticles were synthesised by a precipitation method similar to the one described in Chapter 4, section 4.2.1.²⁰

5.2.2 Synthesis of C₈-Fe particles

1.00 g of iron micro particles (<10 micron, 99.5 %, Alfa Aesar, Germany) were mechanically stirred in 5.0 mL of 0.25 M HCl for 15 min. Next, the particles were magnetically separated from the solution and washed with water, ethanol and acetone respectively. Then the particles were dried for 1 h at 60 °C. Then, 1.8 mL of triethoxy(octyl)silane (97 %, Sigma-Aldrich, Spain) was mixed with 50 mL of absolute ethanol (Sharlau, Spain) for 2 h under 50 °C. Later, a sonicated suspension of pre-treated 0.53 g of Fe particles in 10 mL absolute ethanol was added to the triethoxy(octyl)silane/ethanol solution and stirred for 2 h. After that, the particles were separated with a magnet and thoroughly washed with ethanol for 3 times. Finally, the particles were heated at 120 °C for 2 h to obtain C₈-Fe magnetic particles.

5.2.3 Fabrication of the Janus bead

First, 5 mg of TiO₂ nanotubes were mixed with 1 mL of 1 % (w/v) of alginate (Sigma-Aldrich, Spain) (1.00 g alginate/100 mL distilled water) for 15 min under sonication, followed by 48 h magnetic stirring (TNT/alginate polymer suspension). Next, 5 mg of C₈-Fe magnetic particles were added to the TNT/alginate composite and the mixture was vortexed for 5 min. Then, the glucose biosensing assay was added to the polymer blend.

The same enzymatic and colorimetric ratios mentioned in Chapter 4, section 4.2.3. were applied for the Janus bead. 5 µL of 0.4 mg mL⁻¹ glucose oxidase (GOX) (AG scientific,

Spain) solution, a 5 μL of 0.05 mg mL^{-1} horseradish peroxidase (HRP) (Sigma-Aldrich, Spain) solution and a 5 μL 3,3',5,5' tetramethyl-benzidine (TMB) (Sigma-Aldrich, Spain) in dimethyl sulfoxide (DMSO) (> 99.7 %, Sigma-Aldrich, Spain) (TMB:DMSO, 24:2.25) solution were mixed with 30 μL of the TNT/ C₈-Fe/alginate polymer suspension. The suspension was vortexed for 10 s. A CaCl₂ bath was prepared by filling, with a 2 mL (10 mm height) of 0.2 M CaCl₂ (93 %, Sigma-Aldrich, Spain) solution in a 5 mL glass beaker. A vertical gradient magnetic field was supplied to the bath by keeping a NdFeB permanent magnet (cubic 10 mm magnet, surface 495 mT) right under the beaker. Then, 20 μL of the assay polymer mixture was dripped into the CaCl₂ bath to form the Janus bead. Instantly, the polymer droplet was attracted to the depth of the beaker while cross-linking with the calcium ions, under the magnetic field. The Janus bead was kept in the bath for 3 min. Then, the scaffold was washed with distilled water for 30 s. The obtained scaffolds were air dried for 2 min. to evaporate extra surface water.

5.2.4 Colorimetric signal readout analysis

The Janus beads were kept inside of the 1 mL of whole blood, whole blood diluted with water and PBS (10 and 100 times) to test the performance of the beads in the presence of RBCs. After 6 min, the beads were removed from the baths and washed with water/PBS. Then, the colorimetric signal was captured. For the paper scaffold, circles of 0.7 cm diameter were printed on cellulose filter paper, Whatman filter paper #1 (Sigma Aldrich, Spain) by a Xerox ColorQube 8570 wax printer and the wax barriers were generated with a FLC oven, set at 125 °C for 5 min. Next, a 20 μL of the enzymatic and colorimetric assay (same ratios as in Experimental 2.3 without TNT/ C₈-Fe/alginate nanocomposite) was drop casted on to the sensing region of the paper and allowed to absorb in paper for 10 min. Then, 15 μL of blood was added to the sensing area and the paper was slightly washed with PBS solution after 6 min. Finally, the sensing area image was captured.

5.2.5 Glucose determination by the Janus bead

Three glucose calibration systems were prepared by using phosphate buffered saline (PBS) (137 mM NaCl, 2.7 mM KCl and 10 mM phosphate buffer solution, pH 7.4 at 25 °C, Sigma-Aldrich, Spain), human serum (H4522, from human male AB plasma, USA origin, Sigma-Aldrich, USA) and whole blood solution (use approved by the “comité de ética para las investigaciones con seres humanos, sus muestras y sus datos”

(CEISH-UPV/EHU), code:TI0175). For the PBS calibration system, first 10 mM glucose solution (in PBS) was prepared and then, it was diluted with PBS to obtain the desired glucose concentrations. In the human serum and the whole blood systems, the glucose levels were measured using a commercial glucometer (Freestyle freedom lite abbott glucose meter, UK) and then, the plasma and the blood were diluted with PBS solution to obtain the desired glucose levels. To check the glucose levels through the Janus beads, 15 μ L of the glucose samples were pipetted over the Janus beads, placed on a glass slide, and the images of the beads were captured at 0 and 6 min by a Sony Cyber-shot DSC-RX100 camera, over time, under controlled light conditions. Finally, the obtained images were analysed by Image-J software.²¹

In the case of blood analysis, the beads were rinsed with water to remove surface adhered blood layer. Then, the images were taken and analysed by Image-J software.²¹ In all cases, the intensities of the images were analysed by mean grey value (black and white, B&W value) 0-255 scale (black = 0, white = 255). The difference of the B&W values at 0 min and at 6 min was related with the corresponding glucose concentration.

5.2.6 Characterisation

Scanning electron microscopy (SEM) images of the freeze-dried beads were recorded by a Field Emission Scanning Electron Microscope S-4800 (Hitachi Japan) and a Carl Zeiss EVO 40 (Oberkochen, Germany) equipped with an EDS Oxford Instrument X-Max detector (Abingdon, U.K.). Magnetisation measurements for the iron oxide nanoparticles and the dehydrated beads were carried out in a 7 T Quantum Design MPMS3 SQUID (Superconducting Quantum Interference Device) and homemade VSM (vibrating-sample magnetometer) magnetometer at room temperature. Data, statistical, and image analysis were carried out in Excel, Origin Pro 2018, and Image-J.

5.3 Results and Discussion

5.3.1 Synthesis and characterisation of the Janus bead

The integration of magnetic particles to a hydrogel bead darken its coloration, restricting the possible applicability of the bead for colorimetric signal analysis. In order to avoid the interference of the dark coloration of the bead, the magnetic hydrogel bead was synthesised following the protocol presented in the experimental section 5.2.3,

combining both properties, the colorimetric sensing and the magneto driven capability in the same matrix, called Janus bead. As demonstrated in Figure 5.1a, a droplet of TNT/ C₈-Fe/alginate polymer blend was dripped to the crosslinking Ca²⁺ solution under a 353 mT vertical gradient magnetic field. The COO⁻ groups of the alginate in the polymer blend droplet, started to crosslink with the Ca²⁺ cations over all the interface of the droplet with the calcium ions solution, immediately after the droplet touched the solution.²² At the same time, the magnetic particles present in the polymer blend were attracted to the magnet, following the magnetic field lines as shown in the Figure 5.1a. However, the instantly cross-linked flexible TNT/alginate polymer shell of the bead preventing the physical separation of the magnetic particles from the polymer blend. Therefore, the magnetic phase got deposited at the bottom of the bead, forming a hemispherical magnetic bead (~ 4.3 mm), as shown in the Figure 5.1b (picture 1). The force towards the soft polymer by the magnetic particles led to the flattening of the bottom of the bead, whereas a spherical shape was observed when the magnetic field was not applied.

However, partial contamination of the sensing area with residual magnetic particles was observed during the fabrication process. The 3D network of the polymer (TNT/alginate), which formed rapidly, prevented the movement of the magnetic particles to the bottom of the bead, contaminating the top part of the bead. In order to minimise this process, the Fe particles were chemically modified with alkyl chains (superhydrophobic C₈-Fe particles) to avoid the interactions with the superhydrophilic TNT/alginate suspension. Moreover, the concentration of the Ca²⁺ cross-linker in the solution was reduced to 0.2 M (from the usual concentration of 0.4 M used for the fabrication of non-magnetic alginate beads⁴) to avoid the rapid crosslinking of the polymer shell. This allowed the magnetic particles to reach the bottom of the bead, minimising their trapping, during crosslinking, in the sensing region of the bead. In addition, the height (*h*) of the crosslinking bath was investigated. The induction of the magnetic field on the hydrogel bead is reduced while increasing the value of *h* thus for *h* > 10 mm, the upper surface of the bead was contaminated with magnetic particles. Therefore, *h* was set to 10 mm in order to be able to apply high magnetic forces to the system and to rapidly confine the magnetic particles at the bottom of the bead. Figure 5.1b, clearly shows a picture of a bead with absence of colour interferences from the magnetic particles, when using this optimised protocol, facilitating monitor of possible

optical signals coming from the white surface of the bead. A magnetic bead, fabricated without the magnetic field is shown in Figure 5.1b (picture 3), where is easy to observe the difference in colour. The colour map of the Janus bead, side view in Figure 5.1b (picture 2), clearly illustrates the separation of the magnetic phase (blue/green) and the TNT/alginate sensor phase (orange). Moreover, B&W value histograms in Figure 5.2 demonstrated that the average on the B&W value increased to 206 from 118 in beads where the magnetic field was applied during their fabrication process. In addition, Energy Dispersive X-Ray (EDX) analysis of the top and the bottom areas of the beads indicated a significantly low Fe percentage in the upper surface when compared to the bottom area (Table 5.1 and 5.2 in supplementary information). It is possible to observe that the magnetic particles self-assembled vertically, following the magnetic flux lines at the bottom of the bead (Figure 5.1b-1), which provide the magnetic properties to the Janus beads.

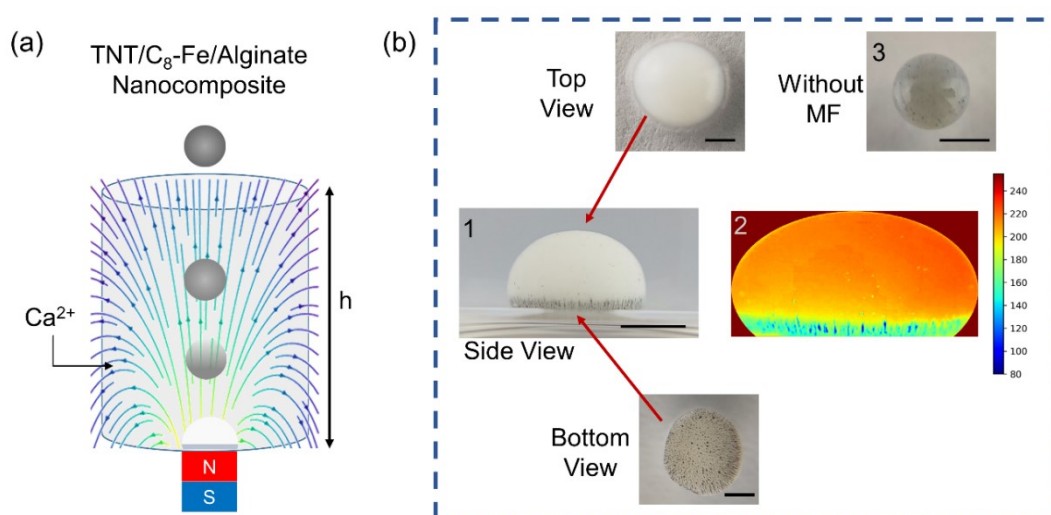


Figure 5.1. (a) Schematic illustration of the fabrication of Janus bead under an applied gradient magnetic field, (magnetic flux density indicated with lines). (b) Side, top and bottom view of the fabricated Janus bead (set of pictures 1). Illustration of the absence of interferences from the magnetic particles in the sensing readout area by a colour map (picture 2). TNT/C₈-Fe/Alginate bead fabricated without a magnetic field (picture 3). Scale bars indicate 2 mm length.

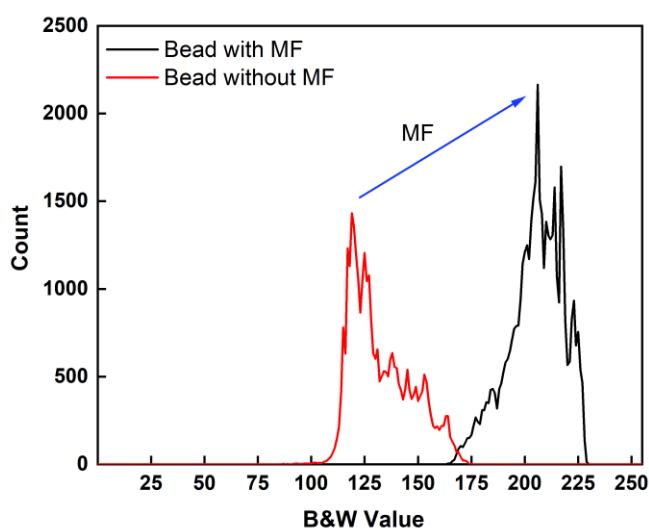


Figure 5.2. B&W histogram of the beads synthesised with and without the magnetic field (MF). The analysis of the pictures of the two beads was done from the top of the beads, see images in Figure 5.1b. The intensities of the images were analysed by mean grey value (black and white, B&W value) 0-255 scale (black = 0, white = 255).

Table 5.1 (EDX) Elemental analysis of Janus bead (bottom area).

| <i>Spectrum</i> | <i>C %</i> | <i>O %</i> | <i>Na %</i> | <i>S %</i> | <i>Cl %</i> | <i>Ca %</i> | <i>Ti %</i> | <i>Fe %</i> |
|-----------------------|------------|------------|-------------|------------|-------------|-------------|-------------|--------------|
| <i>Spectrum 1</i> | 17.35 | 5.69 | 0.20 | 0.39 | 0.46 | 1.63 | 4.09 | 70.18 |
| <i>Spectrum 2</i> | 10.4 | 2.45 | 0.09 | 0.24 | 1.02 | 2.04 | 2.29 | 81.47 |
| <i>Spectrum 3</i> | 39.48 | 24.14 | 0.96 | 0.95 | 2.34 | 3.26 | 4.35 | 24.52 |
| <i>Spectrum 4</i> | 31.18 | 30.46 | 1.13 | 1.50 | 3.38 | 3.70 | 5.46 | 23.20 |
| <i>Spectrum 5</i> | 24.59 | 34.63 | 0.81 | 0.45 | 1.37 | 3.02 | 2.77 | 32.35 |
| <i>Spectrum 6</i> | 14.93 | 9.78 | 0.12 | 0.38 | 1.07 | 1.87 | 3.96 | 67.90 |
| Mean | 22.99 | 17.86 | 0.55 | 0.65 | 1.61 | 2.59 | 3.82 | 49.94 |
| Std. deviation | 10.93 | 13.64 | 0.47 | 0.48 | 1.07 | 0.85 | 1.14 | 26.07 |

Table 5.2 (EDX) Elemental analysis of a Janus bead (top area).

| <i>Spectrum</i> | <i>C %</i> | <i>O %</i> | <i>Na %</i> | <i>S %</i> | <i>Cl %</i> | <i>Ca %</i> | <i>Ti %</i> | <i>Fe %</i> |
|-----------------------|------------|------------|-------------|------------|-------------|-------------|-------------|-------------|
| <i>Spectrum 1</i> | 34.93 | 38.20 | 1.77 | 2.68 | 5.92 | 7.10 | 9.06 | 0.33 |
| <i>Spectrum 2</i> | 22.87 | 24.78 | 0.05 | 3.11 | 7.93 | 15.68 | 23.35 | 2.22 |
| <i>Spectrum 3</i> | 42.82 | 32.60 | 4.98 | 1.35 | 9.31 | 4.22 | 4.51 | 0.22 |
| <i>Spectrum 4</i> | 20.34 | 16.92 | 0.69 | 4.26 | 20.84 | 15.29 | 21.66 | 0.00 |
| <i>Spectrum 5</i> | 38.17 | 40.52 | 0.85 | 1.09 | 3.16 | 3.99 | 7.18 | 5.03 |
| <i>Spectrum 6</i> | 33.16 | 41.54 | 1.97 | 2.19 | 5.69 | 6.61 | 8.68 | 0.16 |
| Mean | 32.05 | 32.43 | 1.72 | 2.45 | 8.81 | 8.82 | 12.41 | 1.59 |
| Std. deviation | 8.77 | 9.81 | 1.75 | 1.17 | 6.26 | 5.32 | 8.00 | 2.11 |

The surface morphology of the Janus bead was investigated, Figure 5.3. A bumpy surface in the bottom side of the bead was obtained due to the embossment of the magnetic colloidal particles, as shown in Figure 5.3a. The magnetic particles were attracted to the bottom side following the magnetic flux lines of the magnet. Therefore, these particle colloids covered the hydrogel and formed the bumpy spots (red arrows in Figure 5.3b) on the surface. A cracked polymer layer in a bumpy spot is shown in Figure 5.3c where the colloids of the magnetic particles were clearly seen inside of the polymer. Moreover, the non-binding behaviour of each individual particle to the polymer was clearly visible. The perfect spherical shape of the particles is visible and reminds separate from the polymer matrix, due to the superhydrophobicity of the C₈-Fe particles.

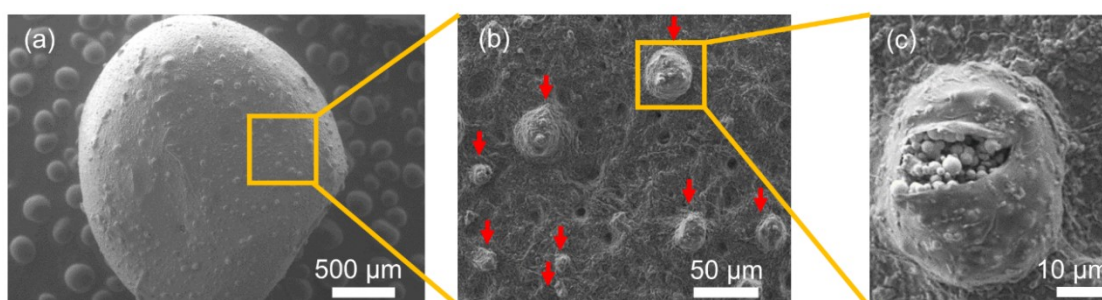


Figure 5.3. SEM images (cryo mode) of the bottom side of the Janus bead, a-c increasing the magnification while focusing on the magnetic particles accumulated spots ↓.

5.3.2 Remote stimuli Janus bead

The magnetic properties of the freeze-dried Janus beads were characterised by SQUID and VSM magnetometers, Figure 5.4a. The octyl-alkyl chain coating on the ferromagnetic Fe particles reduced the saturation magnetisation of the particles to $220 \text{ Am}^2 \text{ kg}^{-1}$ from $239 \text{ Am}^2 \text{ kg}^{-1}$ due to the addition of the non-magnetic octyl-alkyl to the magnetic particles. A saturation magnetisation of $49 \text{ Am}^2 \text{ kg}^{-1}$ was expected when adding 22.3 % (w:w) of $\text{C}_8\text{-Fe}$ to the pre-hydrogel nanocomposite prior the synthesis of the Janus bead, but the obtained value was just $22 \text{ Am}^2 \text{ kg}^{-1}$. The non-magnetic calcium cross-linkers in the bead and the impossibility to form a homogeneous suspension with the low surface energy $\text{C}_8\text{-Fe}$ particles in the nanocomposite are the reasons for this lower saturation value. This behaviour suggests a lower amount of the $\text{C}_8\text{-Fe}$ in the Janus bead than initially loaded in the nanocomposite. However, concerning the magnetic characterisation, it can be concluded that 10 % of $\text{C}_8\text{-Fe}$ are presented in the Janus bead by considering that the magnetic properties remained the same during the hydrogel synthesis and the freeze-dried protocols.

Remote manipulation of hydrogel sensor scaffolds facilitates to build programmable devices and to address the inherent problems faced by hydrogel based sensors. For instance, the diffusion of the sensing assay, presented inside the hydrogel, out of the solution is a major problem in hydrogel based sensors.⁷ Figure 5.5 shows the diffusion of the encapsulated reactants in a conventional alginate hydrogel to the analyte solution, where the reaction is taking place outside of the hydrogel sensor. This leaching process can be minimised by just separating the hydrogel bead from the bulk solution in a controlled manner and time. Moreover, the manipulation of the beads in a device can be difficult and could require extra components, which might diminish the functionality of the final device and its possible miniaturisation. In this case, the magnetic property of the Janus bead can be used to manipulate and control the bead position remotely, and to manage the time the bead is in contact with the solution to be analysed. Figure 5.4b shows the controllability of the Janus bead by just using a 1 x 1 mm NdFeB magnet. First, the Janus bead was dripped into a 1 mM glucose solution and collected back after 1 min. This process reduced the possible leakage of the colorimetric assay reagents, present in the bead, due to diffusion. Once out the solution, the bead was left to react with the glucose soaked into the bead and the colorimetric signal was recorded at 6 min. This process was also investigated using a simple microfluidic device configuration.

Remote handling and transportation, using a magnet, of the Janus bead inside of a microfluidic channel, while glucose is detected is demonstrated by the captured images from a video as depicted in Figure 5.6.

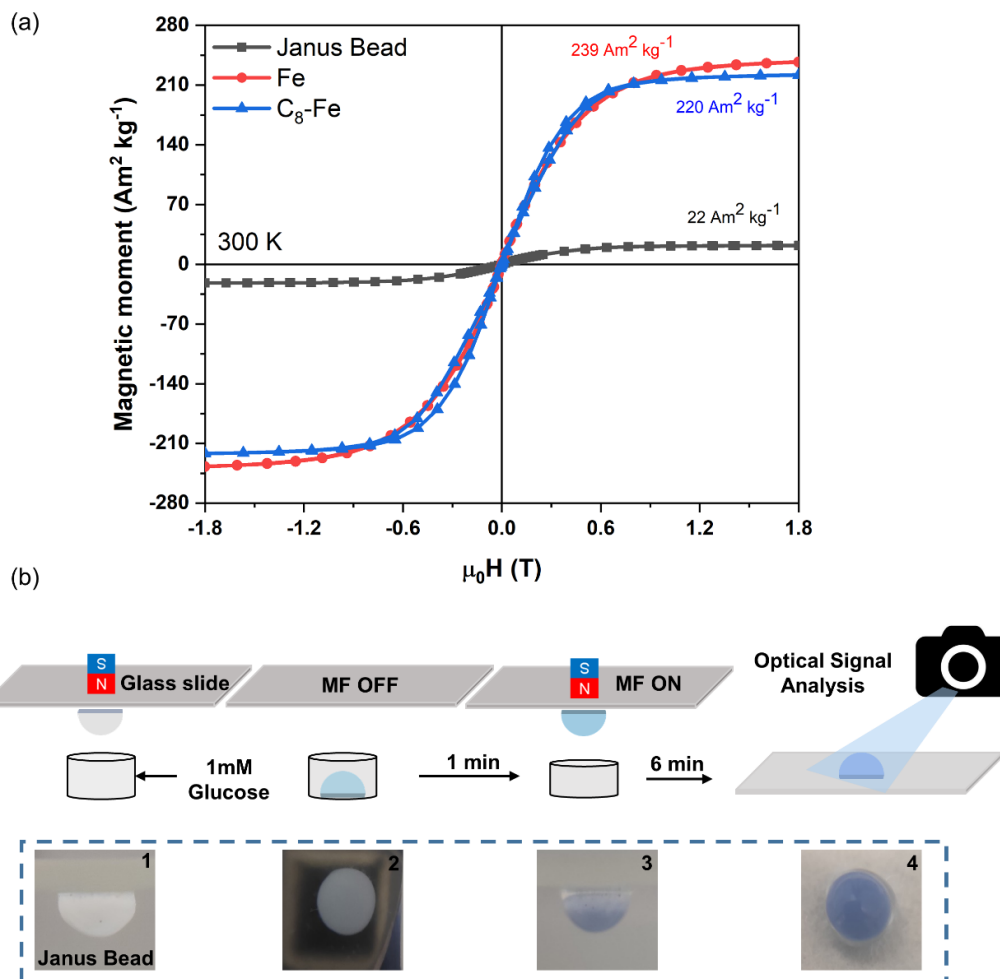


Figure 5.4. (a) Magnetisation (M-H) loops of the Fe, $\text{C}_8\text{-Fe}$ and Janus bead (freeze-dried), which were recorded by SQUID and VSM at room temperature. (b) Scheme of the magneto-manipulation of the Janus bead. The bead was dripped to a 1 mM glucose solution and removed after 1 min using magnetic attraction. Real images of the Janus bead for each step of the process are depicted behind each of the steps.

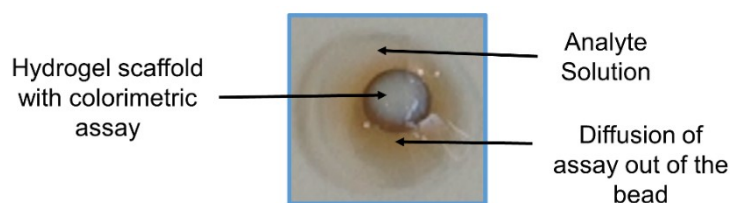


Figure 5.5. Diffusion of the sensing assay molecules from the hydrogel bead during glucose sensing, after 6 min in the solution.

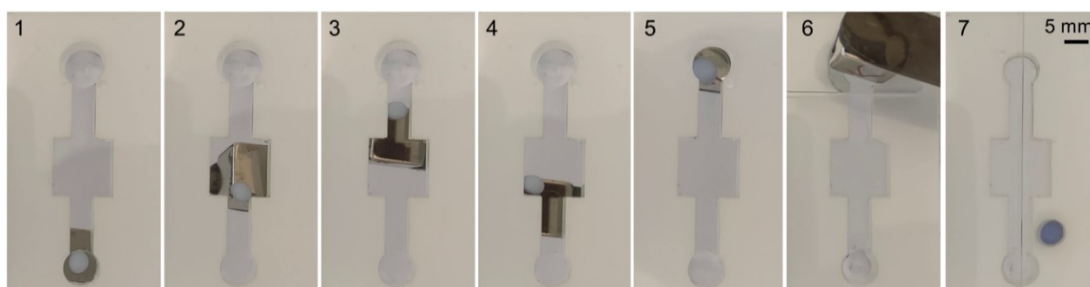


Figure 5.6. Captured images from the video. 1-4 transportation of the Janus bead in the microfluidics channel, 5 resting the bead, 6 removal of the bead from the chip by using a magnet, 7 signal reading.

5.3.3 Non-interference of the red blood cells to the Janus bead

Blood consists of approximately 45 % of red blood cells (RBCs), less than 1% of white blood cells and platelets and 54 % of plasma. That plasma is mainly water with dissolved proteins and other biomolecules such as glucose, lactic acid, uric acid, cholesterol and salts.¹⁷ The fabrication of a one-step colorimetric detection of biomarkers in whole blood remains challenging due to hindering of the optical signal by the red coloration coming from the red blood cells. However, the use of the Janus bead was subjected to detect one of the most demanding biomarkers present in blood, glucose.

The schematic illustration in Figure 5.7a shows the behaviour of the Janus bead when immersed in blood. It was observed that the red colouration of blood, due to the RBCs, was not transferred to the Janus bead, even after remaining 6 min inside of 1 mL blood container, as depicted in Figure 5.7b. This demonstrated that RBCs are too big to diffuse inside the bead due to the small mesh size (absence of micro range mesh) of the surface of the bead. In addition, the RBCs were filtered out from the outer surface of the Janus bead when removed from the solution. The cross section of the Janus bead is shown in Figure 5.7c, where a high porosity ($\sim 150 \mu\text{m}$), considering the space between separated polymer petals, was observed. However, the outer surface of the Janus bead was formed by a $\sim 40 \mu\text{m}$ thick polymer layer as shown in the Figure 5.8. SEM images of the outer surface of a hydrated and dehydrated Janus bead are shown in Figure 5.7d and e, respectively. They clearly showed a rough surface with absence of micro-pores or micron mesh size in the outer surface. Therefore, the surface of the Janus bead is able

to block the entrance of the RBCs, which have a biconcave shape with a diameter of $\sim 8 \mu\text{m}$ and a thickness of $\sim 2.5 \mu\text{m}$,²³ inside the bead. As well, the dimensions of the RBCs are much bigger than the reported mesh size of alginate hydrogels, 6-14 nm,²⁴ thus it is not possible for them to diffuse inside the Janus bead.

However, the haemolysis of RBCs in blood, which occurred due to osmosis while diluting blood samples, released the red coloured haemoglobin molecule (5 nm)²⁵ and entered the Janus bead, Figure 5.7f. In this case, a smart handling of the blood samples could avoid the red coloration of the Janus bead. For instance, the dilution of whole blood with PBS buffer avoids haemolysis and haemoglobin diffusion as shown in Figure 5.7f (right side image).

The optical signal readout performance of the Janus bead was compared with a conventional sensing paper substrate. Figure 5.7g shows the glucose sensing assay absorbed into a paper substrate and into a Janus bead, using the same glucose assay ratio, as mentioned in the Experimental section 5.2.3. Both scaffolds were subjected to the blood glucose detection protocol as mentioned in experimental section 5.2.4 to check the signal readout. A clear blue colour optical signal, due to glucose, was observed in the Janus bead since the RBCs got filtered out of the surface of the bead. This indicates the capability of Janus bead to perform one single step glucose sensing in blood. On the other hand, the blue colour optical signal was hindered in the conventional paper substrate due to the presence of red colouration coming from the RBCs, which were adhered to the surface of the paper.

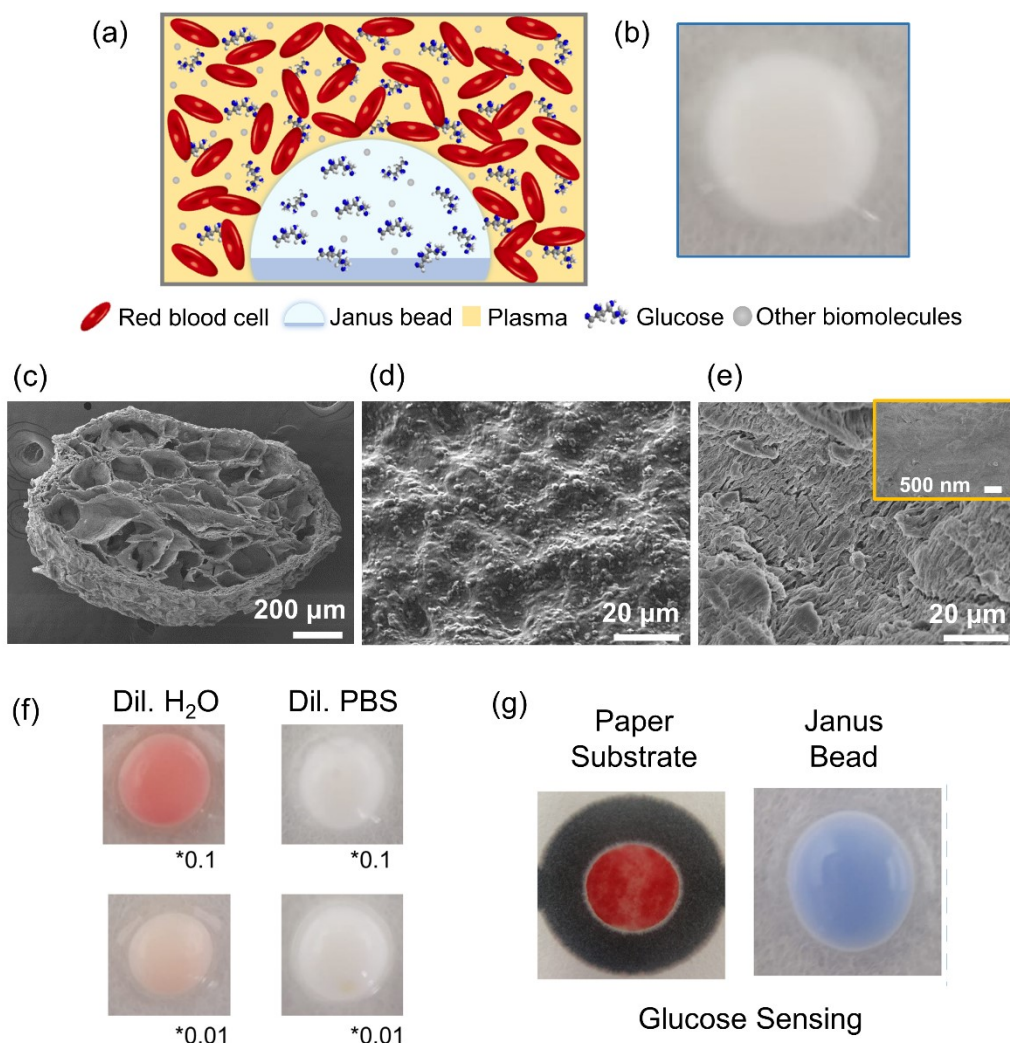


Figure 5.7. (a) Schematic illustration of the diffusion of small molecules, like glucose, into the Janus bead avoiding the absorption of RBCs. (b) The Janus bead (without sensing assay) after 6 min immersed in blood, 1 mL whole blood. The bead was rinsed with PBS before capturing the image, and the bead was magnetically handled throughout all the process. (c) SEM image of the cross-section of a freeze-dried Janus bead. (d) Cryo-mode SEM image of the hydrated and swelled Janus bead surface and (e) SEM image of the freeze-dried Janus bead surface, inset represents a high magnification image of the surface. (f) Janus bead (without sensing assays) after 6 min. remain inside of the 1 mL diluted whole blood with water and PBS under (*0.1)10 and (*0.01)100 dilution factors. (g) Glucose detection using a sensing assay loaded in a conventional paper substrate and in a Janus bead.

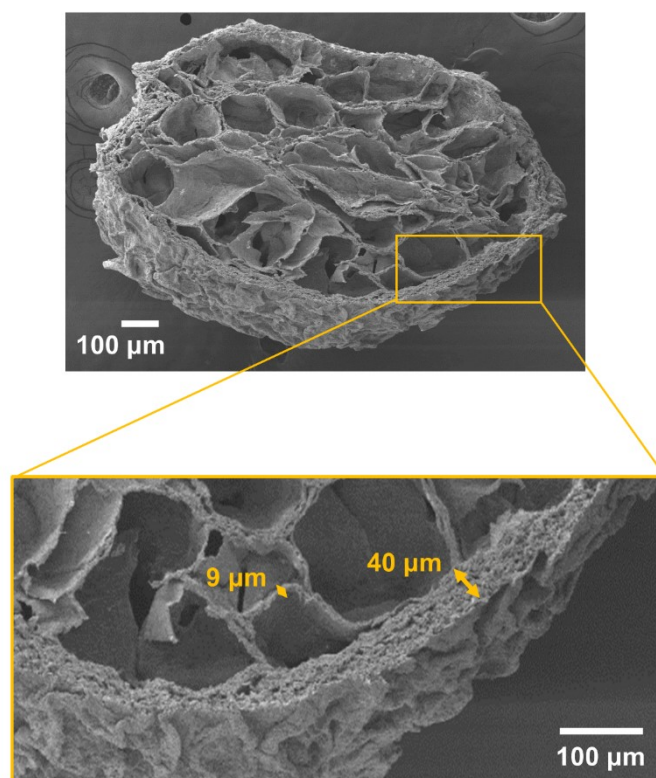


Figure 5.8. Cross-section of a Janus bead and magnification of the 40 μm thick outer surface shell.

5.3.4 Glucose sensing by the Janus bead.

The Janus bead provides a versatile platform for enzymatic chemical reactions by keeping the reactants in a miniaturised scaffold with multiple functionalities, as explained above. Figure 5.9a top image, shows a schematic diagram of the process occurring in the bead.²⁶ In brief, glucose was oxidised to the gluconic acid while the oxygen was reduced to the hydrogen peroxide in the presence of the glucose oxidase, enzymatic catalyst, once the glucose molecules entered the bead. Then, the generated hydrogen peroxide was reduced to water by the enzymatic catalyst, horseradish peroxidase, and the chromophore, TMB, was oxidised, generating a blue colour in the bead. The intensity of the formed colour relates to the concentration of the glucose as shown in the Figure 5.9b bottom images, where different concentrations of glucose in blood were detected using the Janus bead. As recently demonstrated by us,⁴ TiO₂ nanotubes in the hydrogel scaffold increased the sensing rate of the glucose, increasing the glucose absorption efficiency into the Janus bead due to their superhydrophilicity. The colour signal was recorded at 6 min for the Janus bead, while 13 min were

necessary for the bare alginate bead, without TiO₂ nanotubes, in order to obtain the same glucose concentrations values.

The glucose detection performance by the Janus bead was evaluated in human blood, human plasma and PBS solution. The B&W value difference of the Janus beads, before and after glucose detection, were analysed from the captured images of beads at 0 and 6 min for five glucose concentrations. An increased colour intensity (B&W difference) was observed when increasing the concentration of glucose in the different matrixes. Then, the calibration curves were generated. PBS, human plasma, and human blood calibration curves are depicted in Figure 5.9b, c and d, respectively. Linear dynamic ranges, at 6 min recording time, were obtained for the three samples within a glucose range of 0.1-0.8 mM, showing highly reliable correlation coefficients, $R^2 > 0.99$, from the linear regression analysis. The statistical limit of detection (LOD) was calculated to be 0.05 mM with a limit of quantification (LOQ) of 0.16 mM for glucose in PBS solution ($LOD = 3S/K$, and $LOQ = 10S/K$, where S is the standard deviation of the blank sample and K is the slope of the calibration curve). However, the evaluation of the LOD and LOQ was not possible in the case of blood and plasma due to the difficulty in obtaining a zero concentration glucose blank value, as blood/plasma always contains glucose. However, a high deviation from the LOD/LOQ values in PBS should not be expected for blood/plasma detection by the introduced Janus bead.

A random blood sample (10 times diluted with PBS) was tested with the Janus bead to check the accuracy of the glucose concentration obtained by PBS, plasma and glucose calibration curves, compared to a commercial glucometer. The obtained glucose concentrations from the Janus bead analysis (Table 5.3) for the plasma and the blood calibration curves showed nearly the same values to the ones obtained with the instant commercial glucometer. On the other hand, the glucose concentration obtained for the PBS solution significantly deviated from the glucometer values. This unexpected result could be explained considering the artificial PBS sample, which is not an ideal matrix for the quantification of glucose using the commercially available glucometer as opposed the real blood and plasma sample matrixes. Nevertheless, the results obtained when using the Janus beads present a promising multifunctional applied material for the colorimetric determination of glucose concentrations in complex samples such as blood.

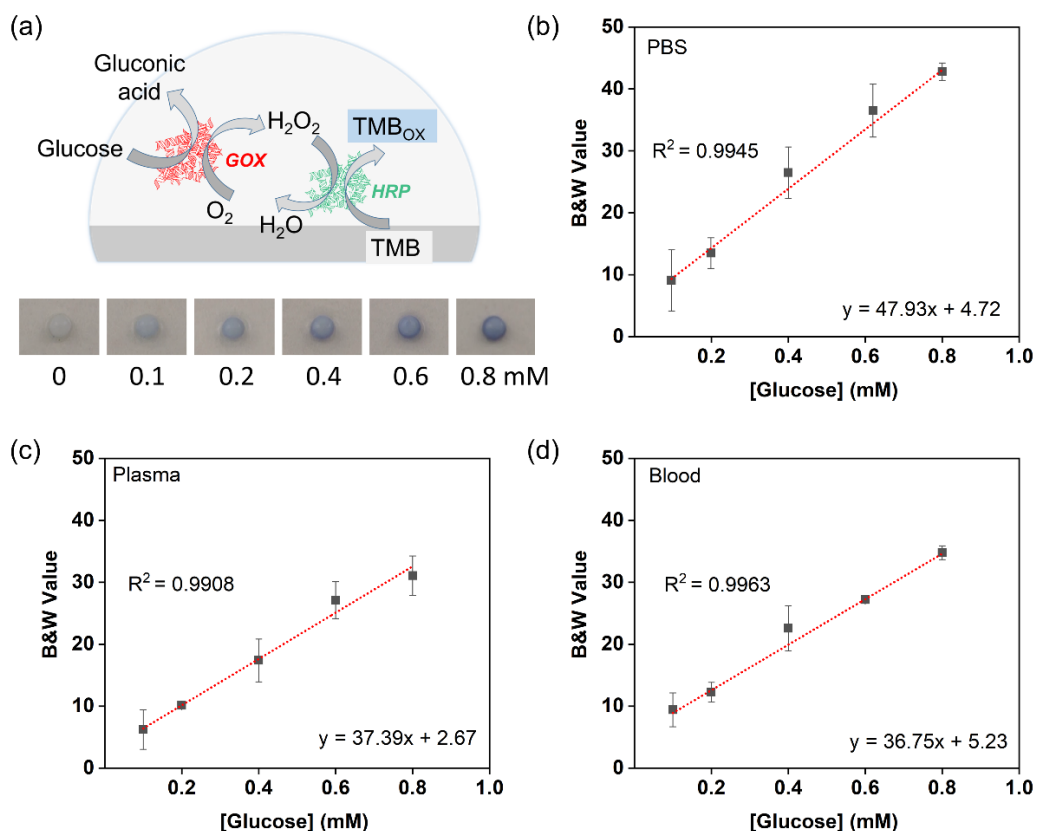


Figure 5.9. (a) Schematic diagram of glucose detection in the Janus bead (top side) and pictures of the Janus beads (bottom side) at different glucose concentration in blood, taken at 6 min time. Calibration curves for glucose in (b) PBS solution, (c) human plasma and (d) human blood by using the Janus bead. Error bars correspond to mean values \pm SD ($n = 3$).

Table 5.3 Comparison of blood glucose concentrations in the sample obtained using the glucometer and the Janus beads by the different calibration curves, ($n = 3$).

| Glucometer | Calibration Curves | | |
|------------------|--------------------|------------------|------------------|
| | PBS | Plasma | Blood |
| 5.0 ± 0.2 mM | 3.5 ± 0.3 mM | 5.0 ± 0.9 mM | 4.4 ± 0.2 mM |

5.4 Conclusion

We introduce the Lab-in-a-Bead concept by fabricating a novel Janus bead with magneto driven and colorimetric sensing capabilities. The introduction of a low surface energy ferromagnetic Fe microparticles into the TNT/alginate hydrogel and the subsequent crosslinking under a controlled magnetic field, facilitates the fabrication of

a novel sensing Janus bead with actuation capabilities. The fabrication avoids the conventional dark colour interference into the bead due to the magnetic phase.

The Janus bead provides a versatile platform to immobilise assays for colorimetric sensing, due to its moisture conditions and the white background colour of the bead. Moreover, the configuration of the Janus bead is able to filter out the RBCs from whole blood samples and colorimetrically detect the desired biomarkers, *e.g.* glucose, without the need to apply RBCs removing protocols like centrifugation or the use of filters. Therefore, the multiple functionalities of this novel Janus bead such as remote handling, magnetic manipulation, assay reagent immobilisation and storage, RBC filtration and biosensing demonstrates the concept of Lab-in-a-Bead.

5.5 References

- (1) Rakow, N. A.; Suslick, K. S. A Colorimetric Sensor Array for Odour Visualization. *Nature* **2000**, *406* (6797), 710–713.
- (2) Han, X.; Liu, Y.; Yin, Y. Colorimetric Stress Memory Sensor Based on Disassembly of Gold Nanoparticle Chains. *Nano Lett.* **2014**, *14* (5), 2466–2470.
- (3) Bandodkar, A. J.; Gutruf, P.; Choi, J.; Lee, K. H.; Sekine, Y.; Reeder, J. T.; Jeang, W. J.; Aranyosi, A. J.; Lee, S. P.; Model, J. B.; Ghaffari, R.; Su, C. J.; Leshock, J. P.; Ray, T.; Verrillo, A.; Thomas, K.; Krishnamurthi, V.; Han, S.; Kim, J.; Krishnan, S.; Hang, T.; Rogers, J. A. Battery-Free, Skin-Interfaced Microfluidic/Electronic Systems for Simultaneous Electrochemical, Colorimetric, and Volumetric Analysis of Sweat. *Sci. Adv.* **2019**, *5* (1), eaav3294.
- (4) Gunatilake, U. B.; Garcia-Rey, S.; Ojeda, E.; Basabe-Desmonts, L.; Benito-Lopez, F. TiO₂ Nanotubes Alginate Hydrogel Scaffold for Rapid Sensing of Sweat Biomarkers: Lactate and Glucose. *ACS Appl. Mater. Interfaces* **2021**, acsami.1c11446.
- (5) Wang, Z.; Liu, Y.; Wang, Z.; Huang, X.; Huang, W.; Zhiwei Wang, C. Hydrogel-Based Composites: Unlimited Platforms for Biosensors and Diagnostics. *View* **2021**, *2* (6), 20200165.

- (6) Zhang, H.; Smith, E.; Zhang, W.; Zhou, A. Inkjet Printed Microfluidic Paper-Based Analytical Device (MPAD) for Glucose Colorimetric Detection in Artificial Urine. *Biomed. Microdevices* **2019**, *21* (3), 1–10.
- (7) Garcia-Rey, S.; Ojeda, E.; Gunatilake, U. B.; Basabe-Desmonts, L.; Benito-Lopez, F. Alginate Bead Biosystem for the Determination of Lactate in Sweat Using Image Analysis. *Biosens. 2021, Vol. 11, Page 379* **2021**, *11* (10), 379.
- (8) Rafieian, S.; Mirzadeh, H.; Mahdavi, H.; Masoumi, M. E. A Review on Nanocomposite Hydrogels and Their Biomedical Applications. *IEEE Journal of Selected Topics in Quantum Electronics*. January 28, 2019, pp 154–174.
- (9) Satarkar, N. S.; Biswal, D.; Hilt, J. Z. Hydrogel Nanocomposites: A Review of Applications as Remote Controlled Biomaterials. *Soft Matter* **2010**, *6* (11), 2364–2371.
- (10) Banerjee, H.; Suhail, M.; Ren, H. Hydrogel Actuators and Sensors for Biomedical Soft Robots: Brief Overview with Impending Challenges. *Biomimetics*. September 1, 2018, p 15.
- (11) Zhao, Y.; Xu, Z.; Niu, H.; Wang, X.; Lin, T. Magnetic Liquid Marbles: Toward “Lab in a Droplet.” *Adv. Funct. Mater.* **2015**, *25* (3), 437–444.
- (12) Gunatilake, U. B; Venkatesan, M.; Basabe-Desmonts, L.; Benito-Lopez, F. Ex Situ and in Situ Magnetic Phase Synthesised Magneto-Driven Alginate Beads. *J. Colloid Interface Sci.* **2022**, *610*, 741–750.
- (13) Kim, S.; Regitsky, A. U.; Song, J.; Ilavsky, J.; McKinley, G. H.; Holten-Andersen, N. In Situ Mechanical Reinforcement of Polymer Hydrogels via Metal-Coordinated Crosslink Mineralization. *Nat. Commun.* **2021**, *12* (1), 1–10.
- (14) Boselli, L.; Pomili, T.; Donati, P.; Pompa, P. P. Nanosensors for Visual Detection of Glucose in Biofluids: Are We Ready for Instrument-Free Home-Testing? *Materials*. April 2, 2021, p 1978.
- (15) Kersaudy-Kerhoas, M.; Sollier, E. Micro-Scale Blood Plasma Separation: From Acoustophoresis to Egg-Beaters. *Lab Chip* **2013**, *13* (17), 3323–3346.
- (16) Park, C.; Kim, H. R.; Kim, S. K.; Jeong, I. K.; Pyun, J. C.; Park, S. Three-Dimensional Paper-Based Microfluidic Analytical Devices Integrated with a

- Plasma Separation Membrane for the Detection of Biomarkers in Whole Blood. *ACS Appl. Mater. Interfaces* **2019**, *11* (40), 36428–36434.
- (17) Li, H.; Steckl, A. J. Paper Microfluidics for Point-of-Care Blood-Based Analysis and Diagnostics. *Analytical Chemistry*. January 2, 2019, pp 352–371.
- (18) Park, C.; Kim, H. R.; Kim, S. K.; Jeong, I. K.; Pyun, J. C.; Park, S. Three-Dimensional Paper-Based Microfluidic Analytical Devices Integrated with a Plasma Separation Membrane for the Detection of Biomarkers in Whole Blood. *ACS Appl. Mater. Interfaces* **2019**, *11* (40), 36428–36434.
- (19) Dai, J.; Zhang, H.; Huang, C.; Chen, Z.; Han, A. A Gel-Based Separation-Free Point-of-Care Device for Whole Blood Glucose Detection. *Anal. Chem.* **2020**, *92* (24), 16122–16129.
- (20) Mahshid, S.; Askari, M.; Ghamsari, M. S. Synthesis of TiO₂ Nanoparticles by Hydrolysis and Peptization of Titanium Isopropoxide Solution. *J. Mater. Process. Technol.* **2007**, *189* (1–3), 296–300.
- (21) Schneider, C. A.; Rasband, W. S.; Eliceiri, K. W. NIH Image to ImageJ: 25 Years of Image Analysis. *Nat. Methods* **2012**, *9* (7), 671–675.
- (22) Braccini, I.; Pérez, S. Molecular Basis of Ca²⁺-Induced Gelation in Alginates and Pectins: The Egg-Box Model Revisited. *Biomacromolecules* **2001**, *2* (4), 1089–1096.
- (23) Kauppila, A.; Karmenyan, A.; Kinnunen, M.; Myllylä, R. Effect of the Size and Shape of a Red Blood Cell on Elastic Light Scattering Properties at the Single-Cell Level. *Biomed. Opt. Express*, Vol. 2, Issue 7, pp. 1803-1814 **2011**, *2* (7), 1803–1814.
- (24) Turco, G.; Donati, I.; Grassi, M.; Marchioli, G.; Lapasin, R.; Paoletti, S. Mechanical Spectroscopy and Relaxometry on Alginate Hydrogels: A Comparative Analysis for Structural Characterization and Network Mesh Size Determination. *Biomacromolecules* **2011**, *12* (4), 1272–1282.
- (25) Erickson, H. P. Size and Shape of Protein Molecules at the Nanometer Level Determined by Sedimentation, Gel Filtration, and Electron Microscopy. *Biol. Proced. Online* **2009**, *11* (1), 32–51.

- (26) Zhang, P.; Sun, D.; Cho, A.; Weon, S.; Lee, S.; Lee, J.; Han, J. W.; Kim, D. P.; Choi, W. Modified Carbon Nitride Nanozyme as Bifunctional Glucose Oxidase-Peroxidase for Metal-Free Bioinspired Cascade Photocatalysis. *Nat. Commun.* **2019**, *10* (1), 1–14.

Magneto Twister: Magneto deformation of water-air interface by a superhydrophobic magnetic nanoparticles layer

This Chapter is partially reproduced from:¹

Gunatilake, U. B.; Morales, R.; Basabe-Desmonts, L.; Benito-Lopez, F. Magneto Twister: Magneto Deformation of the Water–Air Interface by a Superhydrophobic Magnetic Nanoparticle Layer., *Langmuir*, 2022, 38 (11), 3360–3369.

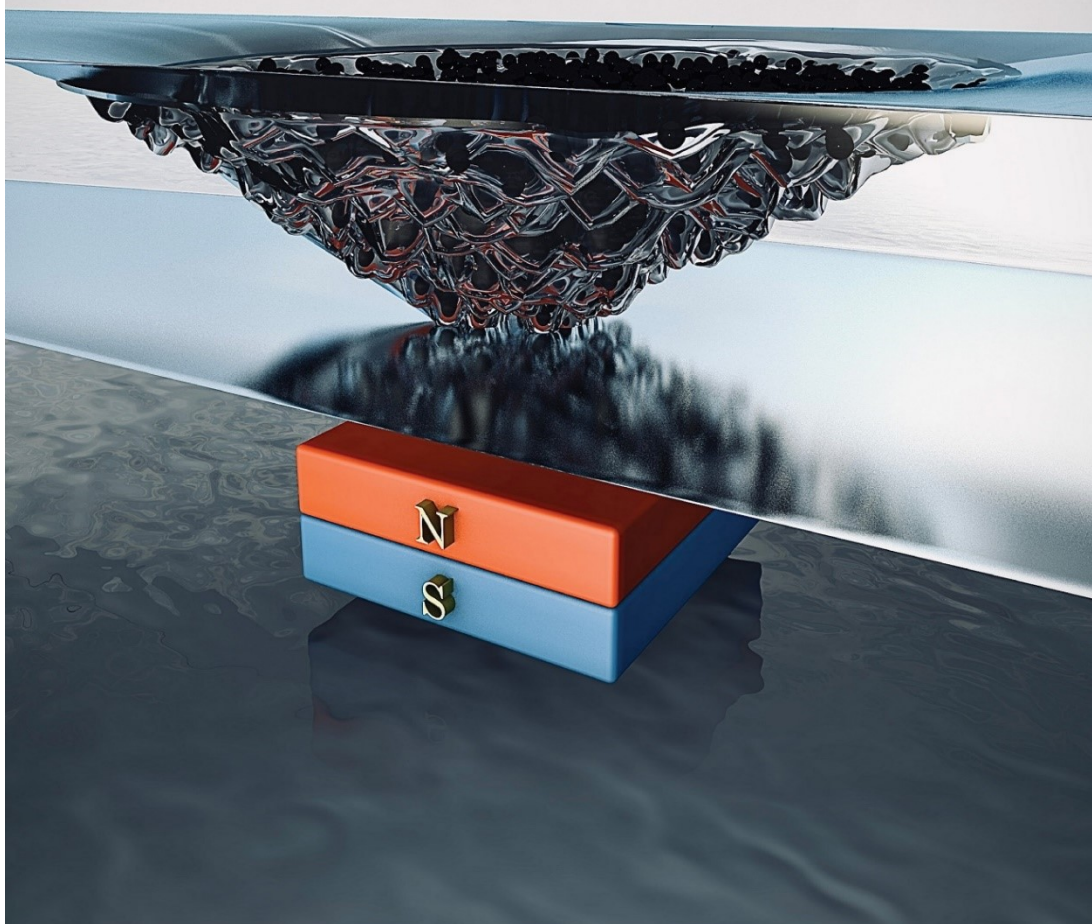
<https://doi.org/10.1021/acs.langmuir.1c02925>

March 22, 2022 Volume 38, Number 11

pubs.acs.org/Langmuir

LANGMUIR

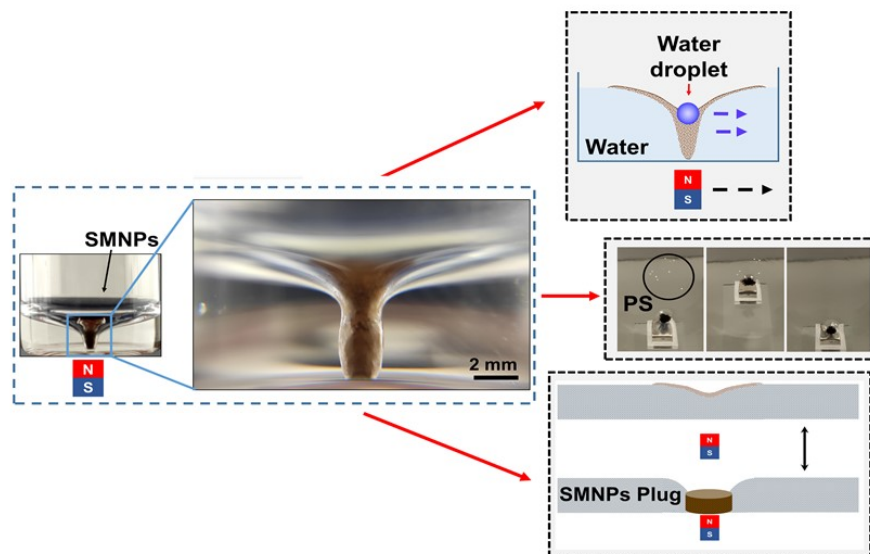
The ACS journal of fundamental interface science



 ACS Publications
Most Trusted. Most Cited. Most Read.

www.acs.org

Abstract. Remote manipulation of superhydrophobic surfaces provides fascinating features in water interface related applications. A superhydrophobic magnetic nanoparticles colloid layer is able to float on the water-air interface and to form a stable water-solid-air interface due to its inherent water repulsion, buoyancy and lateral capillarity. Moreover, it easily bends downwards, under an externally applied gradient magnetic field. Thanks to that, the layer creates a stable twister like structure with a flipped conical shape, under controlled water levels, behaving as a soft and elastic material that proportionally deforms with the applied magnetic field and that it goes back to its initial state in the absence of the external force. When the tip of the twister structure touches the bottom of the water container, provides a stable magneto movable system, which has many applications in the microfluidic field. We introduce, as a proof of principle, three possible implementations of this structure in real scenarios, the cargo and transport of water droplets in aqueous media, the generation of magneto controllable plugs in open surface channels, and the removal of floating micro plastics from the air-water interface.



6.1 Introduction

Inspired by natural water repellent materials like lotus leaf, researchers have investigated and developed interesting superhydrophobic surfaces.²⁻⁴ The general principles of the Superhydrophobicity is discussed in Chapter 2, section 2.7.3.

The integration of magnetic properties into superhydrophobic materials or *vice versa*, promotes remote manipulation of the material while repelling water, providing new insights for potential applications. In literature, magnetic phase reinforced nanocomposites have been developed. For instance, magneto responsive foams, which were fabricated by introducing magnetic nanoparticles to bulk polymer matrices, were reported to remove organic contaminants from water.^{5,6} Moreover, a magnetic elastomer with a superhydrophobic surface was developed for droplet movement⁷ and to switch their dynamic wetting features.⁸ Droplets were manipulated by a local deformation of the surface of the elastomer activated by magnetic field.⁷ Recently, ferrofluid infused laser-ablated microstructured surfaces have been introduced to manipulate gas bubbles in a programmable manner, under magnetic field.⁹ Interestingly, a superhydrophobic magnetic micro cilia array surface was recently reported to manipulate water droplets in air and oil droplets in water.¹⁰

On the other hand, exclusively nano/micro magnetic superhydrophobic particles have gained special consideration among researchers because of their easy manipulation, low remanence and applicability at the micro scale. In this regard, bare superparamagnetic $\text{Fe}_3\text{O}_4/\gamma\text{-Fe}_2\text{O}_3$ nanoparticles and ferromagnetic Fe particles, functionalised with molecules that generate low surface energies as mentioned in Chapter 2, section 2.7.4, are directly applied, without the need to be incorporated into a bulk polymer or ceramic matrix. By using this strategy, magnetic superhydrophobic particles were used to form magnetic liquid marbles, a non-adhesive droplets coated with nano/micro low surface energy magnetic particles, that show extremely low friction when rolling or sliding on solid substrates.¹¹ The properties and the applications of the magnetic liquid marbles were discussed in Chapter 2, section 2.7.5. The state of art the exclusive magnetic superhydrophobic particles and the currently available particles systems are deeply discussed in Chapter 2, section 2.7.

In the present study, we investigate the deformation of a synthesised superhydrophobic and magnetic iron oxide nanoparticles (SMNPs) layer – water interface. The floating

SMNPs layer, bended downwards, forming a manageable and stable water-solid-air interface under an applied magnetic field. The layer formed a flipped conical spike (CS), similar to a storm twister, with the spike structure touching the depth of the water container, using controlled water levels. This system was characterised and used for the transportation of water droplet in aqueous media, as a magnetic plug for liquid partition in open surface channels and to remove microplastics on water surfaces.

6.2 Experimental

6.2.1 Synthesis of superhydrophobic magnetic particles

First, a 0.5 M ferric solution was prepared by dissolving 2.71 g of $\text{FeCl}_3 \cdot 6\text{H}_2\text{O}$ (> 99 %, Sigma-Aldrich, Spain) in 20 mL of distilled water and a 0.5 M ferrous solution was prepared by dissolving 1.39 g of $\text{FeSO}_4 \cdot 7\text{H}_2\text{O}$ (> 99 %, Sigma-Aldrich, Spain) in 10 mL distilled water. Then, 30 mL $\text{Fe}^{3+}/\text{Fe}^{2+}$ ($\text{Fe}^{3+}:\text{Fe}^{2+}$, 2:1) solution (deoxygenated) was added drop by drop in a 40 mL 1 M NaOH (> 98 %, Sigma-Aldrich, Spain) solution kept at 40 °C under vigorous stirring and N_2 atmosphere.¹² A black precipitate was immediately formed. Then, the precipitate was heated at 90 °C for 30 min. After that, the precipitate was separated from the solution with a magnet and washed 3 times with distilled water. Finally, the Fe_3O_4 nanoparticles were dried by rotary evaporation at 40 °C, under vacuum. Next, 1.8 mL of triethoxy(octyl)silane (97 %, Sigma-Aldrich, Spain) was mixed with 50 mL of absolute ethanol (Sharlau, Spain) for 2 h under 50 °C. Then, a sonicated suspension of presynthesised 0.53 g of Fe_3O_4 nanoparticles in 10 mL absolute ethanol was added to the triethoxy(octyl)silane/ethanol solution and stirred for 2 h. Later, the particles were separated with a magnet and thoroughly washed with ethanol for 3 times.¹³ Finally the particles were heated at 120 °C for 2 h to obtain SMNPs.

6.2.2 Magneto deformation of SMNPs confined water-solid-air interface

4 mg of the synthesised SMNPs were sprinkled on the water surface (1 mL water in a glass vial of 5 mL). The gradient magnetic field was supplied by changing the vertical distance (z) between the depth bottom of the glass vial and the NdFeB permanent magnet (cubic 10 mm magnet, 495 mT). The magnetic field (B) was calculated by equation 6.1.¹⁴ Where, B_r is the remanence field, L is the length, W is the width and D the height of the magnet, and z is the distance from the magnet surface.

$$B = \frac{B_r}{\pi} \left\{ \arctan \left(\frac{L.W}{2z\sqrt{4z^2+L^2+W^2}} \right) - \arctan \left(\frac{L.W}{2(D+z)\sqrt{4(D+z)^2+L^2+W^2}} \right) \right\} \quad \text{equation-6.1}$$

The breaking of the conical spike was investigated by adding water to the glass vial at fixed magnetic fields: 350, 153 and 100 mT.

6.2.3 Water droplet transport on aqueous media

A water droplet of 5 μL was placed inside of the conical spike, formed by 10 mg of SMNPs in a container with water height of 6.3 ± 0.5 mm. The magnet was manually moved horizontally to shift the position of the conical spike together with the water droplet. The experiments were carried out using glass and PMMA substrate containers. Superhydrophobic Fe particles (commercially available Fe micro-particles (99.9 % Thermo Fisher, Spain) were treated with diluted HCl (0.25 M) for 10 min and coated with triethoxy(octyl)silane following the same protocol mentioned in section 2.1) and used as well to form the conical spike and water droplet transport experiments. The moving velocities of the magnet and of the magneto twister, with the water droplet, were tracked by video analysis, through the Image-J software coupled with the manual tracking plugin. This was used to track the motion of the magneto twister and the magnet within short time ranges, which allowed to obtain velocity values.

6.2.4 Magneto controllable plugs formation

For the plug experiments a 4 x 2 mm (height/width) open surface channel of 5 cm length, made in polymethylmethacrylate (PMMA), Goodfellow, Spain, with a glass microscope slide as the bottom surface, bounded together by a double side pressure sensitive adhesive (PSA) layer 380 μm (Adhesive Research, Ireland) was used. The PMMA layer was fabricated using a CO₂ Laser System (VLS2.30 Desktop Universal Laser System) equipped with a 10.6 μm CO₂ laser source ranging in power from 10 to 30 W.

The channel was filled with 350 μL of water and then a 2 mg of SMNPs was sprinkled on the open surface water interface. Finally, the magnetic plug was constructed by using the permanent 1 mm cubic magnet (~ 397 mT). The two liquid partitions were coloured using a water-based dye to demonstrate the absence of leaking from the plug. The liquid was withdrawn, by a pipette, in one of the partitions to check the effect of the SMNPs plug.

In order to check there was not any leaking when using the plug, 60 μL of a 31 mM phenolphthalein water solution and 60 μL of a 1M NaOH solution were added to the two generated compartments.

6.2.5 Removal of floating microplastics from the water interface

Polystyrene (PS) microparticles (diameter 0.5-1.0 mm) were suspended in a half-filled glass petri dish ($h = 8.0 \pm 0.5$ mm) and 4 mg of SMNPs was sprinkled on the water surface. The twister shape was formed under the magnetic field (105 mT) and the permanent magnet was moved towards the polystyrene particles. The PS particles were attracted to the twister shape and collected. The twister shape was moved, under a fixed magnetic field, over the surface of the petri dish to collect the PS particles.

6.2.6 Characterisation

The equipment details of the TEM, FTIR, XRD, Raman spectra are mentioned in section 4.2.1 and 3.2.3. Magnetization measurements for the iron oxide nanoparticles and the dehydrated beads were carried out in a 5 T Quantum Design MPMS XL-5 (SQUID) magnetometer at room temperature.

A layer of particles was coated to a PSA tape to obtain the contact angle of the particle layer. Contact angles were measured by DataPhysics OCA 15EC drop shape analyser and the surface energies were obtained by the Owens, Wendt, Rabel and Kaelble (OWRK) model. The images and the videos were recorded by Sony IMX586 Exmor RS 48 megapixel lens with 12X macro lens. The videos and the images were analysed by Image-J software and the particle tracking was done by the manual tracking Image-J plugin.

6.3 Results and Discussion

6.3.1 Synthesis and characterisation of the superhydrophobic magnetic particles

The synthesised low surface energy SMNPs were characterised by Fourier-transform infrared spectroscopy (FTIR), X-ray diffraction analysis (XRD), Raman spectroscopy, Transmission electron microscopes (TEM), Superconducting quantum interference device (SQUID) magnetometer and goniometer.

The Fe_3O_4 nanoparticles were synthesised by the co-precipitation of ferrous and ferric ions under high pH conditions according to reaction-3.1.

The surface energy of the synthesised nanoparticles was reduced by chemically coating the Fe₃O₄ NPs with triethoxy(octyl)silane, as mentioned below. The possible chemical structure of the SMNPs is illustrated in Figure 6.1a, top.

The FTIR spectra of both modified SMNPs and non-modified NPs were analysed in order to investigate the binding of the alkyl chain *via* silane group, Figure 6.1b. The C-H stretching vibrational peaks at 2850, 2900, 2960 cm⁻¹ and Si-CH alkyl group bending vibrational peak at 1457 cm⁻¹ in SMNPs FTIR spectrum, confirmed the presence of the alkyl chain within the SMNPs.¹⁵ Moreover, the stretching vibrational peaks at 860, 990 cm⁻¹ in the SMNPs spectrum were assigned to Si-C, Si-O-Fe bonds respectively, demonstrating the binding of the alkyl chain through the silane group to the NP surface.¹⁵⁻¹⁷ The common peaks of Fe-O stretching, residual water OH stretching and bending were found in both modified and non-modified NPs at the positions of 576/580 cm⁻¹, 3425/3400 cm⁻¹ and 1620 cm⁻¹.¹⁵ However, the intensity of the O-H peaks was reduced in the SMNPs spectrum due to the hydrophobic alkyl groups, inhibiting the absorption of residual water to the surface of the NP.

The wetting properties of both types of the particles were characterised by the static contact angles (CA) of the particle layers, Figure 6.1a, bottom. Bare NPs exhibited a superhydrophilic nature, by instantly absorbing the water droplet, showing nearly 0 ° water contact angle. Surface absorbed hydroxyl groups possess a high affinity to interact with water due to polar-polar attractions between water and pristine magnetic nanoparticles. However, the alkyl chain modified particles, exhibited superhydrophobic properties by showing a ~ 152.0 ° static water contact angle with a low surface energy, 11.85 mJ m⁻². The non-polar octyl-alkyl long hydrocarbon chain repels water molecules by the non-favourable attraction forces occurring between the carbon long chain and water molecules.

Then, the iron oxide phase of both SMNPs and non-modified NPs were characterised by the XRD and Raman spectroscopy, see Figure 6.2. Maghemite phase contamination was found in the magnetite phase, in triethoxy(octyl)silane coated nanoparticles, due to the heat treatment at the coating process. In addition, a non-perfect spherical shape was obtained in both NPs types with 10.8 nm and 9.1 nm particle sizes, respectively, see TEM images in Figure 6.3.

The magnetic properties of both types of NPs were characterised with the SQUID magnetometer as shown in the Figure 6.1c. The chemical modification on Fe₃O₄ NPs cost to drop the saturation magnetization down to 57 Am² Kg⁻¹ from 62 Am² Kg⁻¹. Both types of NPs exhibited closely superparamagnetic behaviour at room temperature, but SMNPs showed lower coercivity and remanence values compared to bare NPs, due to their molecular coating, which reduced the aggregation of the NP, reduce the deviation from the ideal superparamagnetism. Nevertheless, the high saturation magnetisation of the nanoparticles reflected the possibility to be used for remote manipulation under low (< 0.5 T) magnetic fields.

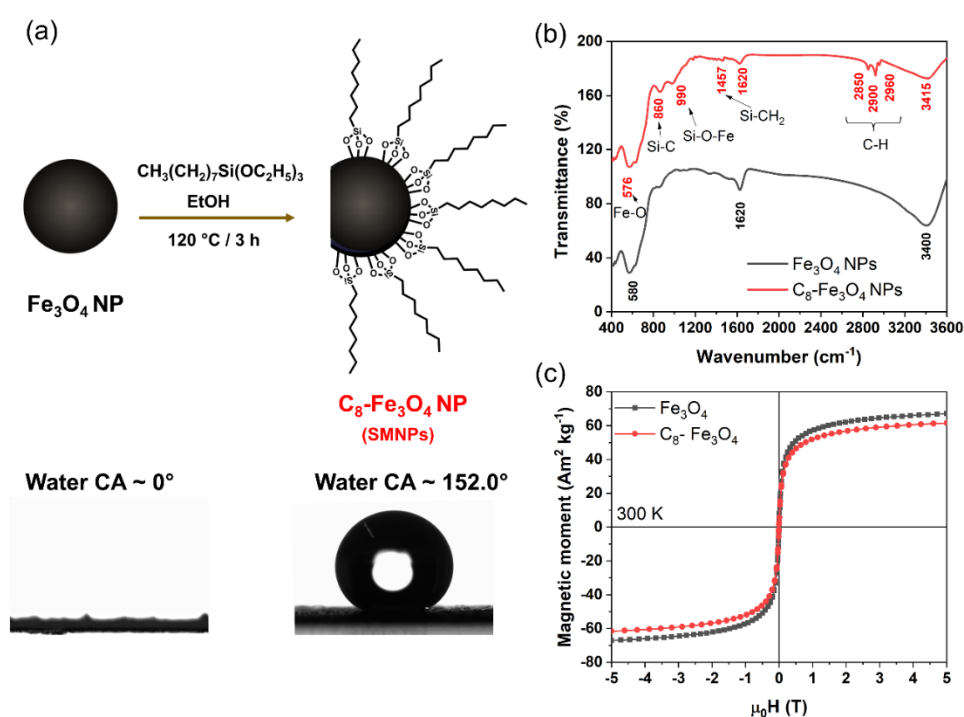


Figure 6.1. (a) Illustration of the chemical modification and the possible chemical structure of the modified SMNPs (C₈-Fe₃O₄), static water contact angles (CA) are shown under each type of particles (b) FTIR spectra and (c) SQUID analysis of the SMNPs (red) and non-modified NPs (black).

The phase of the synthesised iron oxide, both bare and the octyl alky chain coated iron oxide, was investigated by using XRD and Raman spectra. Conventional diffraction peaks related to the magnetite phase, were observed for both bare and octyl alky chain coated nanoparticles at $2\theta = 30.3^\circ/30.4^\circ$, $35.7^\circ/35.6^\circ$, $43.4^\circ/43.4^\circ$, $53.9^\circ/53.8^\circ$, $57.5^\circ/57.4^\circ$, and $63.0^\circ/63.0^\circ$ respectively, (JCPDS 01-088-0315)¹⁸ without showing any significant crystal deviation after triethoxy(octyl)silane coating, as depicted in

Figure 6.1a. Further, Raman spectra were analysed for the both type of particles as shown in Figure 6.1b, to distinguish the magnetite and the maghemite phases since they were not distinguishable by XRD analysis, since they both have the same XRD diffraction angles. The Raman peaks at 670 (strong) and 610 (weak) are attributed to the A_{1g} and T_{2g} Raman modes of the magnetite phase in Figure 6.2b, co-precipitated bare iron oxide nanoparticles. However, the magnetite A_{1g} mode split, and a peak at 702 (maghemite A_{1g} mode) appeared in the C_8 - Fe_3O_4 NPs. Moreover, the 310 magnetite peak was red shifted to 352, reflecting the oxidation of magnetite to the maghemite in the C_8 - Fe_3O_4 NPs, due to the heat treatment during the chemical modification process.¹⁹ This reveals a small amount of maghemite contamination in the chemically modified Fe_3O_4 nanoparticles.

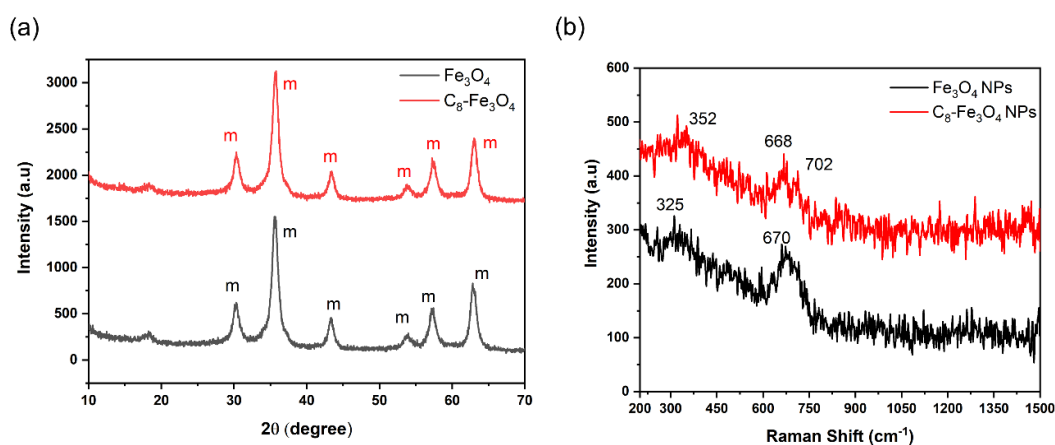


Figure 6.2. (a) XRD spectra (b) Raman spectra of the co-precipitated Fe_3O_4 nanoparticles and the chemically modified Fe_3O_4 nanoparticles (C_8 - Fe_3O_4).

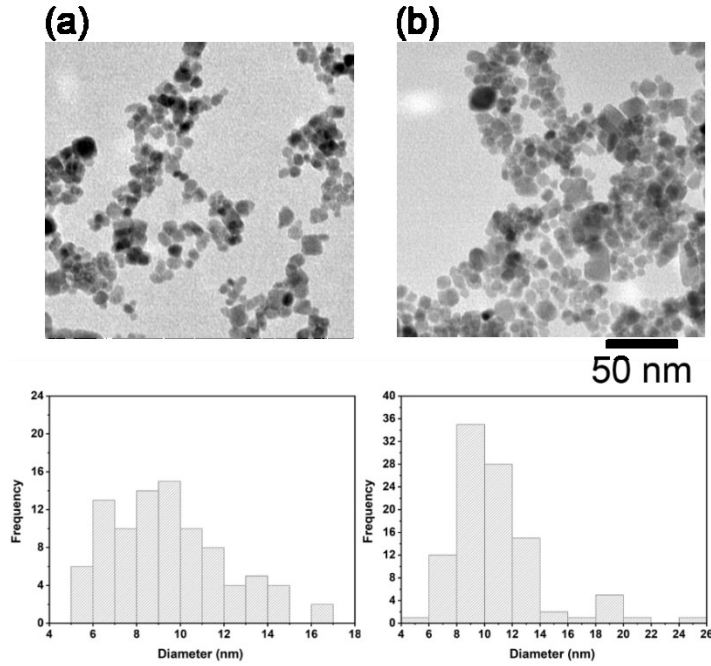


Figure 6.3. TEM images and particle size histograms of (a) co-precipitated Fe₃O₄ nanoparticles and (b) the chemically modified Fe₃O₄ nanoparticles.

6.3.2 Magneto deformation of the water-air interface

Co-precipitately synthesised iron oxide magnetic nanoparticles can be submerged and dispersed in a bulk water medium because of its higher specific gravity, high surface energy and the chemical hydrogen bond attraction between surface hydroxyl of the particles and the water. Nevertheless, long chain alkyl modified low surface energy SMNPs were found to float in water-air interface. Non-favourable attraction between non-polar carbon long chain and the water, avoids the immersing of the particles despite its higher specific gravity. Moreover, the buoyancy and the surface tension forces also contribute to that effect too, keeping the particles in floating state on the water surface, balancing the weight of the particles.²⁰ Aggregation and repulsion between the floating SMNPs are due to the induced lateral capillary forces between the particles, which cause a slight deformation of the particle-water interface (meniscus) being related to the wetting properties of the particle.²¹ As depicted in Figure 6.4, these floating superhydrophobic magnetic nanoparticles polarised under a gradient magnetic field (z direction), attracted towards the magnet by exerting a downwards magnetic force F_m on the magnetic nanoparticles colloid layer floating at the air-water interface. These magnetic forces on the particles are depended of the volume (V_m) of the particles, the difference in magnetic susceptibilities ($\Delta\chi$) of the medium and the magnetic particle

and the magnetic induction intensity (B) and its gradient (∇B), as shown in the equation 6.2.²²

$$F_m = \frac{V_m \Delta \chi}{\mu_0} (B \cdot \nabla) B \quad \text{equation-6.2}$$

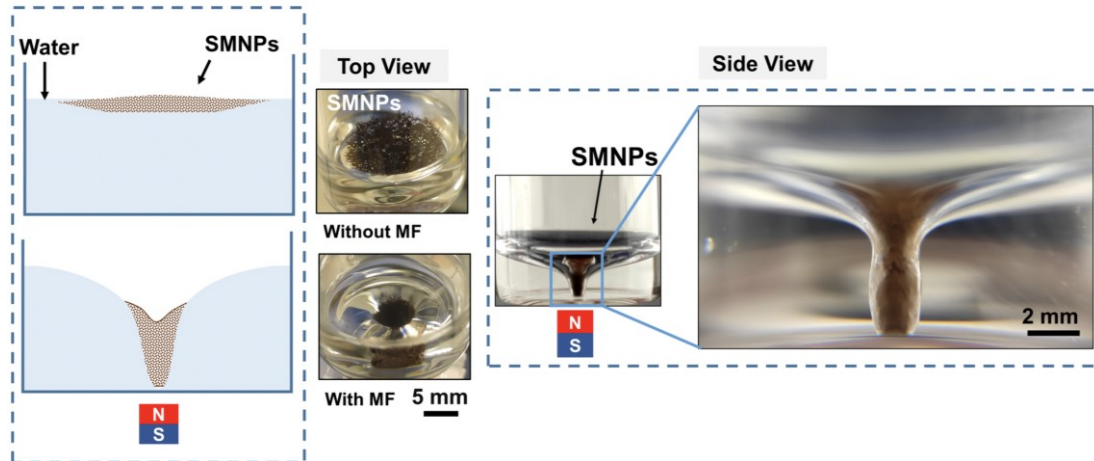


Figure 6.4. Deformation of the SMNPs layer on the water air interface, under a magnetic field (MF) of 42 mT. From left to right: schematic diagram of the formation of the twister, pictures of the top and side view of the magneto twister.

The floating superhydrophobic magnetic nanoparticles colloid layer incurves downwards forming a water-solid/water-air interface under the magnetic field, and the observed bending is more pronounced with the increase of the magnetic field value, see Figure 6.5a. This particle confined water interface deformation behaviour is higher than the Moses effect suffered by a diamagnetic liquid under a magnetic field.^{23,24} As presented in Figure 6.4, the solid-water interface touched the depth of the water container with the increment of the magnetic field, making a stable flipped conical structured water interface, with a twister like shape. However, it was appreciated that the SMNPs exhibited two states, over the water surface. As a monolayer of particles, attracted to the water interface under capillary forces, and as free SMNPs on top of the attracted monolayer at the end of the cone. Free SMNPs accumulated on the water interface at the highest magnetic flux density region (centre of the magnet), where the magnetic field is stronger. This increased particle density, rose the magnetic moment and inflicted an inclination of the magnetic force in the middle of the conical shape, modifying the structure, making it more concave. The variation of the distance (h) between the water-superparamagnetic superhydrophobic nanoparticle (4 mg) interface

and the floor of the glass vial, with the applied magnetic field, is depicted in Figure 6.5a. A rapid increment of the conical shape spike was observed over ~ 30 mT, coming with an abrupt decaying for the h value, see Figure 6.5b. Finally, at ~ 42 mT, the spike touched the glass surface and generated a stable twister shape configuration. Then, the horizontal remote translocation of the twister was investigated by changing the position of the permanent magnet but keeping a constant magnetic field (67 mT), see the captured images from a video in Figure 6.6.

When increasing the amount of magnetic nanoparticles in the system, for instance from 4 to 10 mg, a lower magnetic field was needed for the twister to touch the bottom of the glass vial. This can be explained considering the increment of the magnetic moment in the whole system. Figure 6.7a, shows that the required magnetic field dropped to 31 mT when increasing the particle amount up to 10 mg. In the case of the magneto twister formation, the magnetic force, as shown in the equation-6.2, acts as the main driving force to originate the magneto twister, and it depends on the amount of particles and the applied magnetic field gradient, for the same type of particles and tested water levels. Therefore, the required gradient magnetic field can be lowered (< 31 mT, at the surface of the water container) when using more than 10 mg of SMNPs, and can be raised (> 42 mT, at the surface of the water container) when using less than 4 mg of SMNPs. Nevertheless, it needs to be considered that the required gradient magnetic field is proportional to the height of the water layer in both, low and high concentration of particles.

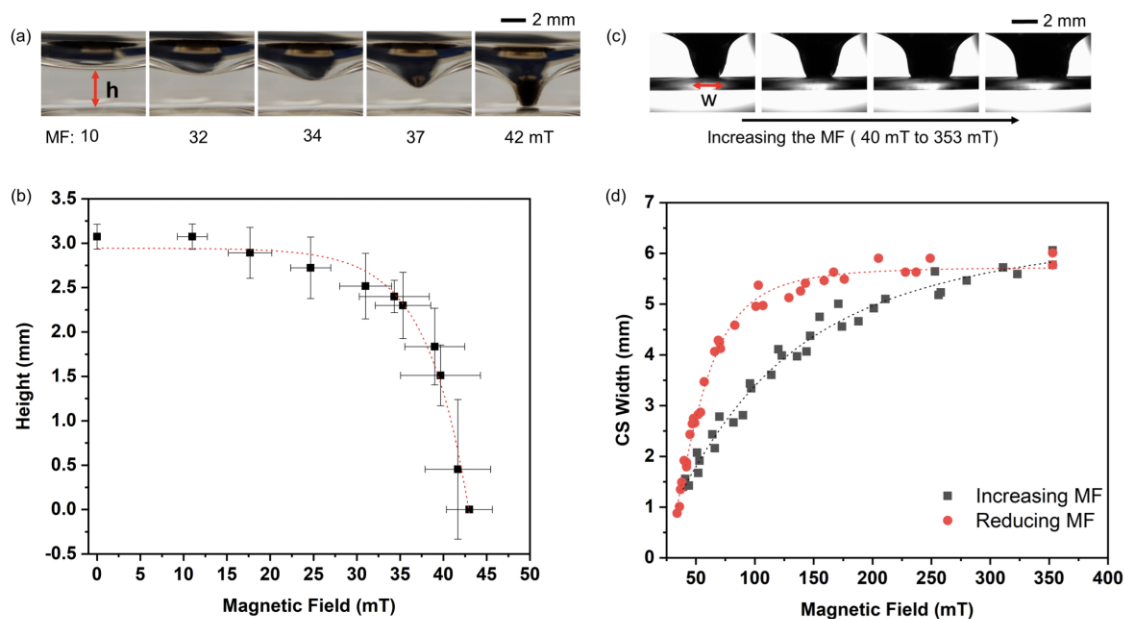


Figure 6.5. (a) Deformation of the SMNPs-water interface under the applied magnetic field. (b) Decay of the distance between the (4 mg) SMNPs-water interface and the bottom of the glass vial of 5 mL (1 mL water volume), $n = 3$. (c) Pictures of the CS at different magnetic fields (over 42 mT) and (d) hysteresis curve of the CS width values under an increasing (grey) and reduced (red) MF.

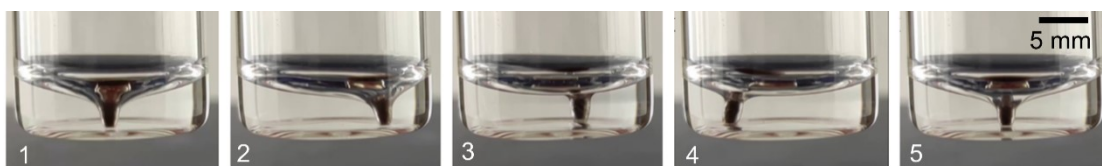


Figure 6.6. Captured images from a video of movement of the twister while changing the horizontal position of the permanent magnet. 1,5 initial position, 2-5 changing the horizontal position by following the magnet.

An interesting observation was a width enlargement of the tip of the CS, once the twister was formed, by increasing the magnetic field up to 353 mT, in both configurations (4 and 10 mg of SMNPs), see Figure 6.5c. Most of the monolayer of SMNPs, which was spread over the water surface by capillarity, travelled to the bottom of CS of the twister when increasing the magnetic field. Interestingly, they moved inclinable downwards on the water surface without leaving the surface due to the lateral capillarity force, keeping the twister shape even during horizontal remote translocation,

Figure 6.6. It is possible to observe that the SMNPs travelled on the water surface under the horizontal (x -direction) gradient magnetic field.

As explained above, the accumulation of SMNPs at the bottom surface of the vial brought an increase in the surface area of the CS of the twister and an enlargement of the width of the spike as depicted in Figure 6.5c. Therefore, the forward and reverse manipulation of the CS neck of the twister was possible by increasing or decreasing the strength of the MF, Figure 6.6d. Interestingly, a significant hysteresis on the width value of the CS was observed when comparing the increasing and the reducing magnetic field paths. This behaviour can be explained considering the adhesion forces between the SMNPs and the bottom of the glass vial, affecting the release of the SMNPs back to the water surface interface. Moreover, the magnetic dipole-dipole interaction could also affect the release process by keeping the particles in an aggregation state at high magnetic fields. However, the buoyancy and the upward surface tension forces start to dominate the movement of the SMNPs back to the previous shape once reducing the MF on the whole system. A higher amount of magnetic SMNPs (10 mg) led to an increase on the size of the width of the CS but it showed the same hysteresis trend, see Figure 6.7b. As well, the amount of the SMNPs directly affects the enlargement of the width in the CS while increasing the magnetic field, after the formation of the magneto twister. In this case, a lower saturation width (< 6.0 mm) and a higher saturation width (> 8.2 mm) are expected when using less than 4 mg or more than 10 mg of SMNPs, respectively.

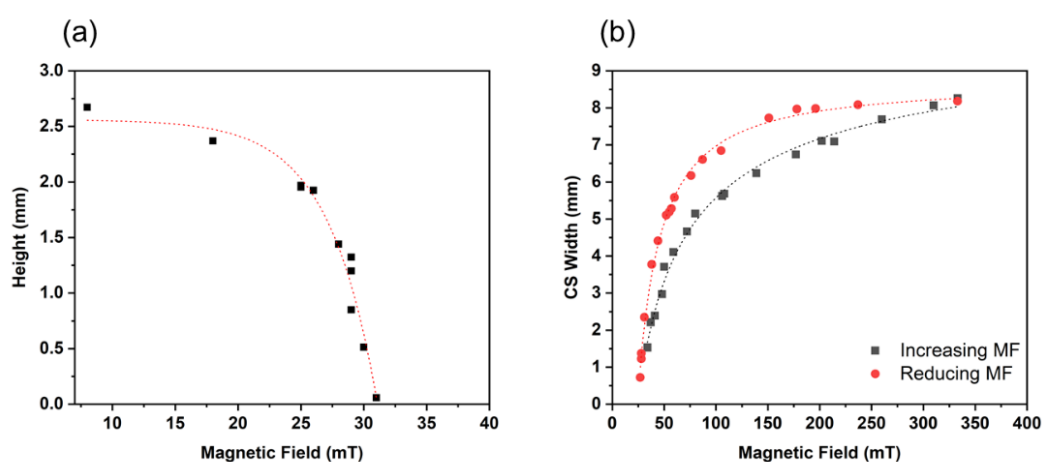


Figure 6.7. (a) Decay of the distance between the (10 mg) SMNPs-water interface and the bottom of the glass vial of 5 mL (1 mL water volume). (d) Hysteresis curve of the conical shape (CS) width values under an increasing (grey) and reduced (red) magnetic field (MF).

Further characterisation of the twister was done, as shown in the Figure 6.8, presented a kind of visible air column attached to the superhydrophobic SMNPs when in water, called plastron effect,^{25,26} which was observed in three different states. In state-1, at low MF, a visible plastron caused the air attraction on the superhydrophobic SMNPs. The inhomogeneous SMNPs layer enhanced the confinement of a thick and stable air layer between the SMNPs and the water surface. However in state-2, the higher MF promoted a more compact SMNPs layer, while increasing the width of the CS, incrementing then, the pressure between the SMNPs layer and the water interface and consequently hindering the visibility of the air plastron; similarly to the effect occurring in a Cassie-Baxter to Wenzel transition.²⁷ Finally in state-3, at even higher magnetic fields (MFs), the attraction of the SMNPs to the external magnet along with their high magnetic flux, promoted the accumulation of a highly visible air plastron layer around the SMNPs, agglomerated at the bottom of the CS of the twister.

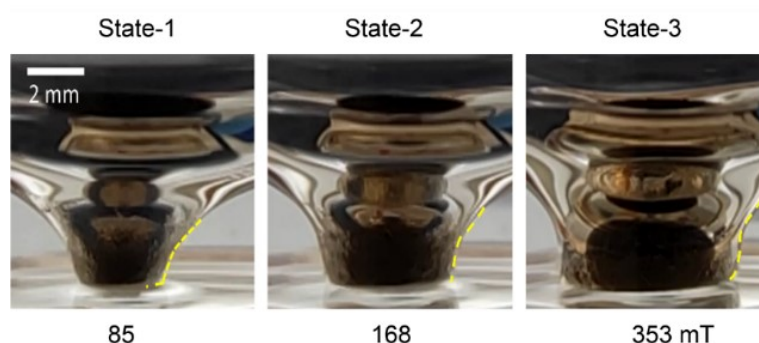


Figure 6.8. Visualisation and characterisation of the diffusion states of the air plastron in the CS of the twister, at different MFs. Broken yellow lines indicate the boundary of the water interface.

The disorder of the twister shape was investigated by increasing the water column in the glass vial under different MFs, Figure 6.9. Incremental amounts of water volumes were added to the vial containing 1 mL of water. The 4 mg of SMNPs were stable maintaining the twister shape at 350, 153 and 100 mT, Figure 6.9. At high MFs, 350 mT, the water-air interface over the CS obtained by the SMNPs tried to stretch itself, by repelling the superhydrophobic phase while adding the water, until complete failure, breaking the twister. At 350 mT, the SMNPs got firmly captured at the surface of the glass vial, getting the water-air interface (left and right water-air interfaces in the 2D side view), closer to each other, as explained above. After the addition of $120 \pm 12 \mu\text{L}$ of water, the water-air interface got fully disrupted and the SMNPs deposited at the bottom of the vial, capturing a bubble, thanks to the applied MF. Nevertheless, when lower MFs were applied, the SMNPs tempted to move upwards through the air-water

interface due to both, upward capillary and buoyancy forces promoted by the opposite lower MFs. In this case, the water intake threshold increased to $240 \pm 20 \mu\text{L}$ in 153 mT and up to $360 \pm 20 \mu\text{L}$ for 100 mT. At low MFs, the capillary and electrostatically attraction of the SMNPs layer on the water interface stretched vertically, reducing the CS diameter, in a more drastic way, when increasing the volume of water, in comparison to the high MFs experiments. As shown in the Figure 6.9c at MFs of 100 mT, the water-SMNPs layer interface was able to get closer to each other, generating narrower cones, while increasing the volume of water in the vial, without breaking the twister shape. This effect can be explained considering that lower magnetic forces affected in a less extend to the SMNPs layer at the top of the twister, leaving a more homogeneous water-SMNPs layer interface, generating more stable twister shapes, even when increasing the volume of water in the vial.

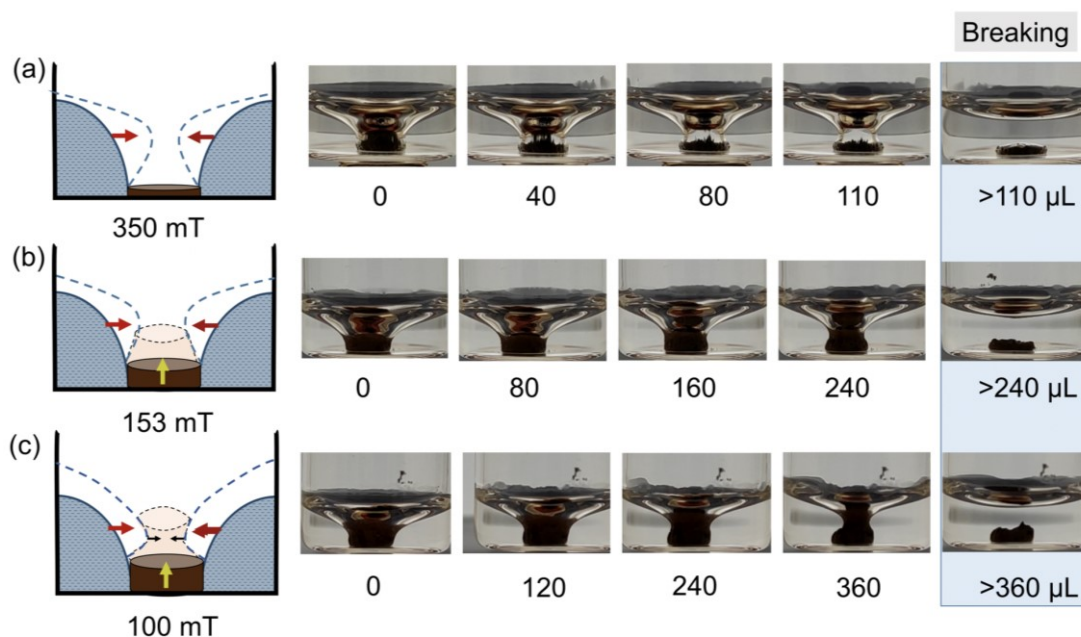


Figure 6.9. Characterisation of the disruption of the CS shape during the addition of water to the twister under different magnetic fields (a) 350 mT, (b) 153 mT and (c) 100 mT.

6.3.3 Water droplet transport on aqueous surface

In digital microfluidics, remote-stimuli movement of micro droplets plays an important role, by handling small volumes of liquids. For instance, Yan Zhao *et al.*¹¹ reported the manipulation of a magnetic liquid marble, a liquid droplet encapsulated by superhydrophobic and magnetic Fe_3O_4 nanoparticles (NPs), to handle discrete volumes

of liquids on a solid surface.²⁸ Both magnetic liquid marbles and the introduced magneto twister operate by water-air interfaces adhered with superhydrophobic magnetic nanoparticles, while an extra amount of energy is utilised in the magneto twister formation. However, the magnetic field induced formation of the magneto twister system facilitates to bend the water-air interface adjacent to the magnetic particles-water interface by introducing a flipped conical structure, separating water-air interfaces beside the magneto twister. This twister formation facilitates additional characteristics such as the bending of the water-air interface, and the tunability of the dimensional parameters of the twister and the substrate solid-magneto twister surface area. These improve the applicability of the twister in both bulk water phases and discrete water droplets, when compared to magnetic liquid marbles. Moreover, for magnetic droplet manipulation, the magnetic liquid marbles show an unstable behaviour while transporting the marbles due to friction and handling forces. In this regards, Mei Kum Khaw *et al.*¹⁴ reported a magnetically actuated floating liquid marble on a water surface to transport the droplet with a minimum friction force, when compared to solid surfaces. However, careful handling is required to manipulate magnetic liquid marbles. For instance, the magnetic shell easily opens by tiny external forces resulting on the mix of the droplet contents with the bulk liquid, smashing the droplet manipulation system. In this regard, our twister system can improve the manipulation of liquid droplets over water surfaces without breaking the system under the unexpected handling forces. The twister structure was able to hold a water droplet over the CS without leaking or losing its volume over time, Figure 6.10a. The droplet was stabilised on the surface of the SMNPs layer and could be transported through the surface using the movement of the external permanent magnet as illustrated in Figure 6.10b. The top view and the side view of the Figure 6.10b show the transport of a water droplet in a water environment, while moving the droplet under a 149 mT magnetic field. At low MFs (< 42 mT, for this particular system), the water droplet sat on the CS of the twister, which is not touching the surface of the water container. In this case, zero friction between the spike and the water surface was anticipated. However, at this state the whole system presented low stability, while moving the permanent magnet, and the droplet easily collapsed to the bulk aqueous system. However, at higher magnetic fields (> 118 mT, for this particular system), the water droplet was stable, moving over the water surface due to the robust and well packed SMNPs layer under the magnetic field.

In contrast, the friction between the CS of the twister and the surface of the water container surface was found to be high, affecting the droplet movement performance. It was observed that the movement of the droplet was regulated by the adhesion force between the SMNPs layer and the container surface. In order for the system to be useful for droplet manipulation, the effect on the translocation of a water droplet was investigated for two different surfaces, a glass (hydrophilic) and a polymethyl methacrylate (PMMA) (less hydrophilic) surface. The moving velocity of the twister structure carrying a water droplet and the driving velocity of the permanent magnet during the translocation process were monitored. When using the glass surface, Figure 6.10c, nearly same average magnet driving (7.64 mm s^{-1}) and droplet moving (7.91 mm s^{-1}) velocities were observed, showing low friction due to the low adhesion force between the glass surface ($\sim 58.40 \text{ mJ m}^{-2}$, surface energy) and the low surface energy of the SMNPs layer of the twister. On the other hand, when using a PMMA surface, the droplet was moved along the surface, but at a certain moment, the droplet collapsed and mixed with the bulk, as shown in the blue vertical line in the Figure 6.10d. The high surface adhesion force between the SMNPs layer and the PMMA surface (surface energy $\sim 41.21 \text{ mJ m}^{-2}$) resulted on the deposition of the NPs coming from the CS on the PMMA surface, destroying the SMNPs layer structure during the movement of the twister.

However, this behaviour was avoided by using superhydrophobic Fe particles, which have a higher saturation magnetisation, $220 \text{ Am}^2 \text{ Kg}^{-1}$, (3.9 times higher magnetisation than SMNPs) as shown in Figure 6.10e. The higher magnetic forces of these particles attracted more firmly to the moving magnet and overcame the high adhesion force between the particles and the PMMA surface, recovering a stable droplet manipulation system. Therefore, the stable droplet manipulation in water was possible by manipulating the surface energy, the magnetic force applied and the chemistry of the particle system forming the twister. This has specific implications on efficient transportation of aqueous based reactive droplets inside of an aqueous medium in a controllable way, in the same compartment without merging two miscible aqueous liquid phases. These findings could provide with a solution to reduce the instability of remotely stimuli magnetic liquid marbles.

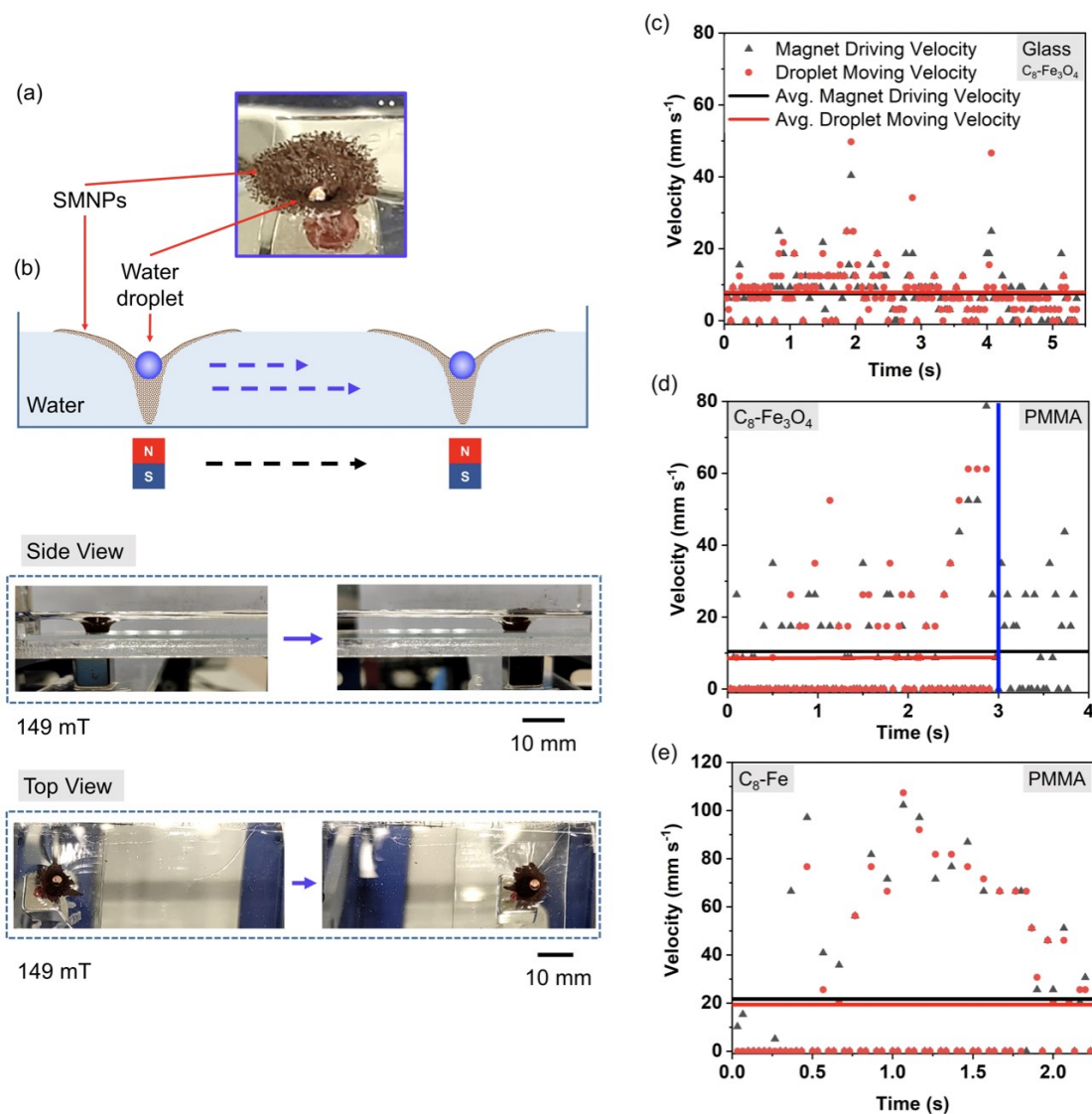


Figure 6.10. (a) Image of the twister carrying a water droplet of 5 μL (top view). (b) Schematic diagram of the water droplet movement on water surface under the displacement of an applied gradient magnetic field. Side view of the movement of a water droplet over the twister, in aqueous environment under 149 mT. Top view of the movement of a water droplet over the twister, in aqueous environment under 149 mT (horizontal translocation of z direction magnetic field). Velocity profiles for the movement of the droplet (red dots) and the permanent magnet (black triangles) by using the SMNPs twister for (c) a glass surface, (d) a PMMA surface in and (e) by using the superhydrophobic Fe particles twister for a PMMA surface in water.

6.3.4 Magneto controllable plugs

Remotely controllable plugs and valves are promising tools to be applied in Lab-on-chip technology. In this regard, magnetic particles with different functionalities have

been used as plugs to analyse biomarkers,^{29,30} magnetic particle impregnated hydrogels as valves³¹ and plugs³² and magnetic particles stabilised liquids (ferrofluids) as valves to change the direction of flow.³³ Interestingly, the deformation of the superhydrophobic magnetic particle-water interface system, can be easily applied for the generation of plugs in open channels, see scheme in Figure 6.11a. The water SMNPs interface deformed to form the twister in the middle of the open channel under an applied MF. By increasing the value of the MF, the SMNPs compacted at the bottom of the channel keeping the twister structure and thus, forming a superhydrophobic plug, separating the liquid in two independent partitions, see picture in Figure 6.11b. The switching of the MF off allowed releasing the particles from the bottom of the channel, bringing them back to the water surface, removing the magnetic plug. Liquid separation was achieved in the channel by the formation of an elongated meniscus, attached to the SMNPs. In another experiment, as depicted in Figure 6.11c, two different liquids (red and blue) were independently stored by the plug, avoiding liquid leakages, mixing or diffusion. Moreover, the stability of the plug was investigated in order to demonstrate that it was possible to reduce the volume in one of the containers, acting as an independent liquid reservoir. By removing liquid from one of the reservoirs, the formation of a non-equivalent meniscus level in both sides of the plug demonstrated the sealing capacity of the plug under the magnetic field. The liquid in the right-side partition (colourless) of the plug was successfully removed (~ 30 % of its volume) by creating a negative flow pressure on the right side of the channel, see Figure 6.11d. No diffusion was observed from the red colour liquid, left, to the right side of the plug was observed.

Moreover, to further demonstrate the perfect separation of the water partitions, a NaOH solution at pH ~ 12.5, colourless, and a solution containing phenolphthalein at pH ~ 6-7, colourless, were separated by the twister structure, Figure 6.11e. After 30 min, no purple/pink colour (colour of the phenolphthalein in basic media) was observed in the surroundings of the partition, demonstrating that the twister prevent leaking or diffusion of the liquids in the partitions. Moreover, the removal of the MF facilitated the mix of the two solutions when releasing the plug, allowing the formation of the purple/pink colour in less than 5 min, Figure 6.11f. This allow the use of these type of switchable plugs for the formation of independent reaction chambers in open channels, which can

be independently manipulated and transformed. The observed effect has important applications in microfluidic devices.

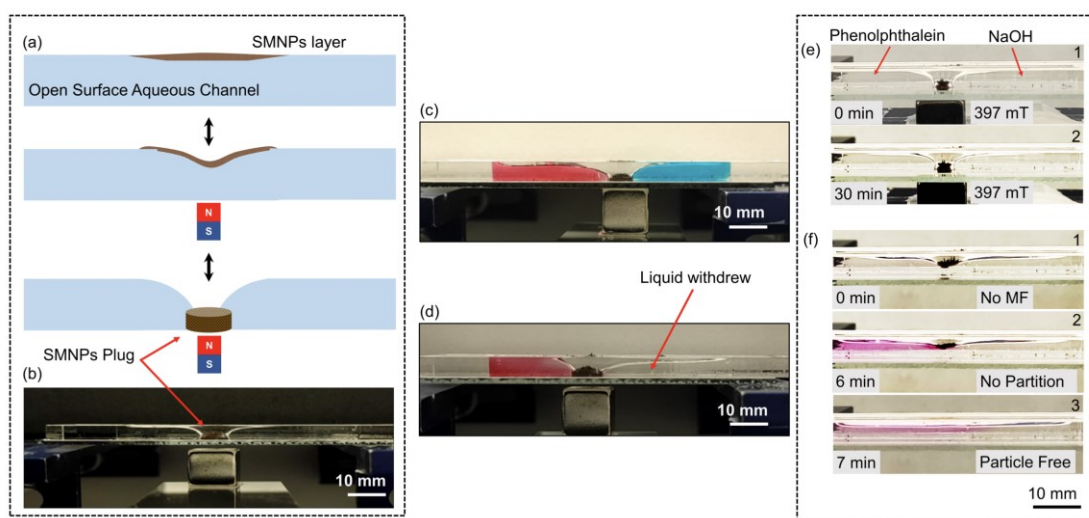


Figure 6.11. (a) Schematic illustration of the formation of the plug. (b) Picture of the magnetic plug in an open surface PMMA channel. (c) Picture showing two different colours of liquid at both sides of the plug, demonstrating the absence of leaking or diffusion after partition. (d) Picture of the open channel after withdrawing some liquid from the right side partition. (e) Pictures of a partition of phenolphthalein (pH indicator) and NaOH solutions by the magnetic plug. (f) Pictures of the removal of the plug by removing the magnetic field, observing the mixing of the two partitions, visually indicated by the formation of the purple/pink colour of the phenolphthalein in alkaline media.

6.3.5 Removal of floating microplastics using the twister from the water interface

The presence and accumulation and floating microplastics in natural waters is a harmful situation that leads to the pollution of the water resources.³⁴ Therefore, to treat and manipulate contaminated water-air interfaces is urgent and needs to be properly addressed. Microplastics contamination is expected as well in miniaturised devices, coming from the fabrication processes of the devices, thus cleaning them by a remote stimulus will provide no additional steps to the process. In this regard, magneto manipulation of the water-air interface deformation by the SMNPs layer could be applied to collect and remove microplastics from the water surface. In order to proof this assumption, polystyrene (PS) particles sprinkled over the water surface of a half-filled glass petri dish, were used as a proof of concept of a “contaminated” water surface. Then, 4 mg of SMNPs were sprinkled at 12.5 mm far from the PS particles. It

was observed that the SMNPs did not attract the PS particles. The PS particles remained static without moving towards to the SMNPs layer, keeping their velocity nearly 0 mm s^{-1} as shown in the Figure 6.12a (MF off). After 5 s, the magnet was approached to the SMNPs layer (100 mT), forming the twister shape structure (MF on), as explained above, activating the water interface deformation, CS, as in Figure 6.4. At that moment, a PS microparticle started to move towards the twister (see the set of pictures in Figure 6.12a), starting to accelerate towards the twister and getting a maximum speed of 47.8 mm s^{-1} just before getting adsorbed by the CS. The trajectory of the PS particle is shown in the Figure 6.12a inset images (right side), in real time, starting with a slow and random movement, which increases velocity when approaching to the centre of the CS. The twister formed a steep water-air interface, which provided a sort of a slide configuration for the particle to move towards to the centre of the twister. Moreover, the lateral capillary forces and the Van der Waals forces between the SMNPs and the PS microparticle acted as interacting forces accelerating the movement of the particle.³⁵

Considering this finding, the translocation of the twister, using the external magnetic field, was used to capture the non-magnetic PS particles present at the surface of the water by just moving the permanent magnet and so the twister. Figure 6.12b shows a set of images, taken from a video, of the movement of the twister, capturing multiple PS microparticles. By moving the twister around the water surface, all the PS microparticles can be easily collected since they hold to the SMNPs of the twister by the lateral capillarity and Van der Waals forces while displacing the magnetic twister. Therefore, this novel strategy provides an easy and cheap technique to remove water surface contaminated plastic particles by using the magnetic twister.

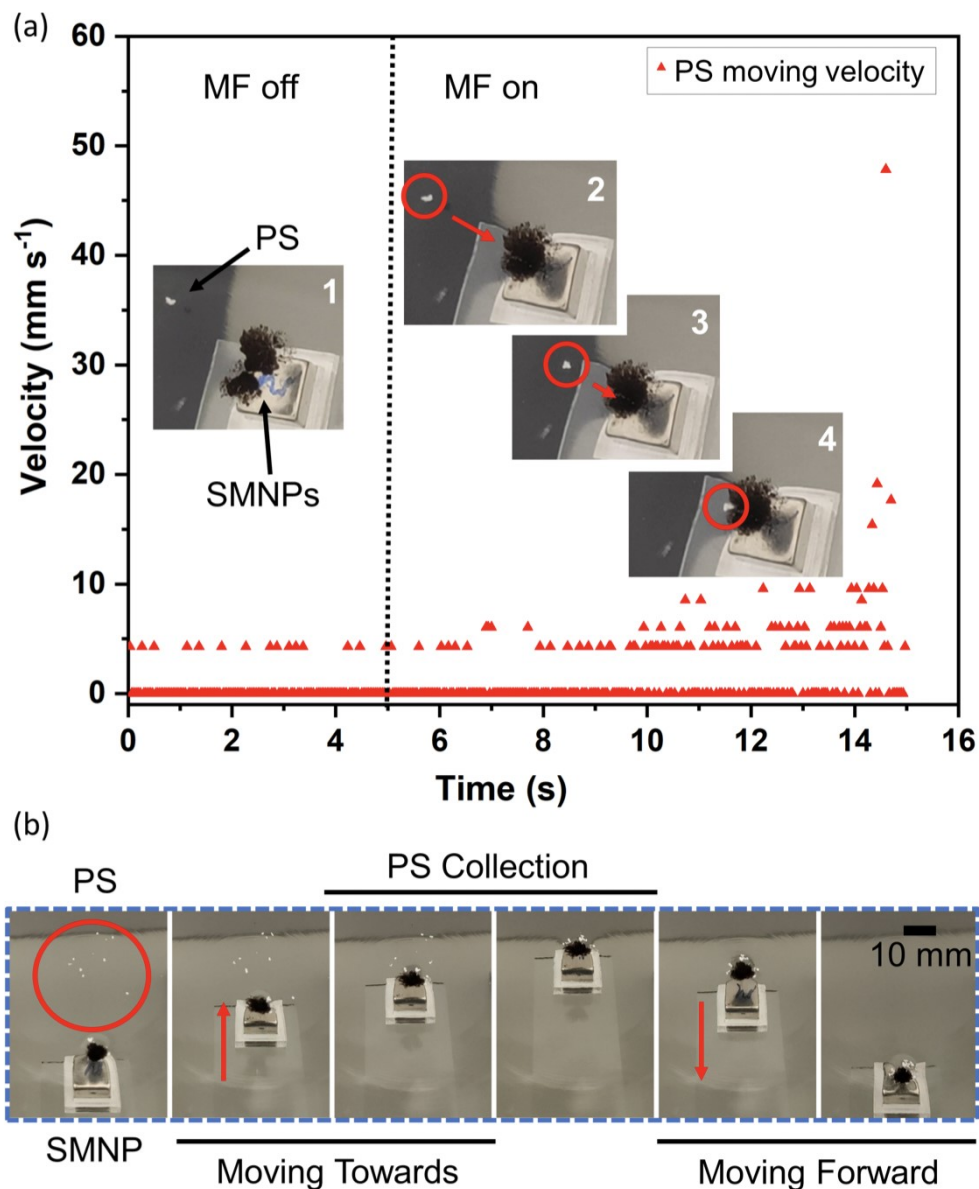


Figure 6.12. (a) Velocity of a PS particle attracted towards to the twister, without a MF applied to the SMNPs layer (before 5 s time, Picture 1) and with a MF of 100 mT, (after 5 s time, Pictures 2-4). (b) Set of images taken from the Video S6.7. The water surface was “contaminated” with PS microparticles, and then the twister moved towards the PS microparticles and removed them from the surface.

6.4 Conclusions

In conclusion, a novel low surface energy superhydrophobic magnetic particle system is introduced, called “Magneto Twister”, which is a stable magneto tunable and movable, flipped conical structured solid-water interface, which resembles a storm twister in shape. The magneto twister was fully characterised to elucidate the properties

and limitations of the system. The applicability of this system was reported for three different potential microtechnological applications. First, the magneto twister was used to manipulate water droplets in a water environment by just placing a water droplet over the twister and transporting the droplet by displacing the applied magnetic field, facilitating water droplet translocation in aqueous media. The robustness of the magneto twister is able to manipulate the droplets in a stable manner, which is a problem commonly faced in magnetic liquid marble particle systems. Further, the twister was introduced as a magnetic plug to separate liquids inside of an open surface channel. Finally, the magneto twister was used to collect and remove floating microplastic particles from the surface of the water by simply moving the twister towards the microplastic to trap and then, remove them by magnetic guiding. This investigation opens up new pathways of using superhydrophobic magnetic nanoparticles in water-air interface assisted applications.

6.5 References

- (1) Gunatilake, U. B.; Morales, R.; Basabe-Desmonts, L.; Benito-Lopez, F. Magneto Twister: Magneto Deformation of the Water–Air Interface by a Superhydrophobic Magnetic Nanoparticle Layer. *Langmuir* **2022**, *38* (11), 3360–3369.
- (2) Fürstner, R.; Barthlott, W.; Neinhuis, C.; Walzel, P. Wetting and Self-Cleaning Properties of Artificial Superhydrophobic Surfaces. *Langmuir* **2005**, *21* (3), 956–961.
- (3) Darmanin, T.; Guittard, F. Superhydrophobic and Superoleophobic Properties in Nature. *Mater. Today* **2015**, *18* (5), 273–285.
- (4) Yong, J.; Chen, F.; Yang, Q.; Huo, J.; Hou, X. Superoleophobic Surfaces. *Chem. Soc. Rev.* **2017**, *46* (14), 4168–4217.
- (5) Chen, N.; Pan, Q. Versatile Fabrication of Ultralight Magnetic Foams and Application for Oil–Water Separation. *ACS Nano* **2013**, *7* (8), 6875–6883.
- (6) Li, L.; Li, B.; Wu, L.; Zhao, X.; Zhang, J. Magnetic, Superhydrophobic and Durable Silicone Sponges and Their Applications in Removal of Organic Pollutants from Water. *Chem. Commun.* **2014**, *50* (58), 7831–7833.

- (7) Seo, K. S.; Wi, R.; Im, S. G.; Kim, D. H. A Superhydrophobic Magnetic Elastomer Actuator for Droplet Motion Control. *Polym. Adv. Technol.* **2013**, *24* (12), 1075–1080.
- (8) Chen, S.; Zhu, M.; Zhang, Y.; Dong, S.; Wang, X. Magnetic-Responsive Superhydrophobic Surface of Magnetorheological Elastomers Mimicking from Lotus Leaves to Rose Petals. *Langmuir* **2021**, *37* (7), 2312–2321.
- (9) Zhu, S.; Bian, Y.; Wu, T.; Chen, C.; Jiao, Y.; Jiang, Z.; Huang, Z.; Li, E.; Li, J.; Chu, J.; Hu, Y.; Wu, D.; Jiang, L. High Performance Bubble Manipulation on Ferrofluid-Infused Laser-Ablated Microstructured Surfaces. *Nano Lett.* **2020**, *20* (7), 5513–5521.
- (10) Ben, S.; Zhou, T.; Ma, H.; Yao, J.; Ning, Y.; Tian, D.; Liu, K.; Jiang, L. Multifunctional Magnetocontrollable Superwetable-Microcilia Surface for Directional Droplet Manipulation. *Adv. Sci.* **2019**, *6* (17), 1900834.
- (11) Zhao, Y.; Fang, J.; Wang, H.; Wang, X.; Lin, T. Magnetic Liquid Marbles: Manipulation of Liquid Droplets Using Highly Hydrophobic Fe₃O₄ Nanoparticles. *Adv. Mater.* **2010**, *22* (6), 707–710.
- (12) Laurent, S.; Forge, D.; Port, M.; Roch, A.; Robic, C.; Vander Elst, L.; Muller, R. N. Magnetic Iron Oxide Nanoparticles: Synthesis, Stabilization, Vectorization, Physicochemical Characterizations and Biological Applications. *Chem. Rev.* **2008**, *108* (6), 2064–2110.
- (13) Li, C.; Sun, Y.; Cheng, M.; Sun, S.; Hu, S. Fabrication and Characterization of a TiO₂/Polysiloxane Resin Composite Coating with Full-Thickness Super-Hydrophobicity. *Chem. Eng. J.* **2018**, *333*, 361–369.
- (14) Khaw, M. K.; Ooi, C. H.; Mohd-Yasin, F.; Vadivelu, R.; John, J. S.; Nguyen, N. T. Digital Microfluidics with a Magnetically Actuated Floating Liquid Marble. *Lab Chip* **2016**, *16* (12), 2211–2218.
- (15) Wang, J.; Meng, G.; Tao, K.; Feng, M.; Zhao, X.; Li, Z.; Xu, H.; Xia, D.; Lu, J. R. Immobilization of Lipases on Alkyl Silane Modified Magnetic Nanoparticles: Effect of Alkyl Chain Length on Enzyme Activity. *PLoS One* **2012**, *7* (8), e43478.

- (16) Herth, E.; Zeggari, R.; Rauch, J. Y.; Remy-Martin, F.; Boireau, W. Investigation of Amorphous SiO_x Layer on Gold Surface for Surface Plasmon Resonance Measurements. *Microelectron. Eng.* **2016**, *163*, 43–48.
- (17) Devouge, S.; Conti, J.; Goldsztein, A.; Gosselin, E.; Brans, A.; Voué, M.; De Coninck, J.; Homblé, F.; Goormaghtigh, E.; Marchand-Brynaert, J. Surface Functionalization of Germanium ATR Devices for Use in FTIR-Biosensors. *J. Colloid Interface Sci.* **2009**, *332* (2), 408–415.
- (18) Gates-Rector, S.; Blanton, T. The Powder Diffraction File: A Quality Materials Characterization Database. *Powder Diffr.* **2019**, *34* (4), 352–360.
- (19) Schwaminger, S. P.; Bauer, D.; Fraga-García, P.; Wagner, F. E.; Berensmeier, S. Oxidation of Magnetite Nanoparticles: Impact on Surface and Crystal Properties. *CrystEngComm* **2017**, *19* (2), 246–255.
- (20) Ooi, C. H.; Plackowski, C.; Nguyen, A. V.; Vadivelu, R. K.; John, J. A. S.; Dao, D. V.; Nguyen, N. T. Floating Mechanism of a Small Liquid Marble. *Sci. Rep.* **2016**, *6* (1), 1–8.
- (21) Kralchevsky, P. A.; Nagayama, K. Capillary Interactions between Particles Bound to Interfaces, Liquid Films and Biomembranes. *Adv. Colloid Interface Sci.* **2000**, *85* (2), 145–192.
- (22) Pankhurst, Q. A.; Connolly, J.; Jones, S. K.; Dobson, J. Applications of Magnetic Nanoparticles in Biomedicine. *J. Phys. D. Appl. Phys.* **2003**, *36* (13), 167–181.
- (23) Bormashenko, E. Moses Effect: Physics and Applications. *Adv. Colloid Interface Sci.* **2019**, *269*, 1–6.
- (24) Meir, Y.; Jerby, E. Insertion and Confinement of Hydrophobic Metallic Powder in Water: The Bubble-Marble Effect. *Phys. Rev. E - Stat. Nonlinear, Soft Matter Phys.* **2014**, *90* (3), 030301.
- (25) Verho, T.; Korhonen, J. T.; Sainiemi, L.; Jokinen, V.; Bower, C.; Franze, K.; Franssila, S.; Andrew, P.; Ikkala, O.; Ras, R. H. A. Reversible Switching between Superhydrophobic States on a Hierarchically Structured Surface. *Proc. Natl. Acad. Sci. U. S. A.* **2012**, *109* (26), 10210–10213.
- (26) Shirtcliffe, N. J.; McHale, G.; Newton, M. I.; Perry, C. C.; Pyatt, F. B. Plastron

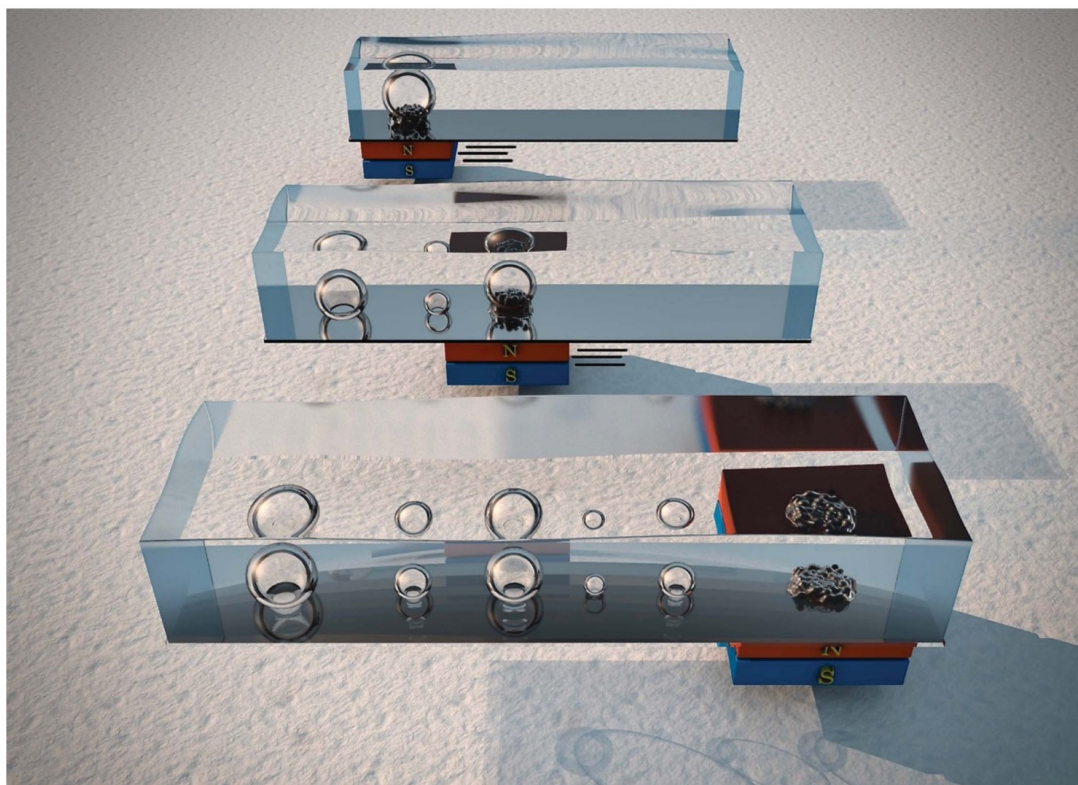
- Properties of a Superhydrophobic Surface. *Appl. Phys. Lett.* **2006**, *89* (10), 104106.
- (27) Murakami, D.; Jinnai, H.; Takahara, A. Wetting Transition from the Cassie-Baxter State to the Wenzel State on Textured Polymer Surfaces. *Langmuir* **2014**, *30* (8), 2061–2067.
- (28) Zhao, Y.; Xu, Z.; Parhizkar, M.; Fang, J.; Wang, X.; Lin, T. Magnetic Liquid Marbles, Their Manipulation and Application in Optical Probing. *Microfluid. Nanofluidics* **2012**, *13* (4), 555–564.
- (29) Phurimsak, C.; Tarn, M. D.; Pamme, N. Magnetic Particle Plug-Based Assays for Biomarker Analysis. *Micromachines* **2016**, *7* (5), 77.
- (30) Bronzeau, S.; Pamme, N. Simultaneous Bioassays in a Microfluidic Channel on Plugs of Different Magnetic Particles. *Anal. Chim. Acta* **2008**, *609* (1), 105–112.
- (31) Satarkar, N. S.; Zhang, W.; Eitel, R. E.; Hilt, J. Z. Magnetic Hydrogel Nanocomposites as Remote Controlled Microfluidic Valves. *Lab Chip* **2009**, *9* (12), 1773–1779.
- (32) Philippova, O.; Barabanova, A.; Molchanov, V.; Khokhlov, A. Magnetic Polymer Beads: Recent Trends and Developments in Synthetic Design and Applications. *Eur. Polym. J.* **2011**, *47* (4), 542–559.
- (33) Hartshorne, H.; Backhouse, C. J.; Lee, W. E. Ferrofluid-Based Microchip Pump and Valve. *Sensors Actuators, B Chem.* **2004**, *99* (2–3), 592–600.
- (34) Zhang, K.; Gong, W.; Lv, J.; Xiong, X.; Wu, C. Accumulation of Floating Microplastics behind the Three Gorges Dam. *Environ. Pollut.* **2015**, *204*, 117–123.
- (35) Liu, D.; Weng, D.; Wang, J. Collection of Nanoparticles at the Air-Liquid Interface by Surface Tension Gradients. *Colloids Interface Sci. Commun.* **2019**, *33*, 100205.

Underwater Magneto-Driven Air De-bubbler

This Chapter is partially reproduced from:¹

Gunatilake, U. B.; Alvarez, Y; Ojeda, E.; Basabe-Desmonts, L.; Benito-Lopez, F. Underwater Magneto Driven Air De-bubbler., *Journal of Materials Chemistry A*, 2022, 10, 12832-12841.

<https://doi.org/10.1039/D2TA01009G>

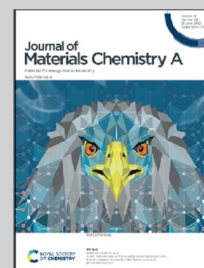


Showcasing research from the Microfluidics Cluster UPV/EHU, a group led by Profs. Fernando Benito-Lopez and Lourdes Basabe-Desmonts, University of the Basque Country, Spain.

Underwater magneto-driven air de-bubbler

An efficient strategy to magnetically collect, merge, transport, and evacuate free and deposited underwater air bubbles from underwater surfaces and microfluidic channels is developed. The de-bubbler consisted of superhydrophobic magnetic particles with underwater superaerophilicity and high magneto-responsive properties, which facilitates trapping the underwater air bubbles and the remote manipulation of the de-bubbler under a magnetic field. This system will open an easy and cheap way to address the inherent air-bubble contamination issue presented in most of the microfluidics applications, without integrating any advanced tools or processes.

As featured in:



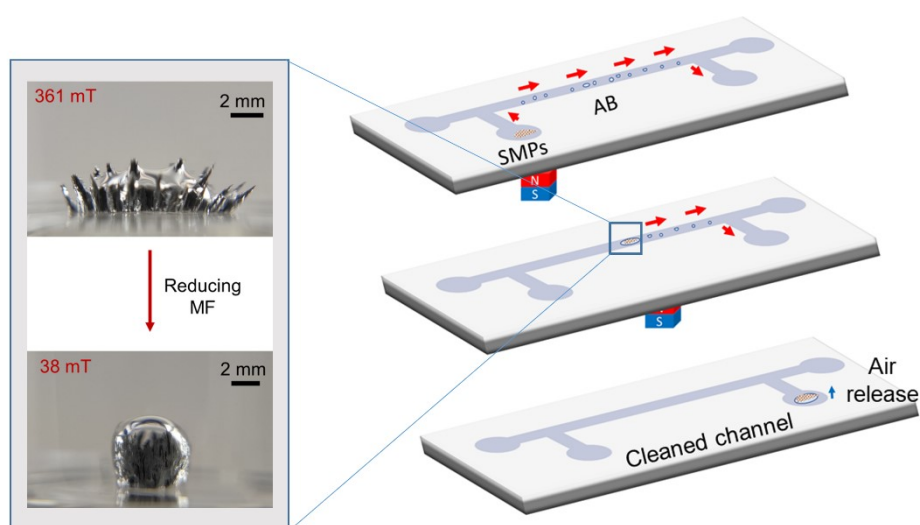
See Lourdes Basabe-Desmonts, Fernando Benito-Lopez *et al.*, *J. Mater. Chem. A*, 2022, 10, 12832.



rsc.li/materials-a

Registered charity number: 207890

Abstract. The accumulation and deposition of undesired air bubbles on the surface of microfluidic channels and on underwater functional systems is a major drawback, which worsen their performance. Present de-bubbling strategies are usually complex and require of advanced tools or tedious operation protocols. In this Chapter, we propose a flexible and easily adaptable strategy to efficiently collect, transport and evacuate the underwater deposited air bubbles by a remote stimulus, using superhydrophobic ferromagnetic particles. The low surface energy of the superhydrophobic ferromagnetic particles assures the trapping of underwater air bubbles, due to their underwater superaerophilicity, while the high magnetisation of the superhydrophobic ferromagnetic particles facilitates the manipulation of the formed particles-bubble system by using an external magnetic field, induced by a simple permanent magnet. The properties of the system were characterised for different bubble deposited surfaces. Remarkably, a 99 % air bubble removal efficiency was observed in microfluidic channels, providing an easy and cheap strategy to address the air bubble accumulation issue faced by microfluidic technology without integrating any advanced tools or protocols in the device.



7.1 Introduction

Unexpected nucleation, growth and deposition of air bubbles in underwater systems, particularly in aqueous channel surfaces, negatively affect the functionality and the performance of the system.² Gas nucleation is expected in supersaturated liquids, when overcoming the energy barrier required rupturing the liquid, allowing the formation of a gas bubble, homogeneous nucleation. This effect is often observed in microfluidics channels.² On the other hand, defects present on underwater solid surfaces act as gas nucleation spots, being responsible of a heterogeneous gas nucleation. Surface crevices or surface defects propagate preoccupied gas spots (Harvey nuclei), which formed during filling of the liquid in low wettability conditions, resulting in the growth of gas bubbles by trapping them to the pre-existing gas nuclei spot.³ In addition to that, the direct injection of gas bubbles, with radii over the critical bubble value at liquid saturated conditions, makes the bubbles to be deposited on the surfaces of the underwater systems and channels.

In particular, bubbles in the channels of a microfluidic device affect its performance by reducing or inhibiting flow, generating unexpected reactions or damaging the channel surface and deviating specific functional conditions in the device.⁴⁻⁶ For instance, cell viability and cell culture media in microfluidics devices are highly affected by bubbles. The burst of bubbles in the presence of cells can rupture the membrane of the cell. Moreover, bubbles can block the fluid flow of the cell culture medium in continuous flow systems, damaging the cell culture.⁶ To remove surface deposited gas bubbles is an acutely difficult task, which requires performing additional operations in the system. Therefore, investigations focus on the prevention of the formation and the removal of the bubbles on those systems. In this regard, the geometry of the channels has to be specifically designed to avoid micro-structured defects. Moreover, the use of connecting grooves with vents,⁷ or the tuning of the surface properties, by using chemical treatments such as oxygen plasma, have been investigated to reduce bubble formation.⁸ In addition, integrated external/internal modules within the microfluidic devices have been employed to trap and remove air bubbles from the system. For instance, Meng *et al.*⁹ presented a hydrophobic bubble sink plate, integrated in the wall of a microfluidic device, with venting holes to remove air bubbles. Later, a new configuration based on gas permeable membranes were investigated to trap and purge gases. Liu *et al.*¹⁰ reported an upstream liquid directed nozzle type channel with a

poly(tetrafluoroethylene) (PTFE) venting membrane placed on top for rapid bubble removal. Moreover, Cho *et al.*¹¹ reported a disposable degassing method based on a microchannel network with an integrated poly(dimethylsiloxane) (PDMS) membrane. The reusable membrane, containing micro-support arrays, can be assembled and disassembled by vacuum pressure. The device was able to collect and vacuum the air from the membrane. In another example, Williams *et al.*¹² presented an externally integrated rapid de-bubbler module, sandwiching a hydrophobic PTFE membrane between two poly(methyl methacrylate) (PMMA) slabs to avoid the bubble to enter into the microfluidic channels. Recently, Huang *et al.*¹³ reported an in-line sloped PDMS micro structured system, fabricated through two-photon polymerisation technique, in which the bubbles are able to accumulate on the top of the device, due to buoyancy force and to a smart venting configuration combined with vacuum.

Interestingly, air bubble manipulation systems have found promising approaches to address bubble contamination in underwater and aqueous based microfluidics systems. For instance, Yu *et al.*¹⁴ introduced a silicone-oil-infused slippery surface to manipulate bubbles in an aqueous environment. Their lubricant-infused shaped slippery (LIS) tracks were used to guide bubble delivery and so, to facilitate continuous bubble distribution. In this case, the movement of the bubble on the LIS was driven by buoyancy force. Later, Guo *et al.*¹⁵ reported a magnetic responsive slippery gel surface, fabricated in PDMS doped with iron powder and silicone oil, for underwater bubble smart manipulation. On the slippery magneto responsive gel surface, the sliding behaviour of bubbles was reversibly controlled by alternately applying or removing an external magnetic field, showing extended stability compared to underwater slippery liquid-infused porous surfaces. As well, Yu *et al.*¹⁶ introduced a superhydrophobic helix to directionally deliver air bubbles in a controllable manner. More recently, Zu *et al.*¹⁷ presented a high performance manipulation strategy for gas bubbles by utilising ferrofluid-infused laser-ablated micro-structured surfaces (FLAMS), which facilitated ultrafast horizontal transport of air bubbles in a programmable manner, under a magnetic field. In general, all these techniques rely on specifically fabricated flat or channel surfaces, which need to be chemically modified by smart bubble manipulating materials, being difficult to implement in real applications.

In order to fulfil the request for an easy to use and at the same time, affordable method to remove bubbles at the microscale, we propose a magneto responsive, underwater

bubble collection, merging, transportation and manipulation system applicable on surfaces and microfluidic channels, which avoids the need for chemical modification of their surfaces. Herein, we chemically modified the surface of ferromagnetic iron (Fe) particles to reduce their surface energy, named as superhydrophobic magnetic particles (SMPs). Two properties of the SMPs were considered, their underwater supererophilicity and their magneto responsiveness. Underwater inserted particles were magnetically guided and then attracted to the deposited air bubbles due to their superaerophilicity. Subsequently, by displacing the magnetic field, the attracted air bubbles were transported and thus, easily removed from the underwater surface or the microfluidic channel, Figure 7.1. Bubble collection and transportation properties of the SMPs-bubble system (called de-bubbler) were investigated with low and high surface energy underwater surfaces and within microfluidic channels. Then, the properties of the SMPs-bubble system were fully characterised to understand the air bubble loading capability of the particle system and to identify the required magnetic fields needed to hold the desired volumes of the air bubbles on different underwater surfaces. Finally, the best performance was validated, obtaining nearly 99 % efficiency on air bubble removal in a PMMA based microfluidic channel.

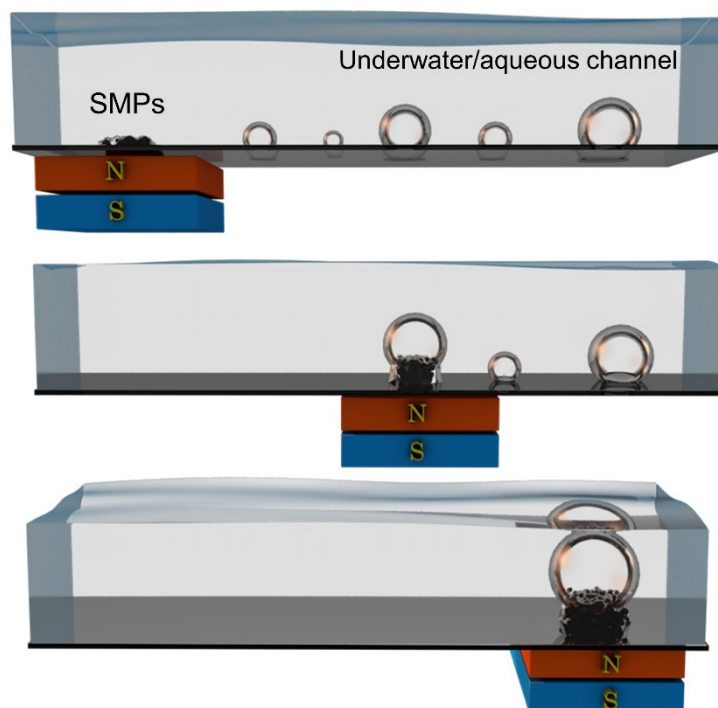


Figure 7.1. Schematic diagram of the magneto collection of air bubbles by SMPs in a microchannel, de-bubbler.

7.2 Experimental

7.2.1 Characterisation of the SMPs and the SMPs de-bubbler

The same synthesis protocol as mentioned in Chapter 5, section 5.2.2 was used to obtain superhydrophobic Fe particles (C₈-Fe, SMPs). FTIR, SQUID, Contact angle was characterised by using the same equipment mentioned in sections of 3.2.3, and 6.2.6. Scanning electron microscopy (SEM) images of the particles were recorded by Hitachi S-4800 (Hitachi Japan) at an accelerating voltage of 5 kV.

4.0 mg of the SMPs was sprinkled to the water surface of containers of different materials, and the particles were brought to the bottom surface (depth) of the container using a NdFeB permanent magnet (cubic 10 mm magnet). Known volumes of air were loaded to the underwater SMPs using a gas syringe (Agilent, 50 µL) under different magnetic fields and using two surfaces, glass and PMMA. The gradient magnetic field was calculated by the equation 6.1

Magneto collection, merging and manipulation of underwater air bubbles were investigated by pre-depositing known volumes of air bubbles on the bottom of glass, PMMA and PDMS containers filled with water. 4.0 mg of the SMPs was introduced into the containers in the same way as mentioned above and the magnet was displaced together with the SMPs to collect, merge and manipulate the deposited air bubbles.

The synchronisation effect of the magnet and the de-bubbler while horizontal translocation under the magnetic field was characterised by measuring the velocities of the de-bubbler and the magnet. The moving (manual) velocities of the magnet and the air bubble attached to the SMPs, were tracked by video analysis, through the Image-J software coupled with a manual tracking plugin.¹⁸ This was used to track the motion of the de-bubbler and the magnet within short time ranges, which allowed obtaining velocity values.

7.2.2 Fabrication of the microfluidic devices and removing of the air bubble in the channels.

The microfluidics devices were fabricated by the following protocol. The layers of the PMMA microfluidics device (Figure 7.2a) were assembled together and sealed by thermocompression bonding in a roller laminator (Vivid Matrix Duo Laminator MD-460/MD-650, Vivid, United Kingdom) at 105 °C. PMMA sheets were cut by a CO₂ Laser System (VLS2.30 Desktop Universal Laser System, VERSA Laser, USA)

equipped with a 10.6 μm CO₂ laser source ranging in power from 10 to 30 W. 1.1 mm thick PMMA (ME303010, clear, Goodfellow, United Kingdom) was used for the channel layer of the device and 175 μm thick PMMA (ME303016, clear, Goodfellow, United Kingdom) was used for the bottom and top cover layers. The microchannel dimensions were 1.5 mm width x 40.0 mm length x 1.1 mm height. All the cartridges included a 2.0 mm diameter inlet and outlet (on the top PMMA layer) in order to move the liquid through the channel. To facilitate the loading of the SMPs, two side channels (1.0 mm width x 2.5 mm length x 1.1 mm height) with two additional inlets (2.0 mm diameter) were added to the design of the cartridges.

The glass base microfluidics device (Figure 7.2b) was built by multiple-layer lamination. Microfluidic channels (1.5 mm width x 40.0 mm length x 1.1 mm height) were cut by a Graphtec cutting Plotter CE6000-40 (CPS Cutter Printer Systems, Spain) on sheets of Pressure Sensitive Adhesive layers (127 μm thick ARcare[®] 8939, Adhesive Research, Ireland) and by CO₂ Laser System (VLS2.30 Desktop Universal Laser System, VERSA Laser, USA) on sheets of 1.1 mm thick PMMA substrate (ME303010, clear, Goodfellow, United Kingdom). A glass slide (25 x 75 mm, Deltalab, Spain) was used as the bottom base of the device and the top cover was cut on sheets of 380 μm thick PMMA substrate (ME303001, clear, Goodfellow, United Kingdom). All the cartridges included a 2.0 mm inlet and outlet in order to move the liquid through the channel. To facilitate the loading of the magnetic beads, two side channels (1.0 mm width x 2.5 mm length x 1.1 mm height) with an additional inlet (2.0 mm diameter) were added to the design of the cartridges. The assembly and lamination of the Glass, PSA and PMMA layers, one on top of the other, generated the complete microfluidic network.

SMPs (~ 1.0 mg) were introduced into the microfluidic channel (filled with water) by the inlet chamber and then, the deposited air bubbles were collected by the SMPs, when translocating the magnet. The collected air bubbles were transported towards the outlet chamber and released by removing the magnetic field. The bubble removal efficiency (BRE) for calculated by equation 7.1:

$$\text{BRE} = \frac{i-f}{i} \times 100\% \quad \text{equation 7.1}$$

where, i and f denote the initially contaminated amount of bubbles and the amount of bubbles after the de-bubbler operation. The images and the videos were recorded with a Sony IMX586 Exmor RS 48 megapixel lens with 12X macro lens. The videos and the images were analysed by Image-J software and the objects tracking was done by the manual tracking Image-J plugin.

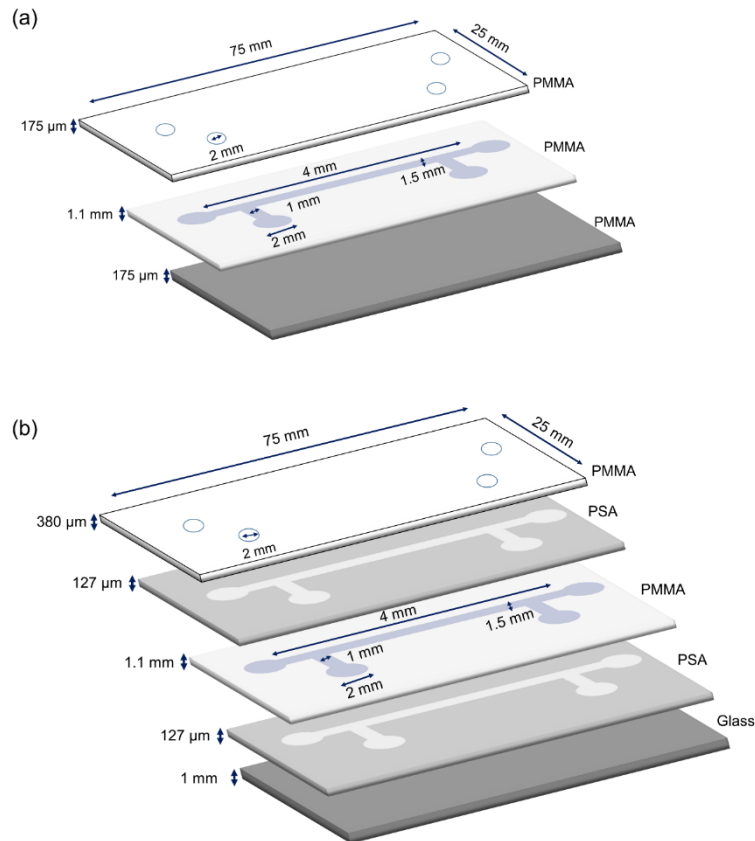


Figure 7.2. Dimensions and materials of the microfluidic devices with (a) PMMA bottom and (b) glass bottom surfaces.

7.3 Results and Discussion

7.3.1 Characterisation of the magneto-driven underwater superaerophilic de-bubbler

For an ideal smooth surface immersed in water media, the surface wetting of a gas bubble correlates with the wettability of the water sessile droplet in air medium. The contact angle for a water droplet in the air (WCA θ_w) and the contact angle for a bubble

in water medium (BCA θ_b) can be deduced by the Youngs equation in equation 7.2 and equation 7.3, respectively,¹⁹

$$\cos \theta_w = \frac{(\gamma_{sv} - \gamma_{sl})}{\gamma_{lv}} \quad \text{equation 7.2}$$

$$\cos \theta_b = \frac{(\gamma_{sl} - \gamma_{sv})}{\gamma_{lv}} \quad \text{equation 7.3}$$

whereas, γ_{sv} , γ_{sl} , and γ_{lv} are the free energies of the solid-vapour, solid-liquid and liquid-vapour interfaces, respectively. Therefore, the correlation between the water and the bubble contact angles can be theoretically determined using the equation 7.4, for an ideal smooth surface.

$$\theta_b = 180^\circ - \theta_w \quad \text{equation 7.4}$$

The FTIR spectra of bare Fe and SMPs (C₈-Fe) was analysed to check the modification of the octyl hydrocarbon chain on the Fe surface. As depicted in Figure 7.3 (C₈-Fe), the high intense distinguish peaks frequency at 2850, 2941, and 2965 cm⁻¹ are due to the stretching vibrations of CH₂ in alkyl chains.²⁰ The peak at 1460 cm⁻¹ can be attributed to the CH₂ bending vibrational peak of the coated molecules. As well, the stretching vibrational peaks at 866, 990 and 1115 cm⁻¹ in the SMPs spectrum were assigned to Si-C, Si-O-Fe and Si-O bonds respectively, demonstrating the binding of the alkyl chain through the silane group to the particles surface. The common peaks of residual water OH stretching and bending were found in both Fe and SMPs at the positions of 3430/3340 cm⁻¹ and 1630/1660 cm⁻¹.²⁰⁻²³ However, the intensity of the O-H peaks was reduced in the SMPs spectrum due to the hydrophobic alkyl groups, inhibiting the absorption of residual water to the surface of the Fe particle.

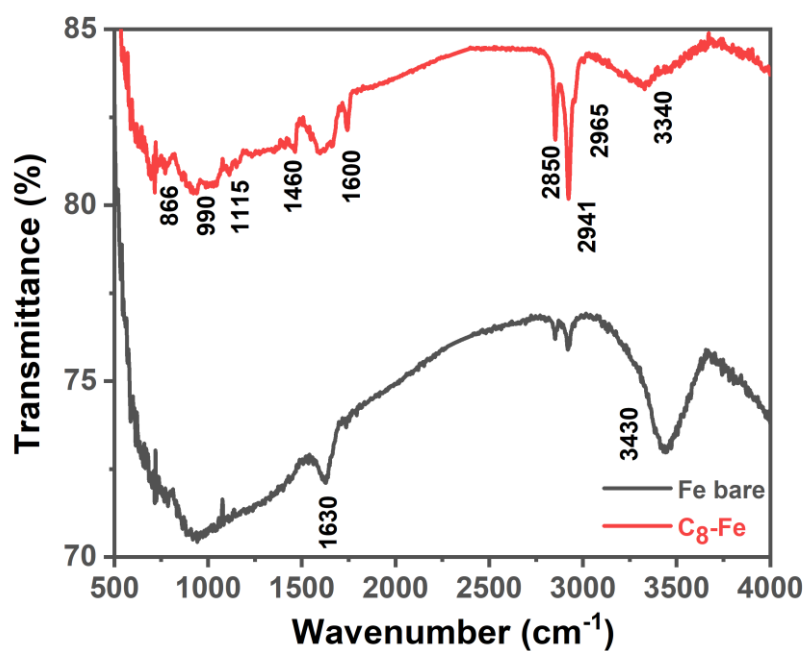


Figure 7.3. FTIR spectra of bare Fe microparticles (black spectrum) and the chemically modified SMPs (C₈-Fe) (red spectrum).

According to the SEM images (Figure 7.4 a and b) of the bare (Fe) and chemically modified (SMPs) particles, the roughness texture of the surface of the bare Fe changed to a smooth texture in the SMPs, proving the successful long chain hydrocarbon coating on the particles. As depicted in the Figure 7.4c, the SMPs size distribution is in the 0.7 - 5.5 μm range, with the higher percentage in the 1 - 4 μm range. Moreover, some aggregation of particles can be seen in Figure 7.4d.

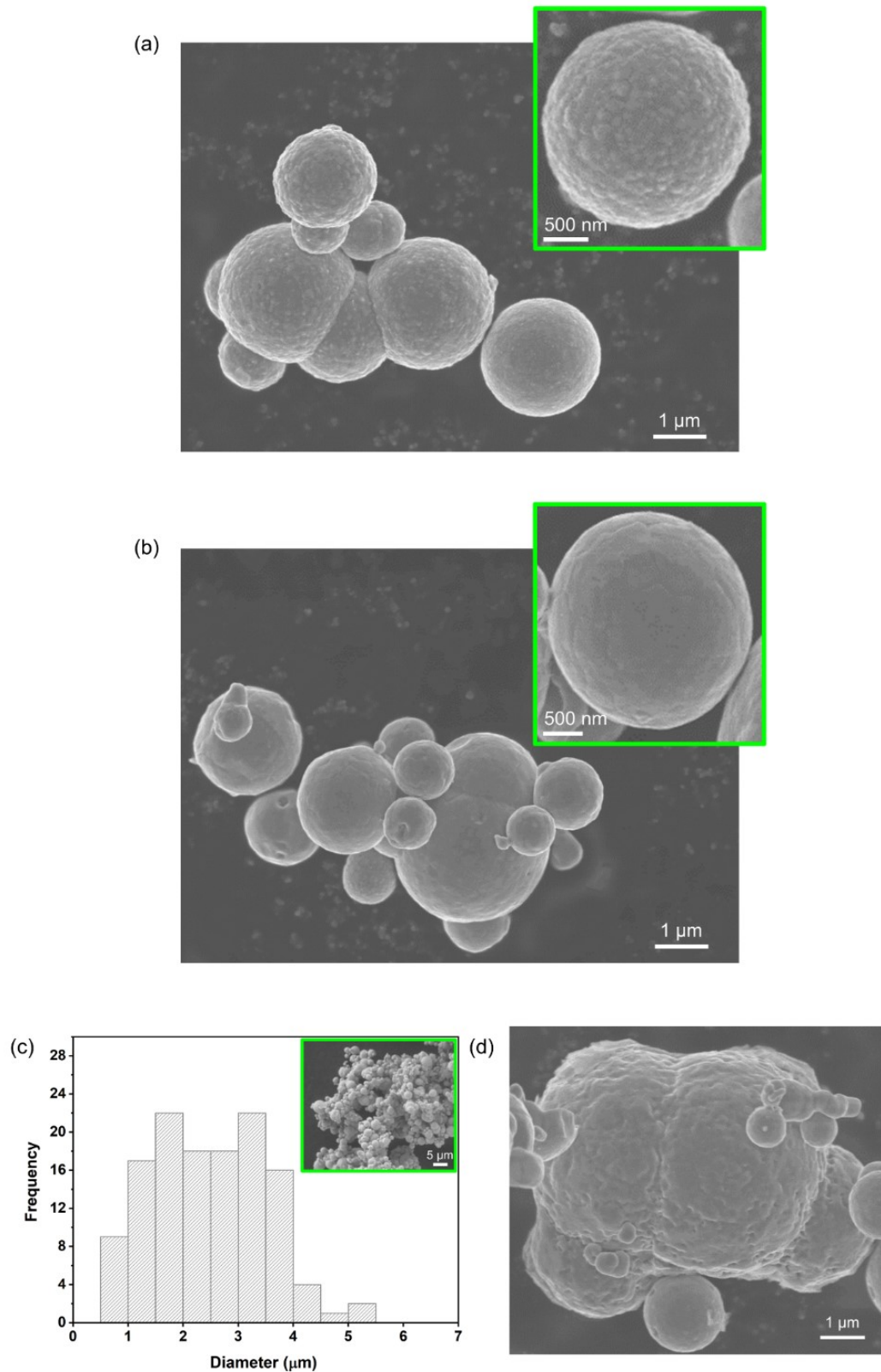


Figure 7.4. SEM images of (a) Fe particles, (b) SMPs. (c) Size distribution of the SMPs and SEM picture of the SMPs. (d) SEM of an aggregate of SMPs.

Thus, a superhydrophilic surface in air behaves as a superaerophobic surface underwater, while a superhydrophobic surface in air presents superaerophilic properties underwater.²⁴ Figure 7.5a, shows this behaviour, where the WCA $\sim 152^\circ$ was converted to the BCA $\sim 19^\circ$ for the superhydrophobic magnetic particles.

The immersion of the chemically modified iron particles (C_8 -Fe) in water, under the gradient magnetic field, facilitated the formation of self-assembled microstructural spikes over the surface, as shown in the top image of Figure 7.5b. The particle-particle and the particle-external field magnetic interactions affected the self-assembly of the particle system differently with the value of the externally applied magnetic field. These interactions depend on the magnetisation, dimensions, shape of the magnetic particles and shape of the magnet, as well as, the distance and the orientation of the magnetic components.²⁵ These octyl alkyl modified, soft ferromagnetic particles were fabricated keeping a high saturation magnetisation, $220 \text{ Am}^2 \text{ kg}^{-1}$, compared to the saturation magnetisation of Fe ($239 \text{ Am}^2 \text{ kg}^{-1}$), Figure 7.5c. These modified magnetic particles showed superhydrophobic properties, Figure 7.5a (left side image), maintaining a static water contact angle of $\sim 152^\circ$, due to the non-favourable interaction between polar water molecules and the non-polar octyl alkyl in magnetic particles. As shown in Figure 2b top image, the superhydrophobic particles system with the attraction of air underwater, self-assembled under the induced magnetic field, by forming a crown-shaped microstructure, called from now on as “particle-air Crown (P-aCrown)”. It was found that for a 4.0 mg of SMPs $\sim 12 \mu\text{L}$ air volume (plastron) was transported to the water medium from the water-air interface when immersing the SMPs. At this state, the air layer was confined within the magnetic self-assembled structure, following the spike pattern because of the high magnetic forces towards the underwater supererophilic particles. Nevertheless, in reduced magnetic fields, the magnetic force towards the particles was minimised, and due to that, the P-aCrown reassembled its structure and the air layer deformed to a spherical bubble, minimising its surface area, as depicted in Figure 7.5b, bottom image. Moreover, the particles shifted upwards due to their bouncy forces and remained attached to the air-water interphase of the bubble due to the lateral capillary forces, forming a bubble marble.²⁶ Further reduction of the magnetic field (38 mT, for 4.0 mg of SMPs) or switching off the magnetic field facilitated the relaxation of the particle-air system and the detach of the air bubble from the glass surface, since the bouncy force of the bubble dominated the behaviour of the system at that stage. The

superhydrophobicity/underwater superaerophilicity and high magnetisation of the C₈-Fe particles promoted the remote manipulation of underwater air bubbles with different shape states under the tuneable external magnetic field.

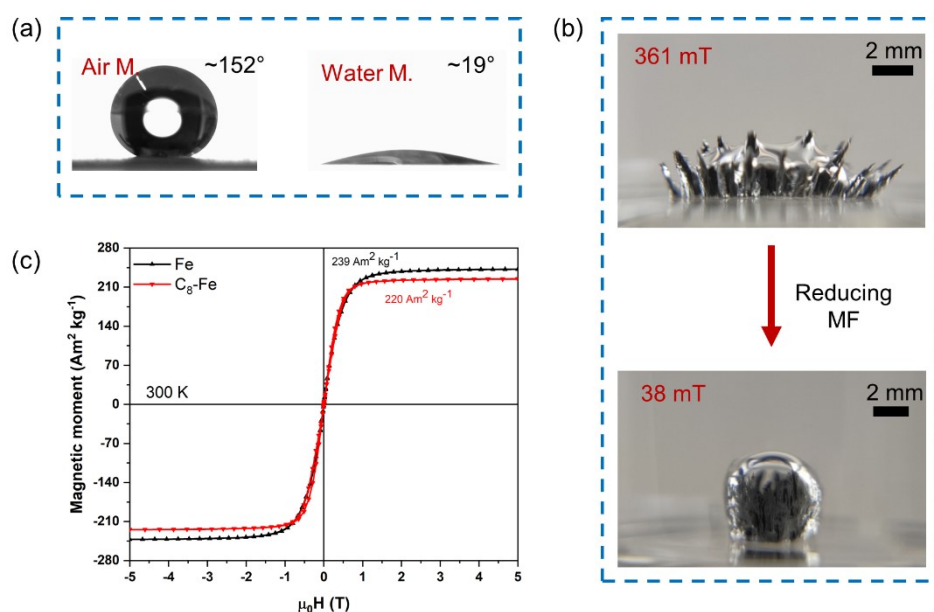


Figure 7.5. (a) Water droplet contact angle in air medium (Air M), WCA $\sim 152^\circ$, and air bubble contact angle in water medium (Water M), BCA $\sim 19^\circ$ over a C₈-Fe deposited thin layer. (b) Magneto tunable, underwater superaerophilic particle-air system de-bubbler, showing images of the particle-air P-a-Crown assembly under the influence of two magnetic fields. (c) SQUID analysis of the superhydrophobic C₈-Fe and the commercial Fe particles.

The stability of the SMPs was tested by settling the particles under different types of solutions (H₂O, PBS, 0.01 M HCl, 1 M HCl, 0.01 M NaOH and 1 M NaOH). The magneto attracted underwater SMPs strongly repelled water, due to the low surface energy molecular arrangement of the surface of the particles. Figure 7.6 shows the stable air trapping ability of the SMPs under H₂O and PBS up to 24 h. In these non-ionic and high ionic density conditions (pH ~ 7), SMPs maintained their superaerophilic stability and showed no oxidation of the particles or degradation of the long chain carbon coatings of the SMPs, for the time investigated and they could be reusable under these conditions. At alkaline solutions, 0.01 M (pH ~ 12.1) and 1 M (pH ~ 13.9) of NaOH, the SMPs behaved as well as superaerophilic, and showed stable behaviour up to 24 h. However, it was observed that some particles lost their superaerophilicity at extremely high pH conditions (pH ~ 13.9), due to the degradation of the long carbon

chains on the surface of the particles. Nevertheless, the bubble attraction ability of the SMPs system was tested to be stable up to 10 days, under the mentioned solutions.

In acidic conditions, $\text{pH} \sim 2.1$, the SMPs were stable up to 1 h, losing their superaerophilicity soon after. On the other hand, at $\text{pH} \sim 0.2$, extremely high acidic conditions, the SMPs were unstable, oxidising the iron particles as could be observed in Figure 7.7, by the formation of hydrogen gas. To avoid this behaviour, the same long chain carbon molecule was used to modify iron oxide ($\text{C}_8\text{-Fe}_3\text{O}_4$) nanoparticles (SMNPs). Then, the SMNPs stability was tested under these acidic solutions. The synthesis and the characterisation of the SMNPs can be found in a previous Chapter 6, section 6.2.1.²² As shown in the Figure 7.7, the SMNPs presented a stable behaviour in the $\text{pH} \sim 2.1$ acidic medium up to 24 h, and even after 10 days. Nevertheless, they were just stable for 15 min in highly acidic solutions, $\text{pH} \sim 0.2$, where the SMNPs rapidly started to lose their superaerophilicity and began to dissolve, forming $\text{FeCl}_3/\text{FeCl}_2$. Therefore, this underwater bubble trapping and manipulation protocol can be used for rapid operations, less than 15 min, in highly acidic solutions, and shows good stability in slightly acid, neutral and basic solutions for long periods of time.

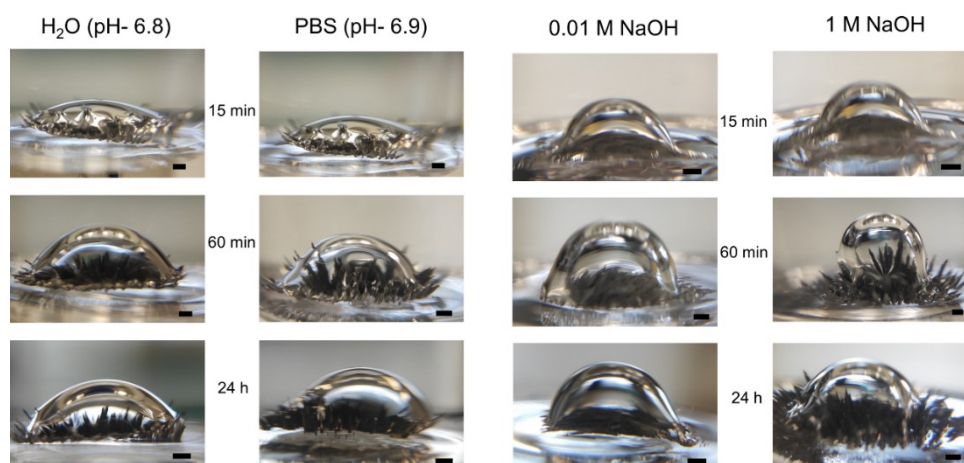


Figure 7.6. Superaerophilic stability of the SMPs under water, PBS solution, alkaline solutions of 0.01 M ($\text{pH} \sim 12.1$) and 1 M ($\text{pH} \sim 13.9$) NaOH. The particles were discharged to the surface of the water by removing the magnetic field in each solution after 15 min, 60 min and 24 h. Then, they were re-submerged inside the solution under the magnetic field followed by the loading of air volumes of 20, 40, 40 and 40 μL respectively, to demonstrate their superaerophilicity. Scale bar: 1 mm.

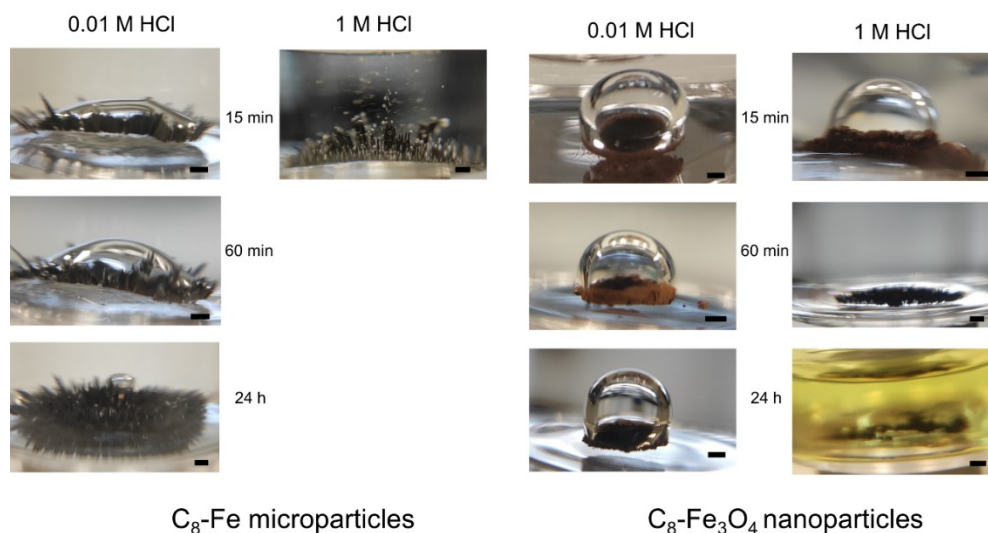


Figure 7.7. Superaerophilic stability of the SMPs (C_8 -Fe microparticles) and the SMNPs (C_8 - Fe_3O_4 nanoparticles) under acidic solutions of 0.01 M (pH \sim 2.1) and 1 M (pH \sim 0.2) HCl. The particles were discharged to the surface of the water by removing the magnetic field in each solution after 15, 60 and 24 h. Then, they were re-submerged inside the solution under the magnetic field followed by the loading of air volumes of 20, 40, 40 and 40 μ L respectively, to demonstrate their superaerophilicity. Scale bar: 1 mm.

7.3.2 Gas loading/attraction of SMP under the magnetic field

The maximum air bubble loading capacity of the magnetic P-aCrown (4 mg of SMPs) was investigated by loading air into underwater P-aCrown, which was settled at the bottom surface of a glass vial, under 353 mT. As depicted in Figure 7.8a, the maximum air bubble capacity was found to be 60 μ L. Further addition of air, provoked to the air bubble to leave the P-aCrown system but leaving a small portion of air within the P-aCrown spikes (12 - 20 μ L depending on the P-aCrown shape). The bubble started to leave the P-aCrown system when the bouncy force ($F_{b(g)}$) of the bubble exceeds the adhesion force ($F_{a(gp)}$) of bubble-SMPs and the bubble-substrate surface force ($F_{a(gs)}$) (here glass). Besides that, the stress between the upward bouncy force ($F_{b(g)}$) and downward adhesion forces ($F_{a(gp)}$, $F_{a(gs)}$), stretch and break the bubble. The bubble substrate and the SMPs adhesion forces depend on the surface tension of the liquid, contact diameter and the contact angle hysteresis of the bubble.²⁷ The mentioned forces acting on the bubble and on the SMPs are highlighted in Figure 7.8b. Moreover, a higher loading capacity, 130 μ L, was observed when using lower surface energy substrates compared to the glass such as PMMA, due to the higher adhesion force of

the bubble-substrate surface under water. In particular, when using the bare PMMA surface (without magnetic P-aCrown) it was possible to observe up to 40 μL air bubbles stack to the surface, whereas in the bare glass surface, air bubbles were unable to get stack (0 μL) due to the high surface energy and the inherent underwater repulsion of the air bubbles, as demonstrated using the equation 5.

Another parameter to be considered in order to control the air loading capacity of the de-bubbler is the applied magnetic field. The minimum magnetic field required to hold a desired volume of air bubble for a fixed amount of SMPs is presented in Figure 7.8c. In this case, 4.0 mg of SMPs were hold by an external magnetic field, in a glass surface. A power trend line was observed while increasing the air volume at the minimum required magnetic field. This effect can be explained considering the higher magnetic force ($F_{m(p)}$) needed to hold bigger volumes of air to counter strike on the higher buoyancy forces ($F_{b(p)}$) at higher air bubble volumes. In this case, the air bubble was attracted to the SMPs through the adhesion forces between air and the particles, while the magnetic particles held to the glass vial surface via magnetic forces. At low magnetic fields, the buoyancy force of the SMPs ($F_{b(p)}$) and bubble ($F_{b(g)}$) dominated the de-bubbler behaviour. The SMPs travelled and settled alongside the water-air interface in the bubble due to surface tension forces and capillarity. By further reducing the magnetic field, the magnetic force ($F_{m(p)}$) over the SMPs was reduced too, thus the SMPs left the glass surface carrying the air bubble, with the SMPs inside of the bubble. However, in a bit higher magnetic fields, the magnetic force dominated the SMPs behaviour, over the buoyancy force of particles ($F_{b(p)}$) and capillarity thus, the bubble left the de-bubbler by making a secondary bubble. This behaviour was explained considering the higher buoyancy force of the bubble ($F_{b(g)}$) over the adhesion force ($F_{a(gp)}$), which promoted the air bubble to leave the system. Both, behaviours are shown in the Figure 7.9.

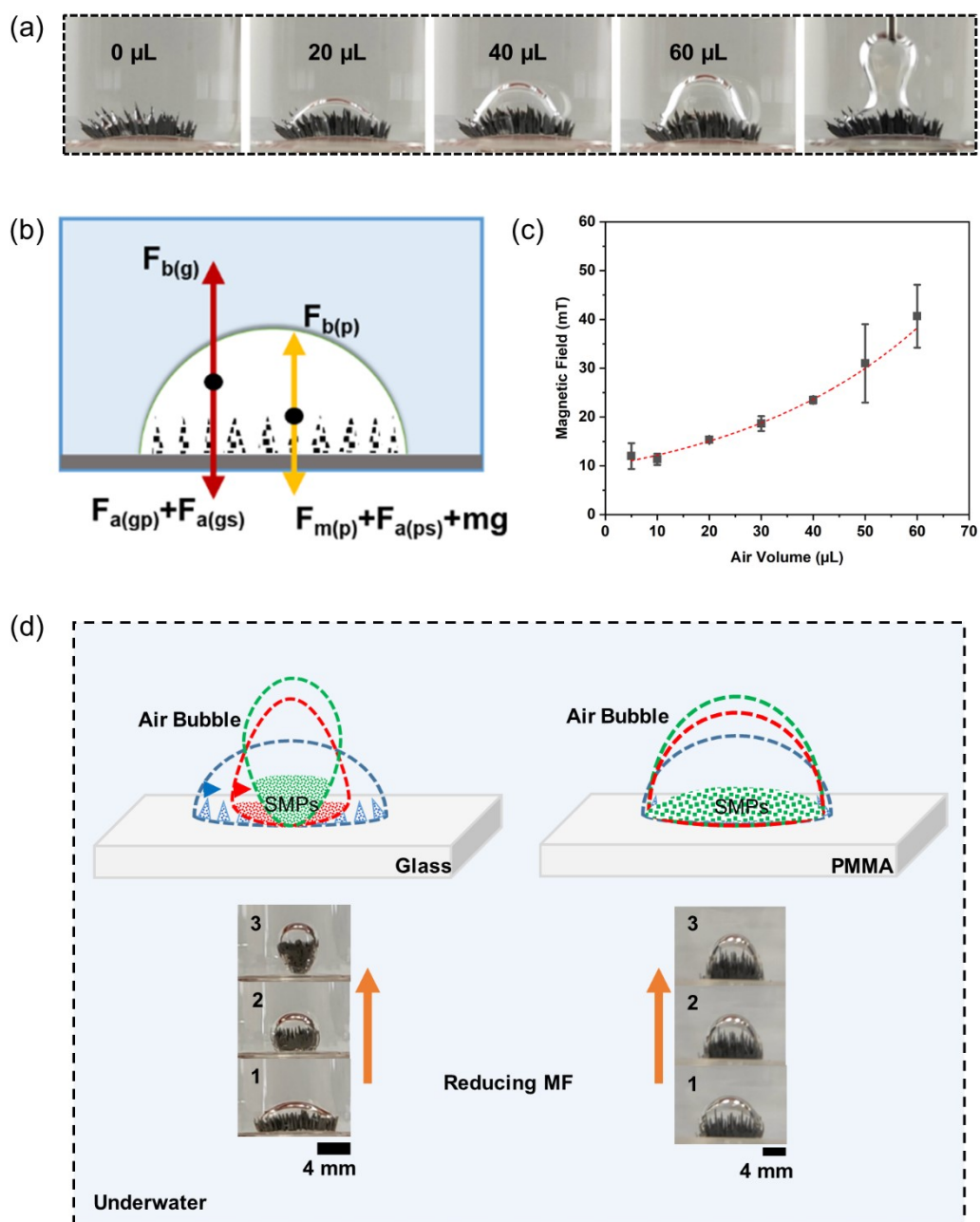


Figure 7.8. (a) Air loading in a 4.0 mg SMPs ($\text{C}_8\text{-Fe}$) under 353 mT (MF value on the glass vial surface) gradient magnetic field. (b) Simplified schematic diagram to show the main forces on the air bubble on the SMPs, $F_{b(g)}$ buoyancy force on air bubble, $F_{a(gp)}$ adhesion force between air and the particles, $F_{a(gs)}$ adhesion force between air and substrate surface, $F_{b(p)}$ buoyancy force on SMPs, $F_{m(p)}$ magnetic force on the SMPs, $F_{a(ps)}$ adhesion force between the particles and the surface substrate, m mass of the SMPs, g acceleration due to the gravity on the SMPs. (c) Required minimum magnetic field to hold the desired air volume on a 4.0 mg SMPs de-bubbler, ($n = 3$). (d) Reshaping of the underwater de-bubbler with an attracted air bubble, while reducing the magnetic field on high surface energy glass substrate (left) and on a low surface energy PMMA substrate surface (right). (top – schematic illustration, bottom – behaviour of the SMPs

attracted air bubble (30 μL) while reducing the magnetic field). Colours of the lines illustrate the states of the air bubbles while reducing the magnetic field.

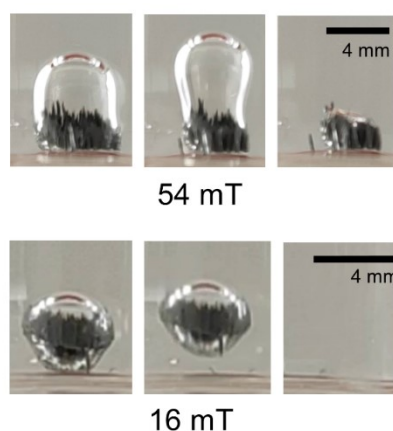


Figure 7.9. (a) 60 μL air bubble leaving the SMPs (4.0 mg) at 54 mT magnetic field (MF). (b) 10 μL air bubble leaving the glass surface together with the SMPs (4.0 mg) at 16 mT.

The SMPs are in the range of 0.7 μm to 5.5 μm . In order to investigate the possible influence of the particle size on the system, the micron size ferromagnetic $\text{C}_8\text{-Fe}$ (SMPs) and the nano size (~ 11 nm) ferrimagnetic $\text{C}_8\text{-Fe}_3\text{O}_4$ (SMNPs) were compared. The loading capacity of the air is increased in SMNPs (~ 80 μL) compared to the SMPs (~ 60 μL) due to their higher surface area as shown in the Figure 7.10a. However, the low saturation magnetisation of the nanoparticles (Figure 7.10b) significantly affects bubble manipulation. In the SMNPs system, although the nanoparticles can be deposited on the surface with air the bubble, the horizontal moving of the magnet with the collected bubble was not efficient due to the low magnetic attraction forces. In this case, higher magnetic field gradients would be required to manipulate the bubble particle system.

The deformation of the air bubble within the SMPs, while reducing the magnetic field is depicted in Figure 7.8d. The SMPs and the air bubble showed low attraction to the glass surface due to the non-polarity of the particles and the underwater superaerophobicity of the glass surface, respectively. Therefore, the particle-air system reduced their surface area over the glass surface while reducing the external magnetic field holding the SMPs. The shape of the de-bubbler reconfigured, as shown in the Figure 7.8d-left, by increasing the particle-air bubble contact angle. When reaching lower magnetic forces, the attraction force (due to the magnetic field) between the

particles and the glass surface decreased, allowing the particles to leave the glass surface with the attached air bubble. However, when using low surface energy substrates, the bubble and the particles were strongly held to the surface due to their higher bubble-substrate surface adhesion force ($F_{a(gs)}$) and particle-substrate adhesion forces ($F_{a(ps)}$). Therefore, in this second case, the variation of shape in the de-bubbler was found to be insignificant, compared to the one of superhydrophilic or underwater superaerophobic surfaces, as shown in Figure 7.8d-right for the PMMA surface.

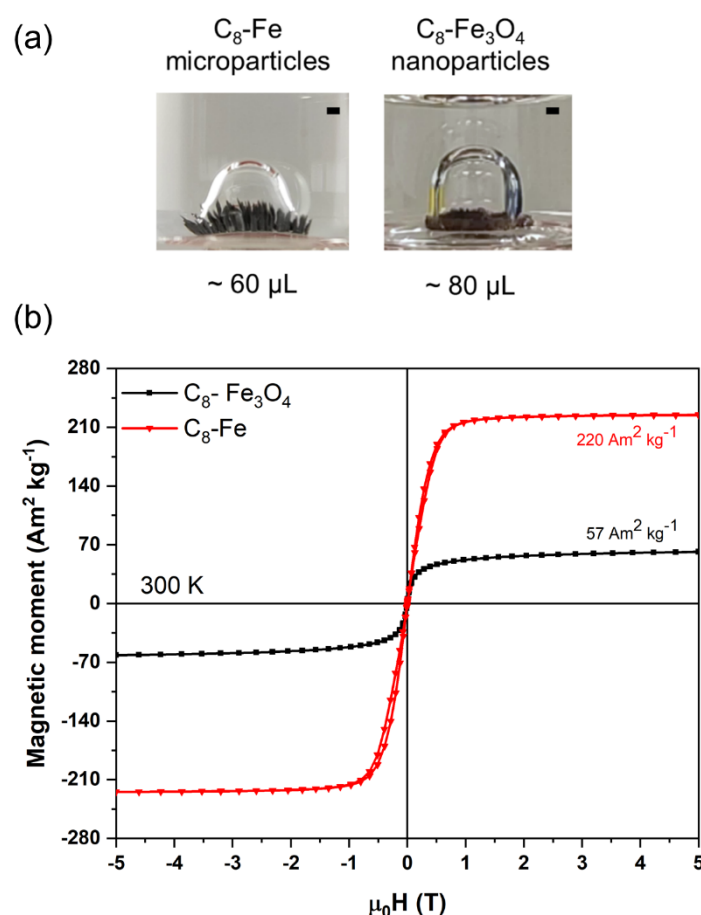


Figure 7.10. (a) Air loading capacity of 4.0 mg SMPs (C_8 -Fe) and SMNPs (C_8 - Fe_3O_4) under 353 mT (MF value on the glass vial surface) gradient magnetic field. (b) SQUID analysis of the SMPs and SMNPs.

7.3.3 Underwater surfaces air de-bubbler: magneto targeted air collection, merging and manipulation

The transportation properties and the transport efficiency of the accumulated bubbles are important in underwater bubble removing applications. Figure 7.11a presents the

air transportation capability of $\sim 38 \mu\text{L}$ of air on a 4.0 mg of SMPs de-bubbler, using a 189 mT magnetic field on an underwater PMMA surface. The de-bubbler followed the magnet without leaving any air bubble or particle fractions on the PMMA surface during movement, providing an efficient magneto-driven bubble system. The magnet driving velocity and the induced bubble system moving velocity were determined as shown in the Figure 7.11b, and were found to be similar. The average velocity of the magnet and the bubble were calculated to be 17.9 mm s^{-1} and 17.7 mm s^{-1} , respectively.

The magnetic particles with the attracted air bubble hold to the magnet by magnetic forces while the horizontal translocation of the magnetic field (movement of the magnet) acted as the main driving force for the de-bubbler movement over the surface. However, the de-bubbler retention force (F_r) consisted of a bubble-surface adhesion force ($F_{a(\text{gs})}$), a particle surface adhesion force ($F_{a(\text{ps})}$) and the aqueous environment fluid dragging force (F_d) of water, which acted oppositely to the magneto driving force. Therefore, the net driving force determined the efficiency of the de-bubbler movement. In Figure 7.11a a PMMA surface was used as the bubble manipulating surface, where comparable low $F_{a(\text{gs})}$ and $F_{a(\text{ps})}$, due to the underwater aerophobicity, and the weak polar and non-polar interactions promoted the de-bubbler translocation. In this case, a magnetic field of 189 mT was sufficient to hold the de-bubbler and, at the same time, to translocate the magnet and generate a net driving force, Figure 7.11b. The synchronising capability of the magnet and the de-bubbler under different magnetic fields is depicted in Figure 7.12, where the magnet moved manually on a horizontal plain. In a low magnetic field (29 mT), the magnet and the de-bubbler were not synchronised due to the low magnetic attraction forces (red box). Over 61 mT, the de-bubbler followed the magnet with a small delay (yellow box). Finally, at high magnetic fields, over 203 mT, a good synchronisation was observed, with nearly the same velocities of the magnet and the de-bubbler (green box).

On the other hand, for experiments performed using PDMS surfaces, Figure 7.13, which shows the collection and translocation of air bubbles at different magnetic fields. 189 mT was inadequate to provide a sustained attraction between the magnet and the de-bubbler, while translocating the magnet to generate a net driving force. (Figure 7.13a) Higher adhesion forces ($F_{a(\text{gs})}$ and $F_{a(\text{ps})}$), due to the underwater aerophilicity and the favourable attraction of the non-polar particles and non-polar PDMS surface, resulted on the de-bubbler to get stuck on the surface, reducing the bubble movement

efficiency. Nevertheless, by increasing the magnetic field to 256 mT (Figure 7.13), the efficiency of the manipulation of the de-bubbler can be improved for the PDMS surfaces. This approach could be applied for other low surface energy materials such as polystyrene and polyurethane.²⁸

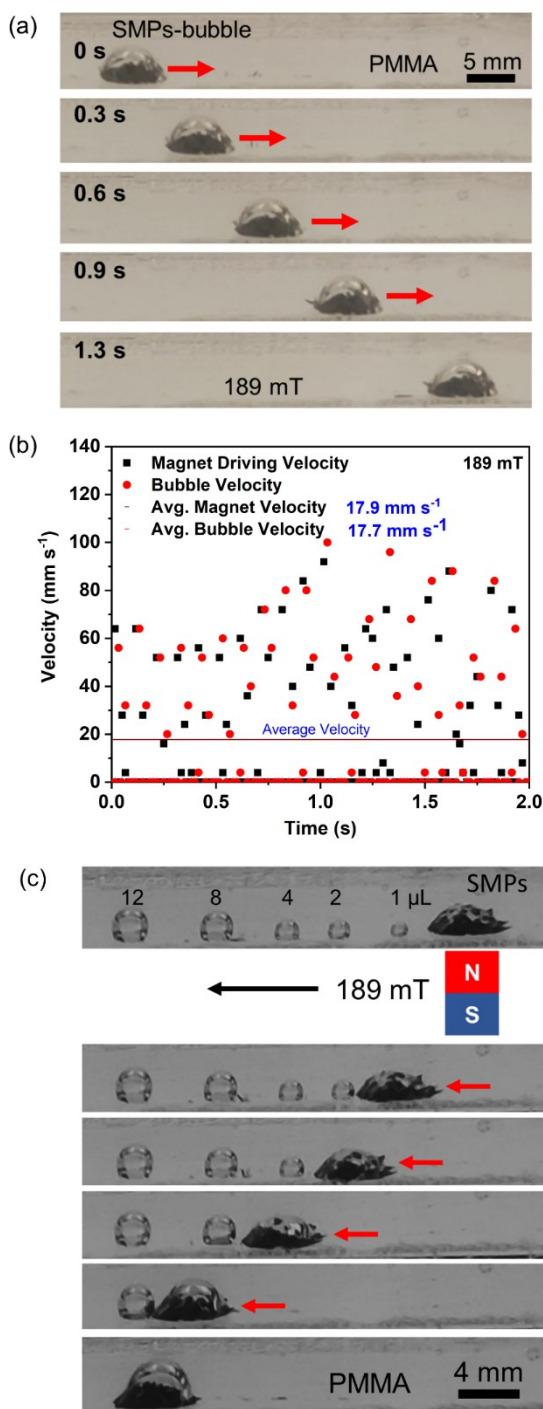


Figure 7.11. (a) Translocation of a 38 μL air bubble ($\sim 11 \mu\text{L}$ at the initial state plus 27 μL of collected air) on the underwater PMMA surface. (b) Comparable estimation of the driving velocity of the magnet and the induced velocity of the air bubble (38 μL) with SMPs, while

transporting on the underwater PMMA surface. Magneto driven collection of air bubbles by SMPs. (c) Merging and collection of different volumes of air bubbles pre-deposited on the underwater PMMA surface (1, 2, 4, 8, 12 μL). A horizontal translocation of 189 mT gradient magnetic field was used to manipulate the air bubbles with 4.0 mg of SMPs.

In order to investigate the behaviour of the air de-bubbler, air bubbles were strategically positioned on an underwater PMMA surface. The volumes of the bubbles were set to be 1, 2, 4, 8 and 12 μL as shown in Figure 7.11c. Then, 4.0 mg of the SMPs was introduced into the underwater PMMA surface, with deposited air bubbles, by the magnet. A horizontal translocation of the magnetic field (189 mT), by moving the magnet, permitted the magnetic manipulation of the SMPs, which attracted the air bubbles on its way, and removed them from the surface. Interestingly, the deposited bubble moved to the SMPs de-bubbler rapidly, leaving the surface, overcoming the adhesive force between the bubble and the surface, facilitating the growth of the bubble deposited on the SMPs de-bubbler. Deposited bubbles have higher internal pressures compared to the bubble in the air de-bubbler thus, they reduce their surface area by merging into the SMPs, reaching a more energetically stable state. Moreover, the underwater superaerophilicity of the SMPs allowed the attraction of the air bubble more efficiently than the PMMA or the glass surfaces, which have lower aerophilicity or aerophobicity, respectively.

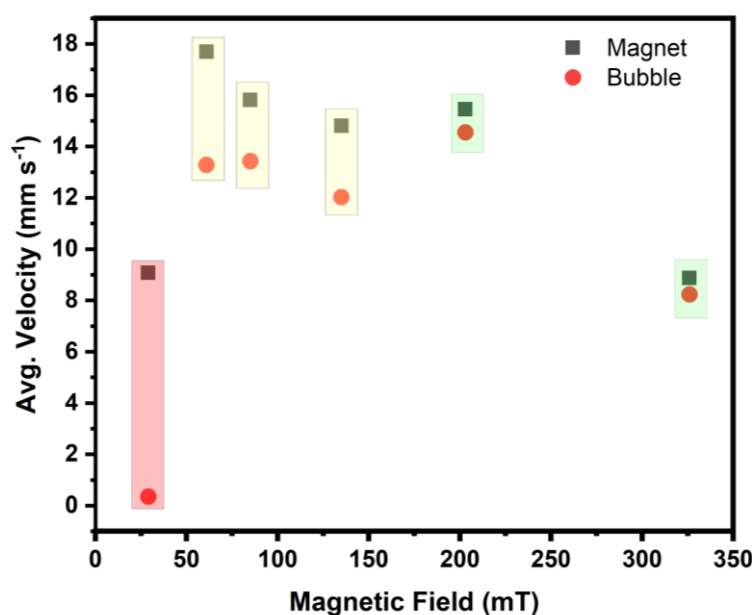


Figure 7.12. Synchronisation of the magnet and the air bubble (38 μL) under different magnetic fields.

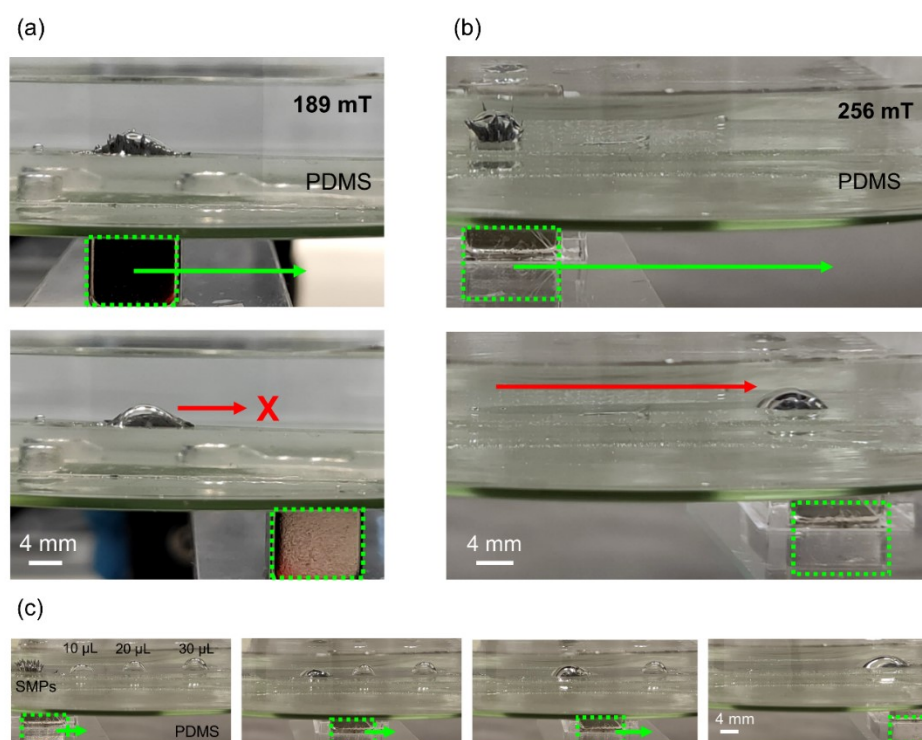


Figure 7.13. Transport of an air bubble settled in a PDMS surface under magnetic field. (a) De-bubbler did not move after magnet translocation due to the low magnetic field, 189 mT. (b) De-bubbler moved with magnet translocation due to the higher magnetic field, 256 mT. (c) Collection of deposited air bubbles of 0, 20 and 30 μL . Magnetic translocation of the bubbles under a 256 mT gradient magnetic field. Translocation of the magnet and the bubble are shown in green and red colours, respectively.

7.3.4 Air de-bubbler application in microfluidics channels

The air de-bubbler was implemented to resolve one of the biggest problems in the microfluidics field, undesired air bubble accumulation in channels.² The novel magneto driven air bubble removal protocol presented above was implemented in a microfluidic device Figure 7.14a (top), as depicted in Figure 7.14a (bottom), schematic illustration. ~ 1.0 mg of SMPs was introduced into the marked inlet compartment and the particles were remotely transported by the magnet to the targeted bubbles present in the main channel. While the de-bubbler passed through the channel, the SMPs collected the bubbles due to the underwater superarophilicity of the particles. Then, the collected bubbles were released at the open outlet and the particles were finally recovered by the magnet at the outlet. As a proof of concept, the removal of a single air bubble (~ 0.3 μL) attached to the PMMA microfluidic channel wall was carried out, Figure 7.14b.

The de-bubbler hold the air bubble due to the underwater superaerophilicity of the particles and the high adhesion force between the air bubble and the (SMPs) particles. A magnetic field of 478 mT provided enough magnetic force to attract the magnetic particles towards the magnet during translocation, overcoming the adhesion forces and to remove and efficiently transport the air bubble along the microfluidic channel. In a second experiment, random multiple air bubbles of different volumes (~ 0.01 - $0.25 \mu\text{L}$ range) and positions were loaded in the PMMA microfluidic channel, getting mainly attached on the top and on the bottom surfaces of the channel, see Figure 7.14c. First, the magnet, and so the de-bubbler, were positioned at the bottom side of the microfluidic device and were moved at 478 mT across the microfluidic channel to sweep (right to the left side) the air bubbles attached to the bottom surface of the wall. 77.3 % of the bubbles were removed at that point. Then, by moving the magnet to the top side of the device, the air bubbles deposited on the top surface were swept (left to the right side) by passing the de-bubbler at 457 mT, achieving 98.9 % total air bubble removing efficiency. Figure 7.4c (right) shows a binary black and white representation chart of the calculation as an example. Moreover, in order to test the performance of the air de-bubbler in other type of surfaces, the system was tested in a microfluidic device in which the bottom and the top surfaces were built by glass and PMMA, respectively. Figure 7.14d shows how air bubbles, deposited at the bottom and top surfaces, were swept by the air de-bubbler using 397 mT for glass and 457 mT for PMMA magnetic fields displacements. It was observed that, the deposition of the air bubbles in the top ceiling surface, PMMA, was higher (96.0 %) when compared to the bottom surface, glass (surface energy $\sim 58.40 \text{ mJ m}^{-2}$), due to the low surface energy and the reduced underwater aerophobicity of the PMMA (surface energy $\sim 41.21 \text{ mJ m}^{-2}$). In this case, a 100.0 % of bubble removal efficiency was achieved by just one single cycle of sweeping. The efficiency was calculated by the evacuated bubble percentage during the magnetic sweeping.

It is worthy to mention here that the efficiency of bubble removal can be improved by increasing the number of sweeping cycles and the amount of SMPs in the air de-bubbler, as long as the SMPs do not block the channel. On the other hand, traces of magnetic particles could get stack at the edges or corners of channels in devices with more complicated channel configurations or when using microfluidic devices with

lower surface energy surfaces. Nevertheless, these particles could be easily recovered by using higher magnetic fields.

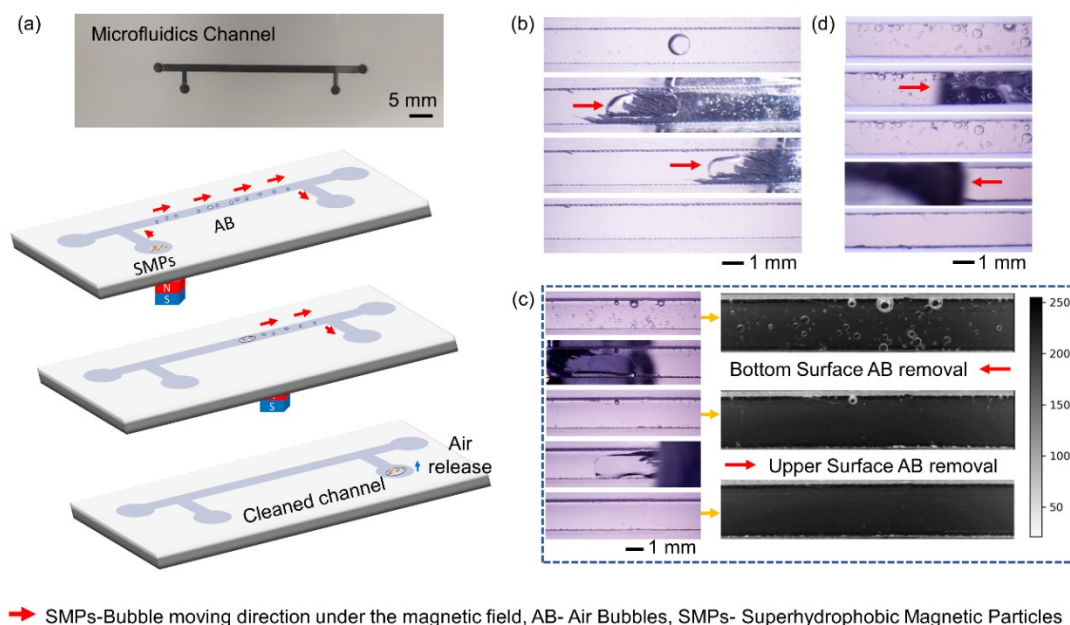


Figure 7.14. (a) Image of the microfluidic device (top), schematic illustration of the mechanism followed by the air de-bubbler in order to remove air bubbles in the microfluidic channel (bottom). Arrows show the direction of the air de-bubbler through the channel. Images of channels with deposited air bubbles before, during and after the application of the de-bubbler system: (b) removal of a single air bubble from a PMMA microfluidic channel under a magnetic field of 478 mT. (c) Removal of multiple air bubbles from a PMMA microfluidic channel under a magnetic field of 478 mT. The magnet was moved through the top and the bottom surfaces for the fully removal of all air bubbles. The right-side image presented the black and white image analysis (bubbles are identified with the white colour border) of the de-bubbled to calculate the efficiency of the bubble removal percentage. (d) Removal of multiple air bubbles in a glass (bottom) and PMMA (top) surfaces microfluidic channel under 397 mT and 457 mT magnetic fields, respectively. The magnet was moved through the top and the bottom surfaces for the fully removal of all the air bubbles.

In this particular case, the influence of the de-bubbler on the performance of the microfluidic device (*e.g.* flow rate) was low since the operation of the de-bubbler was performed in a static mode: (1) liquid flow stops, (2) removal of the bubbles and (3) restarting of the flow. In applications that require a dynamic removal of bubbles, the de-bubbler could perturb the operation of the device. Therefore, for each application, the SMPs passing through the channel will need to be considered and properly evaluated. Nevertheless, this effect can be reduced by using a high surface area magnet

that spread the particles on the channel surface. This would avoid their accumulation in a single spot and so would minimise the inhibition or reduction of the flowing rate. However, the friction effect on the liquid flowing through the channel could be reduced due to the superhydrophobicity of the spread SMPs.

7.4 Conclusion

In summary, we successfully developed an efficient protocol to magnetically collect, merge, transport, and evacuate free and deposited underwater air bubbles from underwater surfaces and microfluidic channels. The de-bubbler consisted of synthesised superhydrophobic magnetic particles with underwater superaerophilicity and with high magneto responsive properties. The underwater superaerophilicity of the particles allowed to trap the underwater air bubbles, while the ferromagnetic property of the particles promoted the remote manipulation of the de-bubbler under a magnetic field by targeting the deposited random air bubbles. The air bubbles collection, merging and the transportation capabilities of the air de-bubbler were demonstrated for both, bulk underwater surfaces and inside of microfluidic channels, acquiring a 98.9 % bubble removing efficiency in the channel. Compared to the existing bubble removal systems, the introduced protocol can be applied to deposited or free bubbles by remotely guiding the de-bubbler with a single magnet. This simple underwater air bubble manipulation and evacuation system will open an easy and cheap way to address the inherent air bubble issue present in most of microfluidics applications without integrating any advanced tools or processes.

7.5 References

- (1) Gunatilake, U. B.; Alvarez-Brãna, Y.; Ojeda, E.; Basabe-Desmonts, L.; Benito-Lopez, F. Underwater Magneto-Driven Air de-Bubbler. *J. Mater. Chem. A* **2022**, *10*, 12832-12841.
- (2) Pereiro, I.; Fomitcheva Khartchenko, A.; Petrini, L.; Kaigala, G. V. Nip the Bubble in the Bud: A Guide to Avoid Gas Nucleation in Microfluidics. *Lab Chip* **2019**, *19* (14), 2296–2314.
- (3) Jones, S. F.; Evans, G. M.; Galvin, K. P. Bubble Nucleation from Gas Cavities -

A Review. *Adv. Colloid Interface Sci.* **1999**, *80* (1), 27–50.

- (4) Meng, D. D.; Cubaud, T.; Ho, C. M.; Kim, C. J. A Methanol-Tolerant Gas-Venting Microchannel for a Microdirect Methanol Fuel Cell. *J. Microelectromechanical Syst.* **2007**, *16* (6), 1403–1410.
- (5) Huang, C.; Wippold, J. A.; Stratis-Cullum, D.; Han, A. Eliminating Air Bubble in Microfluidic Systems Utilizing Integrated In-Line Sloped Microstructures. *Biomed. Microdevices* **2020**, *22* (4), 1–9.
- (6) Young, E. W. K.; Beebe, D. J. Fundamentals of Microfluidic Cell Culture in Controlled Microenvironments. *Chem. Soc. Rev.* **2010**, *39* (3), 1036–1048.
- (7) Olanrewaju, A.; Beaugrand, M.; Yafia, M.; Juncker, D. Capillary Microfluidics in Microchannels: From Microfluidic Networks to Capillary Circuits. *Lab Chip* **2018**, *18* (16), 2323–2347.
- (8) Liu, H.-B.; Gong, H.-Q.; Ramalingam, N.; Jiang, Y.; Dai, C.-C.; Hui, K. M. Micro Air Bubble Formation and Its Control during Polymerase Chain Reaction (PCR) in Polydimethylsiloxane (PDMS) Microreactors. *J. Micromech. Microeng.* **2007**, *17* (10), 2055.
- (9) Meng, D. D.; Kim, J.; Kim, C.-J. A Degassing Plate with Hydrophobic Bubble Capture and Distributed Venting for Microfluidic Devices. *J. Micromech. Microeng.* **2006**, *16* (2), 419.
- (10) Changchun Liu; A. Thompson, J.; H. Bau, H. A Membrane-Based, High-Efficiency, Microfluidic Debubbler. *Lab Chip* **2011**, *11* (9), 1688–1693.
- (11) Cho, H.; Kim, J.; Han, K. H. An Assembly Disposable Degassing Microfluidic Device Using a Gas-Permeable Hydrophobic Membrane and a Reusable Microsupport Array. *Sens. Actuators B Chem.* **2019**, *286*, 353–361.
- (12) Williams, M. J.; Lee, N. K.; Mylott, J. A.; Mazzola, N.; Ahmed, A.; Abhyankar, V. V. A Low-Cost, Rapidly Integrated Debubbler (RID) Module for Microfluidic Cell Culture Applications. *Micromachines* **2019**, *10* (6), 360.
- (13) Huang, C.; Wippold, J. A.; Stratis-Cullum, D.; Han, A. Eliminating Air Bubble in Microfluidic Systems Utilizing Integrated In-Line Sloped Microstructures. *Biomed. Microdevices* **2020**, *22* (4), 1–9.

- (14) Yu, C.; Zhu, X.; Li, K.; Cao, M.; Jiang, L. Manipulating Bubbles in Aqueous Environment via a Lubricant-Infused Slippery Surface. *Adv. Funct. Mater.* **2017**, *27* (29), 1701605.
- (15) Guo, P.; Wang, Z.; Heng, L.; Zhang, Y.; Wang, X.; Jiang, L. Magnetocontrollable Droplet and Bubble Manipulation on a Stable Amphibious Slippery Gel Surface. *Adv. Funct. Mater.* **2019**, *29* (11), 1808717.
- (16) Yu, C.; Zhu, X.; Cao, M.; Yu, C.; Li, K.; Jiang, L. Superhydrophobic Helix: Controllable and Directional Bubble Transport in an Aqueous Environment. *J. Mater. Chem. A* **2016**, *4* (43), 16865–16870.
- (17) Zhu, S.; Bian, Y.; Wu, T.; Chen, C.; Jiao, Y.; Jiang, Z.; Huang, Z.; Li, E.; Li, J.; Chu, J.; Hu, Y.; Wu, D.; Jiang, L. High Performance Bubble Manipulation on Ferrofluid-Infused Laser-Ablated Microstructured Surfaces. *Nano Lett.* **2020**, *20* (7), 5513–5521.
- (18) Schneider, C. A.; Rasband, W. S.; Eliceiri, K. W. NIH Image to ImageJ: 25 Years of Image Analysis. *Nat. Methods* **2012**, *9* (7), 671–675.
- (19) Yu, C.; Zhang, P.; Wang, J.; Jiang, L. Superwettability of Gas Bubbles and Its Application: From Bioinspiration to Advanced Materials. *Adv. Mater.* **2017**, *29* (45), 1703053.
- (20) Wang, J.; Meng, G.; Tao, K.; Feng, M.; Zhao, X.; Li, Z.; Xu, H.; Xia, D.; Lu, J. R. Immobilization of Lipases on Alkyl Silane Modified Magnetic Nanoparticles: Effect of Alkyl Chain Length on Enzyme Activity. *PLoS One* **2012**, *7* (8), e43478.
- (21) Herth, E.; Zeggari, R.; Rauch, J. Y.; Remy-Martin, F.; Boireau, W. Investigation of Amorphous SiO_x Layer on Gold Surface for Surface Plasmon Resonance Measurements. *Microelectron. Eng.* **2016**, *163*, 43–48.
- (22) Gunatilake, U. B.; Morales, R.; Basabe-Desmots, L.; Benito-Lopez, F. Magneto Twister: Magneto Deformation of the Water–Air Interface by a Superhydrophobic Magnetic Nanoparticle Layer. *Langmuir* **2022**, *38* (11), 3360–3369.
- (23) Devouge, S.; Conti, J.; Goldsztein, A.; Gosselin, E.; Brans, A.; Voué, M.; De

- Coninck, J.; Homblé, F.; Goormaghtigh, E.; Marchand-Brynaert, J. Surface Functionalization of Germanium ATR Devices for Use in FTIR-Biosensors. *J. Colloid Interface Sci.* **2009**, *332* (2), 408–415.
- (24) Yong, J.; Chen, F.; Li, M.; Yang, Q.; Fang, Y.; Huo, J.; Hou, X. Remarkably Simple Achievement of Superhydrophobicity, Superhydrophilicity, Underwater Superoleophobicity, Underwater Superoleophilicity, Underwater Superaerophobicity, and Underwater Superaerophilicity on Femtosecond Laser Ablated PDMS Surfaces. *J. Mater. Chem. A* **2017**, *5* (48), 25249–25257.
- (25) Zhang, L.; Nelson, B. J.; Dong, L. Magnetic-Field-Based Self-Assembly. *Encycl. Nanotechnol.* **2012**, 1264–1275.
- (26) Meir, Y.; Jerby, E. Insertion and Confinement of Hydrophobic Metallic Powder in Water: The Bubble-Marble Effect. *Phys. Rev. E - Stat. Nonlinear, Soft Matter Phys.* **2014**, *90* (3), 030301.
- (27) Yu, C.; Zhang, P.; Wang, J.; Jiang, L. Superwettability of Gas Bubbles and Its Application: From Bioinspiration to Advanced Materials. *Adv. Mater.* **2017**, *29* (45), 1703053.
- (28) Hu, G.; Kang, J.; Ng, L. W. T.; Zhu, X.; Howe, R. C. T.; Jones, C. G.; Hersam, M. C.; Hasan, T. Functional Inks and Printing of Two-Dimensional Materials. *Chem. Soc. Rev.* **2018**, *47* (9), 3265–3300.

Overall Conclusion

Fundamental studies on materials and their subsequent applicability advance the development of the material sciences field and thus uphold human well-being and the protection of the environment. The main deliverables through this thesis contribute to the understanding of the properties and behaviour of magnetic materials, improving their usability for future applications. For instance, the knowledge generated on magnetic hydrogels in Chapter 3, provides the fundamental understanding of the properties of differently synthesised magnetic alginate hydrogels (*ex situ* and *in situ*) that would lead to the selection of the appropriate type of magnetic hydrogel synthesis protocol for future applications such as controlled drug delivery systems. In Chapters 4 and 5, the synthesised novel alginate hydrogel-based platform facilitates simultaneous rapid sensing of body fluid biomarkers and remote manipulation. The introduced scaffolds contribute to the advance of novel sensing technologies for Lab-on-a-Chip and Lab-in-a-bead. Finally, the magnetic particle systems presented in Chapters 6 and 7 expand the knowledge of usability of low surface energy magnetic particles for Lab-on-a-chip and environmental applications.

Magnetic alginate hydrogel beads are one of the vastly reported magneto-driven miniaturised nanocomposites, which are used for multiple applications, such as medical, environmental or even as actuators in devices. In these beads, the magnetic phase is integrated into the polymer matrix by direct blending, *ex situ*, or by *in situ* nucleation, to obtain magneto driven hydrogel matrixes. However, these two types of beads, which are fabricated through two different protocols in Chapter 3, show divergent stabilities in non-identical ionic density aqueous media. For instance, the *in situ* synthesised beads degrade rapidly, showing low stability behaviour in neutral pH/ low ionic density aqueous media. On the other hand, the *ex situ* synthesised beads are stable in the same conditions, showing an opposite behaviour. The reason for that is the generation of ionic by-products inside of the bead (*in situ*) during the mineralisation of the magnetic phase inside of the bead, which increases the ionic density in the bead. Therefore, in order to stabilise the ionic density of the bead and so to reduce its ionic density, water molecules penetrate inside of the bead through the alginate membrane, when the bead is in a low ionic density aqueous media. These types of media are commonly used in environmental and biological applications. At those conditions, *in situ* synthesised beads start to degrade when the crosslinking bond strength exceeds the maximum bead swelling capacity, due to the diffusion of water inside the beads,

promoted by their high ionic density, which tries to stabilise with the media. Nevertheless, they show advantages compared to *ex situ* synthesised beads, like their cheap, in one-step, fast fabrication method.

In order to overcome the inherent low stability behaviour of *in situ* synthesised beads, a coating process to generate an extra alginate layer on the bead is necessary. This investigation provides with a fundamental framework to understand the properties of *ex situ*, *in situ* and modified *in situ* synthesised magnetic metal-oxide based alginate hydrogels, directing the path to select the most adequate magnetic bead mode (*ex situ*, *in situ*, and modified *in situ*) according to the required magneto-driven hydrogel application. As an example, the findings of this investigation support the use of a specific bead-fabrication protocol for, for instance, a required, controllable drug delivery system, whether employing a quick or a prolonged release of molecules, for a particular application.

It is interesting to point out that the *in situ* synthesised nanoparticles, exhibit a low particles size of ~ 3 nm when compared to *ex situ* synthesised Fe_3O_4 nanoparticles, ~ 8 nm. This is explained considering the confinement of $\text{Fe}^{3+}/\text{Fe}^{2+}$ in the alginate hydrogel matrix during the nucleation and growth of the Fe_3O_4 nanoparticles inside the bead. In the future, further investigation of this effect would lead to formalise a model to control the particle sizes with respect to the hydrogel conditions (monomer and cross linker ratios), by introducing a universal method to synthesise specific particles in a hydrogel media. In addition, these *in situ* synthesised particles show a magnetite crystal phase with a low tendency to oxidise due to the alginate coating. Their magnetisation values, in combination with their low magnetic hysteresis, enable them to be used for magneto-driven applications.

Magneto-driven colorimetric sensors provide remotely handling, guiding and manipulating capabilities when the sensors are integrated into a Lab-on-a-Chip system. In this regard, the functionalities of the sensor scaffold are important since directly define the quality and the efficiency of the microfluidic device. In this regard, TiO_2 nanotubes alginate scaffolds could be used as sensing optical materials due to the secure, high loading capacity of the colorimetric and enzymatic assays, and the rapid sensing. Then, these scaffolds can be used for the colorimetric detection of biomarkers

in biological fluids (*e.g.* lactate and glucose), when integrating the required enzymatic assay. As a proof of concept of this technology, a scaffold is fabricated by immobilising enzymatic catalytic assays of LOX/GOX and HRP with TMB chromophore in a TNT/alginate nanocomposite, Chapter 4. A rapid colorimetric signal (blue colour optical signal read out) is observed for artificial sweat biomarkers in the TNT/alginate hydrogel platform. Concerning the other reported scaffolds, TNT/alginate scaffold shows high loading capacity of the sensor assays and rapid optical readout recording, due to the contribution of the hydrogel and the superhydrophilicity of the TiO₂ nanotubes. Moreover, the TNT/alginate scaffold can be combined with other materials, such as paper, for the generation of a simple paper-based microfluidic device. The new functionalities of this scaffold open new avenues to improve microfluidic paper-based analytical devices by just incorporating alginate-based materials. Therefore, this biocompatible colorimetric biosensor scaffold is a promising tool to implement real time detection of sweat biomarkers in wearable devices.

Continuing with the development of novel magneto driven colorimetric sensors, the next step is the addition of magnetic properties to the TNT/alginate scaffold, by introducing a magnetic phase (Fe₃O₄ nanoparticles or Fe particles) into the hydrogel matrix. Nevertheless, those types of particles destroys the colorimetric sensing property of the scaffold since they interfere on the colour detection due to the inherent black colour of the magnetic particles. Therefore, it is desirable to be able to fabricate a C₈-Fe/ TNT/alginate scaffold containing both magnetic actuation and colorimetric sensing properties. In order to do that a novel fabrication process is presented. The application of a magnetic field while crosslinking the hydrogel scaffold, allows to confine the superhydrophobic magnetic Fe particles to the bottom of the hydrogel bead without interfering to the optical signal read out recording area on top. As well, the so-called Janus bead exhibits soft magnetic properties while keeping an efficient biosensing ability, Chapter 5. The most straightforward application is to be able to perform colorimetric sensing in blood since direct colorimetric sensing of this biofluid is complicated due to the interference of the red colour coming from the red blood cells over the sensing scaffold. The Janus bead, acts as a membrane for red blood cell filtering, preventing the entrance of cells within the scaffold. The scaffold is tested to detect glucose levels in plasma and blood, and the expected blue colour response of the bead was successfully generated without any interference from the red blood cells. This

novel Janus bead shows multiple functionalities such as efficient biosensing, remote handling capability under magnetic field and red blood cells filtering ability. Therefore, it can be considered as a universal hydrogel scaffold for biosensing, named Lab-on-a-bead system in the microfluidic field. This miniaturised system has a versatile opportunity to be integrated into small-scale and large-scale devices with the above-mentioned functionalities. Besides that, as an example, this system can be used to sense analytes in unapproachable spots by remotely sending the bead to a specific location, immobilising the required chemical assays within the bead. Then, after performing the detection, the bead can be collected back by using the magnetic field, and perform the signal reading.

The reduction of the surface energy of the magnetic particles differs the attraction towards the solutions or polymer solutions when compared to the bare magnetic particles, which are discussed in Chapter 3. Particularly, their surface wetting behaviour facilitates these compelling systems to be applied in microfluidics as magnetic liquid marbles, oil capturing systems, and bubble marbles. Spanning the studies within the state of the art, an exclusive superhydrophobic magnetic particles system is introduced, called magneto twister, Chapter 6, which includes the properties provided by magnetic liquid marbles in droplet microfluidics, such as the transportation of liquid droplets. The floating superhydrophobic magnetic particle collide layer in water-air interface, incurves downwards with the water-solid/water-air interface under the magnetic field, where the observed bending is more pronounced with the increase of the magnetic field value. The solid-water interface touches the depth of the water container with the increment of the magnetic field, making a stable flipped conical structured water interface, with a twister shape providing a stable magneto movable system. This magneto twister is used to manipulate water droplets in a water environment by just placing a water droplet over the twister and transporting the droplet with the displacing of the applied magnetic field, facilitating water droplet translocation in aqueous media. As well, this system successfully overcomes the instability and unexpected destruction behaviour of the conventional magnetic liquid marbles by providing a robust system while handling the droplets. Further, the applicability of the magnetic twister, as a magnetic plug to separate liquids inside of an open surface channel is successfully demonstrated. Finally, the magnetic twister is used to collect and remove floating microplastic particles from the surface of water. Since the twister

has a steep water-air interface slide is capable to move the particle towards the twister, enabling the collection of particles and subsequent removal of the particles away by just translocating the magnet underneath the twister. This unconventional magnetic twister system opens up new pathways to utilise superhydrophobic magnetic nanoparticles for water-air interface applications. For instance, water-miscible aqueous droplets are transported over aqueous media without mixing, in a controllable manner, by using this system, providing a versatile and facile way to manipulate two miscible aqueous mediums.

Similar superhydrophobic magnetic particles can be applied to address one of the fundamental problems in microfluidics, the deposition of air bubbles in the surface of the channels when filled with aqueous solutions, Chapter 7. Low surface energy magnetic particles are used as a smart material to trap, collect and eliminate deposited air bubbles in aqueous systems, surfaces and in microfluidic channels. The underwater superaerophilicity and the high magnetisation of the particles led to trap, manipulate and to remove air bubbles in a controlled manner, without contaminating the aqueous sample, in a simple way. This novel and versatile protocol secures bubble-free underwater surfaces or microfluidics channels. The air bubbles collection and the transportation capability is demonstrated for both a bulk underwater surface system and inside of a microfluidic channel, acquiring ~ 99% bubble removing efficiency in the channel. This simple underwater air bubble manipulation and evacuation system will open up an easy and cheap way to address the air bubble issue without integrating any advanced tools or mechanisms. Moreover, this protocol is also promising in many underwater applications such as, removing deposited gas bubbles in electrodes.

In this thesis, several fundamental aspects of magnetic hydrogels and magnetic particle platforms have been developed. The key objectives of this work were driven by the urgent need of understanding applied magnetic materials to be used in applications such as remotely manipulable microfluidics and body fluid sensing. The findings of this thesis, concerning the different sub-objectives, generated new knowledge on the behaviour and properties of alginate base magnetic hydrogels, on magneto driven body fluid scaffolds and on magnetic particles systems, for their latter integration in microfluidic devices.

Acknowledgements

Last three years, I spent most of my time at the University of the Basque Country in Vitoria-Gasteiz and a short period at Trinity College, Dublin and Microliquid. The accomplishments I gain so far would not be possible without the support of many people and I take this opportunity to appreciate their support and kindness.

First and foremost, I thank Assoc. Prof. Fernando Benito and Prof. Lourdes Basabe for selecting me as an early stage researcher to the Microfluidics Cluster UPV/EHU group under the Marie Skłodowska-Curie innovative training network. Fernando and Lourdes are great humble scientists and it was my privilege to call them as my research supervisors, advisors and mentors. Over the past three years, I mostly worked with Fernando and I was amazed of his positive visualisation of observations and ability to look at anything positively, which is exceptionally fascinating. Lourdes is one of the best humble female scientists I have ever worked with, and her constructive criticism with fruitful discussions always help me to polish my work. As well, their confidence in me, and providing a perfect balance of freedom and guidance during my work, facilitate me to grow up as an independent researcher.

I would like to show my sincere appreciation for the main funding support received from the Marie Skłodowska-Curie innovative training network, European Union's Horizon 2020 research and innovation program under grant agreement No. 766007. Grateful acknowledgments must go to the Faculty of Pharmacy in the University of the Basque Country and the Lascaray research institute for providing me with laboratory facilities. Further, I thank Prof. Luiz Lezama, director of the doctoral program in Materials Science and Technology, for allowing me to read the doctoral degree and organising fruitful seminars and sessions. As well, I thank the MAMI (magnetism and microhydrodynamics) European project that organised multiple training workshops and meetings that directly helps to improve my both academic and soft skills.

I am grateful to Prof. Micheal Coey for allowing me to work and complete my research secondment in his laboratory, Magnetism, and Spin Electronics at Trinity College, Dublin. As well, I highly appreciate the immense support given by Dr. Munuswamy Venkatesan during my stay in Dublin.

Over the past three years, I received help from all of my lab mates and I am especially grateful to Dr. Edilberto Ojeda who helped me to settle in Vitoria-Gasteiz at the beginning of my arrival to Spain and I am glad that I had good research collaborations with him. As well, my warmest thanks go to Vahid Nasiri who arrived to the microfluidics Cluster UPV/EHU around the same time as I did, and later Daniel Patko, to having great discussions at all times and being good friends. Further, I thank all the members in the microfluidics cluster including Raquel Catalán, Alba Calatayud, Enrique Azuaje, Yara Alvarez, Sandra García, Jon Mercarder, Maite Hernández, Janire Saez, Sergi Cinca, Juncal Alonso, Adriana Abalos and the members in Magnetism and Spin Electronics at Trinity College, Tim Butcher, Sruthy Poulouse, Lucy Prendeville, Anup Kumar, Rui Zhang and Zexiang Hu. As well, I thank Dr. Rafael Morales for his collaboration and support in my research work. As well, I would like to thank all my colleagues and the mentors in MAMI European project for their academic support and enjoyable moments.

I am grateful to Markel Lafuente, my neighbour lab colleague for his numerous support, and Alicia Sanchez, Alejandro Díez, Alfredo Sarmiento, Aitor Larrañaga and Ricardo Andrade for the support in material characterisation and the special appreciation goes to SGIker of the University of the Basque Country for providing equipment and technical access.

It was an honour and a privilege to work at the Microfluidics Cluster UPV/EHU at the University of the Basque Country. There were people outside of my academic who helped me in numerous ways and without them, the time I spent in Vitoria could be hard. Especially I thank Delia Garcia, for all the support she has given to me and my family in my last three years, could be helped me to peruse my carrier without wasting time.

Finally, I am grateful to my parents, my brother, my wife and my daughter for their immense love, care, support and encouragement. Without them, I would not be where I am today.

Curriculum Vitae

Udara Bimendra was born in Kandy, Sri Lanka. After completing the General Certificate of Education (GCE) Advanced Level in the physical science stream, he was able to be selected to the Faculty of Science, University of Peradeniya to read for his primary degree in Science. After a two months internship and one-year research project of conducting polymers and antistatic textiles under the supervision of Prof. Gamini Rajapakse, he obtained Bachelor of Science (B.Sc.) Special Degree in Chemistry. Subsequently, he engaged with the Energy & Advanced Material Chemistry Research Group at National Institute of Fundamental Studies, Sri Lanka as a research assistant and he received a three-year research scholarship from the National Science Foundation, Sri Lanka to continue his research activities. During this time, he completed his Master of Philosophy (M.Phil.) degree under the supervision of Prof. Jaysundera Bandara. The title of his thesis was “Fabrication of underwater superoleophobic and superhydrophilic membranes to purify oil contaminated wastewater” and Postgraduate Institute of Science, University of Peradeniya, Sri Lanka, offered the degree. Afterward, he worked as a Technology Entrepreneur at Research & Innovation Department at Stretchline Holdings, and undertook the projects of wearable technology and smart textiles before he started his doctoral studies. In 2018, he joined to the Microfluidics Cluster UPV/EHU at the University of the Basque Country, Spain as an early stage researcher under the Marie Skłodowska-Curie Actions ITN grant and started his doctoral research on Magneto-driven smart materials under the supervision of Assoc. Prof. Fernando Benito and Prof. Lourdes Basabe. While progressing in Spain, he completed a research secondment at Magnetic and spin electronics group, Trinity College Dublin, Ireland for five months and one-month Secondment at Microliquid. His research interest relates on investigate fundamentals to generate knowledge while focussing on applied material systems to develop human and environmental needs.

Publications and Conferences

Publications

- (1) **Gunatilake, U. B.**; Garcia-Rey, S.; Ojeda, E.; Basabe-Desmots, L.; Benito-Lopez, F. TiO₂ Nanotubes Alginate Hydrogel Scaffold for Rapid Sensing of Sweat Biomarkers: Lactate and Glucose., *ACS Applied Materials and Interfaces*, 2021, 13 (31), 37734–37745. <https://doi.org/10.1021/ACSAMI.1C11446>
- (2) **Gunatilake, U. B.**; Venkatesan, M.; Basabe-Desmots, L.; Benito-Lopez, F. Ex situ and in situ Magnetic Phase Synthesised Magneto-Driven Alginate Beads., *Journal of Colloid and Interface Science*, 2022, 610, 741–750. <https://doi.org/10.1016/j.jcis.2021.11.119>
- (3) **Gunatilake, U. B.**; Morales, R; Basabe-Desmots, L.; Benito-Lopez, F. Magneto Twister: Magneto deformation of water-air interface by a superhydrophobic magnetic nanoparticles layer., *Langmuir*, 2022 38 (11), 3360-3369. (*Cover article*) <https://doi.org/10.1021/acs.langmuir.1c02925>
- (4) **Gunatilake, U. B.**; Alvarez, Y; Ojeda, E.; Basabe-Desmots, L.; Benito-Lopez, F. Magneto Targeted Underwater Air De-bubbler., *Journal of Materials Chemistry A*, 2022, 10, 12832-12841. (*Back cover article*) <https://doi.org/10.1039/D2TA01009G>
- (5) **Gunatilake, U. B.**; Abalos, A.C. ; Garcia-Rey, S; Ruiz, J.M; Basabe-Desmots, L.; Benito-Lopez, F Lab-in-a-Bead: Magnetic Janus Bead Probe for the Detection of Biomarkers in Whole Blood., *Small*, (18-03-2022) Under review- ID smll.202201710.
- (6) Garcia-Rey, S., Ojeda, E., **Gunatilake, U. B.**, Basabe-Desmots, L., & Benito-Lopez, F. Alginate Bead Biosystem for the Determination of Lactate in Sweat Using Image Analysis., *Biosensors*, 2021, 11(10), 379. <https://www.mdpi.com/2079-6374/11/10/379>

Conferences

- (1) **U. B. Gunatilake**, E. Ojeda, S. Garcia-Rey, L. Basabe-Desmouts, F. Benito-Lopez. TiO₂ Nanotubes-Hydrogel Biosensor Scaffold for Sweat Monitoring 24th International Conference on Miniaturized Systems for Chemistry and Life Sciences, Micro Total Analysis Systems, Online μ -TAS-2020, October 2020 (POSTER).
- (2) **U. B. Gunatilake**, Y. Alvarez, Y, E. Ojeda, L. Basabe-Desmouts, F. Benito-Lopez. Air Bubbles Trapping, Collection, and Elimination in Aqueous Channels, 25th International Conference on Miniaturized Systems for Chemistry and Life Sciences, Micro Total Analysis Systems, μ -TAS-2021, USA, October 2021. (POSTER)
- (3) **U. B. Gunatilake**, L. Basabe-Desmouts, F. Benito-Lopez. Maximization of magneto driven alginate beads, New Materials for a Better Life: Advanced devices and Materials as Key Enabling Technologies for Sustainable Environment" (NM4BL 2019) Conference at Leioa, Spain, October 2019. (POSTER)
- (4) **U. B. Gunatilake**, E. Ojeda, S. Garcia-Rey, L. Basabe-Desmouts, F. Benito-Lopez. TiO₂ Nanotubes Alginate Hydrogel Scaffold for Rapid Sensing of Sweat Biomarkers – Lactate and Glucose, New materials for a better life!: Advanced Materials for next-generation Biomedicine, Biotechnology and Bioelectronics, (NM4BL 2021) Leioa, Spain, October 2021. (POSTER)
- (5) **U. B. Gunatilake**, Y. Alvarez, Y, E. Ojeda, L. Basabe-Desmouts, F. Benito-Lopez. Magneto Assisted Underwater Bubble Manipulation, WE-Heraeus Seminar on "Optoelectronic Processes at Nanostructured Interfaces", Bad Honnef, Germany, March 2022. (POSTER)
- (6) **U. B. Gunatilake**, L. Basabe-Desmouts, F. Benito-Lopez. Biocompatible, in-situ generated magnetic alginate beads, Biomimetics Symposium, Max Planck

Institute for Dynamics and Self-Organization, Göttingen, Germany, July 2020.
(ORAL)

- (7) **U. B. Gunatilake**, L. Basabe-Desmots, F. Benito-Lopez. Magneto Driven Smart Materials for Biosensing and Actuation, Neutron & Synchrotron Radiation for Science & Technology Symposium, LLB, Paris, France, December 2021.
(ORAL)
- (8) **U. B. Gunatilake**, L. Basabe-Desmots, F. Benito-Lopez, Low Surface Energy Magnetic Particle-Systems for Microtechnology, Magnetic Microhydrodynamics- An Emerging Research Field, Mittelwhir, France, June 2022. (ORAL)
- (9) S. Garcia-Rey, E. Ojeda, **U. B. Gunatilake**, L. Basabe-Desmots, F. Benito-Lopez. Alginate Bead Biosensors for the Determination of Lactate Levels Using Image Analysis, 25th International Conference on Miniaturized Systems for Chemistry and Life Sciences, Micro Total Analysis Systems, μ -TAS-2021, USA, October 2021. (POSTER)

